Numerical Investigation of Particles Breakage and Growth in Gas-Solid Processes: Spiral Jet Milling and Polyolefin Polymerization in Fluidized Bed Reactors

Doctoral Dissertation
Doctoral Program in Chemical Engineering (34^{th} cycle)

Numerical Investigation of Particles Breakage and Growth in Gas-Solid Processes: Spiral Jet Milling and Polyolefin Polymerization in Fluidized Bed Reactors

Carmine Sabia

* * * * * *

Supervisors
Maurizio C. Barbato, Supervisor
Antonio Buffo, Co-supervisor
Daniele L. Marchisio, Co-supervisor & Tutor

Doctoral Examination Committee:
Prof. Marco Vanni, Politecnico di Torino
Prof. Timothy F.L. McKenna, Referee, University of Lyon
Prof. Alberto Cuoci, Referee, Politecnico di Milano
Prof. Giuseppe Storti, Politecnico di Milano
Dr. Tommaso Casalini, AstraZeneca

Politecnico di Torino
June 2022

I hereby declare that, the contents and organisation of this dissertation constitute my own original work and does not compromise in any way the rights of third parties, including those relating to the security of personal data.

. . . . . .

Carmine Sabia

Turin, June 2022

A mio padre,
a mia madre,
ai miei fratelli.

Summary

This thesis aims at studying the spiral jet milling process of active pharmaceutical ingredients (APIs) and the polyolefins polymerization process by means of Eulerian-Eulerian simulations.

The micronization of pharmaceutical powders via spiral jet milling is an industrial process that uses high-energy gas to realize collisions between particles, which eventually break down into smaller size components.
The physics behind the process is complex and its understanding is not trivial. Particles are moved by a high-velocity compressible gas flow and impacts force powders to undergo a fragmentation process that reduces the particle size by order of magnitudes, making the spiral jet milling description really challenging.
A well-known problem of the APIs processing is the formation of large solid aggregates that stick on the spiral jet mill walls and reduce the micronization chamber volume, compromising the process effectiveness and taking the final size of particles out of target. This phenomenon, called caking, requires the apparatus stoppage to mechanically remove the formed crusts that have to be wasted. The large cost associated to many pharmaceutical powders and the time needed to clean the system cause a huge economic loss.
This work is focused at numerically studying the caking mechanism to understand the effect that the chamber diameter reduction has on the gas velocity fields for standard operating conditions of the spiral jet mill. A simple mimic strategy is proposed to emulate the chamber volume reduction due to crusts formation and the system fluid dynamics is studied by means of single-phase CFD simulations to determine the causes that take the final particles size out of specific.
Simulations show that caking causes the deterioration of the classification capabilities of the system if the gas mass-flow rate is kept constant, especially near the spiral jet mill upper and lower walls, allowing larger particles to escape the micronization chamber. In order to avoid the forced transport of massive particles towards the system outlet, the nozzle absolute pressure has to remain constant to keep the fluid spin ratio and the classification characteristics unchanged while caking is building up.

Spiral jet milling still lacks of a solid theoretical ground able to properly describe the physics behind the process and the determination of substance-specific operating conditions is usually based on expensive experimental campaigns driven by the technicians' experience. This, together with the impossibility of experimentally characterize the system to avoid the multiphase flow field corruption, put big constraints on the experimental study of the process and problems that may affect it, such as caking, are not studied in detail.
In this framework, the work reported in this thesis also describes the construction of a novel uncoupled quasi-3D model able to study the spiral jet milling at process scales and times.
The gas velocity fields computed through 3D single-phase CFD simulations are provided as input in a 1D compartmentalized model to calculate solid velocities along the micronization chamber radial direction. Mass and momentum balance equations are used to build a computational model in which the solids velocities are calculated availing of simple algebraic relationships developed for pneumatic transport. The particles size reduction is taken into account through a breakage kernel that is function of gas energy and solid holdup. A set of parameters is tuned through *ad hoc* experiments to consider the substance-specific breakage behaviour and the characteristics of the inlet particle size distribution.
The model performance are evaluated for lactose and paracetamol by validating the predictions for D10, D50 and D90 against design of experiments data taken as reference.
In good agreement with the assumptions made at the beginning of the derivation, model predictions are better if an high-specific energy process is considered, *i.e.,* high pressure and low solid feed-rate (dilute flow conditions). The best results are obtained if small particles are processed (low Stokes number) and if the inlet particle size distribution is narrow.
It is shown that simulation predictions can be improved if a specific-pressure parameters set is calculated, especially when treating fragile materials with wide inlet distributions.
Finally, suggestions on some possible model formulation enhancements and future works are given.

The second topic studied in this thesis is the simulation of polydisperse Eulerian-Eulerian gas-solid flows for analyzing the polymerization process of polyolefins in fluidized bed reactors (FBRs).
In order to study such a process, modelling tools represents a valid and necessary option to design the operating conditions and ensure the desired product quality in terms of final particle size and molecular properties.
Two modelling approaches are usually employed to this end, multiscale kinetic

models and detailed CFD-based models. The first type of framework, usually involving compartmentalized models, has the major advantage to be computationally affordable, offering the possibility of implementing detailed single particle models. On the other hand, the reactor fluid dynamics is usually described through semi-empirical relationships that makes them suitable for a narrow range of applications.
CFD models, instead, provide the fully detailed calculation of the multiphase flow field but at computational cost that is not always affordable, especially if applied to real-scale systems.
This study focuses on the calculation of the fluidization properties of FBRs by comparing the results obtained through a simplified 1D compartmentalized model and those coming from detailed 2D multiphase CFD model with the kinetic theory of granular flows to account for the granular nature of solid particles.
The behaviour of a bed composed by Geldart A-B type particles is analyzed for different operating conditions in a system without reaction and solid injection or withdrawal, focusing on the steady-state fluid dynamics behaviour of monodisperse and polydisperse particles populations.
Results show that the simplified compartmentalized approach is capable to predict the solid mixing in the bubbling fluidization regime for high-density polyethylene particles. Average volume fractions are close to the values predicted by the CFD model along the whole cylindrical part of the reactor, especially for monodisperse particles. Predictions are in good agreement also for broad size distributions, especially in terms of average diameters. Considering the negligible computational cost associated to compartmentalized models if compared to CFD and their versatility to implement complex kinetic schemes, such multiscale approaches represent an effective tool for industrial process design.
Anyway, the detailed description of the polymerization process during time can be extremely helpful in predicting the flow rates and the particle size of the final product.
In this context, CFD approaches constitute a reliable tool for determining the operating conditions needed to obtain given output particles properties.
The scientific literature does not offer any mature modelling set-up able to study FBRs in the continuous operating mode since large production plants require a huge computational effort to correctly discretize the system in space and time.
The last part of the thesis aims, therefore, at understanding if a 2D scaled geometry can effectively describe the continuous polymerization process by correctly predicting average particles size and solid holdups.
Starting from a desired particles residence time and typical operating conditions, simple material balances are used to calculate the scaled-down reactor volume and

a CFD-PBM model is implemented to simulate the multiphase fluid dynamics inside the reactor. The polymerization process is modeled through the DQMOM approach and a simple particle growth model is validated against an analytical solution. Different solid withdrawal positions along the reactor axis and inlet flow rates are studied to determine their influence on the final solid holdup and average particle sizes within the reactor.
The results show that the solid holdup does not change remarkably if the outlet position is varied along the reactor height but it increases if the catalyst feed-rate is increased. The reactor is well-mixed at any location and, as for the non-reactive cases, the particles average size does not change remarkably along the reactor axis. Large particles are found only in the very bottom part of the reactor.
Calculations show that the computational approach proposed allows the description of a steady-state operation by simulating a limited physical time (order of 10^2 s). On the other hand, it is not possible to correctly calculate the reactor holdup since the system tends to empty itself for every condition and solid outlet topology tested.

Acknowledgements

Grazie a Maurizio, per la supervisione di questi anni ed avermi dato l'opportunità di lavorare nel suo gruppo di ricerca. Grazie per avermi sostenuto nell'impegno di studiare in una prestigiosa Scuola Dottorale.
Grazie a Daniele ed Antonio, per la supervisione e la guida durante il percorso del Dottorato.
Grazie a Jetpharma SA, partner del progetto MACH. Grazie a Luca Martinoli, per la cortese disponibilitá e l'impegno profusi durante il progetto, e a Giovanni Frigerio, per il sostegno tecnico e le proficue discussioni sullo spiral jet milling.
Grazie al Prof. Storti, per le interessanti e stimolanti discussioni scientifiche. Grazie per la supervisione e l'aiuto.
Grazie a Tommaso ed a Luca per la collaborazione nei vari ambiti di ricerca che abbiamo affrontato.
Grazie ai colleghi con i quali ho lavorato in questi anni.
Grazie a chi mi è stato vicino.

Grazie alla mia Famiglia.

Contents

Chapter 1

Introduction

1.1 Current Challenges in Multiphase CFD Simulations for Gas Solid-solid Flows

Multiphase modeling for computational fluid dynamics is still a challenging task and the construction of reliable and general computational frameworks is difficult because models are derived for specific applications and they usually cannot be extended to other fields without modifying them.
This study is focused on two particular applications involving gas-solid mixtures: the spiral jet milling (SJM) for pharmaceutical active ingredients (APIs) micronization and the polyolefins polymerization in fluidized bed reactors (FBRs).
While the multiphase flow-fields description in FBRs is a mature argument is scientific research and the tematic has been extensively studied in the past, SJM and related particle-particle interactions constitute a florid research field since the physics behind the process is complex and the current understading is still based on a practical know-how which lack of a solid theoretical ground.
Both the processes need investigations to evaluate the current modeling capabilities or propose approaches able to describe the whole process in an affordable computational time, providing particle information at quasi-steady state regime, overcoming the current limitations due to model complexity or excessive computational domain size.

The next sections aim at motivating this work without entering the argument in detail because a complete description of the current modelling frontiers is given in the applications chapters.

1.1.1 A Brief Introduction to Spiral Jet Milling Problems and Simulation

Spiral jet milling is an industrial process used to micronize active pharmaceutical ingredients. Although it is mainly used to treat medical substances, some of which are expensive such as steroids and anti-tumor drugs, the spiral jet miling and the apparatus in which the process is carried out are little studies and much of the technical knowledge about operating parameters comes from expensive and time-consuming experiments.
A well-know problem of the process is caking. It consists in the formation of rigid aggregates that stick on the micronization chamber walls and reduce its useful volume, deteriorating the performance of the system and taking the finish product particle size distribution (PSD) out of specific. In order to eliminate or mitigate the problems induced by caking, which often ends in the apparatus stoppage for cleaning purposes and the waste of the crusts formed by APIs, the understanding of the gas flow corruption due to the aggregates formation and subsequent chamber reduction is of paramount importance. In this framework, CFD simulations constitute an interesting tool to investigate the flow-field properies without strumenting the micronization chamber, to avoid problems related to the usage of probes in high-velocity and highly-loaded gas-solid flows.
Among the different approaches that can be adopted, Eulerian-Lagrangian simulations are usually employed to study the flow established inside spiral jet mills. CFD-DEM models give detailed information on the particles dynamics but they are computationally intensive and currently do not allow for the simulation of industrial-scale processes in a reasonable time. In addition, the inclusion of appropriate constitutive laws describing particle breakage provides further modeling and numerical challenges (Higashitani *et al.* [1]).
It was however proven in different works that precious information on the fate of the solid particles can be gained by simpler single-phase approaches (Boccardo *et al.* [2–5]; Crevacore *et al.* [6, 7]; Icardi *et al.* [8]) in which the focus is on the continuous fluid (gaseous in this case) phase.
The simulation of particle-particle and particle-wall interactions for a fully coupled CFD-DEM solution is still far from describing the whole process and current published works can provide information on the first few instants of the micronization process only [9–13].
In this scenario, a novel modeling structure able to provide process-scale information such as the particle size distribution of substances at the end of the micronization at reasonable computational cost would constitute an undoubted help in defining the best operating conditions for milling a given API, reducing the expensive experiments nowadays used to gather this information.

1.1.2 A Brief Introduction to Fluidized Bed Reactors Simulation

The polyolefins polymerization process is carried out in apparatus called fluidized bed reactors. In this kind of systems, an ethylene mixture is passed through a granular material consisting in catalyst or pre-polymerized particles. The gas flow fluidizes the solid that works as active sites to initiate the poymerization reaction at pressures ranging between 20 and 40 MPa and temperatures around 100 °C.
The pressure exerted by the polymer growing within the catalyst pores breaks the particles into small pieces that remain inglobed inside the polymer formed in parts per million. Once the polymer particles weight is large enough to win the drag exerted by the ascending gas flow, the solid starts to fall down due to gravity and it is gathered at the bottom of the reactor. At this position, the particles can be discharged through the withdrawal outlet.
The operation of FBRs has been simulated with different approaches for many years and it still constitutes a florid research field.
Among the computational tools available, multi-scale kinetic models such as compartmentalized approaches are very popular because they offer the possibility of implementing complex single-particle models at a reasonable computational cost. Their major drawback consists in the simplified fluid dynamics description used to calculate the phases motion.
On the other hand, CFD multiphase models allows for the detailed description of the interplay between the gas and solid phases in geometries close to the real-plant ones but they requires a much more demanding computational effort. Moreover, the implementation of complex polymerization kinetics is not trivial and an increase in the model complexity usually results in a deterioration of the tool stability.
Even though the fluidized beds CFD multiphase features have been extensively studied in the past, to the best of the author knowledge, no attempts of describing the continuous operation of FBRs have been made.
Indeed, this type of simulations are usually ran in batch mode without any solid injection or withdrawal location. CFD models are exploited to develop hydrodynamic and drag laws [14–16], formalize new numerical methods [17] or assess existing ones [18, 19], derive and implement physical models [20–22] or investigate the bubbles dynamics [23–25], always operated in batch.
In this scenario, the assessment of the volume fraction and average size distribution predictions obtained through computationally-efficient compartmentalized approaches by comparison with detailed CFD models would give important information about the affidability of such a simplified fluid dynamics description. Moreover, the evaluation of the possibility of simulating the FBRs continuous operation availing of CFD multiphase models would help in the enhancement of this

kind of predictive tools.

1.2 Objectives

According to the motivation given in the above section, the objectives of this work consist in studying the caking mechanism, proposing a simple strategy to mimic the chamber volume reduction due to aggregates formation and to study the influence that crusts have on the velocity fields, by means of single-phase CFD simulations. The work is completed by the construction of a novel computationally-efficient model for the description of spiral jet milling at process-times and scales.

Alongside to the main research line constituted by the micronization process, the particle distribution inside fluidized bed reactors has been anayzed to asses if a simplified approach based upon standard three-phase compartmentalized models can be effectively used for predicting the solid volume fractions and particle average size distribution inside the reactor. To this end, compartment-based model results are compared to detailed CFD simulations. In addition, a strategy to scale down the reactor geometry and to simulate the polymerization process through particle growth modeling has been developed and tested to understand if the FBRs continuous operation mode can be simulated in a reasonable computational time.

1.3 Thesis Outline

Chapter 2 is intended to introduce the CFD approaches usually adopted to model multiphase flows with particular focus on gas-solid mixtures. A short description of multiphase regimes and classification, along with relevant non-dimensional numbers, is given to provide the basic knowledge needed to understand the current computational approaches used to model multiphase mixtures, namely the Eulerian-Lagrangian and the Eulerian-Eulerian methods. The latter is described in detail and a motivation about the numerical model chosen is given.
Chapter 3 introduces the population balance equations for describing the polydispersity of real populations of particles and the computational methods available to solve them numerically. The description concludes with the solution method selection.
Chapter 4 describes the spiral jet milling process and the simple methodology adopted to simulate the effect that caking has on the gas flow-fields inside the system. A novel model for the prediction of the particle size distribution at the end of the micronization is presented and validated against experimental results.

Chapter 5 focuses on the analysis of the polyolefins polymerization process and, more in detail, on the comparison between solid distribution results obtained through a detailed CFD multiphase model and a 1D-cost effective compartment-based model to assess if the simplified approach proposed by the latter can be used for predictions purposes. The last part of the work deals with the derivation of a procedure to scale-down the reactor geometry to propose a computational framework for simulating the polymerization process in continuous operation mode.
Eventually, Chapter 6 concludes the thesis by summarizing the work carried out and underlying the major findings. A perspective on the needed next steps and further models improvments is also given.

The work described in this thesis is based upon the following journal pubblications:

- C. Sabia, G. Frigerio, T. Casalini, L. Cornolti, L. Martinoli, A. Buffo, D.L. Marchisio & M.C. Barbato, "A detailed CFD analysis of flow patterns and single-phase velocity variations in spiral jet mills affected by caking phenomena". Chem. Eng. Res. Des. 174 (2021) 254-253.

- C. Sabia, T. Casalini, M. Spaggiari, L. Cornolti, G. Frigerio, L. Martinoli, A. Martinoli, A. Buffo, D.L. Marchisio & M.C. Barbato, "A novel uncoupled quasi-3D Euler-Euler model to study the spiral jet mill micronization of phar,maceutical substances at process scale: model development and validation". Submitted to Powder Technol.

- C. Sabia, A. Buffo, T. Casalini, D.L. Marchisio, M.C. Barbato & G. Storti, "FBR for polyolefin production in gas phase: validation of a two-phase compartmentalized model by comparison with CFD". Macromol. React. Eng. 2100058.

This Ph.D. thesis is written in the framework of a larger project called MACH (Modeling and Amelioration of micronization process in spiral jet mills controlling the Caking pHenomenon - grant nr. 37766.1 IP-ENG) funded by the Swiss Innovation Agency (Innosuisse) along with Jetpharma SA, under the scientific supervision of Politecnico di Torino.

The arguments presented in the above pubblications along with the material written in this document are the output of the work performed by the writer and his supervisors.
Note that the material reported in the listed sections comes from the collaboration with other people:

i. Chapter 4, Section 4.2, Sub-section 4.2.2 - Experimental Activities. The Ph.D. candidate, along with Mr. Frigerio (CTO of Jetpharma SA), designed the experimental campaign, defined the micronization operating conditions and supervised part of the experiments. The Design of Experiment was produced by Mr. Spaggiari (SUPSI, now FHNW Brugg-Windisch) while micronization experiments were carried out in Jetpharma production plants in Balerna (CH) by specialized technicians.

ii. Chapter 4, Section 4.4, Sub-section 4.4.3 - 1D Compartmentalized Model. The Ph.D. candidate worked on the compartmentalized model development and testing with Dr. Casalini (SUPSI, now AstraZeneca Sweden) and Dr. Cornolti (SUPSI).

iii. Chapter 5, Section 5.3 - Two-phase Compartmentalized Model. The Ph.D. student conducted the research on fluidized bed reactors under the guidance of Prof. Storti (ETH Zurich, now Politecnico di Milano). Prof. Storti's major contribution was in the two-phase compartmentalized model derivation.

Chapter 2

CFD Simulation of Gas-Solid Flows

This chapter is intended to briefly describe the most important features of multiphase flows and their classification according to the level of coupling between phases. The two main CFD approaches used to treat multiphase flows, namely the Eulerian-Lagrangian and the Eulerian-Eulerian approaches, are presented. More information about Eulerian-Eulerian models is given because they are the most common option to simulate industrial processes at real-scale. The research work reported in this thesis is mainly based on this latter category of computational methods.

2.1 A Brief Introduction to Multiphase Flow Modeling

A phase is a region of space with uniform properties (density, concentration, ...) that can exists in different forms, *i.e.,* gas, liquid and solid states.
Two or more phases coexisting at the same time form a multiphase flow. Along with the concept of multiphase flow, the notion of volume fraction has to be defined as:

$$\alpha_i = \frac{\mathrm{V}_i}{\mathrm{V}} \tag{2.1}$$

where V_i indicates the volume occupied by a generic phase i and V stands for the total volume. The volume fraction can vary from 0 to 1.
Moreover, a phase is called *primary* if it occupies the largest volume and its motion governs the multiphase mixture, while a phase is called *secondary* if it occupies a

smaller volume into the domain and it is transported by the primary phase.
From a modeling point of view, besides the classification done on thermodynamic basis, a futher separation can be determined according to particular physical properties that cause a given material to behave differently to an external stress.
For example, let us assume to have a gas-solid mixture in which a wide distribution of particles is moved by a fluid flow in a reactor. The solid particles are all made by the same material with the same physical properties (density and shape factor) but their entrainment and velocity depends on their size. Small particles, indeed, will follow strictly the gas stream while larger ones will move with a certain detachment from the carrier phase that depends on their own inertia.
This suggests that an important distinction can be done accordingly to the particles mass and therefore volume, and different solid phases can be defined to model the behaviour of differently-sized objects.

Another important multiphase flow classification is given by the relative distribution of phases. A flow can be *separated*, if the phases exhibit a sharp interface, or *dispersed*, if the secondary transported phase is homogeneously distribuited within the carrier one.
Figure 2.1 depicts a sketch representing two typologies of separated flows and two different disperse flows examples.
To the first category belong multiphase flows showing a sharp interface and a well defined relative position, such as a water river moving below a gas atmosphere (b), or mixed bulks of different liquids occupying the same volume (c).
The second category, instead, incorporates homogeneously distributed mixtures where a secondary phase is evenly dispersed into the carrier one, such as solids in a fluidized bed, gas bubbles in a liquid flow (d) or water droplets moving in an air duct (e).
In many applications the two flow typologies may be simultaneously present (*e.g.* boiling flows) - (a) and, in addition, it may happen that along with the transition, the primary and secondary phase invert one with the other (*e.g.* bubble risers).

Multiphase flows move with different properties according to the so-called flow regime or maps. These maps help in having an overview on overall mixture properties for given operative conditions (flow rates) in some particular regimes. In the case of gas-solid flows, for example, the conventional fluidization of solid particles may occur in steps called fixed bed, minimum fluidization, bubbling fluidization, slugging fluidization and turbulent (or dilute-phase flow) fluidization [26].
The gas velocity that moves particles increases passing from the fixed bed operation mode, where the fluid that laps the solid has a velocity that it is not sufficient to sustain the particles, to the turbulent fluidization, where the gas has a velocity

so high that the solid is moved in a pure pneumatic transport mode.
These flow maps are useful in designing industrial system such as fluidized bed that usually operates in the bubbling fluidization regimes.

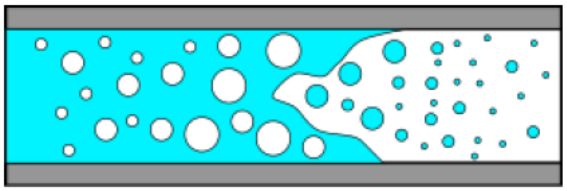

(a) transient two-phase flow

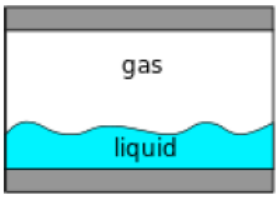

(b) stratified flow

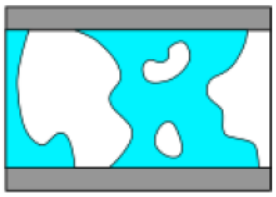

(c) separated bulk flow

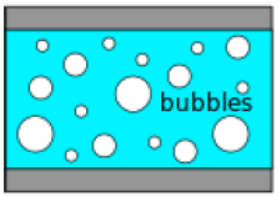

(d) bubbles in a liquid

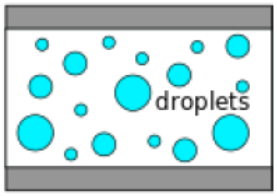

(e) droplets in a gas

Figure 2.1: Schematization of a transitional flow with the simultaneous presence of dispersed and separated phases (a), of separated flows composed by a liquid flowing below a gas phase (b) and two mixed bulks of fluids (c) exhibiting a sharp interface. Sketch of two dispersed flows composed by gas bubbles in a liquid (d) and liquid droplets in a gas (e). Taken from Marchisio, 2021 [27].

Relevant Dimensionless Numbers

Multiphase flows can be categorized using a large quantity of non-dimensional groups. The majority of them, listed in Table 2.1, characterizes dispersed flows whose this tractation is limited to. All the relationships reported refer to the dispersed phase through the subscript d and to the continuous/carrier one availing of the subscript g.
The first two groups, called phase-density ratio and phase-mass ratio, both make use of phases densities to give information on the importance of inertial effects (ϕ_ρ) or to understand if a flow is dilute or dense, through the usage of volume fractions (ϕ_m).
The disperse-phase Reynolds number, better known as particle Reynolds number

if it is used for gas-solid flows, describes the relative importance of the inertial effects of disperse objects with a given diameter with respect to the continuous phase. It can be used to identify the typology of the phases interactions.
Some of the numbers listed in Table 2.1 apply only to fluid-fluid disperse multiphase flow, such as the phase-viscosity ratio ϕ_μ, or are mainly used for gas-liquid applications, such as the Eötvös number or the Morton Number. These, in fact, are usually employed to characterize the shape of bubbles moving in a fluid since an increase of them corresponds to the generation of ellipsoidal, wobbling, dimpled ellipsoidal-cup, skirted and spherical-cap bubbles [27]. The capillary number is used to determine if a bubble can break-up when subjected to a certain shear rate $\dot{\gamma}$.

Table 2.1: Non-dimensional groups used to characterize multiphase flows. Subscript d indicates the dispersed/secondary phase while subscript c indicates the continuous/primary phase. ρ identifies the mass density, μ stands for the molecular dynamic viscosity, α is used to describe the volume fraction while σ and $\dot{\gamma}$ are the interfacial tensione between the disperse and the continuous phase and the shear-rate associated to the primary phase. τ_c identifies the characteristic time scale of the carrier phase. $\mathbf{u}$ is the velocity vector, d identifies the diameter of the disperse element and g is the acceleration due to gravity. Taken from Marchisio, 2021 [27].

Definition	Formula
phase-density ratio	$\phi_\rho = \frac{\rho_\mathrm{d}}{\rho_\mathrm{c}}$
phase-mass ratio	$\phi_\mathrm{m} = \frac{\alpha_\mathrm{d}\rho_\mathrm{d}}{\alpha_\mathrm{c}\rho_\mathrm{c}}$
phase-viscosity ratio	$\phi_\mu = \frac{\mu_\mathrm{d}}{\mu_\mathrm{c}}$
disperse-phase Reynold number	$\mathrm{Re_d} = \frac{\rho_\mathrm{d}\lvert\mathbf{u}_\mathrm{d}-\mathbf{u}_\mathrm{c}\rvert\mathrm{d}}{\mu_\mathrm{c}}$
Eötvös number	$\mathrm{Eo} = \frac{\mathrm{d}^2\mathrm{g}\lvert\rho_\mathrm{c}-\rho_\mathrm{d}\rvert\mathrm{d}}{\sigma}$
Morton number	$\mathrm{M} = \frac{\mathrm{g}\mu_\mathrm{c}^4\lvert\rho_\mathrm{c}-\rho_\mathrm{d}\rvert\mathrm{d}}{\rho_\mathrm{c}^3\sigma^3}$
Capillary number	$\mathrm{Ca} = \frac{\mu_\mathrm{c}\dot{\gamma}\mathrm{d}}{2\sigma}$
Stokes number	$\mathrm{St} = \frac{\rho_\mathrm{d}\mathrm{d}^2}{18\mu_\mathrm{c}\tau_\mathrm{c}}$

One of the most important and used non-dimensional groups in multiphase flow modeling is the Stokes number that is obtained by formalizing a simple force balance acting on a spherical object, either a bubble, a droplet or a solid particle.

It describes the time required by the disperse phase to adapt to a continuous phase velocity variation. If St<< 1 the disperse phase moves closely to the continuous phase while a condition with St≥ 1 corresponds to have a particle that moves with its own velocity field, decoupled to the continuous phase.

Phase Coupling

The mutual influence that one phase exterts on the other strongly depends on their volume fractions. The continuous phase mainly governs the mixture motion and for this reason it is called primary phase. The other transported or adiacent phases, present in lower quantity, are called secondary phases and the coupling level is defined accordingly to their volume fractions.
Figure 2.2 depicts a simple representation of three different coupling levels. The sketch shows small solid particles immersed in a surrounding continuous fluid.

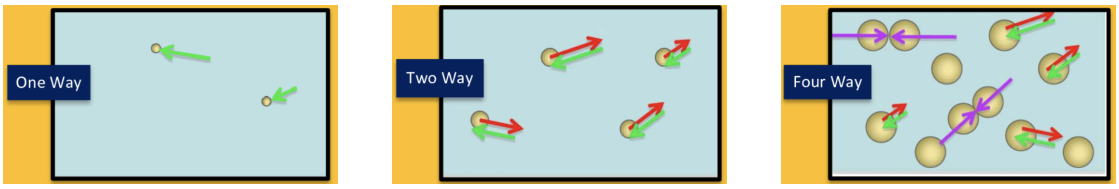

(a) one-way coupling $\alpha_s \leq 10^{-3}$ **(b)** two-way coupling $10^{-3} < \alpha_s \leq 10^{-2}$ **(c)** four-way coupling $10^{-2} < \alpha_s \leq 10^{0}$

Figure 2.2: Schematic representing the fluid-particle interactions for different levels of coupling between phases.

The two phases are said to be one-way coupled if the continuous phase determines the motion of the disperse phase but the latter is so dilute that it can not affect the carrier. This condition is usual when the disperse volume fraction is below 0.001.
When the volume fraction of the secondary phase increases such that $10^{-3} < \alpha_s \leq 10^{-2}$, the phases motion is mutually coupled and one phase influences the other and viceversa. This condition is known as two-way coupling.
If the phsysics evolves towards a dense regime, then the disperse phase objects interact through collisions may resulting in coalescence (for bubbles and droplets), aggregation (particles), agglomeration (particles) and breakage (particles, bubbles and droplets) in the so-called four-way coupling regime.

2.2 Computational Models for Multiphase Flows

Multiphase flows can be investigated via computational models which can be divided into two categories, namely:

- the Eulerian-Lagrangian formulation;
- the Eulerian-Eulerian formulation.

The Eulerian-Lagrangian computational models describe the primary phase as a continuum while the secondary phase is treated as an ensemble of discrete objects, whose motion is governed by the Newton second law of motion and the momentum exchange with the primary phase.

The Eulerian-Eulerian formulation, instead, considers all the simulated phases as continuous mediums but the level of detail of the flow solution can be different, according to the approach chosen for describing the interface between the phases. If the phases interface is explicity tracked, the detailed motion of the thin region separating the two phases is characterized availing of the popular volume-of-fluid (VOF) or level-set method (LSM). These two approaches are direct numerical simulation (DNS) models because they provide information on the phases presence availing of an indicator function that directly solves the volume fractions equations, by accurately describing the space presence of one or the other phase.
Becuase of the explicit tracking of the interface, these fluid-fluid methods are computationally intensive and cannot be used to model large domains.
In order to reduce the computational cost associated to the simulation of large multiphase systems, another approach called two-fluid model (TFM) or, if more than two phases are simulated, multi-fluid model (MFM) can be used to compute average fields of polydisperse fluid-fluid and fluid-solid flows (Marchisio [27]). Depending on the secondary phase flow characteristics, usually considered through the Stokes number, the multi-fluid model can be implemented with or without the solution of momentum balance equations for the disperse phase and the velocity is computed only at mixture level. This particular approach is called Mixture model (MiM) and allows for retrieving the single-phase velocity field by availing of the instantaneous equilibrium hypothesis by solving an algebraic equation [27] or, in a later evolution of the approach, by solving an alternative velocity formulation obtained exploiting the mixture and relative velocities.

Because of the affordable computational cost and the possibility of modeling polydisperse multiphase flows, multi-fluid models are preferreded to Lagrangian approaches in many engineering applications.

This tractation is limited to gas-solid flows and the description that follows is aimed at reporting relationships holding for a gas phase (subscript g) and for a particulate disperse phase (subscript p), underlying the hypothesis at the base of each model and its applicability.

2.3 The Eulerian-Lagrangian Approach

In the Eulerian-Lagrangian approach the secondary phase, where secondary phase means solid particles, is tracked resolving transport equations for each phase involved in the simulation as shown by the following relationhip [28]:

$$\frac{\mathrm{d}\mathbf{u}_\mathrm{p}}{\mathrm{d}t} = \frac{\mathbf{F}_\mathrm{D}}{\mathrm{m}_\mathrm{p}} + \mathbf{g}\frac{\rho_\mathrm{p} - \rho_\mathrm{g}}{\rho_\mathrm{p}} + \mathbf{A} \tag{2.2}$$

where $\mathbf{A}$ is an acceleration force per unit mass and $\mathbf{u}_\mathrm{p}$ is the disperse particle velocity vector. ρ_p is the particle density and ρ_g is the primary phase density. The relation considers gravity effects through the gravitational acceleration vector $\mathbf{g}$.

As shown by Equation (2.2), a force balance is solved to compute the particle velocity and, therefore, the trajectory.

The drag force $\mathbf{F}_\mathrm{D}$ per unit particle mass m_p (N/kg) is written as:

$$\frac{\mathbf{F}_\mathrm{D}}{\mathrm{m}_\mathrm{p}} = \frac{18\mu_\mathrm{g}}{\rho_\mathrm{p}{\mathrm{d}_\mathrm{p}}^2} \cdot \frac{\mathrm{C}_\mathrm{D}\mathrm{Re}_\mathrm{p}}{24}|\mathbf{u}_\mathrm{p} - \mathbf{u}_\mathrm{g}|. \tag{2.3}$$

C_D is the drag coefficient, $\mathbf{u}_\mathrm{g}$ is the carrier phase velocity vector, μ_g is the dynamic viscosity of the primary phase, d_p is the particles diameter or their characteristic length while Re_p is the relative or particle Reynolds number (with the same definition of the disperse-phase Reynolds number), defined as:

$$\mathrm{Re}_\mathrm{p} \equiv \frac{\rho_\mathrm{g}\mathrm{d}_\mathrm{p}|\mathbf{u}_\mathrm{p} - \mathbf{u}_\mathrm{g}|}{\mu_\mathrm{g}}. \tag{2.4}$$

The motion of the primary continuous phase is, instead, described by the following equation written in Eulerian framework:

$$\frac{\partial \alpha_\mathrm{g}\rho_\mathrm{g}}{\partial t} + \nabla \cdot (\alpha_\mathrm{g}\rho_\mathrm{g}\mathbf{u}_\mathrm{g}) = \mathrm{S}_\mathrm{mass}; \tag{2.5}$$

$$\frac{\partial \alpha_\mathrm{g}\rho_\mathrm{g}}{\partial t} + \nabla \cdot (\alpha_\mathrm{g}\rho_\mathrm{g}\mathbf{u}_\mathrm{g}\mathbf{u}_\mathrm{g}) = \alpha_\mathrm{g}\nabla p - \alpha_\mathrm{g}\nabla \cdot \boldsymbol{\tau}_\mathrm{g} - \mathbf{S}_\mathrm{g} + \alpha_\mathrm{g}\rho_\mathrm{g}\mathbf{g} + \mathbf{F} \tag{2.6}$$

where α represents the volume fraction, ρ is the density, S_mass is the mass source term that is present when there is exchange of mass between the phases, $\mathbf{S}_\mathrm{g}$ is the

momentum source terms due to exchange of momentum between phases, while **F** represents generic volume forces.
Subscripts g and p refer to the carrier phase and particulate disperse phase, respectively.
Depending on flow characteristics and the problem nature, different forces can be included in the model. The drag force is usually always present, while others such as lift or virtual mass force have to be taken into account depending on the phases coupling, which is a property usually defined by the particle loading, and the disperse phase physical characteristics.
Since each particle is tracked and the simulation resolves the motion for each one of them (including discrete events such as collisions,...), a large computational effort is needed and only very dilute flows can be treated with this approach. The rigorous calculation of the entire particles population makes the description of polydispersity a straightforward task, allowing the motion of each discrete entity with its own velocity field.

2.4 The Eulerian-Eulerian Approach

In Eulerian-Eulerian models all phases are treated as continuum media. The full Eulerian approach is well suited to treat separated flows, availing of the VOF or the LSM models by directly tracking the phases interface, or to study dispersed flows, either with low or high particulate loading [29], when the analysis focuses on the distribution and the overall behavior of the secondary phases rather then the detailed motion of single particles.
Since the main assumption of the model consists in considering all the phases as continuum media, this approach works better when the volume fraction of the disperse phase is quite large, making this method particularly suited for dense flows. It is possible to simulate also dilute flows ($\alpha_\mathrm{p}/\alpha_\mathrm{g} \leq 0.01$) with an acceptable description of the mixture properties.

The full Eulerian formulation solves a variable number of equations, depending on the velocity formulation chosen for each component present in the computational domain. Coupling between phases is achieved through a shared pressure equation while inter-phase exchange coefficients (*e.g.*, drag force) are modeled to consider the mutual influence that one phase exerts on the other.
The distribution of phases is computed by means of transport equations for volume fractions written for each phase minus one, exploiting the continuity constraint that volume fractions sum to unity.
Within the Eulerian-Eulerian approach, two different models can be identified,

according to the disperse phase velocity formulation:

- Mixture formulation;
- Two-fluid/Multifluid formulation.

Besides the Mixture and the Multifluid formulations, the VOF approach [27, 28] was also proposed as a method to effectively treat flows in which phases exhibit a sharp interface.
The latter solves transport equations for the mixture only, without any slip velocity formulation, meaning that all the field variables are shared by phases. An indicator function is solved to track the interface position and the volume fraction equation is calculated for the primary phase only. The volume fraction of the secondary phase is computed by means of an algebraic equation based upon the continuity constraint.
Interface-capturing models are suitable for studying well-separated flows, such as external flows (*e.g.* air-water interface of rivers) or the detailed bubbles dynamics. Since phenomena here described involve interpenetrating media, these approaches are not considered as an option and they are not described in the following pages.

The Mixture Model

The Mixture model is used to describe well-mixed or homogeneous flows with strong coupling between phases, advected by the same velocity field. It is usually recommended for dilute flows with small particles because the volume fraction of the dispersed phase is so low that the forces exerted on the primary phase are negligible and the system is supposed to be dominated by one-way coupling. Small and low-density particles move with small Stokes numbers, without requiring the solution of a separated momentum equation for the secondary phase in order to consider its own particles motion.
The Mixture model applied to a N-phases system (either fluid or particulate) solves the momentum, continuity and energy equation for the mixture, the volume fraction equation for the primary phase only and, in its simplest formulation, an algebraic expression for the relative motion, based upon the slip velocity concept. In general, this approach is reccomended when the particulate loading is so low that the secondary phase motion is not of interest and the dispersed phase can be assumed as totally driven by the primary one, neglecting any particular behavior that may have relevance for the particles distribution.

Depending on the hypothesis at the base of its derivation, the Mixture model can be categorized into three sub-models which basically differ because of the coupling level assumed for the turbulent interaction terms.

The simpler mixture model, called Algebraic Slip Mixture Model (ASMM), implements an algebraic velocity formulation for computing a slip between the primary and the secondary phase. If constant-density phases are assumed to have a strictly coupled motion, then the Drift-Flux Model (DFM) can be formalized, serving as the most popular and diffused formulation of the Mixture model family. This work is intended to briefly describe the newly proposed Diffusion Mixture Model (DMM), which represents the most sofisticated and complete model of this typology, consisting in a generalization of the DFM able to calculate the motion of small Stokes number objects such as bubbles in water columns. A precise and rigorous descripton of the mathematical derivation of it is given by the work of Tronci *et al.* [30] and this elaboration is based upon its manuscript.

DMM solves the multiphase system as a pseudo-single phase system by writing governing equations for average quantities.
The concept of averaging the mixture properties, which is at the base of the model, comes out if the single-component transport equations for continuity and momentum balances for a generic phase i are written:

$$\frac{\partial \alpha_i \rho_i}{\partial t} + \nabla \cdot (\alpha_i \rho_i \mathbf{u}_i) = \Gamma_i; \tag{2.7}$$

$$\begin{aligned}\frac{\partial \alpha_i \rho_i \mathbf{u}_i}{\partial t} + \nabla \cdot (\alpha_i \rho_i \mathbf{u}_i \mathbf{u}_i) = -\alpha_i \nabla p_i - \nabla \cdot [\alpha_i (\tau_i + \tau_{ti})] \\ + \alpha_i \rho_i \mathbf{g} + \mathbf{M}_i.\end{aligned} \tag{2.8}$$

If we sum over the N phases that compose the multiphase system, we have:

$$\frac{\partial}{\partial t} \underbrace{\sum_{i=1}^{N} (\alpha_i \rho_i)}_{\rho_\mathrm{m}} + \nabla \cdot \underbrace{\sum_{i=1}^{N} (\alpha_i \rho_i \mathbf{u}_i)}_{\rho_\mathrm{m} \mathbf{u}_\mathrm{m}} = 0. \tag{2.9}$$

Eq. 2.9 incorporates two new variables, namely the mixture density ρ_m and the mixture velocity $\mathbf{u}_\mathrm{m}$:

$$\rho_\mathrm{m} = \sum_{i=1}^{N} (\alpha_i \rho_i)\,; \qquad \mathbf{u}_\mathrm{m} = \frac{1}{\rho_\mathrm{m}} \sum_{i=1}^{N} (\alpha_i \rho_i \mathbf{u}_i). \tag{2.10}$$

Exploiting the fact that the sum over all the volume fractions has to give the unity and introducing a new term $\mathbf{u}_{\mathrm{M}i} = \mathbf{u}_i - \mathbf{u}_\mathrm{m}$ called diffusion velocity, the DMM equations become:

$$\frac{\partial \rho_\mathrm{m}}{\partial t} + \nabla \cdot (\rho_\mathrm{m} \mathbf{u}_\mathrm{m}) = 0; \tag{2.11}$$

$$\frac{\partial \rho_{\mathrm{m}} \mathbf{u}_{\mathrm{m}}}{\partial t} + \nabla \cdot (\rho_{\mathrm{m}} \mathbf{u}_{\mathrm{m}} \mathbf{u}_{\mathrm{m}}) = -\nabla p_{\mathrm{m}} - \nabla \cdot (\tau_{\mathrm{eff}}) + \rho_{\mathrm{m}} \mathbf{g} \tag{2.12}$$

where:

$$\tau_{\mathrm{eff}} = \tau_{\mathrm{m}} + \tau_{\mathrm{Tm}} + \tau_{\mathrm{Dm}} \tag{2.13}$$

and:

$$\tau_{\mathrm{m}} = -\mu_{\mathrm{m}} \sum_{i=1}^{N} \left[\nabla \mathbf{u}_i + (\mathbf{u}_i)^{\mathrm{T}} - \nabla \cdot \frac{2}{3} \mathbf{I} \mathbf{u}_i \right]; \tag{2.14}$$

$$\tau_{\mathrm{Tm}} = -\mu_{\mathrm{Tm}} \sum_{i=1}^{N} \left[\nabla \mathbf{u}_i + (\mathbf{u}_i)^{\mathrm{T}} - \nabla \cdot \frac{2}{3} \mathbf{I} \mathbf{u}_i \right] - \frac{2}{3} \rho_{\mathrm{m}} k_{\mathrm{m}} \mathbf{I}; \tag{2.15}$$

$$\tau_{\mathrm{Dm}} = -\nabla \sum_{i=1}^{N} \left(\alpha_i \rho_i \mathbf{u}_{\mathrm{M}i} \mathbf{u}_{\mathrm{M}i} \right); \tag{2.16}$$

$$\mu_{\mathrm{m}} = \sum_{i=1}^{N} \alpha_i \mu_i; \tag{2.17}$$

$$\mu_{\mathrm{Tm}} = \sum_{i=1}^{N} \alpha_i \mu_{\mathrm{T}i}. \tag{2.18}$$

The term τ_{m} is the viscous stress related to the molecular viscosity defined for the mixture while τ_{Tm} is the turbulent stress tensor linked to the turbulent viscosity. Eventually, τ_{Dm} is used to consider the stresses generated by the interaction of the phases composing the multiphase mixture.

The DMM formulation is based on the definition of the diffusion velocity $\mathbf{u}_{\mathrm{Mi}}$. In order to compute it, a new variable called relative velocity ($\mathbf{u}_{\mathrm{r}}$) has to be introduced. If, for sake of semplicity, the tractation is restricted to two phases only in which the subscript 1 refers to the primary continuous phase and the subscript 2 refers to the secondary disperse phase, the relative velocity is linked to the diffusive velocities as follows:

$$\mathbf{u}_{\mathrm{M1}} = \mathbf{u}_1 - \mathbf{u}_{\mathrm{m}} = \frac{\alpha_2 \rho_2}{\rho_{\mathrm{m}}} \mathbf{u}_{\mathrm{r}}; \tag{2.19}$$

$$\mathbf{u}_{\mathrm{M2}} = \mathbf{u}_2 - \mathbf{u}_{\mathrm{m}} = \frac{\alpha_1 \rho_1}{\rho_{\mathrm{m}}} \mathbf{u}_{\mathrm{r}}. \tag{2.20}$$

The relative velocity can be formulated as an algebraic slip relationship or as a full differential equation, depending on the characteristics of the disperse phase motion or the level of detail that has to be achieved.

The two-fluid/multifluid model

The two-fluid model (TFM) is a pure Eulerian formulation that allows to study the motion of many phases that interact and exchange momentum. Types of mixtures that can be treated with this approach are solid/liquid, liquid/liquid and gas/liquid.
If more than two phases are considered, then the multifluid model (MFM) can be used as extension of the TFM. It is based upon a formalism that is in complete analogy to the two-phase model, allowing the solution of polydisperse multiphase systems with wide size distributions.

TFM and, more in general, MFM differ and extend the Mixture model since they account for the detailed motion of the secondary phases by solving a momentum transport equation for each mixture component, making the approach suitable to treat also multiphase systems in which the instantaneous equilibrium assumption is not feasible. In this cases, typical for large St numbers, the motion of the disperse phases is governed by both the continuous phase and their own inertia, and the solution of the phase-dependent velocity field is required to model segregation or other phenomena related to dimensions of the disperse phase sizes.

The multifluid model does not prescribe any limitation about the maximum number of coexisting phases that can be simulated, but constraints are put by modern computer architectures. Large systems with more than three secondary phases require an important computational effort which is, in many cases, not affordable for real-scale industrial applications. The convergence behavior can be affected from the number of phases also, since increasing them usually corresponds to an increase in the problem complexity.
TFM and MFM solve a number of equations that is a function of the number of phases considered and, while the pressure equations is shared, momentum and continuity equations are computed separately for each phase.

The continuity equations of a two-phase granular model with no temperature changes written for a continuos (Equation 2.24, generic fluid phase g) and a dispersed phase (Equation 2.25, generic solid phase θ) can be written as [31]:

$$\frac{\partial \alpha_{\mathrm{g}} \rho_{\mathrm{g}}}{\partial t} + \nabla \cdot (\alpha_{\mathrm{g}} \rho_{\mathrm{g}} \mathbf{u}_{\mathrm{g}}) = \sum_{\theta=1}^{N} (\dot{\mathrm{m}}_{\theta \mathrm{g}} - \dot{\mathrm{m}}_{\mathrm{g}\theta}); \tag{2.21}$$

$$\frac{\partial \alpha_{\theta} \rho_{\theta}}{\partial t} + \nabla \cdot (\alpha_{\theta} \rho_{\theta} \mathbf{u}_{\theta}) = \sum_{\theta=1}^{N} (\dot{\mathrm{m}}_{\mathrm{g}\theta} - \dot{\mathrm{m}}_{\theta \mathrm{g}}) \tag{2.22}$$

where α_{g} and α_{θ} are the gas and solid phase volume fractions, ρ_{g} and ρ_{θ} the

gas and solid density, respectively, $\mathbf{u}_\mathrm{g}$ the velocity vector for the gas phase, and $\mathbf{u}_\theta$ the solid phase velocity vector.

Note that θ serves as index for the secondary N solid phases and the sum of all the related volume fractions gives the total solid quantity, labeled with the subscript s. The sum of the whole solids and the continuous phase has to give the total volume of the multiphase mixture:

$$\sum_{\theta=1}^{N} \alpha_\theta = \alpha_\mathrm{s}; \qquad \alpha_\mathrm{s} + \alpha_\mathrm{g} = 1. \tag{2.23}$$

In the case of no mass transfer mechanisms, the momentum balances have the form:

$$\frac{\partial \alpha_\mathrm{g}\rho_\mathrm{g}\mathbf{u}_\mathrm{g}}{\partial t} + \nabla\cdot(\alpha_\mathrm{g}\rho_\mathrm{g}\mathbf{u}_\mathrm{g}\mathbf{u}_\mathrm{g}) = -\alpha_\mathrm{g}\nabla p + \nabla\cdot\boldsymbol{\tau}_\mathrm{g} + \alpha_\mathrm{g}\rho_\mathrm{g}\mathbf{g} + \sum_{\theta=1}^{N}\mathbf{R}_{\theta\mathrm{g}}; \tag{2.24}$$

$$\begin{aligned}\frac{\partial \alpha_\theta\rho_\theta\mathbf{u}_\theta}{\partial t} + \nabla\cdot(\alpha_\theta\rho_\theta\mathbf{u}_\theta\mathbf{u}_\theta) = -\alpha_\theta\nabla p - \nabla p_\theta + \nabla\cdot\boldsymbol{\tau}_\theta + \alpha_\theta\rho_\theta\mathbf{g} \\ -\mathbf{R}_{\theta\mathrm{g}} + \sum_{\vartheta=1;\vartheta\neq\theta}^{N}\mathbf{R}_{\vartheta\theta}\end{aligned} \tag{2.25}$$

where p is the pressure shared by phases, $\boldsymbol{\tau}_\mathrm{g}$ and $\boldsymbol{\tau}_\theta$ are the gas and solid stress-strain tensor, respectively:

$$\boldsymbol{\tau}_\mathrm{g} = \alpha_\mathrm{g}\mu_\mathrm{g}\left[\nabla\mathbf{u}_\mathrm{g} + \nabla(\mathbf{u}_\mathrm{g})^\mathrm{T}\right] - \left(\frac{2}{3}\alpha_\mathrm{g}\mu_\mathrm{g}\right)(\nabla\cdot\mathbf{u}_\mathrm{g})\,\mathbf{I}; \tag{2.26}$$

$$\boldsymbol{\tau}_\theta = \alpha_\theta\mu_\theta\left[\nabla\mathbf{u}_\theta + \nabla(\mathbf{u}_\theta)^\mathrm{T}\right] + \alpha_\theta\left(\lambda_\theta - \frac{2}{3}\mu_\theta\right)(\nabla\cdot\mathbf{u}_\theta)\,\mathbf{I}. \tag{2.27}$$

Equation 2.26 and 2.27 share the same structure but the latter considers the exchange of momentum induced by particles translations and collsions through the solids shear viscosty μ_θ and the solids bulk viscosity λ_θ, accounting for the resistance of the granular particles to expansion and compression.

2.4.1 Granular Flows

Granular flows are defined as fluid-particle mixtures in which particle-particle interactions have an important role, together with the shear-induced stress due to the flow motion, in the momentum exchange mechanism [32]. These flows are

composed by a primary carrier phase and a disperse one, namely a granular material, which consists of a large collection of solid particles, big enough to make the Brownian motions irrelevant [33].
Granular flows are, therefore, dominated by particle-particle collisions; this means that the volume fraction has to be large enough to induce interactions between discrete entities. Examples of this kind of flows are quite various, ranging from fluidized beds to mining and milling operations, from ploughing to abrasive water jet or machining, food processing and debris flows.

It is known that the mechanics governing granular flows and, more in general, multiphase flows can present big differences with respect to single-phase systems, especially if high-loading (dense flows) is considered. The motion of the primary phase, at certain volume fractions, can be strongly influenced by the particles physics and momentum exchange between phases can not be neglected. Early studies on rapid granular flows usually consider particle-particle interactions as simple binary collisions employing the so-called *hard particle model*, where most of the real behavior of the solid phase is neglected or simplified. In contrast to the previous approach, the *soft particle model* firstly proposed in late seventies is aimed at taking into account the rheology of the solid phase and its elastic behavior when collisions take place.

Depending on the flow pattern, that is, the typology of the flow studied, granular flows can be classified according to their inertia:

- *slow granular flows*: simplified flows where the random kinetic energy is neglected and quantities related to it, such as the granular temperature, are not modeled;
- *rapid granular flows*: particle-particle and particle-wall interactions have major effects on the mixture hydrodynamics and their effects can not be neglected.

This sub-chapter is aimed at introducing physical principles that govern the motion of rapid granular flows.

At high shear rates, indeed, the collisionless behavior assumed for slow, dilute fluid-solid flows does not hold anymore and impacts often results in dilation that make the granular material behave like a molecular gas [32]. In this kind of flows, the kinetic energy associated to particles velocity can be decomposed into averaged and fluctuation components. The energy contribution due to random motion is treated in analogy to the concept of thermodynamic temperature, introducing the concept of *granular temperature*, whose basic translational definition reads as [28]:

$$\Theta_s = \frac{1}{3}|\mathbf{u'}_s|^2 \tag{2.28}$$

where $\mathbf{u}'_s$ represents the fluctuating velocity of the solid phase in the Euclidean space.

2.4.2 The Kinetic Theory of Granular Gases

Modeling approaches for multiphase flows here presented are largely based upon the so-called *kinetic theory of granular gases* [33].
The expression granular gas is referred to the existing analogy between the behavior observed for granular mixtures and classic gases, where the molecules are massively spaced and interacts through collisions.
The main difference between molecular and granular gases consists in considering granular particles as inelastic entities, that is, each collision is a dissipative event and some of the energy is converted irreversibly into heat. Due to this reason, it is necessary to inject energy into the system to keep it in motion.
Moreover, particles are usually carried by lighter fluids, for example air or water, and they are subject to aggregation and breakage, attrition or coagulation (*e.g.* colloidal mixtures). All these phenomena make the analysis of granular flows difficult.

Granular gases can be characterized by macroscopic fields such as granular temperature, velocity or density.
A gas, for example, moves at a velocity whose macroscopic definition is obtained by averaging the single molecule velocity. The random motion of the gas particles can be obtained by subtracting the macroscopic velocity to the instantaneous one and the local thermodynamic temperature of the gas is related to the average of the square of the fluctuating velocity components. This is the definition of temperature that comes from statistical mechanics and it is similar to the definition of granular temperature, being defined as described by Equation 2.28, where the mean square of velocity components are those of grains fluctuations.

Kinetic theories are used to describe the dynamics of granular flows and they all assume that particles are able to interact through dissipative collisions only [33].

Some Notes about the Standard Kinetic Theory

The *standard kinetic theory*, or kinetic theory of gases, states that a gas is an ensemble of microscopic entities which randomly moves and exchange momentum

through particle-particle and particle-wall (if confined) collisions. These molecules are supposed to have large inter-particle spaces, meaning that most of the volume that they occupy is empty, with the following assumptions and hypotheses:

- molecules size is small compared to the volume that they occupy;
- molecules are in constant (random) motion;
- the number of molecules is large enough to make a statistical treatment applicable;
- the interaction between molecules is limited to collisions;
- the average kinetic theory of gas particles depends on the absolute temperature of the gas only.

The kinetic theory explains macroscopic properties of gases, such as temperature, pressure or viscosity, as a result of interactions that the fluid exhibits at molecular level, obtaining these fields by averaging microscopic properties.

Collisions are supposed to be always inelastic since part of the kinetic energy is dissipated and lost during impacts. Grains are assumed to be rigid and collisions instantaneous. Particles velocity before and after the collisions are related via the coefficient of restitution e which describes the effectiveness of the impact and the quantity of energy lost.

Collisions can be studied by introducing the concept of friction or not. If impacts are supposed to be frictionless, then the velocity of the colliding particles does admit only normal components while when the friction is taken into account, collisions are charachterized by an impulse having a normal and tangential components.
According to Vescovi [33], two approaches have been proposed to account for the friction behavior of particles.

The first one introduces the angular momentum and the spin of each molecule as key quantities, and relations accounting for the spin energy and the angular momentum conservation have to be included in the granular temperature definition.

The second model applies when friction has a minor role (small values of the friction coefficient μ) and the effect of tangential contacts can be included in a global restitution coefficient. This approach is less rigorous than the one cited before but it has been proven to well perform when included in the hydrodynamic equation.

Some Notes about the Extended Kinetic Theory

The *Extended kinetic theory* is derived from the standard kinetic theory in order to improve the prediction capability for the rate of collisional dissipation when repeated collisions drive the motion of granular flows [33].
The basic idea behind the revised theory is that enduring impacts between granular flow particles reduce the collisional dissipation even though the momentum is still exchanged. Due to this phenomenon, the dissipation rate is actually reduced by the stresses caused.

It is worth to underline that the extended kinetic theory is based upon phenomena observation and it is intended to extend the standard kinetic theory incorporating the pre-collisional velocity correlation.

2.4.3 Turbulence Modelling

Turbulence modelling for multiphase flows is still a challenging and unresolved task for the scientific community since the construction of reliable models with a solid theoretical ground is still far from being achieved. The inclusion of interphase effects and phases interactions still need the usage of semi-empirical laws based upon experimental data that make the models case-sensitive, restricting their applicability to the narrow set of applications which they are written for. Available models are usually obtained by extending single-phase ones considering a proper formulation able to compute fields for a given multiphase regime.

Due to the modelling strategies adopted, two different turbulence formulations have been used:

i single-phase turbulence modelling, through the $k - \varepsilon$ realizable model, for spiral jet milling;

ii Euler-Euler multiphase turbulence modelling, through the $k - \varepsilon$ RNG model (disperse formulation), for calculating the fluidization behaviour in fluidized bed reactors.

The detailed description of the two multiphase models is given in the related application sub-sections.

2.4.4 Polydispersity

Real populations of particles usually show a various range of different sizes known as polydispersity. In many cases, the distribution of diameters is so wide that it

is not possible to approximate the whole population with one class only, making the monodisperse assumption unfeasible.
Moreover, common mechanisms in gas-solid flows such as aggregation, breakage and growth change considerably the particles size during the process, requiring a computational framework able to work with polydisperse distributions. The precise description of each possible particle dimension, theoretically available in Lagrangian methods, is not mathematically (because two-fluid methods work with average properties) and computationally possible, since the addition of many particles classes in a fully coupled solution would require a huge computational power. In this framework, population balance modelling (PBM) constitutes a powerful and affordable method to track in time and space the evolution of a large collection of polydisperse particles through population balance equations (PBE).

2.5 Interfacial forces

If spherical particles with large inertia are considered, that is particles of hundreds of micron diameter, drag is the largely dominant body force and other contributions, such lift, can be safely neglected. This work is specifically written for providing the notions necessary to study the motion of gas-solid particles with the particular application of polyolefins polymerization and spiral jet milling and therefore, besides drag, only turbulent dispersion effects are described.

The interaction between the gas and the disperse phases can be effectively modeled as the product of a coefficient K by the relative velocity between the gas and the solid phases and adding its contribution to the momentum equation:

$$\sum_{\theta=1}^{N} \mathbf{R}_{\theta \mathrm{g}} = \sum_{\theta=1}^{N} \mathbf{R}_{\mathrm{g}\theta} = \sum_{\theta=1}^{N} \mathrm{K}_{\theta \mathrm{g}} \left(\mathbf{u}_{\boldsymbol{\theta}} - \mathbf{u}_{\mathrm{g}} \right). \tag{2.29}$$

The same equation structure can be used to consider the interactions between disperse phases:

$$\sum_{\vartheta=1}^{N} \mathbf{R}_{\vartheta\theta} = \sum_{\vartheta=1}^{N} \mathbf{R}_{\theta\vartheta} = \sum_{\vartheta=1}^{N} \mathrm{K}_{\vartheta\theta} \left(\mathbf{u}_{\boldsymbol{\vartheta}} - \mathbf{u}_{\theta} \right). \tag{2.30}$$

$\mathrm{K}_{\theta \mathrm{g}}$ and $\mathrm{K}_{\vartheta\theta}$ indicate the gas-solid and solid-solid exchange coefficients, respectively.

The detailed description of the models used to account for body forces is given in the applications sections.

2.6 Definition of the Numerical Approach

Despite the enormous technological progress of modern computers, the computational cost associated to Eulerian-Lagrangian simulations makes them often unaffordable.
Let us take the example of spiral jet milling. The solid holdup inside a typical system is usually between 5 g and 30 g and the average particle size may vary from less than 1 μm (micronized powders) to more than 300 μm (raw powders) [34]. Assuming that a mass of 20 g of a powder with density $\rho_s = 1300$ g/m^3 and an average diameter of 50 μm is contained in a given instant within the micronization chamber of the spiral jet mill, it is possible to estimate that $2.35 \cdot 10^8$ particles are present inside the system. The size reduction mechanism inside these apparatus is based upon particle-particle and particle-wall collisions which need, according to Bná *et al.* [9], a time-step down to 10^{-8}-10^{-10}s to be correctly described in a Lagrangian framework.
These data clarify that this physics makes the aforementioned approach not suitable to model the motion and interactions (*e.g.,* collisions) between particles in spiral jet milling or for fluidized bed reactors applications.

The Lagrangian tracking of non-interacting particles constitutes a valid option to investigate the distribution of particles of different diameters within the grinding chamber with a limited computational cost, especially if they are transported over a frozen flow-field, assuming a negligible coupling between the phases at the initial stages of the process (*i.e.,* very low volume fraction). Fluidized beds imply a strong coupling between phases, while the spiral jet milling analysis, in this work, is aimed at developing a method to study particles motion and breakage at process time-scales. Both phenomena cannot be, therefore, studied availing of Lagrangian transport.

According to Krishnan [29], the choice of the right model has to be done considering the level of coupling between phases, their volume fractions and the interface typology, as shown by Table 2.2.
While the multiphase flow field inside fluidized bed reactors can be considered fully mixed and strongly coupled, spiral jet milling is supposed to have two major functioning regimes:

1. *dilute or very dilute regime* at initial stages of the process, when the solid phase is being injected in the grinding chamber;

2. *dilute to dense regime* with localized regions of *high loading*, depending on the position within the milling chamber. The average solid volume fraction inside

Table 2.2: Models applicability. ITM stands for the interface tracking methods, MiM indicates the mixture model while TFM/MFM stand for the two-fluid/multifluid models.

	ITM	MiM	TFM/MFM
Flow Regime	stratified/free-sur. slug flows droplet flows	slurry bubbly flows particle-laden flows	slurry and FBR bubbly/droplet flows
Particle load	-	dilute to mod. dense	dilute to dense
Phase coupling	weak to moderate	weak	weak to strong
Stokes Number	all ranges	St$<<1$	all ranges

the spiral jet mill when the micronization starts is estimated to be $5 \cdot 10^{-3}$ to 10^{-2}[34]. It is known that large particles tend to move towards the periphery of the grinding chamber while smaller ones progressively move towards the classificator to leave the system. This classification phenomenon reasonably induces local concentration of solids in the outer part of the chamber, making the flow moderately dense or dense just in these regions.

In this framework, two different Eulerian-Eulerian approaches are chosen for the studied applications:

1. the polymerization process and the polyethylene particles distribution within fluidized bed reactors are modeled through a CFD Eulerian-Eulerian Multi-fluid model;

2. the spiral jet milling process is studied through i) single-phase CFD simulations to understand the influence that the caking mechanism has on the gas velocity field and ii) by building a simpflied and decoupled Eulerian model to exploit the gas velocity fields computed through CFD for calculating the solids distribution and breakage kinetics.

The detailed description of the approaches and models used is reported in the following chapters.

Chapter 3

Population Balance Modelling

As described in the previous chapter, Eulerian-Eulerian methods do not trivially model polydispersity such as, for example, Lagrangian approaches and accounting for changes in the particle size due to collisions or growth requires a proper modeling strategy. To this end, population balance modeling definitely constitutes a valid option to track in space and time the particle size distribution (PSD).

The following chapter is aimed at giving an insight on the theory and the mathematical description of population balance equations, as well as the solution methods usually employed to solve them numerically.
Infomation given is strongly based upon the work of Marchisio & Fox, reported in the book "Computational models for polydisperse particulate and multiphase systems" [35], the work of Ramkrishna, reported in the book "Population Balances. Theory and Applications to Particulate Systems in Engineering" [36] and the work of Kumar & Ramkrishna [37–39].

3.1 Population Balance Equation (PBE)

The Population Balance equation is a continuity relation written as a number density function. It means that a balance is written for a particle set in arbitrary sub-regions of the physical space $\mathbf{\Omega_x}$ and the phase space $\mathbf{\Omega_\xi}$ with boundary defined as $\partial\Omega_\mathbf{x}$ and $\partial\Omega_\boldsymbol{\xi}$.

The form of a particle-number Population Balance Equation (PBE) can be written as:

$$\frac{\partial}{\partial t}\left(\int_{\Omega_x} \mathrm{d}\mathbf{x} \int_{\Omega_\xi} \mathrm{d}\boldsymbol{\xi} \cdot n_\xi\right) + \int_{\Omega_\xi} \mathrm{d}\boldsymbol{\xi} \int_{\partial\Omega_x} (n_\xi \mathbf{u}) \cdot \mathrm{d}\tilde{\mathbf{A}}_\mathbf{x} + \int_{\Omega_x} \mathrm{d}\boldsymbol{\xi} \int_{\partial\Omega_\xi} \left(n_\xi \dot{\boldsymbol{\xi}}\right) \cdot \mathrm{d}\tilde{\mathbf{A}}_{\boldsymbol{\xi}} = \int_{\Omega_x} \mathrm{d}\mathbf{x} \int_{\partial\Omega_\xi} \mathrm{d}\boldsymbol{\xi} h_\xi \quad (3.1)$$

where $\mathbf{u}$ is the velocity vector of the particles, $\boldsymbol{\xi}$ is the phase-space or internal coordinates vector, n_ξ is the number density function to the internal coordinates, $\dot{\boldsymbol{\xi}}$ is the continuous rate of change in phase space, and h_ξ is the discontinuous jump function representing discrete events.
Regarding the physical meaning of terms appearing in Equation 3.1, the first term of the left-hand side is an integral over the whole considered domain which represents accumulation. The second term is a surface integral taken over the boundaries of the control volume which is related to net flux due to convection in the physical space while the third term represents the convection in the phase space.
The presence of the last two terms indicates that a particle can move inside the domain thanks to the particle velocity $\mathbf{u}$, which is a physical property, while the evolution inside the phase space is described by the rate of change of the internal coordinate (*e.g.*, species concentration, particles volume, particle length scale,...) with respect to the time. The latter is called *internal-coordinate velocity*.

At this point it is worth to underline that, depending on the evolution behavior of the i-th internal coordinate considered, $\boldsymbol{\xi}$ can change *continuously* or *discontinuously*:

- a process is called *continuous* if the internal coordinate considered changes with a time scale much smaller than the one characterizing the solution of the PBE;
- a process is called *discontinuous* if the phase-space variable evolves in such a way that the length scale of the discrete events is of the same magnitude order of the particle size.

For example, the particle growth due to molecular deposition on the surface of other particles can be considered a continuous phenomenon since it takes place in a time that is much smaller than the one related to the particle time and length scale. Its mesoscale description is given by the third term of Equation 3.1 (left-hand side).

Instead, if the size of particles increases because of collisions that make them aggregate, we are in presence of a discontinuous process that causes a rapid variation in phase space properties, which is well-described by the right-hand side of Equation 3.1.

It is possible to convert boundary integrals into volume integrals applying the Reynolds-Gauss theorem:

$$\frac{\partial}{\partial t}\left(\int_{\Omega_x} \mathrm{d}\mathbf{x} \int_{\Omega_\xi} \mathrm{d}\boldsymbol{\xi} \cdot n_\xi\right) + \int_{\Omega_x} \mathrm{d}\mathbf{x} \int_{\Omega_\xi} \mathrm{d}\boldsymbol{\xi} \frac{\partial}{\partial \mathbf{x}} \cdot (\mathbf{u} n_\xi) + \int_{\Omega_x} \mathrm{d}\mathbf{x} \int_{\Omega_\xi} \mathrm{d}\boldsymbol{\xi} \frac{\partial}{\partial \boldsymbol{\xi}} \cdot (\boldsymbol{\xi} n_\xi) = \int_{\Omega_x} \mathrm{d}\mathbf{x} \int_{\partial\Omega_\xi} \mathrm{d}\boldsymbol{\xi} h_\xi. \quad (3.2)$$

According to Marchisio & Fox [35], Equation 3.2 is satisfied for any arbitrary physical and phase control volume, $\boldsymbol{\Omega}_\mathbf{x}$ and $\boldsymbol{\Omega}_{\boldsymbol{\xi}}$, if the following relation holds:

$$\frac{\partial n_\xi}{\partial t} + \nabla_\mathbf{x} \cdot (\mathbf{u} n_\xi) + \nabla_{\boldsymbol{\xi}} \cdot (\boldsymbol{\xi} n_\xi) = h_\xi. \quad (3.3)$$

It is worth to notice that, while $\mathbf{x}$ and $\mathbf{u}$ are standard objects usually found in continuum mechanics with a simple physical meaning, the vector $\boldsymbol{\xi}$ is a generalized vector in which are stored information about internal coordinates.
As usual for this kind of relations, an exact solution for Equation 3.3 exists only for very simplified cases, often driven by very stringent assumptions.
For almost all the problems of engineering interest, it has to be solved numerically with proper initial and boundary conditions, in order to obtain a solution able to provide NDF information for each time instant and physical point of the computational grid.

Depending on the number of internal coordinates considered, the PBE is said to be:

- *univariate*: the PBE is described by one internal coordinate only, for example the particle length ($\xi = L$);
- *bivariate*: the PBE is described by two internal coordinates, for example the particle volume and the particle surface area ($\boldsymbol{\xi} = (v, A)$);
- *multivariate*: the PBE is described by more than two internal coordinates.

Another important case is referred to the level of coupling between internal and physical coordinates. If the particle motion is characterized by its own velocity distribution, then the internal coordinate can coincide with the particle-velocity vector and the equation is called Generalized Population Balance Equation (GPBE).

Since the motion of the secondary phase becomes a variable of the Population Balance Model, the solution of the equations is much more demanding.
This discussion is anyway limited to the standard PBE and all the information given in the continuation of this document does not consider the velocity as an internal coordinate.

Assuming that the internal coordinate is the particle volume (for an univariate PBE), the equation for the number density function, $n(v,t)$, is defined as [28]:

$$\frac{\partial}{\partial t}\left[n(v,t)\right] + \nabla \cdot \left[\mathbf{u}n(v,t)\right] + \nabla_v \cdot \left[G_v n(v,t)\right] = \frac{1}{2}\int_0^v a\left(v-v',v'\right) n\left(v-v',t\right) n\left(v',t\right)\,\mathrm{d}v' - \int_0^\infty a\left(v,v'\right) n(v,t)\, n\left(v',t\right)\,\mathrm{d}v' + \int_{\mathbf{\Omega_v}} pg\left(v'\right)\beta\left(v|v'\right) n\left(v',t\right)\,\mathrm{d}v' - g(v)\, n(v,t) \quad (3.4)$$

where the last term of the left-hand side represents the growth term, the first term of the right-hand side models the birth of particles due to aggregation, the second term of the right-hand side is the death of particles due to aggregation, the third term of the right-hand side describes the birth due to breakage while the last term the death due to breakage events.

The initial and boundary conditions are, respectively:

$$\begin{cases} n(v,t=0) = n_v \\ n(v=0,t)\, G_v = \dot{n}_0 \end{cases} \quad (3.5)$$

where $\dot{n}_0$ is the nucleation rate in $\left[\frac{particles}{m^3 \cdot s}\right]$ and G_v is the growth rate based on particle volume expressed in $\left[\frac{m^3}{s}\right]$.

As cited before, one can see the similarities between Equation 3.2 and Equation 3.4: on the last part of the left-hand side are visible particles growth terms while the right-hand side represents a source term which is used to describe discrete events (aggregation and breakage).
One important information regarding the units that the reader will find in the following pages has to be given: birth rates and death rates, as well as the growth rate in the last term of the left-hand side of Equation 3.4 are expressed as $[s^{-1} \cdot m^{-3}]$. In order to make concepts regarding balances of particles clearer, in some cases, the same unit is reported as $[particles \cdot s^{-1} \cdot m^{-3}]$, without changing the physical meaning of the expression.

This work is focused on particle growth (polyolefins polymerization) and particle breakage (spiral jet milling) only. Therefore, a critical review on PBE equations is given with a particular emphasis on these two mechanisms.

3.2 Solution Methods for PBEs

Scientific literature offers a variety of methods to solve Population Balance Equations. This work focuses on the description of methods that can be used for solving a limited number of internal variables, also referred as coordinates, such as particle size, without extending the discussion to kinetic formulations incorporating the velocity, such as the Generalized Population Balance Equation (GPBE). This chapter is therefore aimed at briefly describing the three most popular approaches nowadays used for numerically solving PBEs:

- the *Class Method* (CM), that discretizes the internal coordinate space to directly solve the PBE;
- the *Method of Moments* (MOM), whose formulation relies on the solution of a limited number of moments of the original number-density function instead of the NDF itself;
- the *Quadrature-Based Moments Methods* (QBMM), consisting in a family of approaches that are based upon the approximation of the number-density function with a Gaussian quadrature, to solve the closure problem of MOM.

3.2.1 Class Method (CM)

The Class or Discrete Method solves the Population Balance Equation by discretizing the internal coordinate space into a certain number of bins, or classes, to obtain a set of balance equations.
If we work with an univariate PBE and we choose the particle volume v as unique internal coordinate, we can use the number-density function $n(t, \mathbf{x}, v)$ to write the generic transport form of the PBE as:

$$\frac{\partial n}{\partial t} + \frac{\partial}{\partial v}(vn) = \frac{\partial^2}{\partial v^2}(\Gamma n) + \mathcal{S}. \tag{3.6}$$

If $N_i \equiv \int_{v_i}^{v_{i+1}} n(t, \mathbf{x}, v)\,\mathrm{d}v$ is the number density in the interval i, then the discretized form of Eq. 3.6 is [40]:

$$\frac{\partial N_i}{\partial t} + \nabla \cdot (\mathbf{u}_i N_i) + \int_{v_i}^{v_{i+1}} \frac{\partial}{\partial v}(G, n)\,\mathrm{d}v = \int_{v_i}^{v_{i+1}} \mathcal{S}\mathrm{d}v \tag{3.7}$$

where $\mathbf{u}_i$ is the i-th class velocity. In order to close integrals of Eq. 3.7, a functional form for them has to be assumed.
Developing the early work of Hidy & Brock [41], Kumar & Ramkrishna [37–39] proposed a number-density function approximation of the form:

$$n\left(t, \mathbf{x}, v\right) = \sum_{i=1}^{M} N_i \delta\left(v - \zeta_i\right) \tag{3.8}$$

which basically concentrate all the particles of the bin around a pivotal point ζ_i (the volume representing the entire population of a class) and assume an homogeneus concentration of the number density in the interval i.

The rate of change of the population number density N_i over time due to nucleation and growth can be written as [39]:

$$\frac{\mathrm{d}N_i}{\mathrm{d}t}|_{\text{nucl.\&growth}} = G(v_i)n(v,t) - G(v_{i+1})N(v_{i+1,t}) + \int_{v_i}^{v_{i+1}} \mathcal{S}(v)\mathrm{d}v \tag{3.9}$$

where $G(v_i)$ is the growth rate for particles of size v_i.
The representation of pure size-dependent growth processes has been worked out by Hunslow *et al.* [42] as:

$$\frac{\mathrm{d}N_i}{\mathrm{d}t}|_{\text{growth}} = \frac{G(v_i)}{v_i}\left(aN_{i-1} + bN_i + cN_{i+1}\right). \tag{3.10}$$

Coefficients a, b and c are estimated by forcing Eq. 3.10 to yield for three moments. The final form of the time-dependent number density equation is:

$$\frac{\mathrm{d}N_i}{\mathrm{d}t}|_{\text{growth}} = G(v_i)\left[\left(\frac{2}{1+r}\frac{N_{i-1}+rN_i}{v_{i+1}-v_{i-1}} - \frac{2}{1+r}\frac{N_i+rN_{i+1}}{v_{i+2}-v_{i-1}}\right)\right] \tag{3.11}$$

with:

$$n(v_i,t) = \frac{2}{1+r}\left(\frac{N_{i-1}+rN_i}{v_{i+1}-v_{i-1}}\right). \tag{3.12}$$

The method developed by Hunslow solves the large oscillations problems shown by previous implementations in regions where N tends to zero but it makes wrong predictions near discontinuities.
In order to fix this numerical issue, Kumar & Ramkrishna developed a new discretization method starting from the general formulation of population balance equations of Eq. 3.7 but modified for constructing a general framework able to incorporate discrete events as [39]:

$$\frac{\partial n(v,t)}{\partial t} + \frac{\partial n(v,t)G(v,t)}{\partial v} = \frac{1}{2}\int_0^v n\left(v-v',t\right) n\left(v',t\right) q\left(v-v',v'\right) \mathrm{d}v' - n(v,t)\int_0^v n\left(v',t\right) q\left(v',v'\right) \mathrm{d}v + \mathcal{S}(v). \quad (3.13)$$

Eq. 3.13 is the starting point for modeling discontinues such as breakage, aggregation, nucleation and growth by modifying the form of the right-hand side of such relationship.
In the very simple case in which $q\left(v',v'\right) = 0$ and $\mathcal{S}(v) = 0$, denoting that neither aggregation nor nucleation are taking place, Eq. 3.13 reduces to:

$$\frac{\mathrm{d}}{\mathrm{d}t}\int_{v_i}^{v_{i+1}} n(v,t)\mathrm{d}v = 0, \quad (3.14)$$

meaning that the total number of particles does not change and indicating that the size ranges change only beacuse of particle growth.
The particle size change can be therefore modeled as simply as:

$$\frac{\mathrm{d}x_i}{\mathrm{d}t} = G(x_i) \quad (3.15)$$

where the particle size x, related to volume through geometric constaints associated to the particles shape (*e.g.,* spherical particles), is a pure function of the particle growth rate G.

If breakage is considered, closure relations for source terms are needed and Kumar & Ramkrishna exploited the same discretization approach (*i.e.,* the fixed-pivot method) to assign the new born elements coming from breakage of larger particles to the nearby pivots to preserve at least two integral properties (usually number and mass of particles) of the number-density function.
The generic form of the right-hand side of Eq. 3.7 accounting for aggregation and breakage written for particle volume (following the notation used for particle growth) is [40]:

$$\int_{v_i}^{v_{i+1}} \mathcal{S}(v)\mathrm{d}v = \frac{1}{2}\sum_{j=1}^{i-1} N_j \sum_{k}^{\left(v'_j,v'_k\right)\in I_i} a(v'_j,v'_k)N_k - N_i\sum_{j=1}^{M} a(v'_i,v'_j)N_j + \sum_{j=1}^{M} b(v'_j)N_j \int_{v_i}^{v_j} \beta(v|v'_j)\mathrm{d}v - b\left(v_i\right)N_i \quad (3.16)$$

where v'_j and v'_k represents two pivotal points while v_i is the volume of the newly formed particle $v_i = v'_j + v'_k$. It is clear that in a fixed-sized grid the class i may not coincide with the pivot of the assigned interval. This causes the overestimation of number-densities, especially for aggregative events, and it results from the impossibility of changing the position of the pivotal point to satisfy the exact value of the particles arising from aggregation or breakage of smaller or larger particles, respectively. In order to solve this problem, the same authors proposed a new approach incorporating a technique to move the position of pivots [38].
The method, called *moving pivot*, is based upon the conservation of specific properties chosen to match the population requirements in terms of size description.

3.2.2 Method of Moments

The Method of Moments (MOM) has been formalized by Hulburt & Katz [43] to track the evolution of the lower-order moments of polydisperse distribution for aerosol applications.
Authors basically stated that a general number-density function contains too many information to be handled effectively in engineering problems. They argued that a limited number of moments is sufficient to properly describe the temporal evolution of a distribution instead of the entire PBE. The concept of moment is attactive because it can be easily coupled to CFD and because of its immediate physical meaning. MOM, indeed, usually involves the usage of low-order moments that has a straightforward physical interpretation such as mass, number of particles, *etc*, and therefore they are measurable quantities.
For example, if the internal coordinate is particle length, than the moment of order 0, m_0, is the total number of particles per unit volume while the moment of order 1, m_1, is the total length density in $[m/m^3]$. Moments ratios can be used to calculate usefull averages such as the average particle diameter given by the total number of particles, $d_{10} = m_1/m_0$ or the commonly used surface area-average particles diameter, $d_{32} = m_3/m_2$.

Limiting the discussion to univariate PBEs and using volume as internal coordinate, the evolution equation for an homogeneous system can be written as [35]:

$$\frac{\mathrm{d}m_k}{\mathrm{d}t} = \overline{S}_k \tag{3.17}$$

where m_k is the generic moment m of order k defined as $m_k \equiv \int_0^\infty v^k n \mathrm{d}v$ and:

$$\overline{S}_k = \int v^k \left[-\frac{\partial v n}{\partial v} + \frac{\partial^2}{\partial v^2} + \mathcal{S} \right] \mathrm{d}v. \tag{3.18}$$

In general, the transport equation for a generic moment of order k describing an homogeneous system undergoing nucleation, growth, diffusion, aggregation and breakage is:

$$\frac{\mathrm{d}m_k}{\mathrm{d}t} = \int Jv^k \mathrm{d}v + k\int vv^{k-1}n\mathrm{d}v + k(k-1)\int v^{k-2}\Gamma n\mathrm{d}v + \frac{1}{2}\int \beta\left(v,v'\right)\left(v+v'\right)^k n(v)n(v')\mathrm{d}v\mathrm{d}v' - \int v^k n(v)\int_0^\infty \beta\left(v,v'\right)n(v')\mathrm{d}v'\mathrm{d}v + \int v^k \int_0^\infty a(v')b(v'|v)n(v')\mathrm{d}v - \int v^k a(v)n\mathrm{d}v \quad (3.19)$$

Eq. 3.19 shows that a number of source terms need a closure, *i.e.,* they have to be written in terms of moments ranging from order 0 to order k, that is:

$$\frac{\mathrm{d}m_k}{\mathrm{d}t} = f_k(m_o, m_1, ..., m_k). \quad (3.20)$$

A way to close the system of equations consists in assuming a functional form for the number-density function by modelling the NDF with a quadrature approximation, *i.e.,* by approximating the unclosed function with a summation of N-weighted density functions. This approach gives rise to a set of methods called Quadrature-Based Moment Methods [44] that are widely coupled to CFD to model the evolution of polydisperse population of particles.

3.2.3 Quadrature-Based Moment Methods

The Quadrature-Based Moment Methods are a family of approaches that attempt to solve the PBE by converting the population balance equation onto moment transport equations [44]. Many different approaches have been proposed, some of them based upon the usage of a Gaussian quadrature to close the unknown source terms of the population balance equation. Among them, the Quadrature Method of Moments (QMOM), firstly proposed by McGraw [45] and later extended to treat bivariate distributions by Wright *et al.* [46], approximates the NDF with a N-node Gaussian quadrature of Dirac delta functions, allowing its application to a broad variety of engineering cases by tracking $2N$ transported moments. The method has been extended to multivariate population balance equations by Yuan & Fox [47]. The same authors [48] introduced the Extended Quadrature Method of Moments (EQMOM) to provide a method to study problems needing a continuous recostruction of the NDF instead of the discrete sum of Delta functions as provided by QMOM.

For sake of brevity, the discussion is restricted to the Direct Quadrature Method of Moments (DQMOM) since it is the method used to model the polydispersity in the CFD-PBM simulations of this work.

The Direct Quadrature Method of Moments

The Direct Quadrature Method of Moments (DQMOM) was firstly proposed by Marchisio & Fox [49, 50] with the main objective of providing a stable method to treat multivariate PBE, where QMOM is problematic because of the absence of robust moment-inversion algorithms [35].
DQMOM tracks transport equations for weights w_θ and wighted abscissas $w_\theta \xi_\theta$ of the quadrature node θ instead of moments and this makes an important difference with respect to QMOM since, if the internal coordinate is the particle size, the governing equations are written in terms of solid phases volume fractions and dimensions.

The distribution function or PSD of can be thought as a summation of a finite number of Dirac delta functions of the form:

$$f(\mathbf{x}, t, v) = \sum_{\theta=1}^{N} w_\theta (\mathbf{x}, t)\, \delta \left[v - \langle v \rangle_\theta (\mathbf{x}, t) \right] \tag{3.21}$$

where N is the total number of delta functions, θ is the quadrature node of the approximation, $w_\theta (\mathbf{x}, t)$ is the weight associated to it and:

$$\delta \left[v - \langle v \rangle_\theta \right] = \delta \left(v - \langle v \rangle_\theta \right). \tag{3.22}$$

$\langle v \rangle_\theta (\mathbf{x}, t)$ is the internal coordinate of node θ in the case of monovariate distributions, for which the population balance equation is characterized by particle volume.
Each quadrature node represents a different particle class.
If an univariate system is considered, the PBE assumes the form:

$$\frac{\partial n}{\partial t} + \nabla \cdot \left(\langle \mathbf{u} | v \rangle\, n \right) + \frac{\partial}{\partial v} \left(G n \right) = \int \mathcal{S} \mathrm{d}\mathbf{u}. \tag{3.23}$$

Transport equations for weights and abscissas have the form [51]:

$$\frac{\partial n}{\partial t} + \nabla \cdot \left(\langle \mathbf{u} \rangle_\theta\, w_\theta \right) = s_\theta^w; \tag{3.24}$$

$$\frac{\partial n}{\partial t} + \nabla \cdot \left(\langle \mathbf{u} \rangle_\theta\, w_\theta \xi_\theta \right) = s_\theta^{wv} \tag{3.25}$$

where $\langle \mathbf{u} \rangle_\theta = \langle \mathbf{u} | v_\theta \rangle$ is the velocity of the quadrature node θ while s_θ^w and s_θ^{wv} are the unknown source terms.

A moment-inversion algorithm is only needed at the beginning for initializing DQ-MOM variables, reducing the algorithm complexity especially if a large number of quadrature nodes is employed.

The first $(2N-1)$ moments of the weight function can be used to find N weights and N abscissas. In order to do that, a system of non-linear equations as the one reported below has to be solved:

$$\begin{aligned} m_0 &= \sum_{\theta=1}^{N} w_\theta, \\ m_1 &= \sum_{\theta=1}^{N} w_\theta \xi_\theta, \\ &\dots \\ m_{2N-2} &= \sum_{\theta=1}^{N} w_\theta \xi_\theta^{2N-2}, \\ m_{2N-1} &= \sum_{\theta}^{N} w_\theta \xi_\theta^{2N-1}. \end{aligned} \tag{3.26}$$

The smartest way to solve the Equation-set 3.26 consists in using algorithms applied to exploit the recursive relationship of Equation 3.27:

$$P_{\theta+1}(\xi) = (\xi - a_\theta) P_\theta(\xi) - b_\theta P_{\theta-1}(\xi), \qquad \theta = 1, 2, \dots \tag{3.27}$$

These algorithms are less prone to initial guesses than well-known Newton-Raphson and their convergence to the final solution is ensured by conditions on the *consistency* of the moment set.
The recursive relation, in matrix form, is given by:

$$\xi \begin{bmatrix} P_0(\xi) \\ P_1(\xi) \\ P_2(\xi) \\ P_3(\xi) \\ \vdots \\ P_{N-2}(\xi) \\ P_{N-1}(\xi) \end{bmatrix} = \begin{bmatrix} a_0 & 1 & \dots & & & & \\ b_1 & a_1 & 1 & & & & \\ \vdots & b_2 & a_2 & 1 & & & \\ & & b_3 & a_3 & \ddots & & \\ & & & \ddots & \ddots & \ddots & \\ & & & & \ddots & a_{N-2} & 1 \\ & & & & & b_{N-1} & a_{N-1} \end{bmatrix} \begin{bmatrix} P_0(\xi) \\ P_1(\xi) \\ P_2(\xi) \\ P_3(\xi) \\ \vdots \\ P_{N-2}(\xi) \\ P_{N-1}(\xi) \end{bmatrix} + \begin{bmatrix} 0 \\ 0 \\ 0 \\ 0 \\ \vdots \\ 0 \\ P_N(\xi) \end{bmatrix} \tag{3.28}$$

The eigenvalues of the tri-diagonal matrix of the System 3.28 are the roots of the polynomial $P_N(\xi)$. A Jacobi matrix can be obtained by making a diagonal similarity transformation, without changing the eigenvalues:

$$\mathbf{J} = \begin{bmatrix} a_0 & b_1^{1/2} & \dots & & & & \\ b_1^{1/2} & a_1 & b_2^{1/2} & & & & \\ \vdots & b_2^{1/2} & a_2 & b_3^{1/2} & & & \\ & & b_3^{1/2} & a_3 & \ddots & & \\ & & & \ddots & \ddots & \ddots & \\ & & & & \ddots & a_{N-2} & b_{N-1}^{1/2} \\ & & & & & b_{N-1}^{1/2} & a_{N-1} \end{bmatrix} \tag{3.29}$$

The weight associated to each node can be computed according to the equation:

$$w_\theta = m_0 \varphi_{\theta 1}^2 \tag{3.30}$$

where $\varphi_{\theta 1}$ is the first component of the θ-th eigenvector $\boldsymbol{\varphi}_\theta$ of the Jacobi matrix.

As it can be seen by the matrices reported above, the numerical procedure requires the knowledge of coefficients a_θ and b_θ. Their value can be computed resorting the orthogonality condition, exploiting the moments of the distribution. In order to effectively carry out these operations, the Wheeler [35, 52, 53] or the product-difference [35, 54] algorithm represent a valid option.

Increasing the number of nodes enhance the accuracy of the approximation but it is also known to increase the probability of having similar quadrature nodes. This is not recommended to prevent singularity and ill-conditioned systems [35].

Besides its robustness and the possibility of working without any moment-inversion algorithm, DQMOM is effective in modelling segregated systems bacause each

quadrature node corresponds to a specific solid phase advected with its own velocity field. Quadrature nodes are directly related to the particle sizes through the transported effective size $w_\theta \xi_\theta$ and momentum equations are updated with correct class diameters during the computation.

3.2.4 Solution Method Selection

The selection of the solution method is based upon the physics of the system of interest and the computational effort required to run the simulations.

The Class Method needs a numerous number of bins to properly described polydisperse population of particles, especially if they have bimodal shape or they are very polydisperse. This results in the necessity of tracking many particles classes, causing computationally intensive models that cannot be afforded for describing large and complex real-scale industrial systems such as spiral jet mills. A CFD-PBM fully coupled solution based upon this approach is not possible.

The Quadrature Method of Moments would constitute a good option because of its computational efficiency and its intrinsic conservativeness. QMOM does not allow for considering the different inertia of polydisperse particles class because the solid phase is entirely advected with the same velocity, making the modeling of segregated systems impossible.

The Direct Quadrature Method of Moments provides the best modelling framework for applications in which an important effect induced by phases segregation is expected. Fluidized bed reactors for polyolefins production need solid segregation to classify particles that can leave the system from particles that are continuosly sustained by the gas flow to undergo polymerization. For these reasons, DQMOM is the chosen solution method for CFD-PBM coupling in this work.

Spiral jet mills base their working principle upon the aerodynamic classification mechanism and velocity differences between solid phases are of paramount importance in defining the radial position of particles within the micronization chamber. The large computational power required to run fully coupled CFD-PBM simulation on real-scale system for interesting time-scales is unaffordable by modern computers architectures [9, 34]. For this reason, it is decided to model the micronization process availing of an uncoupled CFD-PBM model in which population balance equations are discretized through a class method with a logarithmic scale, whose extremes come from experimental raw and final PSD. The gas velocity field is computed through single-phase CFD simulations and it is used as input in a 1D finite volume code to calculate the solids velocity and breakage kinetics.

Chapter 4

Application 1: Spiral Jet Milling

This chapter presents the numerical models used to study the spiral jet miling process with the aim of understanding how the caking phenomenon influences the gas flow fields inside the micronization chamber.
The second part of the work deals with the derivation of a novel computational approach able to describe the micronization process at steady-state operation by using the gas velocity profiles computed through CFD simulations and calculating the breakage kinetics of lactose and paracetamol using a semi-empirical kernel tuned over experiments.
The proposed model aims at developing a robust computational strategy to predict output particle size distributions at process time and size scales.

4.1 Process Description and Current Modelling Capabilities

4.1.1 The Spiral Jet Milling Process

Spiral jet milling (SJM) is a widely used industrial process able to reduce in size solid particles without the usage of any mechanical or moving part. The application fields of this technology are different, ranging from the micronization of pigments or mineral materials to the production of APIs (active pharmaceutical ingredients) for the pharmaceutical industry [55].
The absence of mechanical components in relative motion avoids powders contamination and leads to the possibility of obtaining highly pure and very fine particles with a narrow particle size distribution (PSD). Pharmaceutical active substances are micronized to achieve selected sizes, to increase specific surface area which enhances their dissolution rate, to maximize drug bioavailability and to dry powders from solvents used during the crystallization process [56].

SJM is often added at the end of a separation process (such as crystallization or freeze-drying) to tailor and homogenize the PSD [57].

Their simple working principle consists in using a high-speed gas flow to mill solid particles (see schematic in Fig. 4.1). Raw powders, with usually a mean particle or crystal size of 300-700 μm and a solid feed rate of 0.5-300 kg/h [55], are entrained into the gas flow and injected into a cylindrical volume called grinding or micronization chamber. In the latter, a high-speed dry air or nitrogen flow is guaranteed by a variable number of nozzles (from 4 to 12, depending on the mill dimensions).

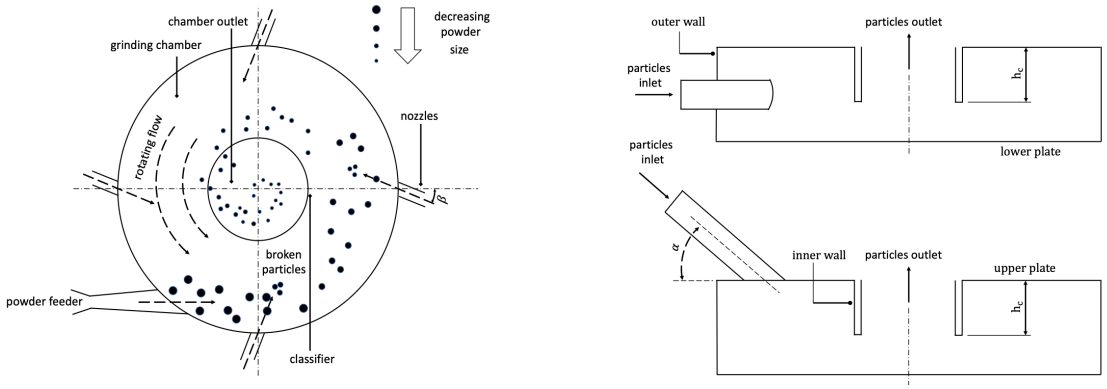

(a) working principle **(b)** powder inlet typologies

Figure 4.1: Spiral jet milling working principle and system schematic.

The position and the orientation of the nozzles (showed as angle β in Fig. 4.1a) are set to establish a vigorous swirled flow within the chamber. The gas gathers and moves the particles, accelerating and making them collide, striking one against the other and impacting the chamber walls. The collisions cause mechanical stresses on powder crystals, ending in fragmentation and breakage. The particles size reduction is usually controlled by changing the solid feed rate and the so-called grinding pressure, that is the pressure at the nozzles inlets. The latter is set depending on the particular powder milled and it usually ranges from 4 to 12 bar(g)[*].
Spiral jet mills are built in two variants, according to the position of the powder feeder: the first has the feeder located tangentially to the milling chamber (Fig. 4.1b, top), the second has the feeder located with an inclination on the upper

[*]The bar(g) is a unit indicating gauge pressures. For example, a pressure p = 2 bar(g) is equal to p_g = 2 bar which is equal to p_{abs} = 2 + p_{atm}, where the subscript atm indicates "athmospheric".

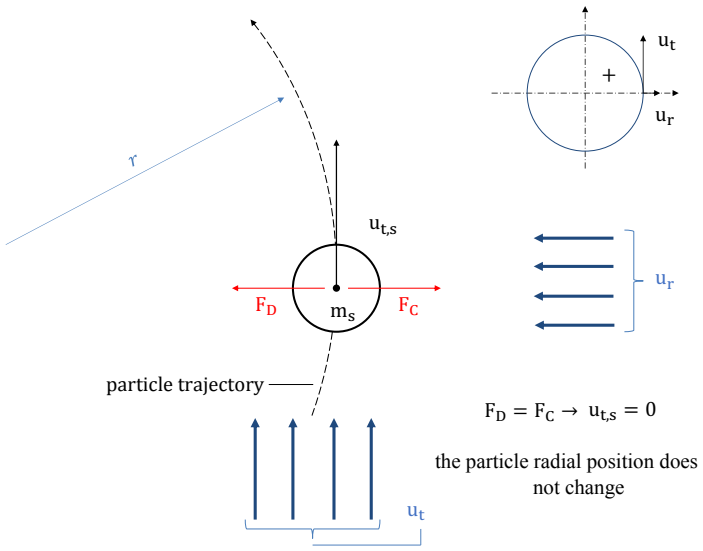

Figure 4.2: Schematic of the forces acting on a particle moving within the micronization chamber. Note that the subscript r indicates radial while the subscript t stands for tangential.

plate of the micronization chamber (Fig. 4.1b, bottom). To the best of the author knowledge, there are no studies in the literature in which the effects of these different approaches has been investigated to assess which has the best comminution efficiency.

As depicted by the schematic of Fig. 4.2, the solid particles classification (which governs the PSD in the outlet stream) is determined by the balance between drag and centrifugal forces experienced by the particles, and thus by the radial and tangential components of the velocity and particle size/mass. Centrifugal forces drive the larger particles to the outer periphery and away from the mill outlet, while drag forces dominate for finest particles that are carried out of the mill with the process gas.

4.1.2 Particles Dynamics and Breakage in Spiral Jet Milling

The comprehension and the preliminary discussion of particles motion are mandatory to understand which flow properties influence the solids trajectory and to correctly analyze the micronization process.
In spiral jet mills, the particles position is determined by a force balance in which the competitive effects of radial and tangential components of velocity induce drag and centrifugal forces (see Fig. 4.2). A certain slip between particles and the fluid

velocities is established with a magnitude that is function of the object inertia (diameter and density), as showed by a early work of Konno & Saito [58, 59].
The quantity of solid particles that is instantaneously present within the grinding chamber is called mass holdup and essentially defines the spatial-average particulate loading. The mass holdup, W, is related to powder feed-rate, $\dot{m}_{s,in}$, and the average resident time of particles, rt_s, (usually 10/15 s up to more than 100 s as showed by Mueller *et al.* [60]) inside the grinding chamber, reaching usual values of 5 to 30 g of powders [9]:

$$W = \dot{m}_{s,in} rt_s. \tag{4.1}$$

The higher is the mass holdup, the lower is the average inter-particles distance, with collisions that become more frequent when the solid feed-rate is increased. The ratio between solid and gas volume fraction, κ, gives the relative volume of particles with respect to the carrier phase:

$$\kappa = \frac{\alpha_s}{\alpha_g} = \frac{\alpha_s}{1 - \alpha_s} \tag{4.2}$$

where α_s is the average solid phase volume fraction.
The inter-particles (non-dimensional) distance, L/d_s, can be estimated availing of parameter κ, through the relation given by Crowe *et al.* [61]:

$$\frac{L}{d_s} = \left(\frac{\pi}{6}\frac{1+\kappa}{\kappa}\right)^{1/3}. \tag{4.3}$$

When the local α_s approaches 10^{-2} or larger values, the particles motion can influence the gas flow-field and the inter-particles collisions may change significantly the particle trajectory.
Eq. 4.3 clearly shows that increasing the solid volume fraction results in an increase in the volume fraction ratio that causes a reduction on the inter-particle distance. Averaged quantities obtained from pure mass-flow analysis usually predict a dilute flow condition, with L/d_s ranging between 15 and 30.
The knowledge of the single-phase gas flow field is important to understand the particles driving force origin and the gas velocity maps in regions expected to have dilute concentrations. A certain quantity of the particles moving within the grinding chamber, indeed, aggregates on walls (Sowa *et al.* [62]) while the remaining part is more or less evenly distributed in the micronization volume, except for regions near corners. The latter can be used to compute the average volume fraction associated to particles that are not clustered and that are actually moving.
If, for example, the process takes place in a 200 mm spiral jet mill and 10 g of particles with a density of 1300 $kg\,m^{-3}$ are assumed to move within the chamber, it is possible to compute an average particulate loading ranging between $5 \cdot 10^{-3}$

and 10^{-2}, making reasonable the assumption of having a dilute flow condition (*i.e.*, the solid particles do not influence the fluid flow).
The tendency of a particle to follow the fluid stream is strongly dependent on the Stokes number (St, defined in Table 2.1) that represents the ratio between the characteristic time of particles or droplets to the characteristic time of the fluid that moves them.
St is proportional to particle density, the square power of particle diameter and a characteristic velocity that can be defined as the average gas velocity. It is, instead, correlated to the inverse of the gas viscosity and a characateristic length that, according to Zhang *et al.* [63], is the chamber diameter for spiral jet mills.
For St<< 1 the particles inertia is negligible if compared to body forces exerted by the fluid and they strictly follow the primary phase streamlines. If St approaches or exceeds the unity (St≈1 or St> 1), then particles can detach from the carrier fluid. Bnà *et al.* [9] reports a four order of magnitude St number variation from 10^{-3} ($d_s = 1$ μm particles following the gas flow) to 10^{-1} ($d_s = 100$ μm, particles moving with their own inertia), indicating that its range within the spiral jet mill can be wide and the particles motion typology in the chamber can vary a lot from side to side.
In order to understand which flow properties influence the particles classification, that is the conditions for which particles can leave the grinding chamber because their orbits becomes smaller than the classifier radius, it is useful to derive a simplified relation able to define the cut-size threshold. Assuming that particles are so small to be moved by the gas without having any relative velocity with respect to the latter (St<< 1) and that the solid volume fraction is small enough to have infrequent particle-particle collisions (dilute flow, $L/d_s > 20$), an analytical expression can be derived [9]:

$$d_{cut} = \frac{3}{8} d_s C_D \frac{\rho_g}{\rho_s} \left(\frac{u_r}{u_t}\right)^2 \tag{4.4}$$

where d_s is the particle diameter, C_D is the drag coefficient, ρ_g is the fluid (gas) density and ρ_s is the particle density. Density and velocities vary non-negligibly near nozzles due to the sudden gas expansion and achieve their maximum in the region near nozzles themselves, just inside the chamber.
Eq. 4.4 also shows that the ratio between the radial (u_r) and the tangential (u_t) fluid velocity components plays a major role in defining the classification capabilities of the system. For this reason, it is convenient to define a non-dimensional group, named spin ratio (as defined by Rodnianski *et al.* [58]), and to carefully study its variation within the chambers:

$$\text{spin ratio} = \frac{u_t}{u_r}. \tag{4.5}$$

The evolution of the disperse phase, especially in the dense flow regime, is not only due to the momentum transfer between phases but it is also caused by instantaneous phenomena that leads to the nucleation of new objects or to their continuous change induced by molecular growth, aggregation, coalescence or breakage.
In this context, the different mechanisms can be classified according to the disperse phase involvment through the order of the process.
This tractation is limited to the mechanisms of interest in this thesis for spiral jet milling, and therefore it is restricted to particle breakage which is the main particle-size modification mechanism for applications of this type.

Particle breakage is usually due to particle-particle or particle-wall collisions and it takes place when the external stresses which the particle is subject to are greater than the cohesion forces that keep the particle intact.
In general, the form of the breakage kernel is a non-linear function of the rupture-to-cohesive force ratio but the specific structure depends on the breakage behaviour of the material that is undergoing the process and, for brittle or semi-brittle particles such as pharmaceutical ingredients, it is usually defined on semi-empirical basis.
In this framework, for example, Ghadiri *et al.* wrote mechanistic models predicting that the breakage rate is proportional to the particle size and to the square of the relative impact velocity [64, 65] or they formalized it as function of a damage ratio [66]. This is written formulating that the particle behaves like an aggregate whose fragmentation is governed by the ratio between the broken to the initial number of bonds and using the relative impact velocity as driving force.

Due to the difficulties encountered in experimentally characeterize the powders mechanical properties at particle level and the impossibility of finding complete physical data of generic pharmaceutical active ingredients (except for few low biological acitivity substances such as lactose), a semi-empiric breakage kernel structure is chosen. Detailed information on the breakage mechanisms modeled are given in Section 4.4.4.

4.1.3 The Caking Mechanism

A well-known problem affecting APIs micronization is the so-called caking, *i.e.*, the formation of large rigid aggregates that stick on the spiral jet mill walls reducing the useful volume of the grinding chamber.
Caking modifies the flow field affecting the classification and the outlet PSD making difficult to match the target requirements set at the beginning of the grinding process. Crusts formation is strongly influenced by the micronized substance and the operating conditions. In some cases, the size of the aggregates increases in

time and reaches a steady-state, as a result of the balance between the caking buildup and erosion forces exerted by the swirled flow field, in many others the apparatus gets chocked. As a consequence, the micronization activity must be regularly stopped for cleaning the jet mill, reducing the effective production time. Moreover, crusts cannot be considered as a micronized product and reduce the process yield.
This loss, along with the high cost of APIs (up to hundreds of thousands USD per kilogram), makes caking doubly detrimental from an economic point of view.

Because of its importance, caking was investigated in scientific literature. Van der Waals and electrostatic interactions as well as the presence of residual humidity have been identified as the main driving forces behind agglomeration (Zafar *et al.*, 2017 [67]; Chen *et al.*, 2018 [68]).
Carpin *et al.* (2017a [69], 2017b [70]) underlined that impurities and powder PSD have a strong influence on agglomeration. It was found that the higher is the particles specific area, the higher is the clustering tendency, meaning that fines have an important effect in generating crusts. It was also shown that the quantity of impurities, especially in humid environments, plays a major role in defining aggregates since they enhance the moisture sorption and water merges powders because of inter-particle bindings.
The same findings were described by Listiohadi *et al.* (2008) [71] while conducting investigations on storage experiments for polymorph lactose. The authors found relevant caking for all the lactose types at almost any relative humidity tested except for anhydrous α-lactose. Caking strength and stiffness were found to change significantly depending on the type of polymorph analyzed. Hardest cakes were obtained for anhydrous β- and spray-dried lactose that formed rigid structures apparently induced by partial fusion between crystals.
More in general, Hartmann & Palzer (2011) [72] found that amorphous powders are prone to form clusters, discovering that the aggregates rigidity can be qualitatively linked to the sinter bridge diameter.
The caking of both crystal and amorphous powders was investigated in the work of Chen *et al.* (2019) [73], who underlined that particles start aggregating mainly because of water (humidity) independently on the amount of crystal phase. Other important factors were reported to be the PSD and the particles shape.
Although studied in general, the caking mechanism for APIs was not extensively investigated and few examples are nowadays available in scientific literature.
Sowa *et al.* (2017) [62] studied the possibility of improving the powder processability by working on the crystallization process of the granules. The authors found that the quantity of aggregates formed increased significantly with time, requiring the process stop to clean the apparatus. Brosh *et al.* (2014) [74] attributed the

sticky behavior of comminuted particles to Van der Walls forces and added their contribution to their Computational Fluid Dynamics – Discrete Element Method (CFD-DEM) simulation model availing of the work proposed by Kalman *et al.* (2009) [75].
The inclusion of the attractive interactions increased the agreement between simulation and experimental data. Among the factors affecting powder aggregation, Branaugh & Smyth (2018) [76] suggested that the amount of fines is one of the most important parameters promoting particles clustering and confirmed that electrostatics interaction due to Van der Waals forces promote caking during spiral jet milling.

A representative example of severe caking is depicted in Fig. 4.3: aggregates with thickness ranging between 10 and 20 mm develop on the chamber periphery, while the crusts reach remarkably larger dimensions in the powder feeder proximity. The image clearly shows how particles agglomeration reduces the grinding chamber effective diameter and internal volume.

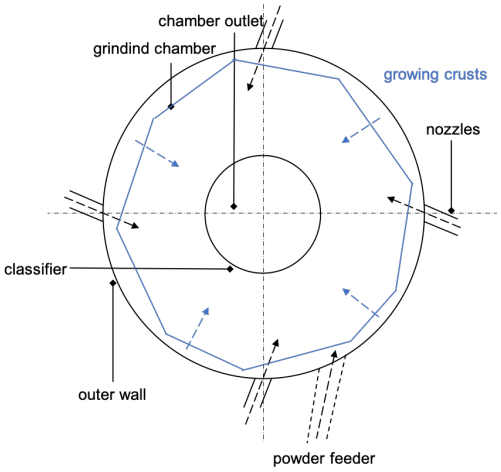

(a) caking growth schematic

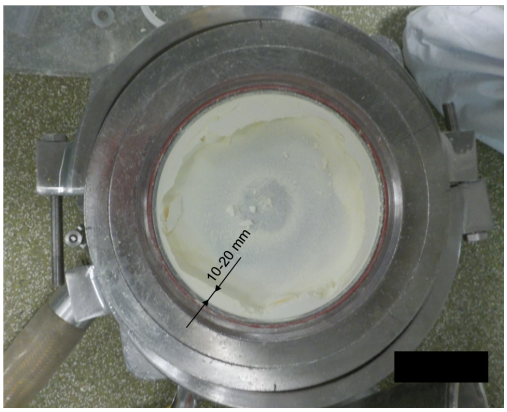

(b) lower plate of a spiral jet mill with svere caking

Figure 4.3: Severe caking case and chamber diameter reduction, courtesy of Jetpharma SA.

A mechanistic understanding of the influence of gas and solid flow on caking and vice versa is currently hindered by the challenging acquisition of experimental data; the effective application of sensors inside the chamber is difficult and can perturb the flow-field, affecting the reliability of the measurement (Ma *et al.*, 2001 [77]).
On top of that, the involved physics are far from trivial, since they include fluid-solid interactions in a compressible, transonic (locally even supersonic) flow-field. Furthermore, caking effects cannot be easily measured even just correlating PSD

values and agglomerates volume, because the latter is not known during the process. An evidence of this correlation can be inferred modeling the "cut size" concept.
The latter is defined as the particle size for which the inertial forces on particles are balanced, *i.e.*, a measure of which particle stays in and which particle goes out the jet mill. This approach requires to evaluate radial and tangential components of the gas flow velocity. MacDonald *et al.* (2016) [78] developed a model for computing cut size as a function of geometrical and process parameters, gas thermodynamic properties and empirically-derived constants. However, many system-dependent parameters must be determined experimentally, potentially affecting the systematic and practical application of this model. It is important to notice that in a milling process affected by caking, these properties, and probably even the constants, would vary with time.
These arguments explain the absence of rigorous studies and the difficulties in predicting the outlet PSD (even without relevant caking phenomena). This scarcity of information leads to trial and error-based approaches, resulting in numerous, expensive and time-consuming tests (Bnà *et al.*, 2020 [9]). The lack of a detailed picture of the involved phenomena and their synergic effects constitutes an obstacle to a more rational mill design and to the development of new effective solutions to avoid or dampen the attainment of caking.

4.1.4 CFD Modelling Challenges

The large cost associated to many APIs makes tests really expensive while the impossibility of performing on-site measurements without deteriorating the velocity fields inside the spiral jet mills prevents a complete understanding of the apparatus fluid-dynamics. In such a scenario, the application of modeling tools like Computational Fluid Dynamics (CFD) constitutes an effective way to obtain those insights that could not be experimentally accessible, since they allow determining the flow field in every point of the grinding chamber, also accounting for the presence of a solid phase.
In this context, Rodnianski *et al.* [58] performed single-phase CFD simulation on a real-scale 3D spiral jet mill with twelve nozzles to obtain average flow fields and developed a classification equation based upon an analytic force model while the particles cut size was defined through experiments.
CFD is usually coupled to a Discrete Element Method (DEM) solution to solve the particles dynamics in detail. This considerably simplifies SJM modelling but it remarkably increases the computational costs since CFD-DEM models need a transient solution for the trajectory of each discrete particle contained in the spiral jet mill. The number of particles within the micronization chamber is huge (see Section 2.6) and can be of the order of $10^8 - 10^9$. Moreover, depending on the level

of coupling between phases, the model solution may need a very small time step, down to 10^{-9} or 10^{-10} s [9]. Hence, the required computational time is huge and this explains the lack of simulations at the characteristic time scales of the process (minutes). In fact, to the best of author knowledge, works reported in scientific literature simulate only the first few instants of the spiral jet milling process.
A pioneering work of Han *et al.* [79] attempted to model the jet milling process by means of CFD-DEM simulations, including particles breakage and chipping through the implementation of the Ghadiri model [64–66]. Authors showed a good agreement between experimental and model results, stating that the solid feeding rate, nozzles angle and fluid pressure have a great effect on final PSD but they did not provide any information about the time step adopted and physical time simulated.
In a recent work, Bnà *et al.* [9] used CFD-DEM to study the motion of one-way Lagrangian particles by simulating the first 70 ms of physical time. They deeply studied the gas velocity profiles and the classification mechanism in spiral jet mills. They tried to describe the influence that an increase of solid holdup has on collision energy and collision frequency, underlining how a soft-coupling between phases is not suitable to describe the interactions of gas and particles where the flow is heavily loaded (near outer walls of the micronization chamber).
Scott *et al.* studied the early stages of the micronization process (up to 100 ms of physical time) inside a spiral jet mill of 50 mm of diameter in order to understand the influence of hold-up [12] and grinding pressure [11, 12] on gas and particle flow patterns for a fully coupled (four-way) solution. It was shown that the gas velocity is influenced by the presence of particles in the periphery of the micronization chamber because of the fast shearing bed of solids that is formed near walls. The higher is the mass loading, the less is the velocity of the gas phase. Authors showed that this mechanism is important only near outer walls and they also underlined how an increase in grinding pressure augments the nozzles jet penetration, generating much more energetic particles collisions.
Bhonsale *et al.* [13] obtained the same results of Scott *et al.* [11, 12] by simulating 150 ms of physical time for a system containing 100'000 particles. The collisions dynamics was studied with a temporal discretization of $2 \cdot 10^{-7}$ s.
These very recent works show that is currently not possible to simulate the entire micronization process, including particle-particle interactions and full mutual coupling between the gas and the solid phase at a process time scale.
This is due to the fact that the computational power offered by modern computers does not allow for a detailed simulation of spiral jet milling in reasonable times. Moreover, the complexity of the physics behind the micronization process makes the construction of robust and reliable particle-particle and particle-wall interaction models for aggregation, breakage and caking not trivial.

Few attempts have been made in the past and they are limited, as shown by the summary given by Table 4.1, to the solution of the first 100-150 ms of milling, allowing for the prediction of the very initial stages of the process. At these time scales, no useful information on the final fate of particles can be gathered. The large cost of many pharmaceutical compounds (up to hundreds of thousands of USD per kilo) still motivates the need of reducing experiments, pushing for the construction of reliable, robust and cheap computational tools able to model the whole process according to its characteristic time scale.
The literature review reported above explains the limitations of current CFD-DEM models and motivates the interest in analyzing the process at single-phase level, getting precious information on the solid particles fate by studying the gas velocity fields only, as showen in different works [2–8].

Table 4.1: Physical time simulated in current CFD multiphase models for spiral jet milling. dt indicates the time step size while t indicates the physical time simulated. App. describes the computational approach used to model the multiphase flow where E-L stands for Eulerian-Lagrangian.

Ref.	Year	App.	Coup.	dt [s]	t [ms]
Bná *et al.* [9]	2020	E-L	one-way	$\propto 10^{-8}$	70
Scott *et al.* [10–12]	2021	E-L	four-way	$4 \cdot 10^{-7} - 10^{-6}$	100
Bhonsale *et al.* [13]	2021	E-L	two-way	$2 \cdot 10^{-7} - 10^{-5}$	150

4.1.5 Objectives

Spiral jet milling is still little studied by the scientific community and the current knowledge has been developed and preserved by the highly-specialized industries working in this field.
The determination of the substance-dependent operating conditions is nowadays based upon expensive experimental campaigns and phenomena, such as caking, that are detrimental for the process and are not characterized.
The currently adopted CFD-DEM computational models can describe only the first few instants of the micronization process but they are not suitable to obtain process-scale information because of the huge computational effort required to run detailed fully-coupled simulations.

Therefore, this work aims at the:

i. determination of a simple and computationally affordable method to imitate the solid aggregates formation on spiral jet mill walls, to study the influence that the caking has on spiral jet mill gas flow-fields;

ii. understandying of the effects that gas velocity modifications causes on the particle classification mechanism by analyzing the radial and tangential velocity components in the micronization chamber;

iii. investigation of the operating conditions influence on the gas flow-field and the proposal of a possible strategy to reduce the velocity variations due to caking establishment during operation;

iv. formalization of a novel computational framework to study the spiral jet milling at process-scales and times;

v. proposal of a suitable breakage kernel to model the fragmentation of pharmaceutical particles;

vi. validation of such a method by comparing model predictions with relevant experimental data.

4.2 Experimental Activities

Note that the Ph.D. candidate partecipated to the experimental activities planning and supervision but he did not complete all the work reported in Section 4.2 by his own.

- Sub-section 4.2.1 - The materials selection has been completed together with Dr. T. Casalini (SUPSI, now AstraZeneca Sweden) and Mr. G. Frigerio (Jetpharma SA).
- Sub-section 4.2.2 - The micronization experiments campaign and tests ranges have been designed by the Ph.D. candidate in collaboration with Mr. G. Frigerio (Jetpharma SA). The design of experiments has been practically produced by Mr. M. Spaggiari (SUPSI, now FHNW Brugg-Windisch). The experiments have been performed at Jetpharma production plants located in Balerna (CH) by specialized technicians following the usual operation techniques for Pharma industry.

4.2.1 Materials and Properties

Lactose and paracetamol are chosen as process compounds because of their different breakage energy, because of the large quantity of mechanical properties data available in scientific literature to design the experiments and their low biological activity.
Moreover, they are cheap, usually available with short lead time and not dangerous.
Table 4.3 reports the hardness (H from nano-indentation), Young modulus (E) and yield pressure (p_Y) with the related references.
Lactose and paracetamol show a comparable hardness but they have a different elastic modulus. Lactose has a higher ductility with respect to paracetamol, meaning that it can absorb more energy before rupture.

Table 4.2: Lactose and paracetamol mechanical properties. # stands for the bibiography entry in references. L identifies lactose while P identifies paracetamol.

Sub.	Ref.	#	H [GPa]	E [GPa]	p_Y [MPa]
L	Masterson & Cao Int. J. Pharm. 362 (2008) 163-171	[80]	0.51 ± 0.22 0.43 ± 0.08 0.18 ± 0.04	-	-
L	Meier *et al.* Powder Technol. 188/3 (2009) 301-313	[81]	0.869	21.44	-
L	Zuegner *et al.* Eur. J. Pharm. Biopharm. 62/2 (2006) 194-201	[82]	1.1	23.7	-
L	O.M. de Vegt PhD thesis U. of Groningen	[83]	0.288	9.7	103
L	Wilson *et al.* Part. II - cap. 9 ISBN:978-1-119-28549-6	[84]	-	-	165-178
P	Cao *et al.* J. Pharm. Sci. 99/10 (2010) 4307-4316	[85]	1 ± 0.2	1.7 ± 0.1	-
P	O.M. de Vegt PhD thesis U. of Groningen	[83]	0.172	3.5	74.7
P	Wilson *et al.* Powder Technol. 143 (2004) 179-185	[86]	0.42 ± 0.03	8.4	-
P	Wilson *et al.* Part. II - cap. 9 ISBN:978-1-119-28549-6	[84]	-	-	102-116

4.2.2 Micronization Tests

Experimental Design

The micronization campaigns are designed, performed and analyzed following an experimental approach based on the DoE methodology (Design of Experiments); as a support, the Design-Expert v11 software [87] was employed.
Given the presence of a categorical factor (*i.e.*, powder typology), tests are split in two independent experimental plans, each consisting of the same number of runs in the same position of the design space.
Two numerical continuous variables, *i.e.*, gas pressure (p) and powder feed rate (FR), are studied and their ranges extremes are defined based on the process expertise and the already available results from previous studies.

Table 4.3: Paracetamol and lactose DoE runs. p is the nozzles pressure while FR is the solid feed-rate.

	Paracetamol		Lactose	
Run	p [bar(g)]	FR [g min^{-1}]	p [bar(g)]	FR [g min^{-1}]
1	7	20	7	600
2	7	310	7	310
3	11	515	12	310
4	7	600	7	310
5	2	310	7	310
6	3	105	7	20
7	7	310	2	310
8	3	515	3	105
9	7	310	7	310
10	7	310	3	515
11	11	310	11	105
12	12	105	7	310
13	7	310	11	515

A response surface – rotatable central composite design (CCD) [88], with 13 runs and capable of supporting a quadratic polynomial model, is built for both lactose

and paracetamol powders. Five of the 13 runs are replicated to estimate the process variability and to get improved model precision in the center of the design space.
Responses, *i.e.*, the results of interest that are analyzed downstream of the experimental activities, are in both cases the size distributions of the particles exiting the mill (D10, D50 and D90).
The capability of the models of finding statistically significant effects is assessed by means of the expected standard deviation (quantified at $\pm$ 3 μm) and the acceptable uncertainty on the responses measurement (equal to $\pm$ 5 μm).

Experimental Set-Up

Experiments were carried out availing of a spiral jet mill called MC with eight nozzles equally distributed and located around the central ring. Nozzles diameters and inclination angle are not described for confidentiality reasons. The micronization equipment, as depicted by Fig. 4.4, was completed by the dosing unit twin-screw volumetric feeder K-Tron T35 and a cyclone dust separator with 600 mm top diameter, equipped with 16 sleeves antistatic polyester filter bag.

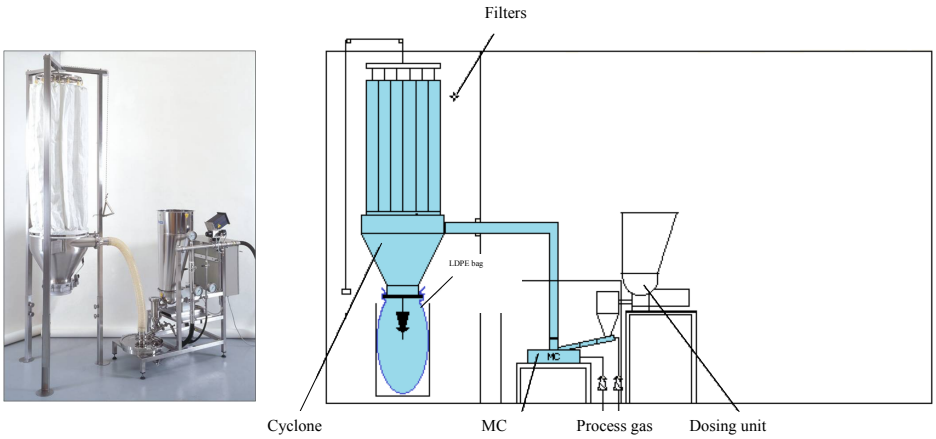

Figure 4.4: Image of the micronization unit (left) and plant schematic with components disposition (right).

The powder feeder linearity has been analysed by weighting the quantity of solid particles delivered by the system in 1 minute of operations and checking 5 different velocities.
The feed rate consistency, *i.e.* the dependency of the quantity of powder on the

filling level of the dosing unit, has been studied by charging the hopper at 10%, 20%, 50% and 80% of its maximum capacity and running it at 310 g min^{-1}.
Each condition has been tested for 5 minutes of operation, checking the actual feed-rate at the beginning, in the middle and the end of the testing time.
Linearity results are shown by Table 4.4 while measure consistency is depicted by values listed in Table 4.5.

Table 4.4: Linearity relation intercurring between powder feeder rotation speed – RPM – and the solid feed-rate – FR. Adjusted $R^2 = 0.9998$.

Feeder speed [RPM]	Feed-rate [g min^{-1}]
0	0
21	22
80	100
165	200
410	500
640	800

Table 4.5: Solid feed-rate provided by the dosing unit for $FR_{nom} = 310$ [g min^{-1}] as function of F and t, with t0 = 0 min, t1 = 2.5 min and t2 = 5 min. F is the percentage of solid loaded into the hopper where F = 100% corresponds to $m_{s,max} = 25$ kg. FR stands for the solid feed-rate.

F [%]	FR @ t0 [g min^{-1}]	FR @ t1 [g min^{-1}]	FR @ t2 [g min^{-1}]
10	308	306	310
20	312	316	314
50	310	308	310
80	312	300	322

Fig. 4.5 show that the dosing unit is able to provide a constant quantity of powder that increases linearly with the feeding screw speed (a) if the filling level of the hopper is taken within 10% and 50% (b). The optimal value of F is maintained for the whole process between 20% and 50%.

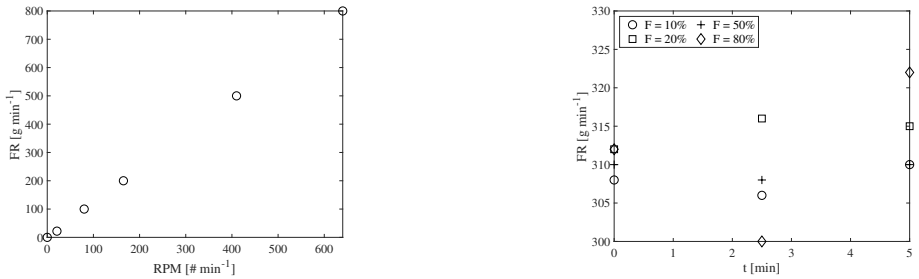

(a) solid volume fraction **(b)** average diameter

Figure 4.5: Powder feed-rate - FR as function of dosing unit screw rotation velocity - RPM (a) and powder feed-rate - FR as function of sampling time- t (b). Filling level F is defined as the ratio between the actual mass of powder loaded in the hopper and the maximum quantity, $m_{s,max} = 25$ kg.

The PSD of raw and micronized powders was measured through a dry laser diffraction analysis with Sympatec HELOS BR with RODOS and Aspiros set up. Both lactose and paracetamol PSD method was validated according to Eu. Ph. <2.9.31>.

Results and Discussion

Experimental D10, D50 and D90 of lactose and paracetamol are shown in Fig. 4.6. Micronization results show that paracetamol requires less energy to be broken with respect to lactose. As expected, at increasing the feed rate FR corresponds an increase in average size while the higher is the nozzle pressure the lower is the particle diameter.
Data gathered through micronization experiments, in terms of mean size values as function of p and FR, can be used for tuning the breakage constant of the model and for validation purposes.

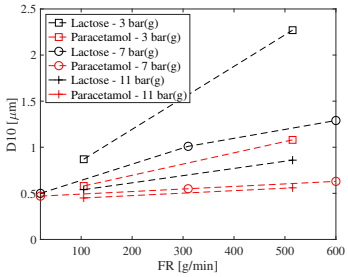

(a) D10, μm

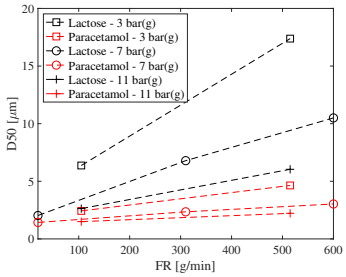

(b) D50 μm

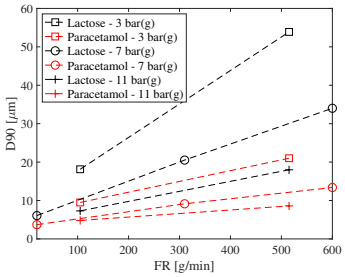

(c) D90 μm

Figure 4.6: Lactose and paracetamol micronization experiments.

4.3 Single-phase Modeling

4.3.1 Caking Mimic Strategy

Assuming that much of the crusts grow takes place on the outer wall of Fig. 4.1, caking is imitated by gradually reducing the chamber diameter to decrease the useful volume and simulate the particles clustering on walls to reproduce the condition depicted by Fig. 4.3. It can be observed from experiments that, in many micronization processes, the thickness of the aggregates sticking on the spiral jet mill walls does not exceed the 20% of the chamber diameter. This guided the computational domain generation and the chamber reduction strategy.
Fig. 4.7 shows that the geometry was designed to allow domain partitioning to build four different jet mills, named with f1 to f4. The four jet mills have a decreasing external diameter with a step equal to 7.5% passing from 100% (reference geometry, f1) to 77.5% (f4). Diameter f1 is taken as reference.

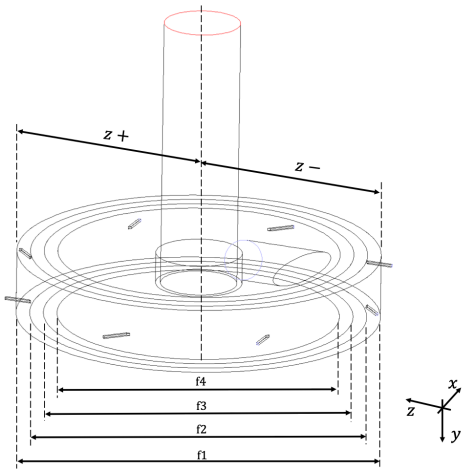

Figure 4.7: Geometry splitting for caking mimic.

Table 4.6 reports the detail of the computational grid splitting and the different chambers produced to mimic caking.

Table 4.6: Detail of the computational grid splitting. The four mesh built uses `f1` as reference and relative dimensions are given as $f_i = 100\,D_i/D_1$ where D_i is the micronization chamber diameter of grid "i" while D_1 is the diameter of `f1`.

Chamber	Relative dimensions [%]
f1	100.0
f2	92.5
f3	85.0
f4	77.5

4.3.2 CFD model

The single-phase flow-field in an inertial reference frame with no gravity effects can be described through a set of partial differential equations of the form [89]:

$$\frac{\mathrm{d}\rho}{\mathrm{d}t} + \nabla \cdot (\rho \mathbf{u}) = 0; \tag{4.6}$$

$$\frac{\mathrm{d}(\rho \mathbf{u})}{\mathrm{d}t} + \nabla \cdot (\rho \mathbf{u}\mathbf{u}) = -\nabla \mathrm{p} + \nabla \cdot \overline{\boldsymbol{\tau}}. \tag{4.7}$$

The viscous shear-stress tensor $\overline{\boldsymbol{\tau}}$ is:

$$\overline{\boldsymbol{\tau}} = \mu \left[\nabla \mathbf{u} + (\nabla \mathbf{u})^{\mathrm{T}} - \frac{2}{3}(\nabla \cdot \mathbf{u})\bar{\mathbf{I}} \right]. \tag{4.8}$$

where ρ is density, μ is the molecular dynamic viscosity, $\mathbf{u}$ is the velocity, p is pressure and $\bar{\mathbf{I}}$ is unity tensor.
Note that the equations reported refer to a simulation in which the flow is composed by a gas only and, therefore, no subscripts are needed to specify a specific phase. The enthalpy ($\mathrm{h} = \mathrm{e} + \frac{\mathrm{p}}{\rho} + \frac{\mathrm{u}^2}{2}$) equation is solved to consider gas compressibility effects, together with the ideal gas equation of state:

$$\frac{\mathrm{d}[\rho(\mathrm{h} + \mathbf{u}^2/2)]}{\mathrm{d}t} + \nabla \cdot \left[\rho \mathbf{u} \cdot \left(\mathrm{h} + \frac{\mathbf{u}^2}{2} \right) \right] = \frac{\mathrm{dp}}{\mathrm{d}t} + \nabla \cdot (\overline{\boldsymbol{\tau}} \cdot \mathbf{u}) + \nabla \cdot \left[\frac{\lambda + \lambda_{\mathrm{t}}}{\mathrm{c_p}} \cdot \nabla \mathrm{h} \right]; \tag{4.9}$$

$$\rho = \frac{\mathrm{p}}{\mathcal{R}\mathrm{T}}. \tag{4.10}$$

h is the specific enthalpy, λ is the molecular thermal conductivity,λ_{t} is the turbulent thermal conductivity, R is the gas constant and $\mathrm{c_p}$ is the constant-pressure specific heat.

The spiral jet mill turbulence flow-field has been computed through the $k - \varepsilon$ realizable model [90]:

$$\frac{\partial}{\partial t}(\rho \mathrm{k}) + \nabla \cdot (\rho \mathrm{k} \mathbf{u}) = \nabla \cdot \left[\left(\mu + \frac{\mu_{\mathrm{t}}}{\sigma_{\mathrm{k}}} \right) \nabla \mathrm{k} \right] + \mathrm{P_k} + \mathrm{P_b} - \rho\varepsilon - \mathrm{Y_M}; \tag{4.11}$$

$$\frac{\partial}{\partial t}(\rho\varepsilon) + \nabla \cdot (\rho\varepsilon \mathbf{u}) = \nabla \cdot \left[\left(\mu + \frac{\mu_{\mathrm{t}}}{\sigma_{\varepsilon}} \right) \nabla \varepsilon \right] + \rho \mathrm{C_1 S}\varepsilon - \rho \mathrm{C_2} \frac{\varepsilon^2}{\mathrm{k} + \sqrt{\nu\varepsilon}} + \mathrm{C_{1\varepsilon}} \frac{\varepsilon}{\mathrm{k}} \mathrm{C_{3\varepsilon}} \mathrm{P_b} \tag{4.12}$$

where k is the turbulent kinetic energy, ε is the turbulent kinetic energy dissipation rate, μ_{t} is the turbulent viscosity, σ_{k} and σ_{ε} are the turbulent Prandtl number for k and ε respectively. $\mathrm{P_k}$ represents the generation of turbulent kinetic energy due to mean velocity gradients while $\mathrm{P_b}$ is the generation of k due to buoyancy. Y_M is due to fluctuating dilatations in ε while $\mathrm{C_1}$, $\mathrm{C_2}$, $\mathrm{C_{1\varepsilon}}$ and $\mathrm{C_{3\varepsilon}}$ are model constants.

Reynolds stresses are computed through the turbulent viscosity concept and they are related to the fluid-flow mean velocity gradients availing of the Boussinesq approximation [91], as described by:

$$-\overline{\rho \mathrm{u}_i' \mathrm{u}_j'} = \mu_\mathrm{t} \left(\frac{\partial \mathrm{u}_i}{\partial \mathrm{x}_j} + \frac{\partial \mathrm{u}_j}{\partial \mathrm{x}_i} \right) - \frac{2}{3} \left(\rho \mathrm{k} \delta_{ij} \right). \tag{4.13}$$

Near-wall modelling is employed through the two-layer approach firstly proposed by Kader [92], in which a continuos law obtained from blending between the linear (laminar) and logarithmic (turbulent) functions used to describe the whole velocity profile near the wall:

$$\mathrm{u}^+ = \mathrm{e}^{\Gamma} \mathrm{u}^+_{\mathrm{lam}} + \mathrm{e}^{1/\Gamma} \mathrm{u}^+_{\mathrm{turb}}. \tag{4.14}$$

The wall-distance based turbulent Reynolds number defines the domain validity regions of the relationships:

$$\mathrm{Re}_\mathrm{y} \equiv \frac{\rho \mathrm{y} \sqrt{\mathrm{k}}}{\mu} \tag{4.15}$$

where y is the first cell-center distance while u^+ is the dimensionless velocity. Γ represents the blending function and it has the form:

$$\Gamma = -\frac{a \left(\mathrm{y}^+ \right)^4}{1 + b \mathrm{y}^+} \tag{4.16}$$

with y^+ corresponding to the dimensionaless wall distance and a and b representing model parameters.

4.3.3 Geometry and Computational Grid

The simplified 3D computational domain consists in the fluid volume of a real-scale spiral jet mill that maintains all the most important features of the real geometry. The geometry is composed by a cylindrical grinding chamber that hosts 8 constant square cross-section nozzles (Fig. 4.8).
The powder feeder is bent by an angle with respect to the chamber upper plate. The latter is connected to an outlet cylinder that allows for particles and process gas exiting.
Geometry data cannot be shared because of confidentiality reasons; all dimensions are scaled with respect to a reference one.

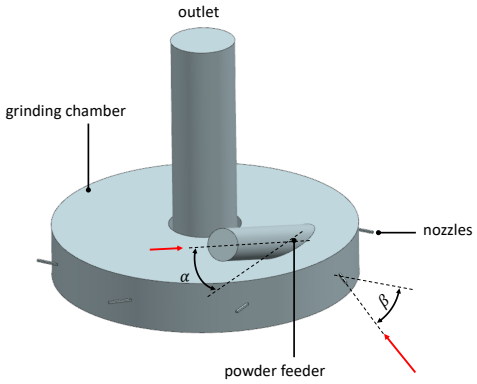

Figure 4.8: Simplified SJM geometric model.

The structured/paved computational grids were built in ANSYS Meshing [93] following a multi-block approach. Elements were aligned with the flow direction in order to properly describe the rapid gradients variations in the flow properties.

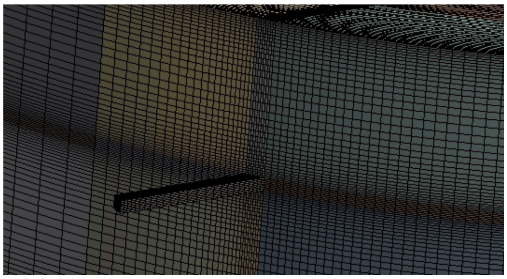

(a) Nozzle-region mesh

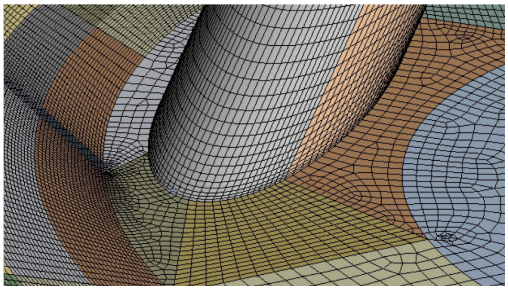

(b) powder inlet mesh

Figure 4.9: Details of the computational grid.

The computational grids have been evaluated controlling the mill maximum velocity with respect to the wall y^+ (Table 4.7) and analyzing the dimensionless absolute pressure ratio (Eq. 4.17), the static temperature and the Ma number variation along nozzles (Fig. 4.11) in the proximity of nozzle 5 of Fig. 4.10a.
Two mesh with a much different grid spacing have been studied. The coarse mesh has a maximum at nozzles walls of 600 while the fine one has a dimensionless wall distance always smaller than 220. The velocity maps obtained for the two grids, visible in the left part of Fig. 4.11, are completely comparable. The position and the shape of the supersonic plume are exactly the same while the difference in the maximum velocity reached is less than 0.65%.

Table 4.7: Mesh sensitivity analysis. y stands for the nozzle cell-center/wall distance, y^+_{max} is the non-dimensional cell-center/wall distance and u_{max} the maximum velocity achieved in the expansion region downstream nozzles.

Chamber	y	y^+_{max}	u_{max}
	[m]	[-]	[m/s]
f1	$8.3 \cdot 10^{-5}$	600	604.74
f1-finer	$2.1 \cdot 10^{-5}$	220	608.87

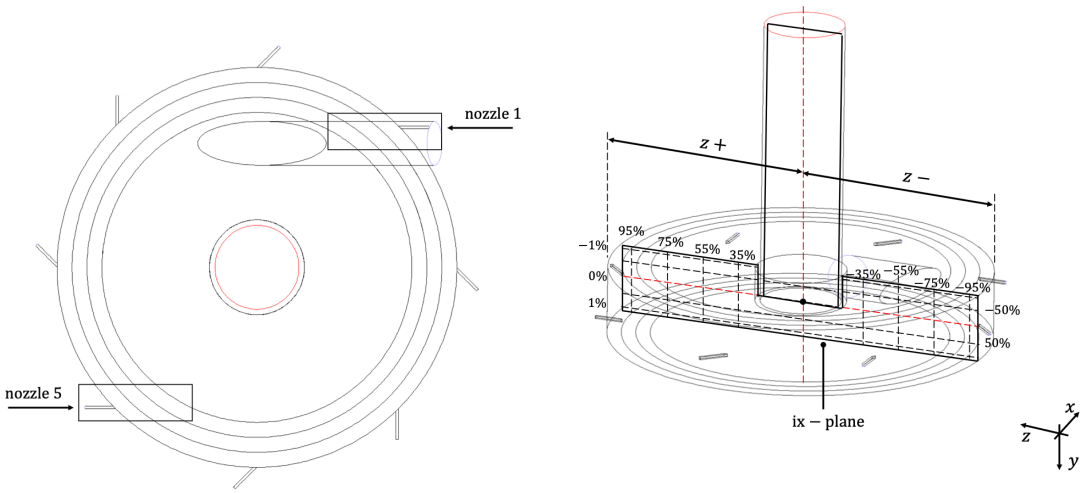

(a) nozzles analyzed **(b)** inspection lines

Figure 4.10: Schematic of inspection lines used for results analysis purposes.

The dimensionless absolute pressure ratio, static temperature and Ma number

evolution along nozzle 5 are depicted by Fig. 4.11. Data show that there is no appreciable variation between the coarse (dots) and the fine (dashed line) grid. The fine grid predicts a slightly larger expansion of the fluid flow, showing a reduction of 6% in static temperature and an increase of 33% of the Ma number.
The variation is limited to the last part of the supersonic plume (between coordinate 0.39 and 0.93 of the non-dimensional segment 0→1) and seems to affect a very localized region of the domain only.
Moreover, there is evidence [9] that the pressure drop between inlets and outlet is well-predicted either with the fine or coarse mesh. Because of these results, together with the agreement between pressure predictions obtained with the coarse and the fine grid of Fig. 4.11, as well as the better convergence behavior obtained with the coarse one, the latter is then used as proper computational grid for the simulations and all the results presented hereafter are obtained with it.

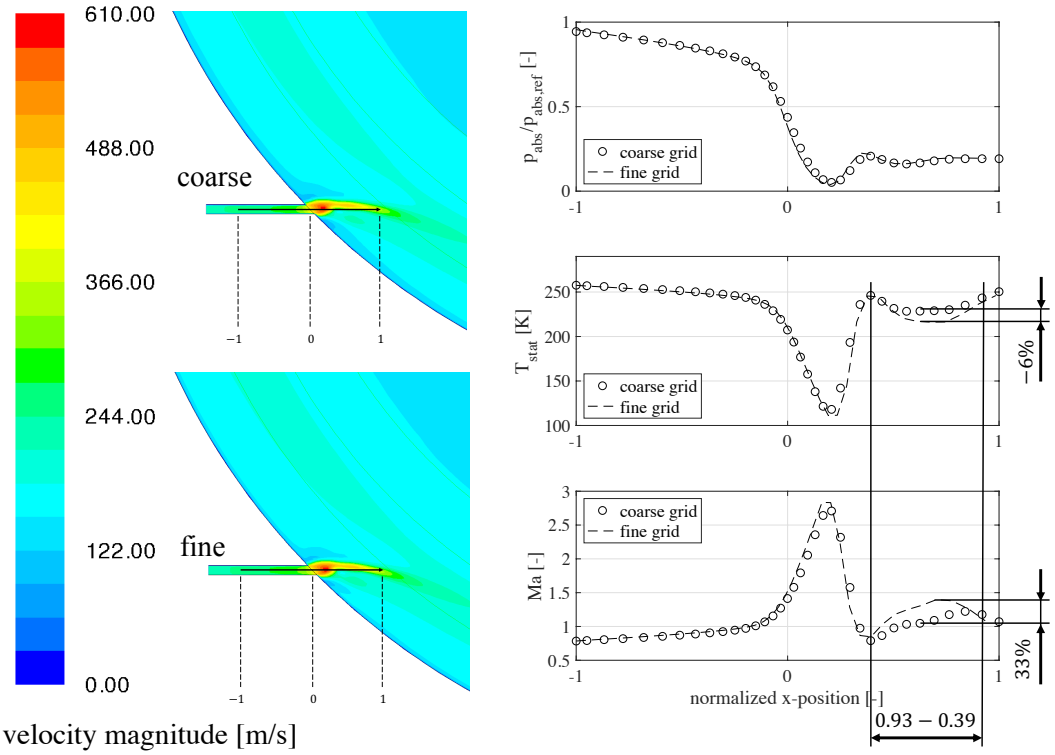

Figure 4.11: Contours of velocity magnitude (left) and properties variation along 0-1 segment (right) for Nozzle 5 in simulation 01 (i/ii), fine and coarse grids.

The computational grids detailed tested for mesh analysis and simulation cases are listed in Table 4.8.

Table 4.8: Computational grids data. # stands for the number of elements used and AR max is the maximum aspect ratio.

Chamber	Elem. type [-]	# [-]	Skewness max [-]	AR max
f1	hexa/prism	4336023	0.93	44.5
f1-finer	hexa/prism	4746167	0.93	44.5
f2	hexa/prism	3393423	0.93	44.5
f3	hexa/prism	2450823	0.93	44.5
f4	hexa/prism	1508223	0.93	44.5

The analysis is conducted comparing the results, in terms of radial and tangential velocity components, over radial domain-crossing lines, as depicted by Fig. 4.10b. The sampling objects are built over the ix-plane and allows for collecting data over five different lines in the radial direction and eight different lines along the chamber height. Relevant properties are also analyzed along the nozzles direction for the different chambers, in order to understand how the expansion of the carrier phase evolves when different geometries are used.
The analysis is completed by evaluating the dimensionless absolute pressure ratio and dimensionless density ratio defined as:

$$p_n = \frac{p_{abs}}{p_{abs,ref}}; \tag{4.17}$$

$$\rho_n = \frac{\rho}{\rho_{ref}}. \tag{4.18}$$

Data is scaled on purpose for confidentiality reasons. Subscript *ref* is used to identify average nozzles inlet properties of 01 case (f1, i/ii) used as reference. The simulation IDs are defined in Table 4.10.

4.3.4 Boundary Conditions

The fluid flow is composed by standard air whose main properties are reported in the following table.

Table 4.9: Fluid properties of standard air @ 298.15 K and 101325 Pa. c_p and c_v are the constant-pressure and the constant-volume specific heat, respectively. λ is the thermal conductivity, μ is the molecular dynamic viscosity and MW is the molecular weight.

Property	Unit	Value
c_p	$\mathrm{J\,kg^{-1}\,K^{-1}}$	1006.43
λ	$\mathrm{W\,m^{-1}\,K^{-1}}$	0.02
μ	$\mathrm{Pa\,s^{-1}\,K^{-1}}$	$1.7894 \cdot 10^{-5}$
c_p/c_v	–	1.4
MW	$\mathrm{g\,mol^{-1}}$	28.01

The determination of proper boundary conditions for the jet mill nozzles is a difficult task. In fact, in spiral jet milling, properties can be usually measured where the gas flow is controlled, *i.e.,* close to regulation valves and discharge points, and their evaluation is usually not possible inside the milling chamber. Therefore, gauge pressure, temperature and volumetric flow rates were gathered during jet mill real operations and then manipulated to compute the gas mass-flow rate and to define local inlet boundary conditions. In particular, the sonic condition was exploited to apply an analytical expression at the nozzle inlets based upon the following assumptions:

i. 1-dimensional and steady-state flow, due to the fact that the gas characteristics change evolving along the nozzle direction, with no time-evolution effects;

ii. adiabatic flow, considering minor thermal exchange effects due to the rapid variations in flow properties;

iii. negligible friction, since the flow can be considered inviscid due to the high-velocity;

iv. ideal gas, since air at those pressure and temperature conditions behaves like and ideal gas.

In these assumptions, the mass flow rate can be evaluated from nozzles chocking conditions, *i.e.*, by the following expression [94]:

$$\dot{m} = p_0 A_t \left[\frac{c_p/c_v}{\mathcal{R} T_0} \left(\frac{2}{c_p/c_v + 1} \right)^{\frac{c_p/c_v+1}{c_p/c_v-1}} \right]^{0.5}, \tag{4.19}$$

that basically states that the mass-flow is controlled by the throat area of the nozzles, A_t, and the total upstream quantities p_0 and T_0. The gas characteristics also play a role, through the values c_p/c_v and $\mathcal{R}$ that are the heat capacity ratio and the gas constant, respectively. In this work, the carrier phase is air and no other gases were accounted for. The influence of different carrier phases on the process can be eventually found in the Ph.D. thesis of Bartholomäus [95].
The spiral jet mill analyzed in this study has 8 grinding nozzles and one powder feeder that is served by another nozzle with a larger throat section. The solution of Eq. 4.19 gives the mass-flow rate passing through each grinding nozzle, and its multiplication by 8 reports the total grinding gas mass per unit time. The total air consumption measured by experiments is then used to compute the air mass flow rate passing through the Venturi tube of the powder feed. The fluid at inlets is assumed to be at the stagnation temperature T_0. As reported by Table 4.10, the simulations of all four mill geometries are conducted for two different operating conditions:

- i: constant absolute pressure @ nozzles inlet while the chamber diameter is reduced by 7.5% (f1 = 100% to f4 = 77.5%);
- ii: constant gas mass flow rate @ nozzles inlet while the chamber diameter is reduced by 7.5% (f1 = 100% to f4 = 77.5%).

Case 01 in Table 4.10 is taken as reference case and its mass-flow rate and absolute pressure conditions, originally computed starting from experimental data, are used to define the boundary conditions for the other simulations, according to condition i or ii.
Condition ii is intended to simulate the usual operating regime experienced by a spiral jet mill with severe caking taking place, in which the gas usage does not vary during the process and its mass-flow rate is kept constant despite the crusts growth (increase in the absolute pressure by 9 to 11%). Condition i is used to test the effect that a reduction of the gas mass flow rate at inlets of 6 to 10% has on the fluid velocities when the diameter is reducing (caking is taking place), with the aim of maintaining constant the chamber absolute pressure and tune the velocities components.

Table 4.10: Simulations IDs and associated chamber dimensions/op.conditions. f1 identifies the largest chamber whose results are taken as reference while f4 is the smallest. Op. condition i stands for a costant absolute pressure (p_{abs}) condition while op. condition ii consists in a costant mass-flow rate (mfr) condition applied at nozzles inlets.

Sim.	Chamber	Op. cond.	$mfr_{in}/mfr_{in,ref}$ [-]	$p_{abs,in}/p_{abs,in,ref}$ [-]
01	f1	i/ii	1.00	1.00
02	f2	i	0.90	1.00
03	f3	i	0.84	1.00
04	f4	i	0.78	1.00
05	f2	ii	1.00	1.11
06	f3	ii	1.00	1.19
07	f4	ii	1.00	1.27

Plots of Fig. 4.12 graphically represent the non-dimensional absolute pressure ratio (a) and non-dimensional inlet mass-flow ratio (b) between the actual value and the reference one as function of the mill chamber dimension and the operating condition.

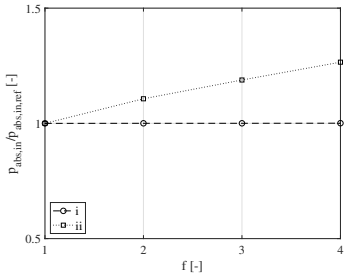

(a) absolute pressure at nozzles inlets

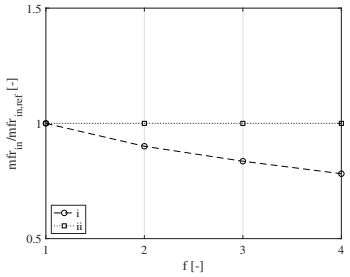

(b) mass-flow rate at nozzles inlets

Figure 4.12: Non-dimensional pressure ratio **(a)** and non-dimensional mass-flow rate ratio **(b)** between the actual and the reference value (01) of the property for the four chambers (f1-f4) and the two operating conditions (i,ii) analyzed.

4.3.5 Solver Details and Settings

The CFD code used in this work is the commercial software Fluent by ANSYS [96].

The gas expansion through nozzles causes high velocities within them and the swirled streamlines inside the chamber causes the Mach Number (Ma) to overcome 0.3 in many regions. Ma gives the ratio between the flow velocity and the local speed of sound at a given temperature and it is defined as:

$$\mathrm{Ma} \equiv \frac{|\mathbf{u}|}{\sqrt{(\mathrm{c_p}/\mathrm{c_v})\mathcal{R}\mathrm{T}}} \tag{4.20}$$

where $\mathbf{u}$ is the flow velocity, $\mathrm{c_p}/\mathrm{c_v}$ is specific heats ratio, $\mathcal{R}$ stands for the specific gas constant and T is the gas temperature.
At these velocities the gas density becomes a strong function of temperature and pressure. In order to account for compressibility effects, air is assumed to behave like an ideal gas while the dynamic viscosity is kept constant to air standard value, since the extremely turbulent nature of the flow makes the eddy viscosity be predominant by orders of magnitude with respect to the molecular one.
In order to provide stability and robustness to the solution, the Pressure-Based Coupled Solver is used to solve Reynolds-Averaged Navier-Stokes equations (RANS). The pressure-correction and momentum equations are treated in a single step while the remaining relations (energy and turbulence model equations) are solved in a segregated manner.
As previously mentioned, turbulence was modeled through the two-equations realizable model built upon the isentropic eddy viscosity approximation (Shih *et al.* [90]).
A two-layers law-at-the wall model is used to switch between the actual computation of the velocity profile till the first cell center ($y^+ \approx 1$) and the usage of wall-functions ($y^+ > 30$).
Gradients are discretized using the Green-Gauss Node-Based method [97] to obtain high-accuracy evaluations also for skewed cells. In order to well describe the pressure variation through nozzles and where the sudden expansions take place, pressure is interpolated at cell faces using momentum equation coefficients as described by Rhie & Chow [98]. Spatial discretization for momentum, energy and turbulent balances is obtained by the second-order upwind scheme, built upon the formalism proposed by Barth & Jespersen, ensuring drastic accuracy improvements with respect to first-order schemes even for mesh zones with abrupt changes in cell size and orientation.
Only steady-state solutions are investigated since the analysis is not aimed at studying the whole temporal dynamics of the system.
Pseudo-Transient Under-Relaxation [99] is used to implicitly under-relax transport equations and improve the convergence behavior by applying an artificial time-stepping.
The pseudo time-step is automatically computed by the solver according to the

flow velocities inside the computational domain. A complete list of simulation numerical settings is given in Appendix C.

4.4 Multiphase Modeling

Note that the 1D compartment-based model presented in Sub-sections 4.4.3 and 4.4.4 has been derived in collaboration with Dr. Casalini and Dr. Cornolti (SUPSI).

4.4.1 Computational Algorithm

The comprehensive model follows the procedure detailed in the flow-chart of Fig. 4.13. The description of the sub-models of the various steps is provided in the following sub-sections. The first stage (green boxes) involves the computation of the gas velocity and density fields through the single-phase, steady-state, 3D CFD simulation of the SJM micronization chamber under given process conditions (in terms of pressure and temperature of the inlet gas pressure). In the second step, this data is lumped into 1D grid that evolved along the chamber radial direction to provide velocity fields to a compartmentalized model. Its formulaic description accounts for i) classification, by computing particles velocity through algebraic expressions and neglecting the influence of solids interactions on the gas flow field, assuming a one-way soft coupling between phases and ii) breakage, by solving mass balance along with a suitable kernel.
While it is known that particles tend to segregate near the walls of the micronization chamber [10–12], the gas-solid mixture can be assumed to be dilute [34] in most of the SJM. This information justifies the previous assumption, at the base of this model.

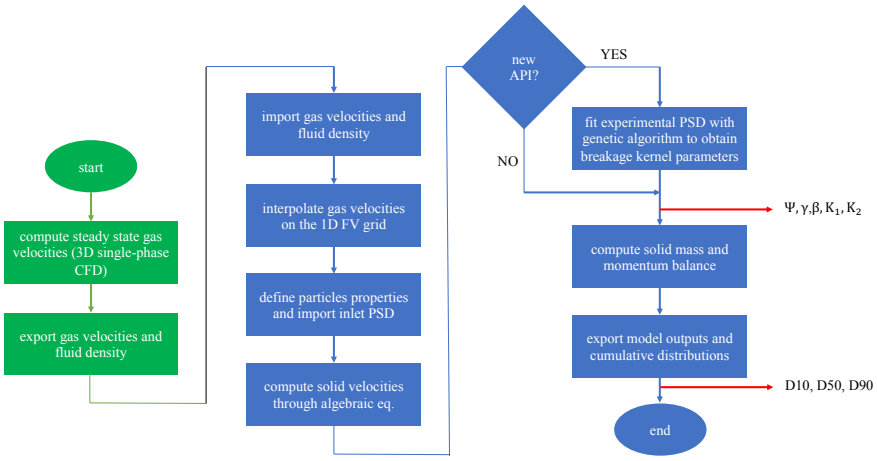

Figure 4.13: Computational algorithm for coupling 3D single-phase CFD simulations (green boxes) with 1D compartimentalized solution for particle motion and breakage (blue boxes).

Starting from radial-dependent gas velocity profiles as well as the inlet particle size distribution, the simplified 1D model solves the mass and momentum balance equations for each considered particle size and it provides the outlet PSD, which can be readily compared with its experimental counterpart if available. In more detail, substance-specific input parameters for breakage kernel were here estimated by fitting experimental outlet PSD through a multi-parameter regression availing of a genetic algorithm. The tuned model can be further employed to estimate the PSD for other process parameters. When a new compound is investigated, some experiments must be performed to provide the measured PSD of the processed powers to the 1D model to estimate the substance-specific parameters of the breakage kernel.

4.4.2 CFD model and SJM domain

The CFD model used to calculate the velocity profiles for the compartment-based model is exactly the same used for single-phase simulations and it is, therefore, not described.
Velocity data are taken over horizontal, radially evolving lines labeled as -1%, -50%, 0%, 50% and 1% in Fig. 4.10b.

4.4.3 1D Compartimentalized Model

The spiral jet mill micronization chamber is schematized as an isothermal reactor of cylindrical shape, discretized according to a cell-centered FVM. Based upon the SJMs working principle, the model assumes that the particles segregation takes place only along the radial direction. Axial inhomogeneities are neglected since the main mechanism governing both micronization and aerodynamic classification is the radial force balance acting on particles.
The computational domain has been discretized into a series of well-mixed compartments of annular shape, each one representing a computational cell of the 1D domain (Fig. 4.14). All the properties are assumed homogeneous in every compartment. The particle size distribution is discretized into M classes selected within the range of the maximum size of the inlet PSD and the minimum particle diameter expected at the end of the micronization. The discretization scale is logarithmic to increase the density of small size classes and to better describe the cumulative distribution.

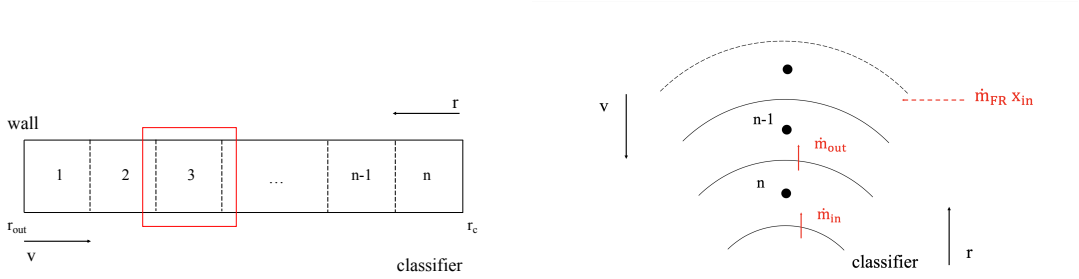

(a) computational grid schematic and radius-velocity sign convention

(b) graphical representation of mass fluxes entering and leaving a toroidal compartment of the model

Figure 4.14: Spiral jet mill micronization chamber schematization: side view with 1D grid discretization (a) and top view with mass fluxes detail (b).

Fig. 4.14 depicts a schematization of the computational domain, with the sign convention for radial velocity and the spatial coordinate (grid mapping). According to the adopted assumptions, the mass balance for the generic j-th compartment and the i-th particle class has the form:

$$V_j \frac{d\omega_{ij}}{dt} = \dot{m}_{in,i} - \dot{m}_{out,i} + \dot{m}_{FR} x_{ij} + G_{ij} V_{ij} = A u_{r,i} \omega_i|_{in} - A u_{r,i} \omega_i|_{out} + G_{ij} V_{ij} \quad (4.21)$$

where ω_{ij} is the mass concentration of particles with diameter d_i in the compartment j, V_j is the volume of the j-th compartment, t is time, r is the radial

coordinate, $\dot{m}_{in,i}$ and $\dot{m}_{out,i}$ are the inlet mass flow rates from the adjacent compartments and their outlet mass flows to the adjacent compartments of particle class i, respectively. $u_{r,i}$ is the radial velocity of particles with diameter d_i, A is the face area corresponding to the lateral surface of a cylinder, $\dot{m}_{FR}$ is the mass feed rate and G_{ij} is birth or death rate of particles due to breakage. In more detail, $\dot{m}_{FR}$ is equal to zero in every compartment except for the one that, according to the adopted radial grid, corresponds to the position of the feed in the experimental apparatus.
Variables ω_{ij} and x_{ij}, which is a weight function describing the relative mass fraction of each particle class passing through the inlet, are defined as MxN matrices where M is the total number of particle classes while N is the number of compartments.
Given that particle fragmentation is by far the predominant mechanism driving the size reduction and particles dimensions at the outlet, aggregation events are not considered in this model at this stage.
Eq. 4.21 needs the evaluation of solid mass flows at cell faces that can be computed by multiplying the solid radial velocities by the face mass concentration. The first quantity is computed by interpolating cell-centers velocities at compartments faces with a central difference scheme while the mass concentration is discretized implicitly with an upwind scheme.
The solid radial velocity as function of the particle diameter, d_i, and radial position (*i.e.*, for each compartment) is computed by solving the simplified steady-state momentum balance in which particles are allowed to exchange momentum with the fluid phase thanks to the drag force only:

$$\frac{\pi}{8} C_D \rho_p d_i^2 \left(u_{r,i} - u_{r,ij}\right) \left|u_{r,i} - u_{r,ij}\right| - \frac{\pi}{6} \rho_s d_i^3 \frac{u^2_{j,ij}}{r} = 0 \tag{4.22}$$

where C_D is the drag coefficient, ρ_s is the solid density, $u_{r,j}$ is the gas velocity in in the j-th compartment, $u_{r,ij}$ and $u_{t,ij}$ are radial and tangential velocities of the i-th particle class in the j-th compartment, respectively.
Eq. 4.22 constitutes a system of uncoupled and weakly non-linear relationships that can be directly solved once the tangential velocity component of particles is known.
For the generic i-th particle class, the latter can be computed from the slip velocity equation developed by Konno & Saito [59] for pneumatic transport:

$$u_{t,ij} = u_{t,j} \left(1 - 0.0638 d_i^{0.3} \rho_s^{0.5}\right) \tag{4.23}$$

where $u_{t,j}$ is the local gas velocity in the j-th compartment computed through 3D single-phase CFD simulations.

The drag coefficient, C_D, and particles Reynolds number, Re_s, is computed according to the Schiller & Naumann [100] relationship:

$$C_D = \max\left[0.44, \frac{24}{Re_s}\left(1 + 0.15Re_s^{0.687}\right)\right] \tag{4.24}$$

where:

$$Re_s = \frac{\rho_g |u_{r,i} - u_{r,ij}| d_i}{\mu_g}; \tag{4.25}$$

with ρ_g equal to the gas density and μ_g is the gas dynamic viscosity.
Writing Eq. 4.22 at steady-state implies the assumption that solid particles are accelerated instantaneously to the final velocity as result of the force balance acting on them. This hypothesis is valid for small particles immersed in a high velocity flow and it has been verified by solving the same momentum balance in transient state, using still particles as initial condition. Simulations show that particles reach the steady-state motion in less than 10^{-2} s, a much shorter time the SJM process scales, corroborating the assumption.
This, together with the assumption of dilute flows conditions, allows for using steady-state velocities in the temporal integration of mass balances, significantly reducing the model complexity and the number of equations that must be solved. The discretized form of Eq. 4.21 generates a system of NxM coupled linear first order ordinary partial differential equations. The coupling among equations is related to the implicit treatment of the convective fluxes, while the coupling among concentration of different particles sizes is achieved because of the source term G_{ij}, which is described in the following section. This system is solved with the ode15s solver provided by Matlab [101]. After about 5 second of physical time, the simulation reaches a steady state solution.
The model consistency is verified through the global mass balance that must be satisfied for each temporal time-step computed:

$$M_{in}(t) + W(t_0) = W(t) - M_{out}(t) \tag{4.26}$$

where $M_{in}(t)$ is the solid mass fed from time zero to time t, $W(t_0)$ and $W(t)$ are the solid mass present in the domain at time zero (t_0) and time t, respectively and $M_{out}(t)$ is the total solid mass escaped from the system from the beginning of the process until time t. Terms of Eq. 4.26 can be computed as:

$$M_{in}(t) = \int_0^t \dot{m}_{FR} dt; \tag{4.27}$$

$$W(t) = \sum_{i=1}^{M}\sum_{j=1}^{N} \omega_{ij} \Delta V_j; \tag{4.28}$$

$$\mathrm{M_{out}}(t) = \int_0^t \sum_{i=1}^{M} \mathrm{Au_{r,}}_i \omega_i|_{\mathrm{out},N} \mathrm{d}t. \tag{4.29}$$

Eq. 4.26 can be used to derive an error function, $\varepsilon(t)$, that allows for evaluating i) the correct implementation of the model in a Matlab code and ii) the numerical inaccuracy introduced by the radial coordinate and particle diameter discretization:

$$\varepsilon(t) = 100 \frac{\mathrm{M_{in}} + \mathrm{W}(t_0) - \mathrm{W}(t) - \mathrm{M_{out}}(t)}{\mathrm{W}(t)}. \tag{4.30}$$

Simulations show that the mass balance is always verified with less than 1% for all the conditions tested.

4.4.4 Breakage kernel

Particles can break because of three different mechanisms: simple breakage, chipping and fragmentation (Salman *et al.* [102]). Pharma powders usually behave like brittle or semi-brittle material but their response is function of the particle diameter. Rowe & Roberts [103], indeed, showed that the breakage typology is dependent on a critical diameter that defines the deformation behavior, ranging from ductile for small particles ($\mathrm{d} < \mathrm{d_{crit}}$) to fragile for larger objects ($\mathrm{d} > \mathrm{d_{crit}}$). The critical diameter is a strong function of the substance itself and its mechanical properties: elastic modulus, hardness and toughness play a major role in defining its value. Shariare *et al.* [104], for example, reported a critical diameter for Paracetamol of about 7 μm.
The description of such a behavior is taken into account through a semi-empirical model that weights the two different breakage dynamics by a parameter Ψ while the dependency on the particle size is considered through exponents γ and β.
Assuming a first-order breakage kinetics, the birth/death rate, G_{ij}, can be written availing of the concept of breakage function and selectivity firstly proposed by Kolmogorov & Epstein and later described by Austin [105] as:

$$\mathrm{G}_{ij} = -\mathrm{S}_{ij}\omega_{ij} + \sum_{k=1}^{i} \mathrm{S}_{ij}\omega_{kj}\mathrm{b}_{ki} \tag{4.31}$$

where S_{ij} is the selectivity associated to particles with diameter d_i in the j-th compartment.
M is the total number of diameter classes, b_{ki} is the probability that the breakage of a particle of size k ends in a smaller particle i. Note that, with this notation, the ordering of the particle size is descending, that is, $\mathrm{d}_1 = \mathrm{d_{max}}$ and $\mathrm{d_M} = \mathrm{d_{min}}$.

The selectivity, computed according to Gommeren *et al.* [106, 107], gives the fraction of particles selected for breakage and is computed as:

$$S_{ij} = \frac{K_1 W_j}{K_2 + W_j^{3/2}} p^2 \sqrt{\frac{d_i}{d_{max}}} \tag{4.32}$$

where K_1, with units $g^{1.5}\,bar(g)^{-1}\,s^{-1}$ and K_2, with units $g^{1.5}$, are substance-dependent parameters that have to be determined experimentally, W_j is the mass holdup in the j-th compartment in g, p is the nozzle pressure in bar(g) and d_{max} is the largest possible diameter value that particles can assume with units μm.
The density breakage function, b_{ki}, is computed as [105]:

$$b_{ki} = B_{ki} - B_{k-1,i} \tag{4.33}$$

where:

$$B_{ki} = \Psi \left(\frac{d_k}{d_i}\right)^{\gamma} + (1 - \Psi) \left(\frac{d_k}{d_i}\right)^{\beta}, \quad \text{for} \quad \frac{d_k}{d_i} \leq 1. \tag{4.34}$$

Parameters Ψ, γ, β of b_{ki} define the breakage mechanism and they have to be determined experimentally. Eq. 4.34 is valid only when $d_i \leq d_k$, *i.e.*, with the employed notation for $k \geq i$, otherwise $B_{ki} = 0$.

The semi-empirical nature of the model imposes a calibration based upon experiments for each tested substance. The Design of Experiments lists the operating conditions used for the experimental characterization performed with a MC spiral jet mill.
The model parameters are determined through a generalized version of the Differential Evolution (GDE3) genetic algorithm presented by Kukkonen & Lampinen [108] and later elaborated and implemented in Matlab by Baur [109].

4.5 Results and Discussion

4.5.1 Part 1: Single-phase Velocity fields and Caking Analysis

Fig. 4.15 reports the dimensionless absolute pressure (a), static temperature (b), dimensionless density (c) and velocity magnitude (d) contour plots inside the grinding chamber f1. Images show an annular region of high velocity flow that moves around the chamber in proximity of nozzles. Pressure, density and temperature contours show that, apart from expansion regions downstream nozzles (detailed in the same figure), there is no abrupt properties variation within the chamber. The velocity maps (d) of Fig. 4.15 shows that the comminution chamber has an internal region in which the velocity is about 120-150 $\mathrm{m\,s^{-1}}$ and another one (previously called "annular region") in which the velocity is in average between 150 and 250 $\mathrm{m\,s^{-1}}$.

Contours of Fig. 4.15 also show that the outer zones have low pressure. Most of the temperature and density variations are localized into mill parts where larger expansions take place. The supersonic jets coming from nozzles appear to be deviated by the air flow already rotating inside the chamber. Plumes disappear washed out by the large volume flow rate passing through the jet mill. This behavior is also confirmed by previous observations made in earlier works (Bnà *et al.*, [9]; MacDonald [78]).

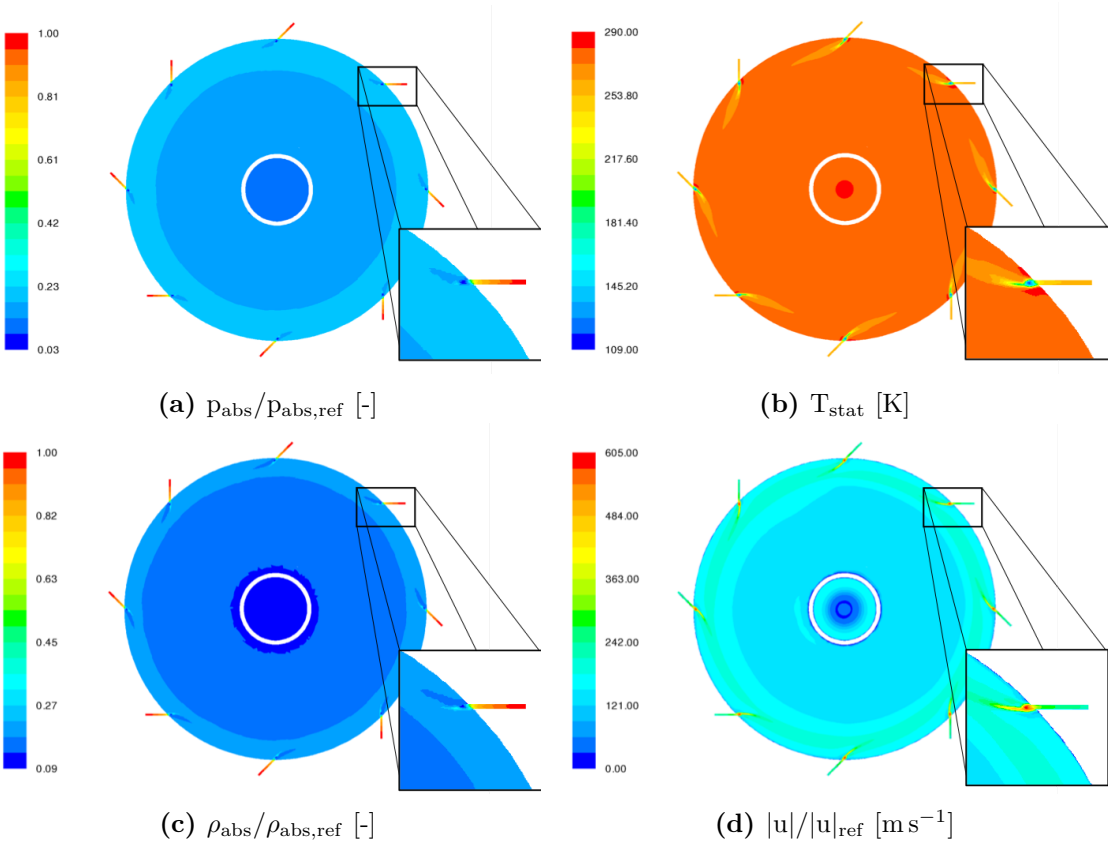

(a) $p_{abs}/p_{abs,ref}$ [-] **(b)** T_{stat} [K]

(c) $\rho_{abs}/\rho_{abs,ref}$ [-] **(d)** $|u|/|u|_{ref}$ [$m\,s^{-1}$]

Figure 4.15: Flow property maps on the nozzles middle plane of simulation 01 (f1, i/ii). Pressure and density fields have ben made simensionless for confidentiality reasons by scaling the cell actual value for the reference taken at inlet nozzles. Details of the maximum expansion region.

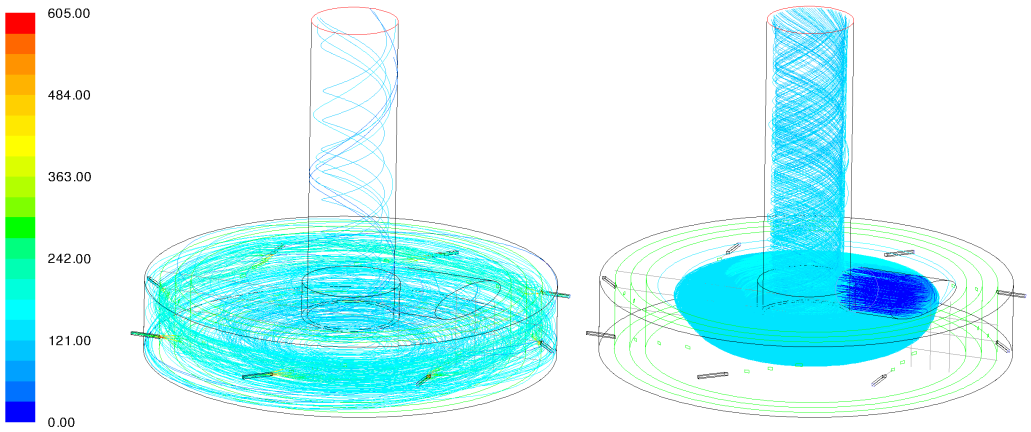

Figure 4.16: Flow pathlines coloured by velocity magnitude ($\mathrm{m\,s^{-1}}$) of simulation 01 (f1, i/ii). The image represents the flow segregation experienced by the process fluid coming from nozzles (left) and the powder feeder (right).

Fig. 4.16 (left) depicts the streamlines generated by the flow coming from nozzles. As it can be seen the gas moves slowly from the outer part to the inner part of the grinding chamber, without an efficient mixing with gas entered by the powder feeder (Fig. 4.16, right).
The right picture of Fig. 4.16 also shows that the air coming from the powder feeder remains segregated within the inner part of the chamber, located in the upper semi-half of the grinding volume. Due to this particular flow pattern drawn by the fluid coming from the powder feeder, it is clear that the classifier height (h_c of Fig. 4.1b) plays a major role in determining the cut size and therefore the classification capacities of the system. Its presence, indeed, constitutes a barrier and prevents the direct exit of fresh air that gathers the raw powders, allowing for keeping particles inside the comminution chamber to be grinded.

Fig. 4.17 shows the evolution of velocity magnitude contours and dimensionless absolute pressure, static temperature and Ma number along nozzle 5 of Fig. 4.10a, a for chambers f1, f2, f3 and f4 when constant pressure is imposed at inlets (operating condition i of Table 4.10). It is interesting to notice that the maximum expansion region is common to all simulations and it is located inside the chamber, while the supersonic condition is reached in the throat section of nozzles. Once chocking is established, the nozzles cross-section starts to enlarge because of the conjunction with the chamber and the flow experiences an enduring expansion similar to what happens in De-Laval nozzles. The largest value for Ma number is found where the most abrupt variation of temperature and pressure is located and the position seems to be not influenced by the chamber dimension and, therefore, by the local flow condition. The maximum Ma value is, instead, a function of the mill diameter and the largest velocity is obtained for the reference chamber (f1), reaching a Ma peak approximately equal to 2.8.

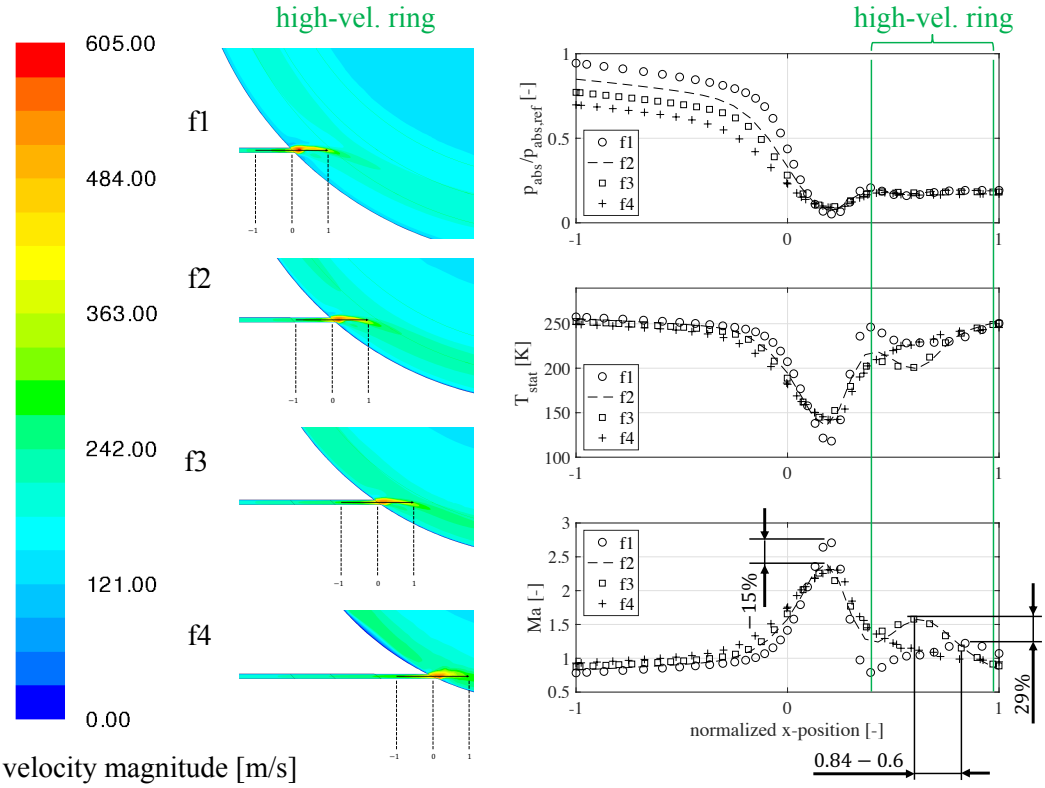

Figure 4.17: Contours of velocity magnitude (left) and properties variation along 0-1 segment (right) for Nozzle 5 in simulation 01-04 (f1-f4, i).

The abrupt expansion takes the fluid temperature down to 108/110 K. The large gradients are limited to the supersonic plume and temperature rapidly raises to 250

K in the space segment 0→1. The absolute pressure also decreases until a value of 5-10% of the reference inlet pressure, well under the standard atmospheric pressure for a very limited portion of chamber. Results show that caking smooths oscillations and gradients after the maximum expansion but the conditions far from the latter are not influenced by the crusts presence. The air already rotating inside the milling chamber tends to wash out the expansion, facilitating the recompression of the fluid at a similar value for all the mill dimensions.
The toroidal region of high velocity fluid that rotates in the outer part of the chamber (green ring in the velocity maps of Fig. 4.17) is pushed towards the mill walls when the chamber radius is decreased, indicating that the rapid flow moving near nozzles is influenced by the spiral jet mill diameter and the gas motion tends to erode the crusts with higher intensity as the clustering becomes more efficient and aggregates occupy the chamber.
Non-dimensional absolute pressure decreases along segment 0→1 as the mill chamber is made smaller while its value through the initial part of the comminution volume does not change significantly (0→1).
The opposite condition is found for temperatures and velocities that are affected by the chamber radius when the flow exiting the nozzles encounter the rotating fluid. A significant change in Ma number is found for chamber f1 with respect to the others, with a difference of 15% of the reference case. Although the reduction in the chamber diameter causes the smoothing of the peak expansion values for each property analyzed, chambers f2 and f3 show an increase of almost 30% of the local Ma number in the segment 0→1. The variation is very limited in space but points out how the caking phenomenon tends to smooth gradients and push high velocity zones towards the outer wall.

The radial and velocity components, as well as the inverse of the spin ratio, are shown in Fig. 4.18 (as function of the non-dimensional radial or z-coordinate) and Fig. 4.19 (as function of the non-dimensional height or y-coordinate). Cell-center data are gathered and plotted for the four mill chambers studied and operating condition i, to simulate the effect that the reduction of the gas mass-flow rate has on the velocity components while caking is advancing.
Radial velocities, as depicted by Fig. 4.18, oscillate between -15 to 15 $\mathrm{m\,s^{-1}}$ over the whole domain except for very limited zones such the grinding chamber zone near the nozzles and the upper semi-half of the comminution volume that is affected by the presence of the powder feeder (Fig. 4.19). Nozzles cause a non-negligible peak in radial velocity, locally reaching a value of over -500 $\mathrm{m\,s^{-1}}$, orders of magnitude larger than the average value in the rest of the chamber.

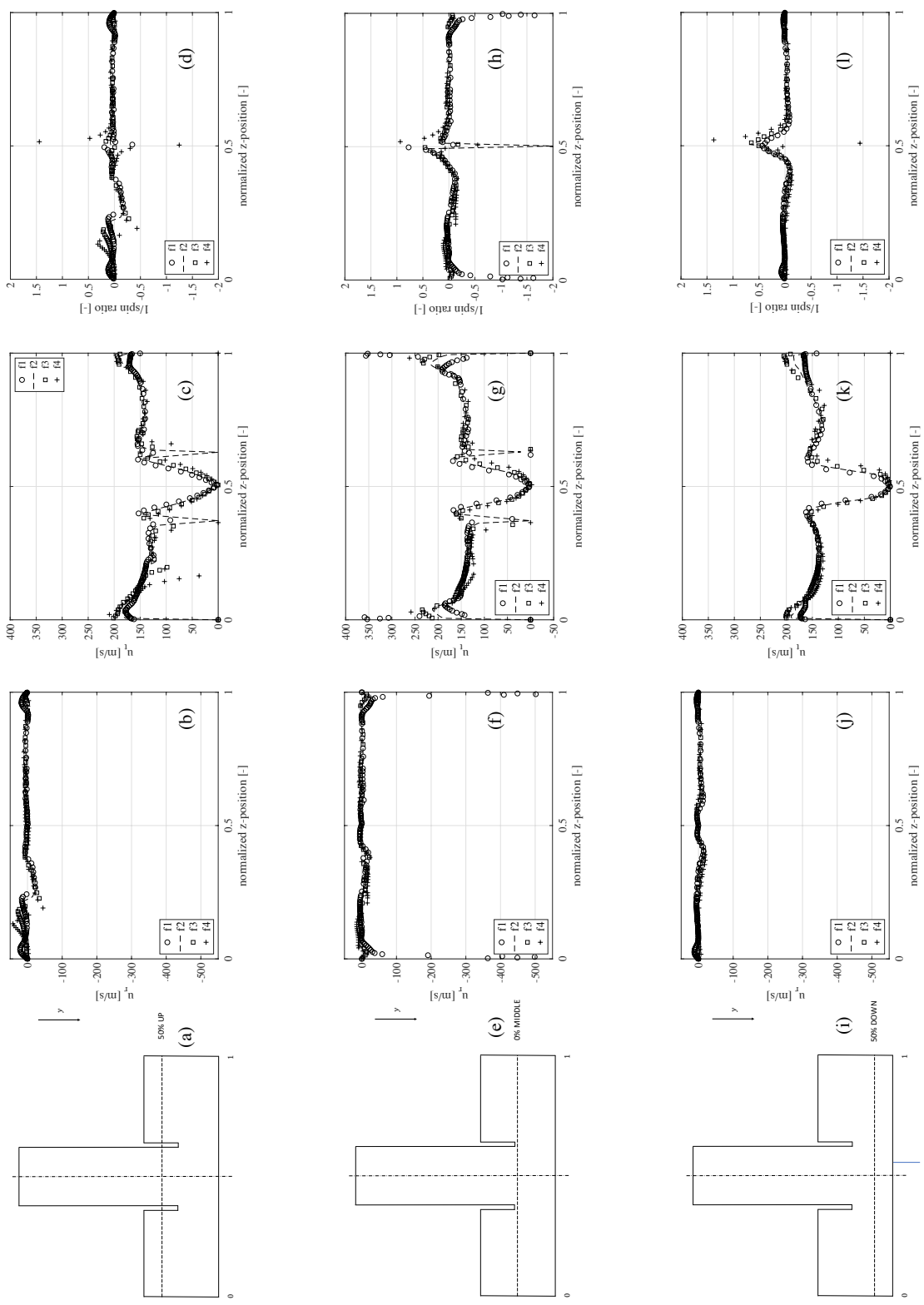

Figure 4.18: Radial velocity, tangential velocity and inverse of the spin ratio as function of normalized z-position along three different chambers height (f1 to f4, i). v_r indicates radial velocity while $v_\theta = v_t$ indicates the tangential velocity.

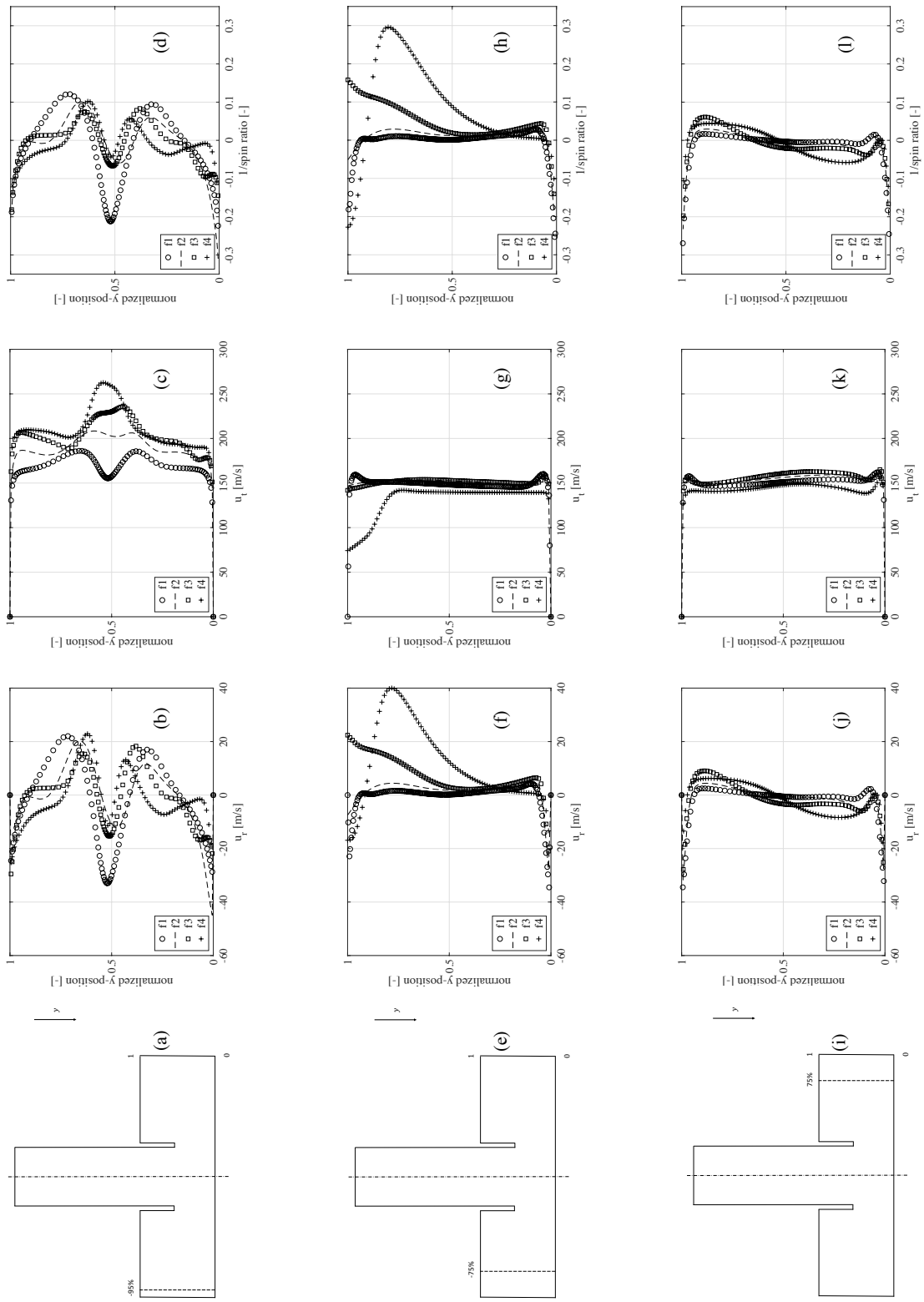

Figure 4.19: Radial velocity, tangential velocity and inverse of the spin ratio as function of normalized z-position along three different chambers radii (f1 to f4, i). v_r indicates radial velocity while $v_\theta = v_t$ indicates the tangential velocity.

According to the scheme reported in Fig. 4.2, particles are often subjected to a null or a small positive radial velocity field and therefore they tend to move with their own direction. The nozzle jets push them towards the inner part of domain (negative radial velocities), especially if particles lie on the nozzles middle plane, where the radial and tangential components assume their highest value.
An equilibrium position can be reached only when particles move in a negative radial velocity field since inward components allow for obtaining a gas drag force that balances the centrifugal forces developed by the rotational motion of particles. Due to this reason, only a limited portion of the chamber is suitable for having a classification mechanism based upon aerodynamic forces.

Fig. 4.18 shows that in all chambers the radial velocities oscillate (b, f and j) changing sign, without the possibility of identifying a large region with a well-defined flow pattern. It is possible to recognize a small portion of negative continuous flow of gas only near the lower and the upper wall due to flow confinement towards plates (Fig. 4.20). Radial negative velocities are also sampled at nozzles height, due to the inward gas flow coming from nozzles.
The tangential velocity in the inner part of the chamber (0.09 < normalized z-position < 0.35 and 0.65 < normalized z-position < 0.91) show a uniform field except for the zones near the outer wall and the regions located in the center of the mill where tangential components go to zero (plots c, g and k).

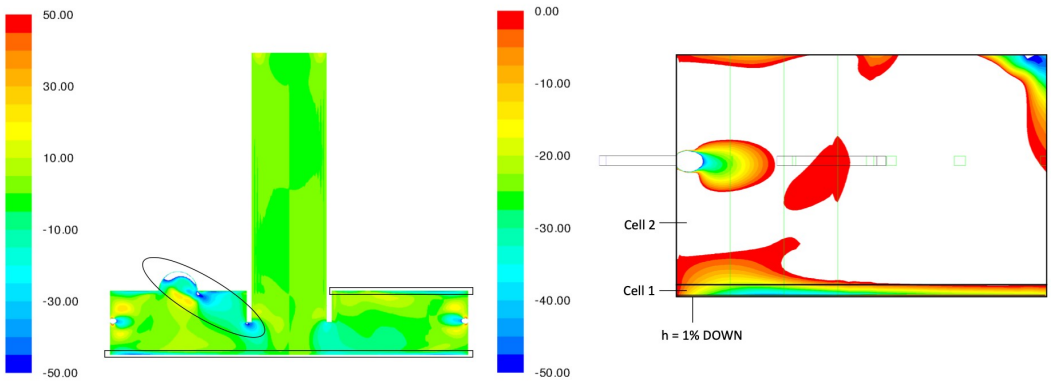

Figure 4.20: Scaled radial velocity ($m\,s^{-1}$) maps on ix-plane (f1-i/ii). The two images are depicted showing cropped scales. White portions of the figures show out-of-scale values (large or smaller).

The same observations made for radial velocity data can be done for the inverse of spin ratio (depicted in d, h, and l), with the remarkable difference of having large values at the center of the mill, induced by the null tangential velocity in that zone. These observations are also clearly stated by plots of Fig. 4.19, representing the radial velocity, tangential velocity and the inverse of spin ratio for the four chambers and operative condition i at three different lines evolving along the chambers height.
Tangential velocity at r = -75% (plot g of Fig. 4.19) gives similar values for every mill dimensions except for chamber f4, that shows a non-negligible decrease with respect to the others. The influence of the nozzles presence and the plume generated from the high-velocity flow coming from them is clearly shown by radial and tangential velocity peaks of plots at r = -95% (plots b and c). It is interesting to notice that the radial velocity peaks show similar values as the chamber diameter is reduced while the tangential velocity component changes remarkably, increasing from f1 to f4. This phenomenon is confirmed by the inverse of the spin ratio, as showed by plot d of Fig. 4.19, that assumes the shape of radial velocity and shows values close to zero except for the near-nozzles regions, the portion of chamber near the powder feeder and the upper/bottom wall zones, where it increases and locally reaches $\frac{1}{\text{spin ratio}} < 0.2$, indicating that these zones are the most efficient in moving and sorting out particles (negative spin ratio with positive tangential velocity means negative radial components and therefore an inward flow).
Plots h and l of Fig. 4.19 show that the original chamber f1 gives the most uniform velocities profile, while the others show an increasing inhomogeneity between the upper and the lower chamber semi-half. The spin ratio in the middle of the chambers does not change remarkably, indicating that the variation of the mill diameter has the major effect of changing the flow components repartition between the lower and the upper part of the grinding volume when the nozzles mass-flow is reduced.
Radial velocity contours plots shown in Fig. 4.20 underline that a large part of the comminution volume has positive radial velocity components. Positive velocities generate an outward flow that promotes collisions but not classification. Two thin regions of continuous inward radial velocity field can be identified near the upper and the lower plates, as depicted by the detailed right plot of Fig. 4.20.
As previously reported, the powder feeder also generates a large inward flow that drives streamlines towards the system outlet.
These observations show that the comminution volume of a spiral jet mill can be divided into three macro regions: a thin and localized zone near the lower wall (Cell 1 of Fig. 4.20 , right) with negative radial velocities, responsible of taking particles towards the outlet, a large zone located in the center of the chamber (Cell

2 of Fig. 4.20 , right) with positive radial velocity components that promotes collisions and another thin cell, similar to Cell 1, located near the upper wall that behaves like the latter.

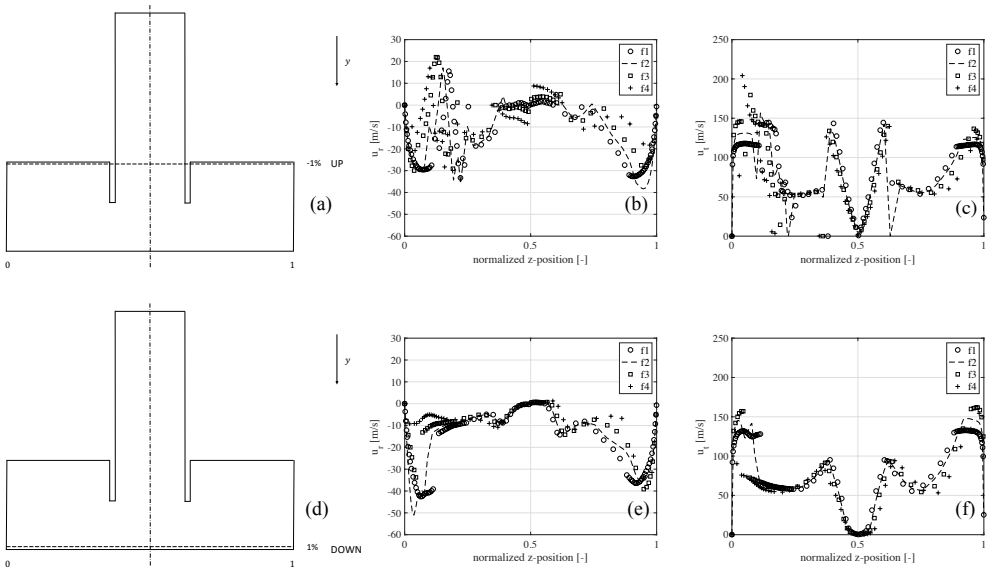

Figure 4.21: Radial and tangential profiles as function of normalized z-position near the upper and lower mill walls (f1 to f4, i).

Profiles located at 1% of the chamber semi-half height are shown by Fig. 4.21. A continuous region of negative radial velocities can be detected along the whole lower plate and along the right semi-half of the upper plate (plots b and e). The inward flow is much more vigorous going from the outer region towards the inlet, indicating that the carrier is more effective near the outer wall and in nozzle proximity. According to the flow dynamics inside the chamber, gas velocity components in Cell 2 are responsible for the colliding particles motion while those of Cell 1 and 3 are responsible for driving particles towards the outlet.
For all the chambers and operating conditions tested, the particles transport towards the outlet takes place only in plates proximity while the particle-particle and particle-wall collisions are promoted in the central part of the comminution volume (cell 2 of 4.20). This functioning principle is proper of all spiral jet mills with tangential solid injection and with an upper discharge.
Tangential velocity profiles shown by plots c and f of Fig. 4.21 are similar in shape to those sampled at h = -50% and 50%, with the peculiarity of having a flatter and more uniform form near the lower plate than near the upper wall.
This is reasonably induced by the powder feeder presence and by the tortuous way imposed by the classifier (h_c in Fig. 4.1b) to the gas flow. Plots b, f and j of Fig.

4.19 clarify that the high-velocity ring generated by the nozzles gas flow reaches also zones near the plates. The powder feeder strongly affects the left semi-half of the chambers, generating chaotic components that make the radial velocity change in sign and generate oscillations in tangential components (plots b and f of Fig. 4.18).

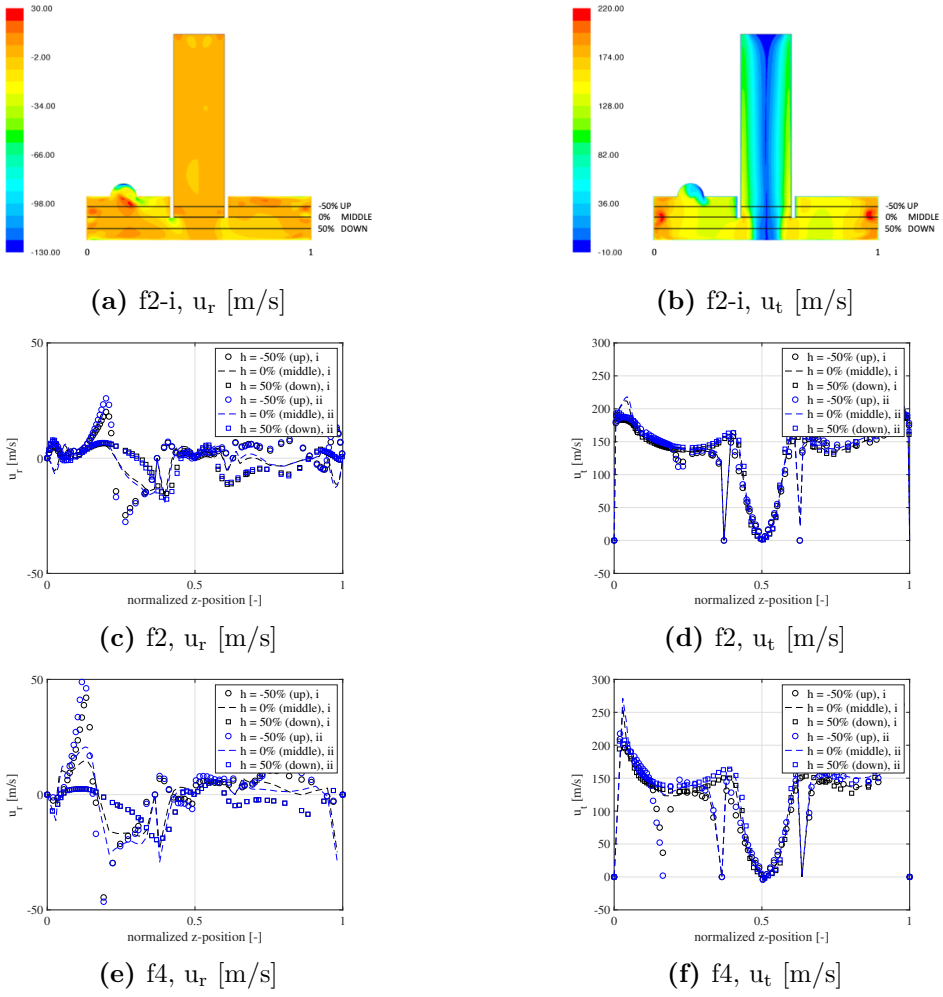

(a) f2-i, u_r [m/s]

(b) f2-i, u_t [m/s]

(c) f2, u_r [m/s]

(d) f2, u_t [m/s]

(e) f4, u_r [m/s]

(f) f4, u_t [m/s]

Figure 4.22: Radial and tangential velocity trends over three different chamber heights (f2/f4,i/ii)

Fig. 4.22 depicts the radial (a) and tangential (b) velocity contours for chamber f2 as well as radial and tangential velocity data at different heights of chamber f2 ((c) and (d) respectively) and chamber f4 ((e) and (f) respectively).
Plots detail the velocity variation along the chambers radius, pointing out the

difference that exists in radial velocity components when the chamber height is changed for the negative semi-plane, due to the powder feeder presence, also for sampling lines crossing the comminution volume in proximity of its median height. It is clear that there is a difference in sign between h = -50% and h = 50% in the positive z semi-half. The upper part of the chamber has only positive radial velocities while the bottom part presents negative values.
This information, as depicted by the radial profiles of Fig. 4.21, plots c and e, confirms that the classification of particles can only take place in limited mill regions such as the lower part of the comminution volume.
The three lines examined show that, in the left semi-plane, there is a negative radial velocity peak near the powder feeder region that is given by the local acceleration that the flow experience to move towards the outlet. This flow pattern is well recognizable for all the four chambers and both the operating conditions studied. The tangential velocity (plots (d) and (f) of Fig. 4.23) slightly increases near walls and drop down, as expected, in the center of the chamber.

As showed by Fig. 4.22 and Fig. 4.23, no remarkable difference is found in radial velocity profiles changing the operating condition from constant pressure (i) to constant mass-flow rate (ii) at nozzle inlets, especially for the sampling lines near the outer walls (r = -95% and r =-75%). A variation is observed only near the powder feeder that acts as a perturbation zone and locally modifies the radial velocity component showing a positive velocity peak (passing from i to ii) in chamber f4.
The tangential velocity, instead, slightly increase in the whole domain, as showed by the difference between black and blue markers. It is interesting to notice that the modification of the gas mass-flow rate results in a variation of the tangential velocity (the higher is the mass-flow rate, the higher is the average tangential velocity), but it does not change remarkably the radial velocity component of the flow field. The variation of operating condition i to ii increases the negative radial velocities in the plates proximity. To summarize, the increase of grinding pressure when the chamber diameter is reduced increases the gas tangential velocity in the central part of the chamber and the negative radial velocity component near plates. It enhances the flow patterns responsible of driving particles collisions but also the velocity field that causes particles classification.
This means that an effective strategy to control the classification capabilities of the spiral jet mills is to adjust the nozzles gas grinding pressure with the aim of tuning the spin ratio and customizing both the particles collision and the particles classification mechanisms.

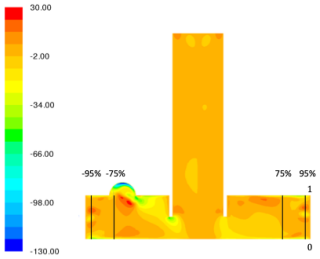

(a) f2-i, u_r [m/s]

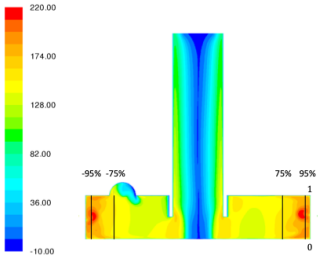

(b) f2-i, u_t [m/s]

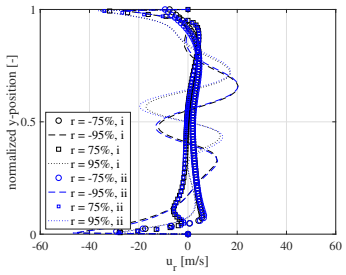

(c) f2, u_r [m/s]

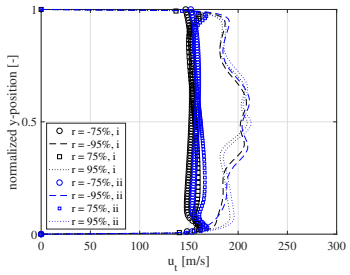

(d) f2, u_t [m/s]

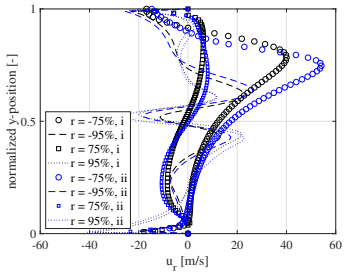

(e) f4, u_r [m/s]

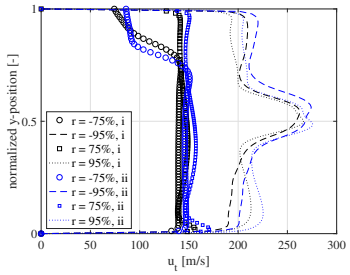

(f) f4, u_t [m/s]

Figure 4.23: Radial and tangential velocity trends over three different chamber radii (f2/f4, i/ii)

4.5.2 Part 2: Uncoupled quasi-3D Euler-Euler Micronization Model

Model Calibration

The usage of the genetic algorithm coupled to the compartmentalized model provides the lactose and paracetamol parameters shown in Table 4.11.

Table 4.11: Model parameters for lactose and paracetamol.

Substance	Ψ [-]	γ [-]	β [-]	K_1 [$g^{1.5}\,bar(g)^{-1}\,s^{-1}$]	K_2 [$g^{1.5}$]
Lactose	$6.97 \cdot 10^{-2}$	$5.00 \cdot 10^{-1}$	3.04	27.93	$1.48 \cdot 10^{-1}$
Paracetamol	$5.03 \cdot 10^{-1}$	52.70	$1.71 \cdot 10^{-1}$	40.36	$1.70 \cdot 10^{-1}$

Results show that the importance of the first term in Eq. 4.34 (weight Ψ) is limited for lactose while it is important for paracetamol. This confirms that the physical mechanism at the base of the particles fragmentation for the two substances is different, since lactose behaves, in general, like a ductile material while paracetamol tends to undergo to a fragile breakage.
Defining the relative error, e, as the difference between experimental and model data as described by Eq. 4.35, it is possible to evaluate the accuracy of the prediction obtained through the usage of parameters of Table 4.11.

$$e = 100\frac{D_{i,exp} - D_{i,mod}}{D_{i,exp}}. \tag{4.35}$$

Table 4.12 and Table 4.13 lists experimental (exp), model (mod) and relative error results for lactose and paracetamol at the same process conditions, respectively. The analysis is carried out on D10, D50 and D90 to evaluate the model performance on parameters describing the whole outlet distributions Table 4.12 shows that the best results are obtained for D50 and D90, with a maximum relative error of 28% circa in the first case and 20% in the second case.
Most of the constraints in terms of PSD of the final product are usually given on D90 and therefore the genetic algorithm is set to minimizes errors for diameters larger than D40. This motivates the worst prediction obtained for fine particles.

Table 4.12: Comparison between the experimental (exp) and predicted model (mod) values for D10, D50 and D90 diameters of output PSD for lactose.

	D10			D50			D90		
Case	exp [μm]	mod [μm]	e [%]	exp [μm]	mod [μm]	e [%]	exp [μm]	mod [μm]	e [%]
7 bar(g) 20 [g min^{-1}]	0.59	0.64	9.54	3.85	3.97	3.08	11.86	12.99	9.54
7 bar(g) 310 [g min^{-1}]	1.14	1.60	39.68	7.75	9.88	27.51	23.13	27.76	19.99
7 bar(g) 600 [g min^{-1}]	1.33	2.04	53.00	10.50	12.99	23.70	34.33	33.31	2.99
11 bar(g) 105 [g min^{-1}]	0.55	0.41	26.20	2.68	2.37	11.44	7.29	8.23	12.92
11 bar(g) 515 [g min^{-1}]	0.90	0.95	9.54	6.08	5.89	2.99	18.14	17.60	2.99
12 bar(g) 310 [g min^{-1}]	0.98	0.62	36.60	5.06	3.74	26.20	13.80	11.86	14.09

Table 4.13 shows that the model calibration for paracetamol is much stiffer than the lactose one, due to different breakage behavior whose particles with a wide distribution are subject to. Paracetamol raw powders, indeed, show a much higher Sauter mean diameter (41 μm) with respect to the one measured for lactose (11 μm) meaning that paracetamol particles undergo to a much vigorous size reduction process than lactose ones.
Large errors are encountered at low gas pressures while good predictions are obtained if high-energy density processes are simulated (high pressure and low/medium solid feed-rates).
Results show that the model does not fit properly data of wide inlet distributions. Eq. 4.32 show, indeed, that the selectivity formula is strongly dependent on the maximum particles size and, therefore, the shape of the function may change remarkably depending on the maximum particles diameter.
Large errors are made especially for fines. This tendency is slightly mitigated if high-energy processes are treated (high pressure and low feed rate), coherently to the model assumption of having dilute flow condition.

Table 4.13: Comparison between the experimental (exp) and predicted (mod) values for D10, D50 and D90 diameters of output PSD for paracetamol.

	D10			D50			D90		
Case	exp [μm]	mod [μm]	e [%]	exp [μm]	mod [μm]	e [%]	exp [μm]	mod [μm]	e [%]
7 bar(g) 20 [g min^{-1}]	0.48	0.08	82.57	1.44	0.069	52.25	3.69	7.99	116.58
7 bar(g) 310 [g min^{-1}]	0.56	0.12	79.39	2.30	2.01	12.58	9.14	23.41	156.20
7 bar(g) 600 [g min^{-1}]	0.64	0.13	79.39	3.12	3.01	3.30	13.67	30.62	123.98
11 bar(g) 105 [g min^{-1}]	0.46	0.07	84.24	1.54	0.44	71.15	4.83	4.36	9.59
11 bar(g) 515 [g min^{-1}]	0.56	0.09	83.71	2.23	1.00	55.35	8.83	11.95	35.31
12 bar(g) 310 [g min^{-1}]	0.53	0.08	84.77	2.01	0.64	68.09	7.72	6.98	9.59

The proposed kernel structure is not appropriate to model the fragmentation of particles population with wide distributions and a small critical diameter because the breakage may vary remarkably with the inlet size. Kernel parameters need, in this case, a pressure-dependent fitting to consider the behavioral change due to the different quantity of energy given to the micronization process.
Table 4.14 reports the pressure-dependent fitting of kernel parameters for paracetamol powders. Results clearly show that the paracetamol behavior at rupture notably change if the pressure is increased. Selectivity (Eq. 4.32) and breakage probability (Eq. 4.34) are computed at different pressures to show their dependency on particles dimensions and gas energy.
Fig. 4.24a depicts selectivity as function of the particle diameter while Fig. 4.24b shows the breakage probability as function of particle diameter ratio (the ratio between the diameter of the particle i colliding against particle k).
A remarkably different behavior is found between medium-pressure and high-pressure curves only for selectivity. The latter is higher at 7 bar(g) and it tends to increase if the particles diameter is augmented at any pressure. Curves obtained

at 11 and 12 bar(g) are completely comparable, indicating that S_{ij} can be studied at two different pressure ranges only. Breakage probability, defined for $d_k/d_i \leq 1$, does not depend on pressure and the weighting parameter Ψ is able to correctly model the different energy response of lactose and paracetamol. Exponent γ drives the shape of the breakage probability and model the different mechanism governing the fragmentation of paracetamol powders. Fig. 4.24 clearly shows that only selectivity varies with pressure, meaning that parameters K_1 and K_2 of Eq. 4.32 need to be defined at each pressure level. Fig. 4.25 depicts the fitting functions used to interpolate the pressure-dependent parameters defined in Table 4.14 through single-pressure model fitting. As depicted, K_1 is a strong function of pressure and it decreases a lot as the energy of the flow increases. K_2 also shows a different behavior passing from medium to high-pressure ranges, doubling its value. A function of their ratio directly multiplies the grinding pressure in the selectivity formulation and they are, for this reason, important in defining the shape of S_{ij}.

Table 4.14: Paracetamol breakage model calibration as function of grinding (nozzles) pressure @ 7 (FR = 20, 310, 600 g min^{-1}), 11 (FR = 105, 515 g min^{-1}) and 12 (310 g min^{-1}) bar(g).

Pressure	Ψ	γ	β	K_1	K_2
[bar(g)]	[-]	[-]	[-]	[g$^{1.5}$ bar(g)$^{-1}$ s^{-1}]	[g$^{1.5}$]
7	$6.32 \cdot 10^{-2}$	21.04	2.02	160.04	$5.14 \cdot 10^{-1}$
11	$7.01 \cdot 10^{-2}$	2.49	2.10	83.56	1.27
12	$1.13 \cdot 10^{-3}$	$6.00 \cdot 10^{-1}$	1.91	61.27	$9.90 \cdot 10^{-1}$

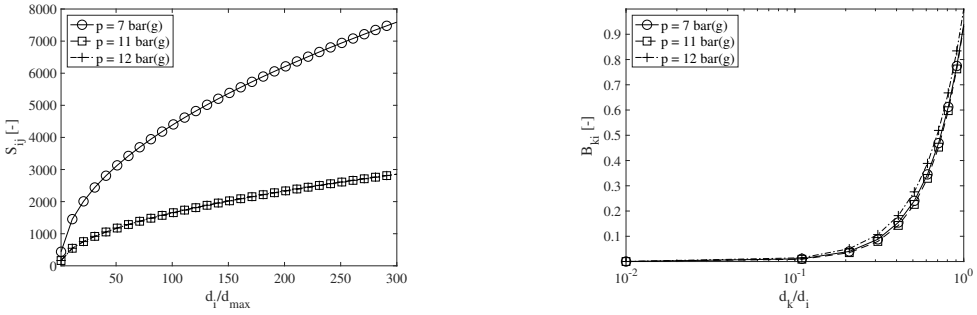

(a) selectivity **(b)** breakage probability

Figure 4.24: Selectivity (S_{ij}) and breakage probability (B_{ki}) obtained from parameters optimization carried out at different pressures for paracetamol powders and assuming a 5 g hold-up.

Both K_1 and K_2 clearly change value passing from medium- to high-pressure processes. This property is coherent with the selectivity shape showed by Fig. 4.24a. β, instead, remains almost equal and the interpolant function returns a quasi-constant value, motivating the behavior of B_{ki}. The weighting function Ψ assigns most of the breakage probability shape to the second term of Eq. 4.34, making negligible the large variations shown by γ. This states that both the paracetamol and lactose fragmentation are driven by one breakage mechanism only with much of the physics complexity contained into the selectivity function formulation.

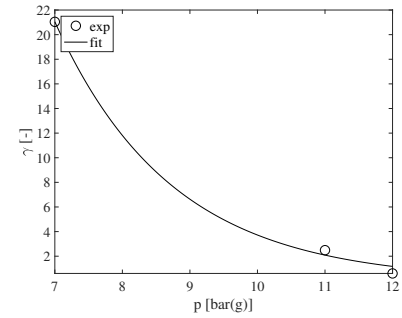

(a) $\gamma = f(p)$

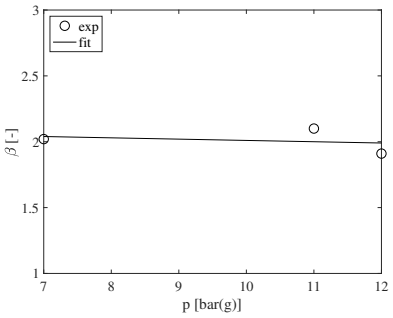

(b) $\beta = f(p)$

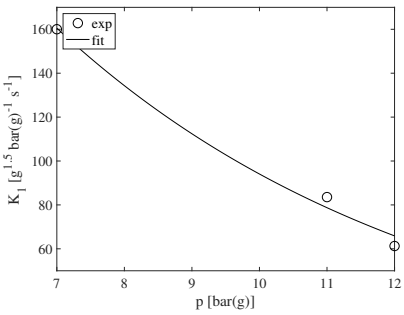

(c) $K_1 = f(p)$

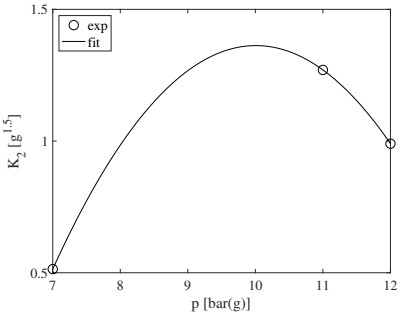

(d) $K_2 = f(p)$

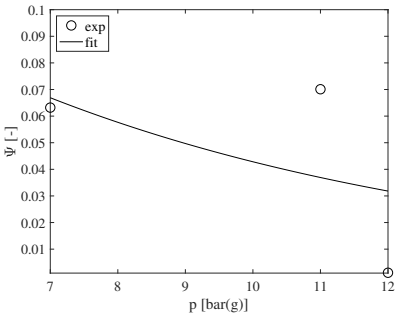

(e) $\Psi = f(p)$

Figure 4.25: Paracetamol breakage kernel parameters determined through pressure-dependent calibration (exp) and model fitting (fit).

Fig. 4.26 shows the comparison between the output cumulative distribution function fitted from the model and data measured experimentally (exp) for a low pressure process (4.26a, p = 7 bar(g) and FR = 20 g min^{-1}) and a high pressure process (4.26b, p = 11 bar(g) and FR = 515 g min^{-1}) for paracetamol.
Results clearly show that the cumulative distributions are extremely well replicated if pressure dependent fitting is performed, especially at high pressures.
Passing from single-pressure parameters set to the fitting functions depicted by Fig. 4.25, the error on D90 at 7 bar(g) and 20 g min^{-1} decreases from 117% circa to 35% while error on D90 at 11 bar(g) and 515 g min^{-1} decreases from 35% to 3% circa.

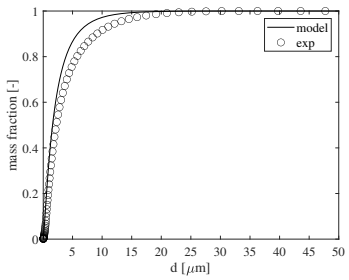

(a) p = 7 bar(g), FR = 20 g min^{-1}

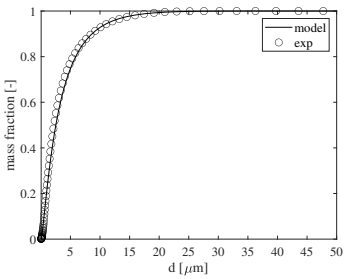

(b) p = 11 bar(g), FR = 515 g min^{-1}

Figure 4.26: Comparison between the cumulative distributions obtained through experiments (exp) and model fitting for paracetamol using fitting functions depicted by Fig. 4.25.

Model Predictions

he results produced by the experimental campaign designed through the DoE for lactose and paracetamol are used to build response equations for D10, D50 and D90.
The structure of the relationship describing the particles dimensions is given by Eq. 4.36, given in μm, and it is function of the gas grinding pressure (p – bar(g)), powders feeding rate (FR – g min^{-1}) and their interaction. The model needs a transformation through a new variable that incorporates the original model output:

$$y' = a + b \cdot p + c \cdot FR + d \cdot p^2 + e \cdot FR^2 + f \cdot p \cdot FR. \tag{4.36}$$

The coefficients and transformation variables are reported in Eq. 4.36 are listed in Table 4.15.

Table 4.15: Reduced quadratic model equations parameters.

Substance	Variables		Coefficients					
	y	y'	a	b	c	d	e	f
Lactose	D10	y	1.5699	-0.3228	0.0044	0.0225	0	-0.0004
Lactose	D50	y	13.4393	-3.0161	0.0344	0.1864	0	-0.0026
Lactose	D90	$\log_{10}(y)$	1.4655	-0.1404	0.0024	0.0055	$-2.0395 \cdot 10^{-6}$	0
Paracetamol	D10	$y^{-2.38}$	0.5379	1.2844	-0.0093	-0.0606	$5.2914 \cdot 10^{-6}$	0
Paracetamol	D50	$\frac{1}{\sqrt{y-0.5}}$	0.5170	0.1138	-0.0013	-0.0053	$1.0526 \cdot 10^{-6}$	0
Paracetamol	D90	$\frac{1}{\sqrt{y-0.5}}$	0.2723	0.0591	-0.0010	-0.0028	$9.1840 \cdot 10^{-7}$	0

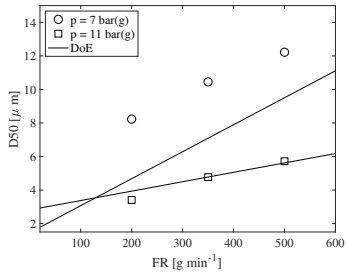

(a) Lactose, D50 = f(p,FR)

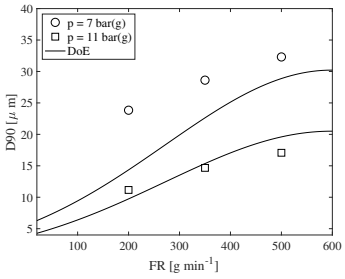

(b) Lactose, D90 = f(p,FR)

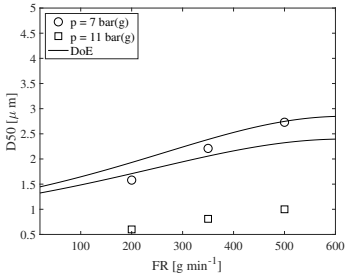

(c) Paracetamol, D50 = f(p,FR)

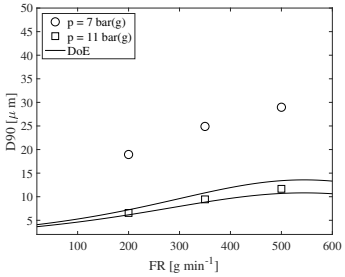

(d) Paracetamol, D90 = f(p,FR)

Figure 4.27: Predicted/model (markers) and experimental/DOE (lines) results comparison for Lactose and Paracetamol at 7 and 11 bar(g) at solid feed rates ranging between 20 and 600 g $\min^{-1}$.

Due to the high quality of the response surfaces (adjusted R^2 always greater than 0.922), predictions obtained through Eq. 4.36 are considered as reference and they are used as "experimental data" to compare model values at process conditions different from those used for model calibrations.
Curves obtained through the DoE functions reported by Eq. 4.36 with the coefficients listed in Table 4.15 are marked in the following plots as "DoE".
The operating conditions tested to understand the model predictions capabilities are p = 7 bar(g), FR = 200, 350 and 500 g min^{-1} and p = 11 bar(g), FR = 200, 350 and 500 g min^{-1}; which are comprised within the validity ranges of the DOE used as reference.
Fig. 4.27 shows the comparison between predicted and experimental D50 and D90 values for lactose (a, b) and paracetamol (c, d) when the kernel parameters reported in Table 4.11 are used.
It is shown that an averaged-pressure set of the breakage kernel parameters properly predict the micronization behavior of lactose, especially at high pressure and medium/low feed rates. This is completely coherent to the important assumption done at the beginning of the decoupled model derivation of having dilute flow conditions. Predictions dramatically deteriorate for paracetamol, with errors of over than 180%, due to its different breakage behavior that is a strong function of pressure and particles diameter. In order to improve the model prediction capabilities for cases with variable selectivity, a pressure-dependent tuning is performed and a parameters definition based upon the flow energy content is implemented.

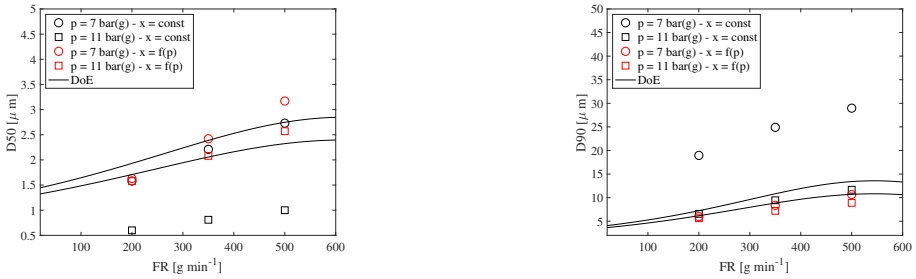

(a) Paracetamol, D50 = f(p,FR) **(b)** Paracetamol, D90 = f(p,FR)

Figure 4.28: Averaged-pressure predicted/model (black markers), pressure-dependent predicted/model (red markers) and experimental/DOE (lines) results comparison for Paracetamol at 7 and 11 bar(g) at solid feed rates ranging between 20 and 600 g min^{-1}. x represents the vector containing the breakage kernel parameters depicted by Fig. 4.25.

Fig. 4.28 gathers results obtained availing of constant kernel parameters (black markers) and results computed though the usage of parameters functions shown by Fig. 4.25 (red markers). Notice that vector x stores the kernel parameters such

that x = const refers to the constant kernel parameters set while x = f(p) is the notation used for the pressure-dependent parameters set.
Results show that pressure-dependent parameters drastically improve the prediction capabilities of the model even when a substance with a complex breakage mechanism is considered. Relative errors, computed according to Eq. 4.35, are in average comprised between 7% and 15% but always lower than 22.6% (worst case obtained for D90 prediction at 7 bar(g) and 350 $\mathrm{g\,min^{-1}}$).
If compared to fully coupled CFD-DEM simulations, the presented model framework provides process-scale results in a tremendously shorter computational time. Once the kernel parameters for an API are determined, the model calculates the final output PSD in approximately 5 minutes of computational time through a serial process on a 4-core (Intel Core i5-3470 @ 3.20 GHz) computer with 16 GB RAM.

4.5.3 Concluding Remarks

The internal gas dynamics of a spiral jet mill subject to caking phenomena was studied via single-phase CFD. A simple approach to mimic the grinding chamber diameter reduction due to solid particle agglomeration at walls was used. Four different caking conditions for the grinding chamber were explored and two different operating conditions, derived from relevant experimental data measured on a real-scale production plant, were reproduced. By focusing the analysis on radial and tangential velocity components as well as their dimensionless ratio (inverse of spin ratio), some general findings were achieved, able to explain the influence that the operating conditions, in terms of nozzles feeding pressure and chamber shrinkage (due to caking), have on the classification capacities of spiral jet mills with upper discharge and tangential solid feeding.
The analysis unveils that:

i. The gas flow is locally supersonic in regions downstream nozzles with large velocity, temperature and pressure gradients that arise from the sudden air expansion. The rest of the grinding chamber is transonic. The sonic choking in the nozzles throat sections is reached in every condition tested. It is possible to asses that caking does not affect the fluid flow in nozzles outlet proximity.

ii. The variation of the chamber diameter, for a given operating condition, has the main effect of modifying the homogeneity of the flow field. The velocity profiles are more uniform with the largest chamber while the others show an inhomogeneity between the upper and the lower semi-half of the comminution volume in terms of radial and tangential velocity profiles.

iii. The reduction of the nozzle grinding total pressure along with the reduction of the chamber diameter (operating condition i) has the effect of keeping almost constant the spin ratio throughout the domain, with the exception of the zones located in the powder feeder proximity. This means that the nozzles mass-flow rate reduction while caking is advancing can control and avoid the classification of large particles due to aggregates formation.

iv. The increase of the nozzle total pressure along with the reduction of the chamber diameter (operative condition ii) causes the increasing of the tangential velocity components but not the radial one in the central part of the chamber. An increase of the radial velocities over the tangential ones is instead observed near plates and in the powder feeder proximity.
The analysis underlined how the inverse of spin ratio increases in the central part of the domain and remarkably decreases near plates, becoming negative,

promoting particles transport and taking larger objects towards the outlet. This highlights that the largest part of the spiral jet mills grinding chamber is not suitable to classify particles since inward radial velocity components can be identified only near mill plates and in a limited region near the powder feeder.

Caking modifies the gas velocity field inside the micronization chamber (operative condition ii – constant mass flow rate at nozzles), by increasing the negative radial velocity component near plates and augmenting the classification capabilities of the system, taking out of specific the PSD of the final product.
In general, the spiral jet mills grinding chamber can be divided into three different cells, according to the radial velocity flow patterns: two thin zones located near plates (Cell 1) where the particles transport towards the outlet takes place and a large central zone (Cell 2) responsible of driving the solids phase collisions.
The reduction of the nozzles inlet pressure is identified as an interesting general control strategy to modulate the spin ratio and modify the classification capabilities of spiral jet mills by changing the radial velocity pattern near the plates and in the powder feeder proximity to counterbalance the effects induced by the crusts grow and keep the system working properly despite caking.
Given that particle segregation mainly takes place near the internal ring of the spiral jet mill and assuming that particles aggregate to form clusters on the outer part of the chamber when they reach large concentrations, the flow is considered as dilute and the analysis here described is limited to the gas fluid-dynamics.

Besides the single-phase flow analysis, a comprehensive model able to study the multiphase interactions and provide patricle-information at process-scale has been built.
The proposed computational procedure calculates the 3D single-phase CFD gas velocity fields and use them in a 1D, radially evolving compartmentalized model to compute particles mass and momentum balances. The solid phase is advected availing of an algebraic velocity formulation and the breakage kinetics is computed according to a semi-empirical model tuned over experimental data.
Ductile (lactose) and fragile (paracetamol) substances are analyzed.
In accordance with the model assumption of dilute flow conditions, the best agreement between the model and the experimental results is obtained for highly energetic processes. Results show that the computational model developed well predicts the output PSD of ductile particles with a single-set of breakage kernel parameters, containing errors within 50%. Fragile powders, which exhibit a variable selectivity depending on pressure and particles diameter, need a pressure-dependent fitting for breakage parameters and predictions show very good agreement to experiments, with a maximum error of 22.6% obtained for D90 at 7 bar(g)

and 350 $\mathrm{g\,min^{-1}}$.
The developed computational procedure is very fast if compared to fully coupled Eulerian-Eulerian or Eulerian-Lagrangian simulations and it provides reliable results at process scales (steady-state micronization for real apparatus) with few minutes of calculation times with good accuracy.
The model predictions quality deteriorates as the pressure range is enlarged, especially for raw powders with wide inlet distributions. In these cases, a pressure-dependent kernel parameters tuning is needed to include all the mechanisms that drives particles size reduction and account for selectivity dependency on pressure. Another kernel formulation able to better describe this phenomenon, along with a tribocharging model for the description of the particle electrification due to particle-particle collisions.

Chapter 5

Application 2: Olefins Polymerization in Fluidized Bed Reactors (FBRs)

This chapter is focused on the multiphase modeling of fluidized bed reactors for the polyolefins polymerization process. The first part of the work deals with the comparison between the predictions of a standard 1D-compartmentalized model with a simplified fluid dynamics description and a detailed CFD Euler-Euler model. Average diameters and solid volume fractions are analysized to assess if a cost-effective compartment-based model can be used to study the particle distributions inside the reactors.
The last part of the work is aimed at understanding if a 2D, scaled-down reactor geometry can be used to simulate the polymerization process in continuous operation mode at a reasonable computational cost.

5.1 Process Description and Current Modelling Capabilities

5.1.1 Olefins Production in FBRs

In polymer chemistry, coordination polymerization is a chain mechanism through which a polymer is produced from a monomer in the presence of a heterogeneous catalyst. The catalyst provides fast reaction as well as effective control of the chain topology. Different catalyst types are available, and the Ziegler-Natta type is still very popular in the polyolefin industry. Large scale reactors are typically applied to contact the solid catalyst (almost instantaneously becoming growing polymer particles) with the gaseous reactant. Even though stirred tanks have been used,

fluidized bed reactors are nowadays the most common apparatus used to carry out the process.
A schematic of them is given in Fig. 5.1.
The gas flow, usually a mixture of ethylene with nitrogen, hydrogen and 1-butene, is blown through a distributor plate arranged at the bottom of the reactor (`Fresh feed`) while the solids, consisting of catalyst or pre-polimerized polymer particles, is fed through a lateral inlet (`Catalyst`). The reaction starts as soon as ethylene laps the catalyst particles. The polymer grows from active sites, filling the particles pores and exerting an increasing pressure on the structure sides. The catalyst particles fragmentate and the catalyst fragments remain embedded by the surrounding polymer in quantity of ppm.

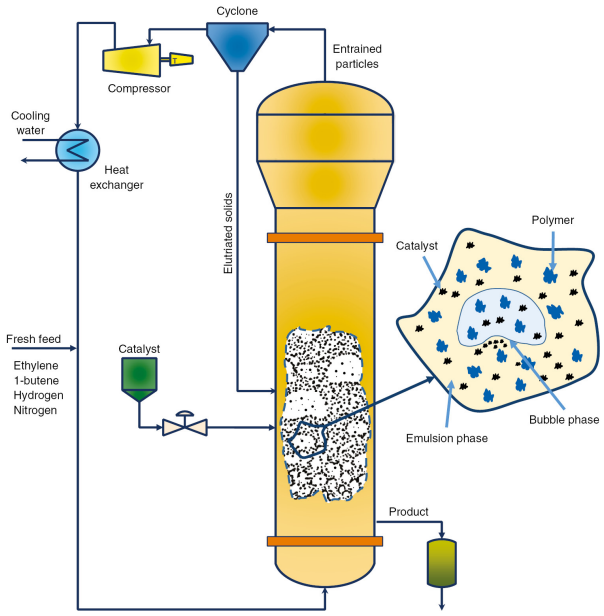

Figure 5.1: Fluidized bed reactor for olefins polymerization, taken from Abbasi *et al.* [110].

The gas mixture has the dual task of feeding the reaction and moving the particles according to their inertia. Large particles fall down and they are gathered from the reactor bottom (`Product`) while smaller ones remain suspended or they are dragged upwards to be expelled by the gas outlet. To remedy to this unwanted phenomenon, known as elutriation, the elutriated particles are separated by the fluid carrier in a `Cyclone` and they are re-entered inside the fluidized bed reactor to undergo polymerization again. The overall particle reaction slows down with time since the concentration of catalyst fragments decreases as the polymer volume increases and monomer diffusion limitations increase at the same time. The

cut-size diameter (the size of polymer particles for which they are allowed to leave the reactor) can be regulated by varying the inlet gas velocity and change the fluid-solid drag.
High-density polyethylene (HDPE) is typically produced with temperatures ranging between 75 and 111 °C and pressure ranging from 20 to 40 MPa.

5.1.2 Fluidization Regimes

When a fluid flows through a granular material, the particles behaviour is converted from a static solid-like state to a dynamic motion in which the multiphase mixture starts behaving similarly to fluids. This particular condition is called fluidization.
Depending on the fluid velocity, several fluidization regimes may be encountered. Fig. 5.2 depicts five different fluidized bed reactor states (top scheme) and the pressure drop as function of the fluid velocity (bottom scheme).

The initial state consists in a reactor containing a certain quantity of granular material arranged as packed bed at the bottom of the vessel. The process starts when a fluid, usually a gas, is passed through a distributor plate investing the particles bed from the reactor bottom. If the drag exerted by the fluid flow is not enough to suspend the particles and they remain at state of rest, the pressure drop resulting from this drag will follow the Ergun equation (a - black/gray part of the graph).

When the gas velocity is increased, at a certain point, the total drag will equal the bed weight and particles will begin to lift and fluidize. This limit condition is obtained with a velocity called **minimum fluidization velocity** and corresponds to the maximum pressure drop experienced in the system (b - red halo).

When the drag exceeds the gravitational force, the particles begin to lift and the bed expands. The porosity of the system reduces and the drag decreases until it balances again the particles weight. If the velocity is increased a little more, instabilities in the flow field are generated and the gas starts moving around the bed, creating bubbles with very low concentration of particles. The solids starts to move chaotically, upward and downward, appearing as a boiling system. This highly mixed operation mode is defined **bubbling** or **aggregative fluidization** and consists in the desired working regime (c - green part of the graph).

A further increase in velocity will result in a chaotic and unstable operating condition called **slug flow** (d - light blue halo).

At extremely high velocities, the gas flow starts to take out the solids from the

reactor, generating a particular condition called **elutriation** (orange/yellow halo). Since the particles concentration decreases and the reactor is emptied, the pressure drop decreases as well. This last condition is clearly deleterious for fluidized bed operation and it is avoided.

Fluidized bed reactors are designed to work within the **bubbling fluidization** regime, where bubbles are formed and a high-mixing characterizes the system.

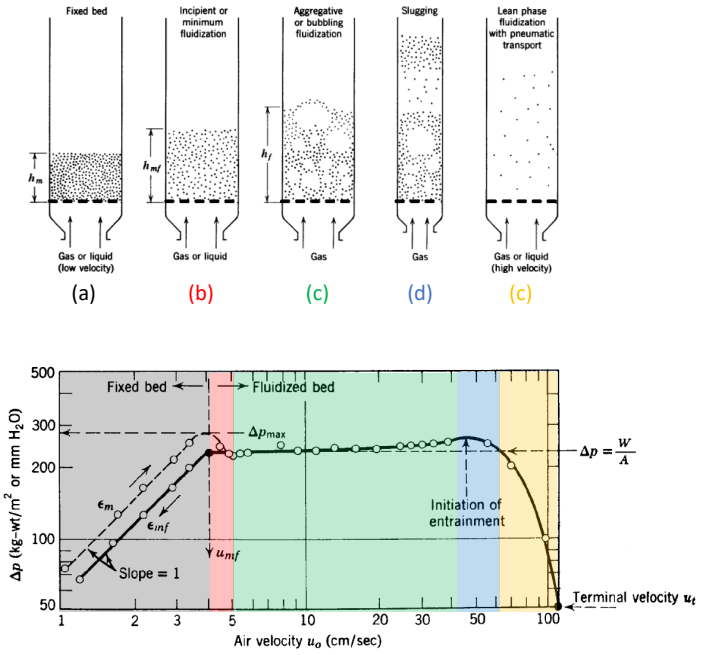

Figure 5.2: Fluidization regimes, adapted from Kunii & Levenspiel [111].

5.1.3 Numerical Modeling of Gas-Solid FBRs

Fluidized bed reactors are the first-choice equipment for the gas phase production of polyolefins [112]. Modeling tools are extremely helpful to design the operating conditions in order to ensure the desired product quality, *i.e.*, particle size and molecular weight distributions. Different modeling approaches have been proposed in the literature to simulate FBRs, ranging from multi-scale kinetic models [113–115] to highly detailed CFD-based models [116, 117].
Among the models of the first type, compartmentalized models are the most popular [118–121]. The reactor is described as combination of compartments (usually fully mixed) properly interconnected in order to simulate the behavior of the different phases. A major advantage of such an approach is that single particle models

can be easily accounted for. Such equations allow for an adequate description of complex particle morphologies along with comprehensive kinetic polymerization schemes [122].
On the other hand, the description of the reactor fluid dynamics is based on empirical relationships (*e.g.*, Ullmann of Elvers [123]), whose applicability is often assumed a priori without further validation. In this respect, CFD simulations represent a major step forward in terms of detailed description of the hydrodynamic interaction between gas and solid particles [124–126].
Even though based on fundamental equations and advanced numerical methodologies, these approaches suffer the major limitation of huge computational effort, especially for 3D cases [25, 127–129].
This practically prevents the use of similar tools in the industrial practice and limits the capability to include detailed descriptions of the particle size distribution and of the reaction features.
In order to partially mitigate this issue, a pseudo-2D approach in which the third dimension is modeled as a thin thickness has been proposed but its application is nowadays limited to particular fields of study such as systems with a symmetry in which much of the phases motion evolves in 2D [130], the bubbles formation [130] or the description of phases heat transfer mechanisms [131].
As shown, the multiphase mixing of fluidized bed reactors have been extensively studied but simulation models are usually run in batch mode. Recent works deal with the derivation and implementation of novel models for the description of particle-particle and particle-wall interactions generating simple charge transport [22] or tribocharging [20]. These complex models are based upon the kinetic theory of granular flows [132]. Others focus on the development of novel physical laws for the description of particle growth [21] or sofisticated drag models [133, 134].
Although the large scientific production for simulating FBRs fluid dynamics, to the best of the author knowledge, no CFD models describing the continuous polymerization of polyolefins have been proposed so far.
In this context, the assessment of a compartmentalized model implementing a simplified fluid dynamics description by comparing the values of selected properties (average solid volume fractions and particle sizes) with those predicted by a detailed CFD model would validate its use as effective design tool for practical applications, that is, under reactive conditions.
Moreover, it is worth to evaluate a possible strategy to scale-down the reactor to have a lower particle residence time and simulate the continuous operation of fluidized beds with solid injection and withdrawal.

5.1.4 Objectives

Given the motivations of the above section, the objectives of this work are the following:

a. the evaluation of the reliability of a standard three-phase compartmentalized model for the description of the solid distribution in fluidized bed reactors by comparison with detailed 2D CFD Euler-Euler simulations for monodisperse and polydisperse populations of particles;

b. the proposal of a strategy to scale-down fluidized bed reactors and to build a CFD multiphase model able to describe the polyolefins polymerization operated in continuous mode;

c. the analysis of different solid withdrawal positions and different solid feed-rates to understand the prediction capabilities of the proposed model in terms of average particle size and solid holdup.

5.2 CFD Multiphase Model

Model equations

In the multi-fluid model, gas and solid phases are considered as interpenetrating continua in a full Eulerian framework. The gas phase is considered as primary phase while solid ones are defined as secondary or dispersed phases. The kinetic theory of granular flows (KTGF) is used to close the solid stress tensor terms.

The multiphase model equations for continuity and momentum balances are described in Sub-section 2.4.
The fluidized bed turbulence is accounted for by solving the $k-\varepsilon$ RNG model, with standard wall functions. Since granular mediums are present, it is solved as dispersed turbulence model.
The RNG turbulence model is supplemented with extra source terms (Π_{ke} and $\Pi_{\varepsilon e}$) to include the effect of the dispersed particles on the primary phase motion and a set of granular quantities are derived to evaluate the variation in secondary phases energy [135]. The momentum exchange between phases can be considered by including a set of interphase turbulent momentum transfer coefficients.

The disperse formulation of the RNG turbulence equations can be written as [15, 136]:

$$\frac{\partial}{\partial t}\left(\alpha_{\mathrm{g}}\rho_{\mathrm{g}}\mathrm{k_g}\right)+\nabla\cdot\left(\alpha_{\mathrm{g}}\rho_{\mathrm{g}}\mathrm{k_g}\mathbf{u}_{\mathrm{g}}\right)= \nabla\cdot\left(\alpha_{\mathrm{g}}\Lambda_{\mathrm{k}}\mu_{\mathrm{g,eff}}\nabla\mathrm{k_g}\right)+\alpha_{\mathrm{g}}G_{k,g}+\alpha_{\mathrm{g}}G_{b,g}-\alpha_{\mathrm{g}}\rho_{\mathrm{g}}\varepsilon_{\mathrm{g}}+\alpha_{\mathrm{g}}\rho_{\mathrm{g}}\Pi_{\mathrm{k_g}}; \quad (5.1)$$

$$\frac{\partial}{\partial t}\left(\alpha_{\mathrm{g}}\rho_{\mathrm{g}}\varepsilon_{\mathrm{g}}\right)+\nabla\cdot\left(\alpha_{\mathrm{g}}\rho_{\mathrm{g}}\varepsilon_{\mathrm{g}}\mathbf{u}_{\mathrm{g}}\right)=\nabla\cdot\left(\alpha_{\mathrm{g}}\Lambda_{\varepsilon}\mu_{\mathrm{g,eff}}\nabla\varepsilon_{\mathrm{g}}\right) + \alpha_{\mathrm{g}}\mathrm{C}_{1\varepsilon}\frac{\varepsilon_{\mathrm{g}}}{\mathrm{k_g}}(\mathrm{G_{k,g}}-\mathrm{G}_{3\varepsilon,\mathrm{g}}\mathrm{G_{b,g}})-\alpha_{\mathrm{g}}\mathrm{C}_{2\varepsilon}\rho_{\mathrm{g}}\frac{\varepsilon_{\mathrm{g}}^2}{\mathrm{k_g}}-\alpha_{\mathrm{g}}\mathrm{R}_{\varepsilon}+\alpha_{\mathrm{g}}\rho_{\mathrm{g}}\Pi_{\mathrm{k_g}}. \quad (5.2)$$

Λ_{k} and Λ_{ε} are equal to the inverse-turbulent Prandtl number or the ratio between the thermal diffusivity and the turbulent viscosity:

$$\Lambda_{\mathrm{k}}=\Lambda_{\varepsilon}=\Lambda=\frac{1}{\mathrm{Pr_t}}. \quad (5.3)$$

The inverse-turbulent Prandtl number can be related to the molecular and effective viscosity as:

$$\frac{\mu_{\mathrm{g}}}{\mu_{\mathrm{g,eff}}} = \frac{\mu_{\mathrm{g}}}{\mu_{\mathrm{g}} + \mu_{\mathrm{t,g}}} = \left|\frac{\Lambda - 1.3929}{\Lambda_0 - 1.3929}\right|^{0.6321} \left|\frac{\Lambda - 2.3929}{\Lambda_0 - 2.3929}\right|^{0.3679} \tag{5.4}$$

with $\Lambda_0 = 1.0$. For usual turbulent flows, $\mu_{\mathrm{t,g}} >> \mu_{\mathrm{g}}$ and therefore $\Lambda \leq 1.393$.

$\mathrm{G_{k,g}}$ is the term accounting for the generation of turbulent kinetic energy due to the mean velocity gradients [28]:

$$\mathrm{G_{k,g}} = \rho_{\mathrm{g}} \overline{\mathrm{u'}_i \mathrm{u'}_j} \frac{\partial \mathrm{u'}_j}{\partial \mathrm{x}_i} = \underbrace{\mu_{\mathrm{t}}}_{\rho_{\mathrm{g}} \mathrm{C}_\mu \frac{\mathrm{k_g^2}}{\varepsilon_{\mathrm{g}}}} \left(2\mathrm{S}_{ij}\mathrm{S}_{ij}\right)^{1/2}. \tag{5.5}$$

The major peculiarity of the $k - \varepsilon$ RNG turbulence model is the presence of the term $\mathrm{R}_{\varepsilon,\mathrm{g}}$, that is of paramount importance in predicting the turbulent destruction in rapid strained flows:

$$\mathrm{R}_{\varepsilon,\mathrm{g}} = \frac{\mathrm{C}_\mu \rho_{\mathrm{g}} \eta^3 \left(1 - \eta/\eta_0\right)}{1 + \beta\eta^3} \frac{\varepsilon_{\mathrm{g}}^2}{\mathrm{k_g}} \tag{5.6}$$

where $\eta = \frac{\mathrm{Sk_g}}{\varepsilon_{\mathrm{g}}}$, $\eta_0 = 4.38$, $\beta = 0.012$.

The model constants are $C_{1,\varepsilon} = 1.42$, $C_{2,\varepsilon} = 1.68$, $C_{3,\varepsilon} = 1.3$, $\mathrm{Pr_{disp}} = 0.75$.
The near-wall regions have been modeled via wall-functions, using the Standard formulation for momentum and turbulence.
The law-of-the-wall for mean velocity yields:

$$\mathrm{U}^* = \frac{1}{\kappa} \ln\left(\mathrm{Ey}^*\right) \tag{5.7}$$

where $\mathrm{U}^* \equiv \frac{\mathrm{u_{g,P}} \mathrm{C}_\mu^{1/4} \mathrm{k}_{\mathrm{g,P}}^{1/2}}{\tau_{\mathrm{w}}/\rho_{\mathrm{g}}}$ is the dimensionless velocity.

The dimensionless distance from the wall is computed as:

$$\mathrm{y}^* = \frac{\rho_{\mathrm{g}} \mathrm{C}_\mu^{1/4} \mathrm{k}_{\mathrm{g,P}}^{1/2} y_{\mathrm{P}}}{\mu_{\mathrm{g}}} \tag{5.8}$$

The quantities reported in the equations are:

- $\kappa = 0.4187$, $[-]$: von Karman constant;
- $\mathrm{E} = 9.793$, $[-]$: empirical model constant;

- $\mathrm{u_{g,P}}$, $[\mathrm{m \cdot s^{-1}}]$: velocity at the first cell-center P over the wall;
- $\mathrm{y_P}$, $[m]$: distance of the first cell-center P from the wall;
- $\mathrm{k_{g,P}}$, $[\mathrm{m^2 \cdot s^{-2}}]$: turbulent kinetic energy at the first cell-center P over the wall;
- τ_w, $[\mathrm{m^2 \cdot s^{-2}}]$: wall shear, defined as:

$$\tau_\mathrm{w} = \mu_\mathrm{g} \frac{\partial u_\mathrm{g}}{\partial y}\bigg|_{\mathrm{y=0}}. \tag{5.9}$$

k equation is solved in the whole domain and the boundary condition imposed at the wall is:

$$\frac{\partial \mathrm{k_g}}{\partial n} = 0, \tag{5.10}$$

where n is the local coordinate perpendicular to the wall itself.

The production of kinetic energy at the wall-adiacent cells is computed via the $G_{k,g}$ term and it is added as source term in the k equation:

$$\mathrm{G_{k,g}} \approx \tau_\mathrm{w} \frac{\partial u_\mathrm{g}}{\partial y} = \tau_\mathrm{w} \frac{\tau_\mathrm{w}}{\kappa \rho_\mathrm{g} \mathrm{C}_\mu^{1/4} \mathrm{k}_\mathrm{g,P}^{1/2} \mathrm{y_P}}. \tag{5.11}$$

The dissipation rate of turbulent kinetic energy is not computed in cells near the wall but ε is obtained from:

$$\varepsilon_\mathrm{g,P} = \frac{\mathrm{C}_\mu^{3/4} \mathrm{k}_\mathrm{g,P}^{3/2}}{\kappa \mathrm{y_P}}. \tag{5.12}$$

The particulate phase is described through the kinetic theory of granular flows firstly developed by Chapman & Cowling [137] and Jenkins & Savage [138]. Granular temperature is introduced to model the random motion of particles and it is defined as one third of the mean square velocity fluctuations of solids:

$$\Theta_\mathrm{s} = \frac{1}{3} |\mathbf{u'}_\mathrm{s}|^2. \tag{5.13}$$

If granular energy does not vary remarkably with time and its dissipation takes place mainly locally, then the following algebraic expression can be written:

$$0 = (-\mathrm{p}_\theta \mathbf{I} + \tau_\theta) : \nabla \mathbf{u}_\theta - \gamma_\theta. \tag{5.14}$$

Note that the used notation describes with the subscript θ a generic solid phase coexisting in the multifluid approach and with the subscript s quantities referred to the total solid. If solid volume fractions are taken as example, the following relationships holds $\sum_{\theta=1}^{N} \alpha_\theta = \alpha_\mathrm{s}$, where N is the total number of solid phases.

The solids pressure is the pressure exerted by particles and it is used for pressure gradient term in solid phases momentum equations. It is correlated to the particles velocity fluctuations and it is, therefore, linked to the granular temperature specific of the phase Θ_θ.
According to the theory proposed Johnson & Jackson [139], the granular solid pressure is constituted by a contribution due to kinetic and collisional events, $\mathrm{p_{kin,coll}}$, and a contribution due to friction, $\mathrm{p_{fr}}$:

$$\mathrm{p}_\theta = \mathrm{p_{kin,coll}} + \mathrm{p_{fr}}. \tag{5.15}$$

Lun *et al.* [140] defined the kinetic part of Eq. 5.15 as:

$$\mathrm{p_{kin,coll}} = \alpha_\theta \rho_\theta \Theta_\theta + 2\rho_\theta \left(1 + \mathrm{e}_{\theta\theta}\right) \alpha_\theta^2 g_{0,\theta\theta} \Theta_\theta, \tag{5.16}$$

while the frictional part is [139]:

$$\mathrm{p_{fr}} = 0.05 \frac{\left(\alpha_\theta - \alpha_{\theta,\mathrm{fr,min}}\right)^2}{\alpha_{\theta,\mathrm{max}} - \alpha_\mathrm{g}}. \tag{5.17}$$

The relative importance of the two contributions changes when the solids approach the packing limit, passing from the so-called compressible condition ($\alpha_\theta < \alpha_{\theta,\mathrm{max}}$) to the incompressible condition ($\alpha_\theta = \alpha_{\theta,\mathrm{max}}$). This transition is governed through a particular relation called radial distribution function ($\mathrm{g_0}$). The latter depends on local and packing volume fractions and, in case of multiple solid phases, has the form [140]:

$$g_0 = \left[1 - \left(\frac{\alpha_\mathrm{s}}{\alpha_{\mathrm{s,max}}}\right)^{1/3}\right]^{-1} + \frac{1}{2}\mathrm{d}_\theta \sum_{\theta=1}^{N} \frac{\alpha_\theta}{\mathrm{d}_\theta}. \tag{5.18}$$

The solids stress tensor contains shear and bulk viscosities due to momentum exchange induced by particles translation and collisions. These two contributions, along with the stress due to the friction experienced by particles when they approach the packing limit, form the so called solids shear viscosity [141]:

$$\mu_\theta = \mu_{\theta,\mathrm{kin}} + \mu_{\theta,\mathrm{coll}} + \mu_{\theta,\mathrm{fr}}. \tag{5.19}$$

The kinetic and collisional viscosity is computed through the model proposed by Gidaspow *et al.* [142]:

$$\mu_{\theta,\mathrm{kin}}+\mu_{\theta,\mathrm{coll}} = \frac{4}{5}\alpha_\theta^2\rho_\theta \mathrm{d}_\theta \mathrm{g}_0\left(1+\mathrm{e}_\theta\right)\left(\frac{\Theta_\theta}{\pi}\right)^{1/2}\alpha_\theta + \frac{10\rho_\theta \mathrm{d}_\theta\left(\Theta_\theta\pi\right)^{1/2}}{96\left(1+\mathrm{e}_\theta\right)\mathrm{g}_0}\left[1+\frac{4}{5}\mathrm{g}_0\alpha_\theta\left(1+\mathrm{e}_\theta\right)\right]^2. \tag{5.20}$$

When the disperse phases volume fraction approach the packing limit, the generation of stresses is mainly governed by friction between particles through the law presented by Schaefer [143]:

$$\mu_{\theta,\mathrm{fr}} = p_{\theta,\mathrm{fr}}\frac{\sqrt{2}\sin(\Phi_{\mathrm{fr}})}{2\left(\mathbf{S}_\theta : \mathbf{S}_\theta\right)}, \tag{5.21}$$

where $p_{\theta,\mathrm{fr}}$ is the frictional pressure and Φ_{fr} is the angle of internal friction (usually 30 degrees).

The granular bulk viscosity is the resistance that particles exhibit to compression or expansion and has the form [28, 140]:

$$\lambda_\theta = \frac{4}{3}\alpha_\theta^2\rho_\theta \mathrm{d}_\theta \mathrm{g}_0\left(1+\mathrm{e}_\theta\right)\left(\frac{\Theta_\theta}{\pi}\right)^{1/2}. \tag{5.22}$$

The equation structure presented in Section 2.5 is used to model the drag force acting on the solid particles.
The Gidaspow model is usually employed to account for the fluid resistance in fluidized beds (Loha *et al.* [136], Che *et al.* [144]). Depending on the local gas volume fraction, the Wen & Yu model or the Ergun equation are used:

$$\mathrm{K}_{\theta\mathrm{g}}(\alpha_\mathrm{g}) = \begin{cases} \mathrm{K}_{\theta\mathrm{g}}(\text{Wen \& Yu}), & \text{for } \alpha_\mathrm{g} > 0.8 \\ \mathrm{K}_{\theta\mathrm{g}}(\text{Ergun}), & \text{for } \alpha_\mathrm{g} \leq 0.8 \end{cases}$$

The Wen & Yu equation [145] is:

$$\mathrm{K}_{\theta\mathrm{g}}(\text{Wen \& Yu}) = \frac{3\rho_\mathrm{g}\alpha_\mathrm{g}(1-\alpha_\mathrm{g})}{4\mathrm{d}_\theta}\mathrm{C}_\mathrm{D}\left|\mathbf{u}_\theta-\mathbf{u}_\mathrm{g}\right|\alpha_\mathrm{g}^{-2.65}. \tag{5.23}$$

The Ergun equation [146] is:

$$\mathrm{K}_{\theta\mathrm{g}}(\text{Ergun}) = 150\frac{\alpha_\theta^2\mu_\mathrm{g}}{\alpha_\theta^2\mathrm{d}_\theta^2} + 1.75\frac{\alpha_\theta\rho_\theta|\mathbf{u}_\theta-\mathbf{u}_\mathrm{g}|}{\alpha_\theta^2\mathrm{d}_\theta^2}. \tag{5.24}$$

The drag coefficient, C_D, is calculated accordingly to the Schiller & Naumann equation [100].

Geometry and computational grid

In absence of experimental data, the physical and numerical set-up adopted has been validated against relevant literature data obtained from the work of Che *et al.* [144]. The reactor geometry, reported in Fig. 5.3, has been reproduced and simulation settings have been chosen to replicate the multiphase flow field taken as reference. A quasi steady-state fluidized bed is examined, assuming constant temperature, no chemical reactions and no solid feed and withdrawal.
This corresponds to the stable condition established in FBR after expansion of the initially charged amount of solid with given particle size distribution.
Although the flow features in fluidized beds are tridimensional, it is very usual to model the fluidization process using 2D computational domains since good results are obtained at a more reasonable computational cost, as shown by Gidaspow & Ettahadieh [14] in the past and Passalacqua & Marmo [24] and Ray *et al.* [20] in more recent years.

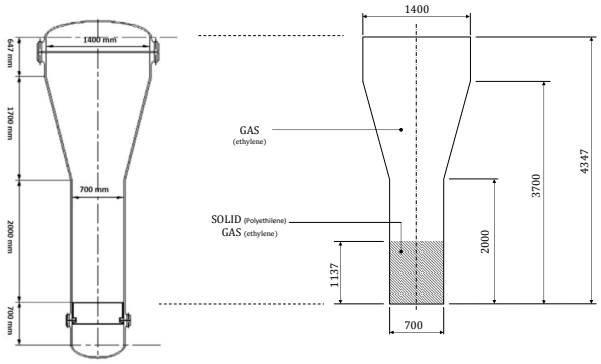

Figure 5.3: Schematic representation of the pilot-scale reactor (left, taken from Che *et al.* [144]) and of the corresponding 2D computational domain (right).

The overall height of the cylindrical reactor is 4.347 m, with diameter of the lower region of 700 mm and diameter of the upper part of 1400 mm. A disengagement conic zone is present to gradually enlarge the cross-section area and reduce the gas velocity, thus preventing solid elutriation and keeping all particles within the polymerization zone. The real system is fed by a gas stream through a distributor plate that is omitted in the computational model.
The multiphase mixture is composed by pressurized ethylene (gas primary phase) and high-density polyethylene (solid disperse phase). Important bulk data such as phase density (ρ), angle of repose [147], viscosity (μ) and coefficient of restitution (e) are listed in Table 5.1.
The fluidization characteristics of the system have been studied for three different uniform inlet gas velocities, 20, 40 and 61 [$\mathrm{cm\,s^{-1}}$]. Solid volume fraction and

Table 5.1: Material properties at T = 361 K and p = 2 MPa (viscosity data taken from Che *et al.* [144]). KTGF stands for Kinetic Theory of Granular Flows.

	ρ	angle of repose	μ	e
	[kg m^{-3}]	[–]	[Pa s]	[–]
Ethylene (g)	20	-	$1.72 \cdot 10^{-5}$	-
Polyethylene (s)	900	30	KTFG	0.9

velocity magnitude data were compared quantitatively by averaging results in time for 50 seconds of operation. In order to exclude the highly transient start-up of the flow motion and to obtain quasi-steady state results, the first 10 seconds of fluidization data were discarded and the averaging procedure was conducted between 10 and 60 s of physical time. The validation of the multiphase simulation model is described in Appendix A.2 and A.3 while the averaging technique is described in detail in the next section.

Methodology analysis

The comparison of the results obtained by the two modeling approaches, detailed CFD and simplified SCM, was carried out in terms of selected properties at different reactor heights, specifically considering four sampling lines placed in the lower cylindrical part of the reactor, as depicted in Fig. 5.4.

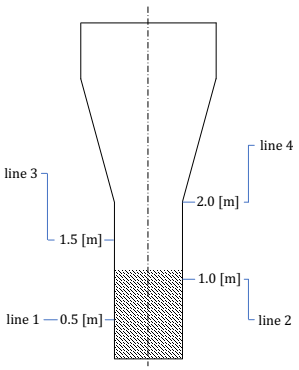

Figure 5.4: Scheme of the inspection lines used for the quantitative analysis.

Eq. 5.25 and Eq. 5.26 show the relations used to average in time the local and average solid volume fraction:

$$\alpha_\theta^j = \alpha_\mathrm{s}^j = \frac{1}{\mathrm{n}} \sum_{i=\mathrm{dt_{init}}}^{\mathrm{dt_{end}}} \alpha_\mathrm{s}^{j,i} \tag{5.25}$$

where n = 50000 is the total number of time step evaluated between time t = 10 s ($\mathrm{dt_{init}} = 10000$) and t = 60 s ($\mathrm{dt_{end}} = 60000$). Data were sampled every 100 time steps, j specifies the computational grid cell while i the time step. Cell-centered values α_s^j were then averaged in space to obtain the mean solid volume fraction as a function of the reactor height, $\alpha_{\mathrm{s,ave}}$. The average gas volume fraction was obtained observing that the total volume has to complement to 1.

$$\alpha_{\theta,\mathrm{ave}} = \alpha_{\mathrm{s,ave}} = 1 - \alpha_{\mathrm{g,ave}}. \tag{5.26}$$

The spatial average particle size has been evaluated on numeral basis as moment of order 4 to moment of order 3 ratio:

$$\mathrm{d_{43}} = \frac{\mathrm{m_4}}{\mathrm{m_3}} = \mathrm{d_{ave}} \tag{5.27}$$

where the generic moment of k-th order is defined as:

$$\mathrm{m_k} = \sum_{\theta=1}^{N} w_\theta \mathrm{d}_\theta^k. \tag{5.28}$$

w_θ is the numebr of particle per unit volume computed dividing the local phase volume fraction by the single-particle volume while d_θ^k is the θ-th solid phase diameter to the k-th powder.
The average diameter is defined in such way to be consistent to average quantities computed through the compartment-based model.

The simulation cases were defined by given set of initial conditions, for both monodisperse and polydisperse populations of particles. Their primary aim was to compare the fluidization properties predicted by the detailed CFD model with those coming from the simplified compartmentalized model. Monodisperse cases were also used to identify proper CFD simulation conditions comparing these results with literature ones (Che *et al.*, [144]). The investigated simulation parameters were:

i. particle average diameter, to study the effect of particles inertia;

ii. standard deviation of the particle size distribution, to study the effect of populations polydispersity;

iii. solid initialization height, to understand the influence that the quantity of particles loaded into the reactor at the beginning has on solid expansion;

iv. gas velocity, to investigate the influence of the carrier stream on the drag exerted on particles and verify the absence of elutriation.

Besides the multiphase flow model validation, described in detail in the next section, an accurate comparison with literature results has been carried out regarding the computational grid construction and the equations discretization order (Appendix A.2), the geometric description (Appendix A.3) and the initial conditions (Appendix A.4).

5.2.1 Pure Fluidization

Computational Grid Design

The mesh size has been chosen after reaching a grid independent solution and to best fit literature data. Results are therefore obtained with a 2D planar grid composed by 225500 high-quality elements with maximum aspect ratio of 1.53 (1 - optimum) and maximum skewness of 0.13 (0 - best; 1 - worst). The validation of the computational grid is discussed in detail in the Appendix A.2.
Fig 5.5 shows the geometry partitioning strategy exploitet to build the fully structured grid, named "fine", used to perform the simulations.

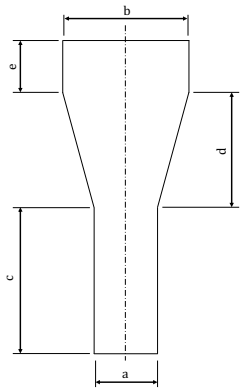

Figure 5.5: Geometry segmentation for mesh construction and definition.

Table 5.2 reports the elements used to build the chosen grid, the complete description of the mesh analyzed is reported in Appendix A.2.

Solver Details and Boundary Conditions

Simulations were performed using the cell-centered finite-volume code Fluent by ANSYS, Inc. [96]. The highly turbulent nature of the flow and its efficient mixing were described through the $k - \varepsilon$ RNG turbulent model with the wall functions

Table 5.2: "Fine" computational grid details, number of elements as function of the geometry feature.

Grid	# a	# b	# c	# d	# e	# tot
fine	220	220	655	300	70	225500

developed by Launder & Spalding [148].
The coupling between pressure and velocity is obtained through the Phase-Coupled SIMPLE (PC-SIMPLE) algorithm firstly developed by Spalding & Patankar [149] and later modified by Vasquez [150] to solve multiphase flow fields. Gradients are discretized through the Green-Gauss Node-Based method (Barth & Jespersen [151]) while pressure is interpolated at cell faces using momentum equations coefficients as proposed by Rhie & Chow [98].
Following the work of Barth & Jaspersen [151], the spatial discretization for momentum and turbulent balances has been carried out by means of second order accurate schemes, thus improving the predictions with respect to first order schemes.
The temporal dynamics of the system has been investigated by solving transient simulations discretized through bounded second-order implicit scheme with constant time step of 10^{-3} s, coherently to reference data (Che *et al.* [144]).
Finally, all used boundary conditions are listed in Table 5.3.

Table 5.3: Simulations boundary conditions. $\mathrm{u_g}$ is the gas velocity value assigned to the boundary. I is the turbulent intensity, C_μ is a turbulence model constant and L is a characteristic length.

Variable	Inlet	Outlet	Walls
$\mathbf{u}_\mathrm{g}$	$\mathrm{u_g}\frac{\mathbf{n}}{\lvert\mathbf{n}\rvert}$	$\nabla\mathbf{u}_\mathrm{g}\cdot\mathbf{n}=0$	no slip
$\mathbf{u}_\theta$	0	$\nabla\mathbf{u}_\theta\cdot\mathbf{n}=0$	$\tau=0$
α_θ	0	$\nabla\alpha_\theta\cdot\mathbf{n}=0$	$\nabla\alpha_\theta\cdot\mathbf{n}=0$
p	$\nabla\mathrm{p}\cdot\mathbf{n}=0$	$\mathrm{p_{atm}}$	$\nabla\mathrm{p}\cdot\mathbf{n}=0$
k	$\frac{3}{2}(I\lvert\mathbf{u}_\mathrm{g}\rvert)^2$	$\nabla\mathrm{k}\cdot\mathbf{n}=0$	wall funct.
ε	$\frac{\mathrm{C}_\mu^{0.75}\mathrm{k}^{1.5}}{\mathrm{L}}$	$\nabla\varepsilon\cdot\mathbf{n}=0$	wall funct.

Phase Turbulent Interaction

In order to assess if supplentary forces need to be taken into account, simulation results have been compared to literature reference data. In addition to drag, the actual relevance of including the mutual interaction effects induced by the presence of the particulate phase on the gas flow has been investigated by assessing the importance of the Simonin model in transport equations for turbulence. Terms Π_{k_g} in Eq. 5.1 and Π_{ε_g} in Eq. 5.2 are defined as:

$$\Pi_{k_g} = C_s \sum_{\theta=1}^{N} \frac{K_{\theta g}}{\alpha_g \rho_g} X_{\theta g}(k_{\theta g} - 2k_g); \tag{5.29}$$

$$\Pi_{\varepsilon_g} = C_{\varepsilon_g} \frac{\varepsilon_g}{k_g} \Pi_{k_g}, \tag{5.30}$$

where C_s is a model constant, usually set equal to 1, and $C_{\varepsilon_g} = 1$. $K_{\theta g}$ is the covariance of the continuous and dispersed phase and $X_{\theta g}$ is a coefficient that for granular flows is usually close to 1 [28, 31]. It is evaluated as:

$$X_{\theta g} = \frac{\rho_\theta}{\rho_\theta + C_{VM}\rho_g}, \tag{5.31}$$

with the added mass coefficient C_{VM} equal to 0.5.

Finally, the influence of turbulent interactions on the disperse phase has been considered through a modified viscosity for the secondary phases:

$$\nu_\theta = \frac{1}{3} k_{\theta g} \tau^t_{\theta g} + \frac{2}{3} k_g \tau^F_{\theta g}. \tag{5.32}$$

The analysis is performed by comparing the contours at different physical times (Fig. 5.6) and the time-averaged cell-centered data (Fig. 5.7) of the solid volume fractions reported by Che *et al.* [144] with those resulting from a simulation without and with turbulent interaction modeling.

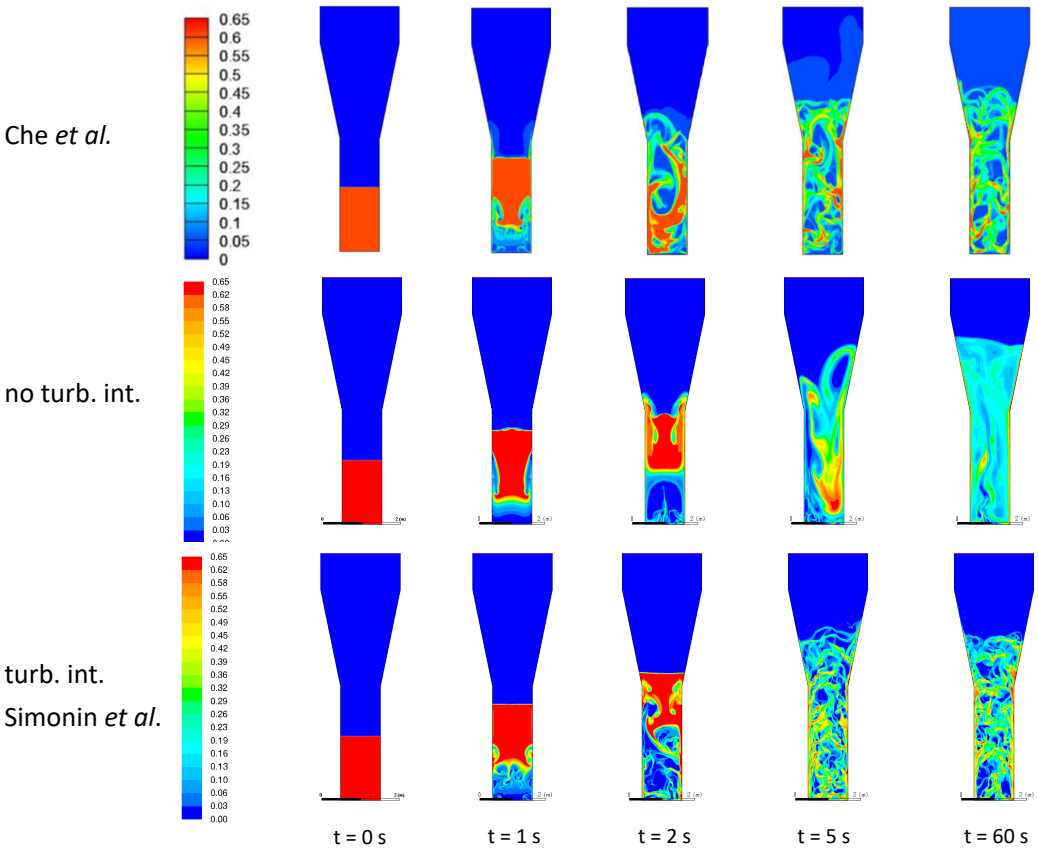

Figure 5.6: Comparison between the solid volume fraction contours, at different physical times, for the reference case (courtesy of Che *et al.* [144]), a case without any interaction and a case with the Simonin *et al.* interaction model [152]. Monodisperse particles with size d = 446 μm, fine computational grid.

The best reproduction of literature results was achieved using the Simonin model for turbulent interaction. Therefore, such contribution is essential to predict the correct fluidization in terms of gas bubble formation and solid phase mixing and it is used in all simulations reported in the following. Moreover, the quantitative data reported in Fig. 5.7 support such statement. The agreement is always quite good when interaction is accounted for, especially at the top of the cylindrical part of the reactor.

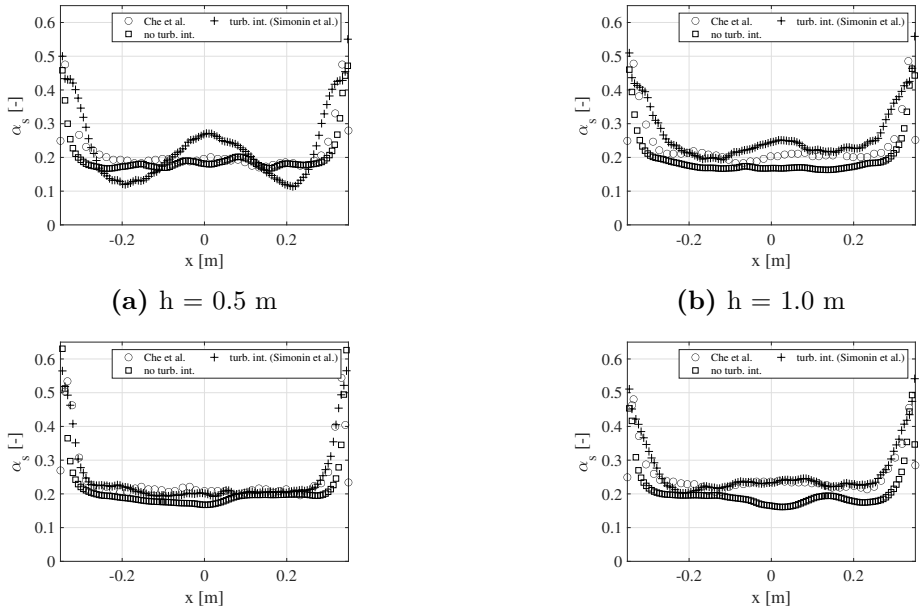

(a) h = 0.5 m **(b)** h = 1.0 m

(c) h = 1.5 m **(d)** h = 2.0 m

Figure 5.7: Comparison between the time-averaged cell-centered data of solid volume fraction at different reactor heights for the reference case (courtesy of Che *et al* [144]), a case without any interaction and a case with the Simonin *et al* interaction model [152]. Monodisperse particles with size d = 446 μm. Monodisperse particles with size d = 446 μm, fine computational grid.

5.2.2 CFD-PBE Olefins Polymerization

The particle residence time distribution in fluidized bed reactors is complex and it is usually of order of hours [153]. Zacca *et al.* [154], for example, reported a value of approximately 2 hours. The fluidization of solid particles is a pure transient phenomenon and the quasi steady-state operation of such systems when operated with continuous solid feed and withdrawal cannot be easily simulated through detailed CFD tools, due to the relevant computational effort needed to calculate the multiphase flow-field and polymerization kinetics for such long residence times, usually also requiring very small time-steps [144].
Moreover, there is no evidence, to the best of the author knowledge, of CFD simulations dealing with the modeling of the continuous polymerization of polyethylene in scientific literature.
Therefore, the idea at the base of the following description consists in proposing a scaling-down procedure to remarkably reduce the expected particle residence time and the computational grid size, exploiting the same 2D reactor geometry and physical/numerical set-up already validated and used for the fluidization study.

The steps followed to scale-down the reactor and speed-up the transient start-up phase of the process are the following.

1. Define a computationally-affordable particle residence time.
2. Choose a reference geometry and select reasonable operating conditions (process gas velocity, pressure, temperature and gas conversion efficiency).
3. Given a gas flow-rate and a single-passage conversion efficiency, estimate the polymer formed and discharged. Note that it is possible to assume that the discharged polymer is equal to the polymerized one if constant holdup condition at steady-state operation is verified.
4. From the desired particles residence time and polymer volume flow-rate, estimate the reactor volume. This can be used, through a scale factor, to design the plant by replicating the reference one.
5. Determine a proper polymerization model.
6. Exploit simple material balances to guess final particle size and the related residence time.
7. Use the estimated particle size to initialize the packed bed and speed-up the transient start-up of the system.
8. Simulate the continuous polymerization for a physical time sufficient to reach a quasi-stady state operation mode (constant holdup and particle diameter).

Calculations are detailed in the next sections.

Reactor Design and Mesh

Since the solid holdup is constant at steady-state, the average residence time of solid particles can be roughly estimated dividing the reactor volume by the discharged particles volume flow rate.
Fluidized bed reactors usually have an height of 8-16 m and a diameter of 1-4 m [112]. From this information, a reactor height, H, of 10 m and a diameter, D, of 2.5 m has been considered, with a volume of approximately 49 m^3.
The typical ranges of operating conditions for this same reactors are summarized in Table 5.4 [112].

Table 5.4: Usual operating conditions of FBRs for polyolefin production. u_g stands for nominal gas velocity, p_{op} is the operative pressure. T is the average temperature and χ the single-passage conversion.

u_g	p_{op}	T	χ
$[cm\,s^{-1}]$	[bar]	[K]	[–]
50-100	20-25	343.15-383.15	0.02-0.3

Assuming average values, that is, a gas velocity, u_g, of 75 $cm\,s^{-1}$, operating pressure of 22.5 bar, operating temperature of 363.15 K and a gas single-pass conversion, χ, of 0.1, one can estimate a gas molar concentration of:

$$\frac{n}{V} = \frac{p_{op}}{\mathcal{R}T} = 756\,mol\,m^{-3}; \tag{5.33}$$

and a gas mass-flow rate of:

$$\dot{m}_g = u_g A \dot{Q}_g \frac{n}{V} MW_{mon} = 78.04\,kg\,s^{-1}. \tag{5.34}$$

If $\chi = 0.1$ is assumed, a polymer mass-flow rate of approximately 7.8 $kg\,s^{-1}$ is obtained which, in turn, corresponds to a volumetric flow rate of 8.7 10^{-3} $m^3\,s^{-1}$ (for ρ_s=900 $kg\,m^{-3}$).
The average residence time can be estimated as the ratio between the reactor volume and the volume-flow rate of discharged polymer:

$$rt = \frac{V}{\dot{Q}_s} = 5362\,s \approx 1.56\,h. \tag{5.35}$$

Such a residence time is too large to be simulated with transient CFD simulations and, therefore, a scale-down procedure to reduce the reactor volume is proposed. Let us consider a (computationally) acceptable residence time of rt = 100 s and u_g = 50 $cm\,s^{-1}$ for a 2D planar geometry with a cross-section area of 0.7 m^2, taking

as reference the Che *et al.* [144] model geometry used for validation purposes.
The gas volume flow-rate is therefore 0.35 $m^3\,s^{-1}$ and the gas mass flow-rate is about 7.4 $kg\,s^{-1}$ that corresponds, assuming again a single-passage conversion for ethylene of 0.1, to 0.74 $kg\,s^{-1}$ ($8.2 \cdot 10^{-4}$ $m^3\,s^{-1}$) of polymer formed.
Rearranging Eq. 5.35, a particles residence time of 100 s and a polymer volume-flow rate of $8.2 \cdot 10^{-4}$ $m^3\,s^{-1}$ gives a reactor volume of $8.2 \cdot 10^{-2}$ m^3.
Scaling down the Che *et al.* [144] model geometry of 7 times, it is possible to design a reactor with a volume of $8.345 \cdot 10^{-2}$ m^3, as specified in Fig. 5.8.

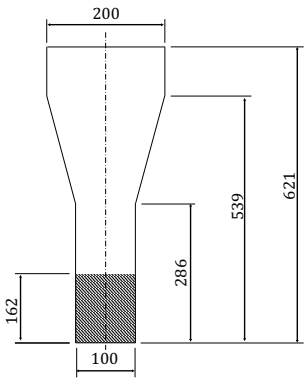

Figure 5.8: Scaled-down computational domain (1/7 of the original one – V = 8.345 10^{-2} m^3).

In order to guess the correct multiphase flow-field and speed-up the start-up phase of the reactor operation, simple material (total mass and catalyst) balances are used to estimate the final size of the particles and set the solids diameters of the packed bed at initialization. This is feasible because it has been shown that FBRs behaves like well-mixed compartment and the particles size is uniform within the reactor (Section 5.4.1 of this chapter).
According to Kim & Choi [155], the polymerization rate is:

$$R_p = K_p M C^* MW_{mon}. \tag{5.36}$$

where K_p is the polymerization rate constant, M is the gas molar concentration, C^* is the concentration of active catalyst sites and MW_{mon} is the monomer molecular weight.

The following material balances are derived for the total mass and the catalyst.

- Total mass balance at steady-state:

$$\frac{dW}{dt} = \dot{m}_{c,in} - \dot{m}_{s,out} + R_p W x_c = 0. \tag{5.37}$$

- Catalyst mass balance at steady-state:

$$\frac{d}{dt}(W x_c) = \dot{m}_{c,in} - \dot{m}_{s,out} x_c = 0. \tag{5.38}$$

$\dot{m}_{c,in}$ is the solid feed-rate of fresh catalyst, $\dot{m}_{s,out}$ is the discharged polymer mass flow-rate, x_c is the mass fraction of catalyst and $R_p W x_c$ gives the mass of polymer formed. W is the total mass in the reactor.
$\dot{m}_{s,out} x_c$ provides the discharged catalyst (exiting the system together with the polymer) if an homogeneous distribution of catalyst inside the reactor is assumed. From Eq. 5.38 it comes that the mass fraction of catalyst inside the rector is given by:

$$x_c = \frac{\dot{m}_{c,in}}{\dot{m}_{s,out}}. \tag{5.39}$$

Using Eq. 5.37 and Eq. 5.38, the discharged quantity of polymer formed can be calculated by solving the resulting quadratic equation:

$$\dot{m}_{c,in} - \dot{m}_{s,out} + R_p W \left(\frac{\dot{m}_{c,in}}{\dot{m}_{s,out}}\right) = 0 \rightarrow \dot{m}_{s,out}^2 - \dot{m}_{c,in}\dot{m}_{s,out} - R_p W \dot{m}_{c,in} = 0; \tag{5.40}$$

$$\dot{m}_{s,out} = \frac{\dot{m}_{c,in} \pm \sqrt{\dot{m}_{c,in}^2 + 4 R_p W \dot{m}_{c,in}}}{2}. \tag{5.41}$$

The feed-rate of catalyst particles, given in $\#\,s^{-1}$, can be estimated dividing the inlet volume-flow rate of catalyst by its single-particle volume:

$$\dot{n}_c = \frac{\dot{m}_{c,in}}{\rho_c k_v d_c^3}. \tag{5.42}$$

where k_v is the shape factor equal to $\pi/6$ for spherical particles.
The volume flow-rate of polymer discharded is:

$$\dot{Q}_{s,out} = \frac{\dot{m}_{s,out}}{\rho_s}, \tag{5.43}$$

while the estimated final particle volume, V_s, gives the final particles diameter:

$$V_s = \frac{\dot{Q}_{s,out}}{\dot{n}_c} \rightarrow d_s^{est} = \sqrt[3]{\frac{v_s}{k_v}}. \tag{5.44}$$

The expected residence time can be calculated through the solid holdup, in kg, and the solid withdrawal rate, in $\mathrm{kg\,s^{-1}}$:

$$\mathrm{rt}^{\mathrm{est}} = \frac{\mathrm{W}}{\dot{\mathrm{m}}_{\mathrm{s,out}}}. \tag{5.45}$$

The following table lists the two solid feed-rates tested and the related expected diameters.

Table 5.5: Operative conditions tested and pre-polymerized particles size (initialization values) for $\mathrm{K_{p,ref}} = 1.87 \cdot 10^7\,\mathrm{cm^3\,mol^{-1}\,s^{-1}}$.

$\mathrm{d_c}$	$\dot{\mathrm{m}}_{\mathrm{c,in}}$	$\mathrm{d_s^{est}}$	$\mathrm{rt^{est}}$
$[\mu\mathrm{m}]$	$[\mathrm{g\,min^{-1}}]$	$[\mu\mathrm{m}]$	[s]
25	100	73.98	10.3
25	10	108.52	32.6

The scaled geometric model allows for the fresh catalysts particles injection on the left side while three different outlet topologies have been analyzed.
Fig. 5.9 shows that the solid withdrawal can take place at the bottom (outlet-down), in the middle (outlet-middle) or in the top part (outlet up) of the cylindrical zone of the reactor. The solid injection is made at the same height of outlet-middle.

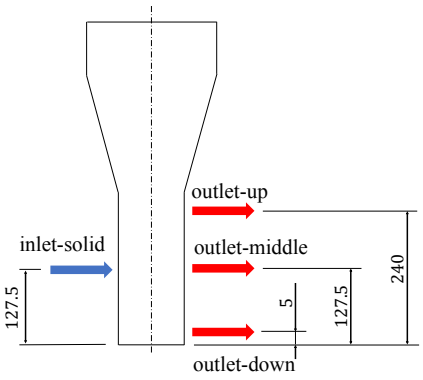

Figure 5.9: Scaled model inlet and outlets conformation.

The computational grid is built following the same procedure adopted for the pure fluidization cases, including solid feed and withdrawal zones. The resulting mesh is composed by 19008 elements with a maximum aspect ratio of 1.8832 (1 - optimum) and a maximum skewness of 0.13 circa (0 - good quality, 1 - bad quality).

Grid statistics indicate a very good quality of the mesh.

CFD Implementation of Particle Growth through DQMOM

Solid particles moving inside a gas flow-field are subjected to continuous and discontinuous events. Continuous events take place with an infinitesimal rate of change and their effects act continuously. A good example is given by body forces such as the drag force. Discountinuous events, or point processes, act instantaneously typically changing the disperse phase momentum balance. An example that fits well for gas-solid flows is the collision between two particles.
Polyethylene particles within fluidized beds are clearly moved by a continuous gas phase undergoing the polymerization process and they are therefore subjected to continuous events but they are also prone to collide one against the other.
This case is focused on simulating a pure particle growth process and, therefore, discontinuous point processes such aggregation and breakage are neglected.

According to Fan *et al.* [17], a solid phase can be approximated by a multivariate distribution function that depends on the particle characteristic size and its velocity. The transport equation has the form:

$$\frac{\mathrm{d}}{\mathrm{d}t}\left[n\left(\mathrm{L},\mathbf{u}_\mathrm{s};\mathbf{x},t\right)\right]+\nabla\cdot\left[\mathbf{u}_\mathrm{s}n\left(\mathrm{L},\mathbf{u}_\mathrm{s};\mathbf{x},t\right)\right]+\nabla_{\mathbf{u}_\mathrm{s}}\cdot\left[\mathbf{F}n\left(\mathrm{L},\mathbf{u}_\mathrm{s};\mathbf{x},t\right)\right]=\mathcal{S}\left(\mathrm{L},\mathbf{u}_\mathrm{s};\mathbf{x},t\right) \tag{5.46}$$

where $\mathbf{x}$ is the spatial coordinate vector and t is time. $\mathcal{S}$ represents the source term associated to the discontinuous events causing the transported variable change, while $\mathbf{F}$ is the body force accelerating particles that can be computed through the solid phases momentum balances described by Eq. 2.25.
The Direct Quadrature Method of Moments is used to track the particle size evolution of the solid phase by approximating the distribution function as a summation of Dirac delta functions, as described by Eq. 3.21, which is, in turn, a function of particle length information (Eq. 3.22).
The solid phase pupulation balance equation has the form:

$$\frac{\mathrm{d}}{\mathrm{d}t}\left[n\left(\mathrm{L},\mathbf{u}_\mathrm{s};\mathbf{x},t\right)\right]+\nabla\cdot\left[\langle\mathbf{u}_\mathrm{s}|\mathrm{L}\rangle n\left(\mathrm{L},\mathbf{u}_\mathrm{s};\mathbf{x},t\right)\right]=\mathcal{S}\left(\mathrm{L},\mathbf{u}_\mathrm{s};\mathbf{x},t\right) \tag{5.47}$$

where $\langle\mathbf{u}_\mathrm{s}|\mathrm{L}\rangle$ is the mean velocity conditioned on the particle characteristic length L:

$$\langle\mathbf{u}_\mathrm{s}|\mathrm{L}\rangle n\left(\mathrm{L},\mathbf{u}_\mathrm{s};\mathbf{x},t\right)=\int_{\infty}^{\infty}=\mathbf{u}_\mathrm{s}n\left(\mathrm{L},\mathbf{u}_\mathrm{s};\mathbf{x},t\right)\mathrm{d}\mathbf{u}_\mathrm{s} \tag{5.48}$$

It is worth to notice that $\langle \mathbf{u}_\mathrm{s} | \mathrm{L} = \mathrm{L}_\theta \rangle = \mathbf{u}_{\mathrm{s}\theta}$.

Weights and abscissas represent the nodes of the quadrature approximation of the moments describing the PSD. They can be thought as independent solid phases advected with their own velocity fields, allowing to model the separation and segregation induced by inertia. Two or three quadrature nodes are usually sufficient to capture the phenomena associated to polydispersivity.
The transport equations for the weights (w_θ) and weighted abscissas ($w_\theta \mathrm{L}_\theta$) are:

$$\frac{\partial}{\partial t}\left(w_\theta\right) + \nabla \cdot \left(w_\theta \mathbf{u}_\theta\right) = \mathrm{a}_\theta; \tag{5.49}$$

$$\frac{\partial}{\partial t}\left(w_\theta \mathrm{L}_\theta\right) + \nabla \cdot \left(w_\theta \mathrm{L}_\theta \mathbf{u}_\theta\right) = \mathrm{b}_\theta. \tag{5.50}$$

where a_θ and b_θ are the source terms.
Volume fractions and effective lengths can be related to quadrature properties as:

$$\alpha_\theta = w_\theta \mathrm{v}_{\mathrm{p},\theta}; \tag{5.51}$$

$$\alpha_\theta \mathrm{L}_\theta = \mathrm{k}_\mathrm{v} w_\theta \mathrm{L}_\theta^4 \tag{5.52}$$

where k_v is a volumetric shape factor that is equal to $\pi/6$ for spherical particles and $\mathrm{v}_{\mathrm{p},\theta}$ is the particle volume of objects belonging to the θ-th solid phase.
The size change due to particle growth can be accounted for by modifying the θ-th solid phase continuity equation and introducing a balance for the effective transported length:

$$\frac{\partial \alpha_\theta \rho_\theta}{\partial t} + \nabla \cdot \left(\alpha_\theta \rho_\theta \mathbf{u}_\theta\right) = 3\mathrm{k}_\mathrm{v} \rho_\theta \mathrm{L}_\theta^2 \mathrm{b}_\theta; \tag{5.53}$$

$$\frac{\partial \alpha_\theta \mathrm{L}_\theta \rho_\theta}{\partial t} + \nabla \cdot \left(\alpha_\theta \mathrm{L}_\theta \rho_\theta \mathbf{u}_\theta\right) = 4\mathrm{k}_\mathrm{v} \rho_\theta \mathrm{L}_\theta^3 \mathrm{b}_\theta \tag{5.54}$$

where b_θ is the growth rate coefficient for the θ-th solid phase :

$$\mathrm{b}_\theta = w_\theta \frac{G_v}{3\mathrm{k}_\mathrm{v} \mathrm{L}_\theta^2} \tag{5.55}$$

with G_v equal to the volumetric growth rate induced by polymerization and L_θ equal to the solid phase characteristic length that is equal to the phase diameter. The particle volume variation occurring because of polymerization is defined as a zero-order process, since it is only due to events taking place in the continuous phase and it does not depend on the disperse phase.
In this context, taking as generic length the diameter d (or the related radius r),

the size variation can be modeled through the oversimplified law proposed by Kim & Choi [155]:

$$\frac{\mathrm{d}r}{\mathrm{d}t} = \frac{\mathrm{r_c^3} \cdot \rho_\mathrm{c} \cdot \mathrm{K_p} \cdot \mathrm{M} \cdot \mathrm{C^*} \cdot \mathrm{PM_{mon}}}{3\,(1-\zeta)\,\mathrm{r}^2 \cdot \rho_\mathrm{s}} = \mathrm{G}. \tag{5.56}$$

r denotes the radius, M is the molar concentration, PM is the molecular weight, ζ is the catalyst void fraction and G is the length-based growth-rate. The Subscript c indicates the catalyst, subscript mon stands for the monomer while subcript s describes the solid/polymer properties.
$\mathrm{C^*}$ and $\mathrm{K_p}$ are expressed as function of reference values $\mathrm{C^*_{ref}}$ and $\mathrm{K_{p,ref}}$ as:

$$\mathrm{C^*} = \mathrm{C^*_{ref}} \cdot 0.0337; \tag{5.57}$$

$$\mathrm{K_p} = \mathrm{K_{p,rif}} \cdot \exp\left\{\left[\frac{-\mathrm{E_{act,p}}}{\mathcal{R}}\left(\frac{1}{\mathrm{T}}\right)\right]\right\}. \tag{5.58}$$

G is equal to the length-based particle growth rate. Following the math of Appendix 5, it can be converted into a volume-based equation to obtain $\mathrm{G_v}$:

$$\frac{\mathrm{d}V}{\mathrm{d}t} = \frac{\mathrm{V_c} \cdot \rho_\mathrm{c} \cdot \mathrm{K_p} \cdot \mathrm{M} \cdot \mathrm{C^*} \cdot \mathrm{PM_{mon}}}{(1-\zeta)\,\rho_\mathrm{s}} = \mathrm{G_v}. \tag{5.59}$$

The monomer, polymer and catalyst particles data are reported in Table 5.6.

Table 5.6: Monomer (mon), polymer (s) and catalyst (c) physical properties (Kim & Choi [155]). Note that the initial particles diameter is taken from the estimation calculated through material balances.

	ρ [kg m^{-3}]	MW [g mol^{-1}]	ζ [Pa s]	r(t=0) [m]
Ethylene (g)	20	28.05	-	-
Polyethylene (s)	900	-	-	$\mathrm{d_s^{est}}/2$ of Table 5.5
Catalyst (c)	2333	-	0.1	$1.25 \cdot 10^{-3}$

The particle growth model parameters and costants are listed in Table 5.7.

Table 5.7: Particle growth model constants and parameters (Kim & Choi [155]).

M	$E_{act,p}$	$K_{p,ref}$	T	C^*_{ref}	$\mathcal{R}$
$[mol\,cm^{-3}]$	$[cal\,mol^{-1}]$	$[cm^3\,mol^{-1}\,s^{-1}]$	[K]	$[mol\,g^{-1}]$	$[cal\,mol^{-1}\,K^{-1}]$
$1.12 \cdot 10^{-4}$	10^{-4}	$1.87 \cdot 10^{-13}$	343.15	$4.18 \cdot 10^{-4}$	1.987

Numerical Set-up, Initial and Boundary Conditions

The numerical solution of the CFD-PBE cases is obtained with a physical and numerical set-up equal to the one used for the pure fluidizaton study. The additional transport equations for the three solid phase effective lengths are solved through the TVD second-order accurate discretization scheme.
The method proposed by Marchisio & Fox [49, 156] is used to calculate a three node quadrature (with nodes indicated with indexes QP0, QP1 and QP2) with DQMOM approach, in complete analogy to what presented in the fluidization study of Section 5.4.1.
The first six moments of the distributions are used to account for polydispersivity and retrieve quadrature quantities, *i.e.*, weights (α_θ) and abscissas ($\alpha_\theta d_\theta$) through the Wheeler moment inversion algorithm [35] and such diameters are assigned to the different solid phases.
The volume fraction of the total pre-polimerized particles forming the packed bed is initialized at 0.4 for replicating the bed expansion conditions obtained from pure fluidization cases. The process gas composed by pressurized ethylene is fed from the reactor bottom while fresh catalyst enters the system from a lateral inlet.
The gas, catalyst and polymer material properties are reported in Table 5.6.
The imposed boundary conditions are shown Fig. 5.10 and reported in Table 5.8.
The inlet gas velocity is between 20 and 40 $cm\,s^{-1}$, depending on the simulation physical time (the description of the computational procedure is given in Section 5.4.2), while the fresh catalyst feed is set to 10 or 100 $g\,s^{-1}$ to investigate its influence on the solid hold-up. Catalyst particles are carried inside the ractor by a constant flow of gas of 1 $g\,s^{-1}$.
As decipted by Fig. 5.9, three different solid outlet topologies are studied to analyze the particle average size and solid distribution when the withdrawal location is changed along the reactor axis.

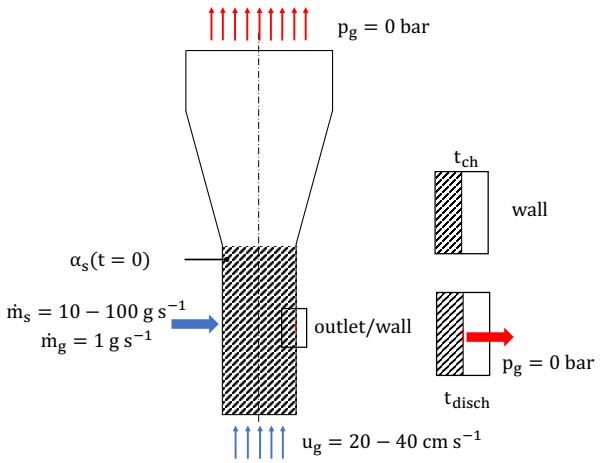

Figure 5.10: Scaled model initial and boundary conditions. The example shown refers to the outlet-middle condition shown in Fig. 5.9.

Table 5.8: Simulations boundary conditions. u_g is the gas velocity value assigned to the boundary. I is the turbulent intensity, C_μ is a turbulence model constant and L is the particle diameter. A is the inlet surface area. $L_{\theta,c}$ represents the inlet catalyst particles diameter.

Variable	Inlet	Outlet	Inlet solid	Outlet Solid	Walls
$\mathbf{u}_g$	$u_g \frac{\mathbf{n}}{\lvert\mathbf{n}\rvert}$	$\nabla \mathbf{u}_g \cdot \mathbf{n} = 0$	$u_g \frac{\mathbf{n}}{\lvert\mathbf{n}\rvert}$	$\nabla \mathbf{u}_g \cdot \mathbf{n} = 0$	no slip
$\mathbf{u}_\theta$	0	$\nabla \mathbf{u}_\theta \cdot \mathbf{n} = 0$	$u_\theta \frac{\mathbf{n}}{\lvert\mathbf{n}\rvert} \rho_\theta A$	$\nabla \mathbf{u}_\theta \cdot \mathbf{n} = 0$	$\tau = 0$
α_θ	0	$\nabla \alpha_\theta \cdot \mathbf{n} = 0$	$\frac{u_\theta}{u_g}$	$\nabla \alpha_\theta \cdot \mathbf{n} = 0$	$\nabla \alpha_\theta \cdot \mathbf{n} = 0$
p	$\nabla p \cdot \mathbf{n} = 0$	p_{atm}	$\nabla p \cdot \mathbf{n} = 0$	p_{atm}	$\nabla p \cdot \mathbf{n} = 0$
k	$\frac{3}{2}(I\lvert\mathbf{u}_g\rvert)^2$	$\nabla k \cdot \mathbf{n} = 0$	$\frac{3}{2}(I\lvert\mathbf{u}_g\rvert)^2$	$\nabla k \cdot \mathbf{n} = 0$	wall funct.
ε	$\frac{C_\mu^{0.75} k^{1.5}}{L}$	$\nabla \varepsilon \cdot \mathbf{n} = 0$	$\frac{C_\mu^{0.75} k^{1.5}}{L}$	$\nabla \varepsilon \cdot \mathbf{n} = 0$	wall funct.
L_θ	$\nabla L_\theta \cdot \mathbf{n} = 0$	$\nabla L_\theta \cdot \mathbf{n} = 0$	$L_{\theta,c}$	$\nabla L_\theta \cdot \mathbf{n} = 0$	$\nabla L_\theta \cdot \mathbf{n} = 0$

5.3 Three-Phase Compartmentalized Model

Note that the compartment-based model development has been completed under the guidance of Prof. G. Storti (ETH Zurich, now Politecnico di Milano). His major contribution was given in the model derivation.

5.3.1 Model Development

Many modeling approaches have been proposed to simulate this type of reactors, classified according to the number of phases accounted for and to the description of the reactor fluid dynamics. Among the different options, the well-assessed three-phase (two solid-rich and one pure gas) compartmentalized model originally proposed by Choy & Ray [157] and later applied by different authors [118, 155, 158] is used. Specifically, both the solid-rich phases (so-called emulsion and bubble wake) are compartmentalized as a series of continuous stirred tank reactors (CSTRs), with solid exchange between the two phases inside each compartment.
Moreover, the particle size distribution of the solid product is considered in order to predict possible segregation phenomena along the reactor axis.
Since the comparison performed in this work is focused on the fluidization behavior, we confine ourselves to non-reacting systems: therefore, the concentration profile along the reactor axis of preformed particles with given size distribution will be evaluated without including any specific polymerization kinetic and single-particle model.
Of course, these additional aspects can be easily implemented in the proposed modeling framework if needed.
The conceptual schematization of the FBR as implemented in the compartmentalized model is shown in Fig. 5.11.
The reactor is represented by a series of fully mixed compartments, each one containing two solid-rich phases, the emulsion flowing down and the bubble wakes flowing up. The pure gas phase flowing up as bubbles is indicated by the big vertical arrow in the background. Inside each compartment, solid exchange between the two phases is taking place.
The net rate of such exchange is evaluated as proposed by Kim & Choi [159], with size-dependent rate coefficients of solid entrainment based on the exponential relationship proposed by Kunii & Levenspiel [111].

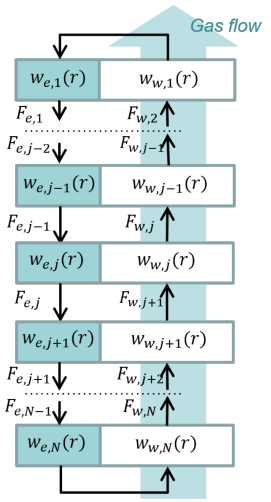

Figure 5.11: Schematic representation of the compertmentalized model. Black arrows indicate the solid flows while light blue arrows indicate the pure gas flow.

The steady-state material and population balances equations are summarizied below, according to Kim & Choi [155].

- Mass balance in emulsion phase, j-th compartment:

$$\mathrm{F_{e,j-1}} - \mathrm{F_{e,j}} = \overline{\mathrm{k}}_{\mathrm{ew},j}\mathrm{W_{e,j}} - \overline{\mathrm{k}}_{\mathrm{we},j}\mathrm{W_{w,j}}; \tag{5.60}$$

- Population balances in emulsion phase, j-th compartment:

$$\mathrm{F_{e,j-1}w_{e,j-1}(r)} - \mathrm{F_{e,j}w_{e,j}(r)} = \mathrm{k_{ew}(r)w_{e,j}(r)W_{e,j}} - \mathrm{k_{we}w_{w,j}(r)W_{w,j}}; \tag{5.61}$$

- Mass balance in wake phase, j-th compartment:

$$\mathrm{F_{w,j+1}} - \mathrm{F_{w,j}} = -\overline{\mathrm{k}}_{\mathrm{ew},j}\mathrm{W_{e,j}} + \overline{\mathrm{k}}_{\mathrm{we},j}\mathrm{W_{w,j}}; \tag{5.62}$$

- Population balances in wake phase, j-th compartment:

$$\mathrm{F_{w,j+1}w_{w,j+1}(r)} - \mathrm{F_{w,j}w_{w,j}(r)} = -\mathrm{k_{ew}(r)w_{e,j}(r)W_{e,j}} + \mathrm{k_{we}w_{w,j}(r)W_{w,j}} \tag{5.63}$$

where $\mathrm{F_{e,j}}$ and $\mathrm{F_{e,j}}$ are the solid mass flowrates of emulsion and wake leaving the j-th compartment, $\mathrm{W_{e,j}}$ and $\mathrm{W_{w,j}}$ the solid mass hold-ups of emulsion and

wake of the same compartment, and the particle size distributions in emulsion and wake on mass basis (weight fractions), $\mathrm{w}_{\mathrm{e},j}$ and $\mathrm{w}_{\mathrm{w},j}$ and are the size-dependent rate coefficients of particle entrainment (emulsion to wake) and spillage (wake to emulsion), respectively.
Note that the corresponding compartment-average rate coefficients appearing in the mass balances are readily evaluated as a function of the rate coefficients and the size distribution as:

$$\overline{\mathrm{k}}_{\mathrm{ew},j} = \int_0^\infty \mathrm{k}_{\mathrm{ew}}(\mathrm{r})\mathrm{w}_{\mathrm{e},j}(\mathrm{r})\mathrm{dr} \quad \text{and} \quad \overline{\mathrm{k}}_{\mathrm{we},j} = \int_0^\infty \mathrm{k}_{\mathrm{we}}\mathrm{w}_{\mathrm{e},j}(\mathrm{r})\mathrm{dr}. \tag{5.64}$$

Assuming no solid elutriation, the following equalities apply to any pair of flowrates in between two adjacent compartments:

$$\mathrm{F}_{\mathrm{e},j-1} = \mathrm{F}_{\mathrm{w},j} \quad \text{and} \quad \mathrm{w}_{\mathrm{e},j-1} = \mathrm{w}_{\mathrm{w},j}. \tag{5.65}$$

Plugging the last equation into Eq. 5.63, the following relationship between the solid weight fractions of the particle of a given size is obtained:

$$\mathrm{w}_{\mathrm{e},j+1} = \mathcal{C}_j(\mathrm{r})\mathrm{w}_{\mathrm{w},j}(\mathrm{r}) \tag{5.66}$$

where:

$$\mathcal{C}_j(\mathrm{r}) = \frac{\mathrm{F}_{\mathrm{e},j-1} + \mathrm{W}_{\mathrm{w},j}\mathrm{k}_{\mathrm{we}}(\mathrm{r})}{\mathrm{F}_{\mathrm{e},j} + \mathrm{W}_{\mathrm{e},j}\mathrm{k}_{\mathrm{ew}}(\mathrm{r})}. \tag{5.67}$$

Given the number of compartments N as well as solid flow-rates and hold-ups, Eq. 5.66 ($j = 1, N$) along with the second Eq. 5.65 ($j = 2, N-1$) are a system of $(2N-1)$ algebraic linear equations in the $2N$ unknowns $\mathrm{w}_{\mathrm{e},j}$ and $\mathrm{w}_{\mathrm{w},j}$. The residual degree of freedom is readily saturated by imposing the consistency with the overall amount of solid particles of that size into the entire reactor, that is:

$$\mathrm{w}_{\mathrm{tot}}(\mathrm{r}) \sum_{j=1}^{N} (\mathrm{W}_{\mathrm{e},j} + \mathrm{W}_{\mathrm{w},j}) = \sum_{j=1}^{N} (\mathrm{W}_{\mathrm{e},j}\mathrm{w}_{\mathrm{e},j}(\mathrm{r}) + \mathrm{W}_{\mathrm{w},j}\mathrm{w}_{\mathrm{w},j}(\mathrm{r})) \tag{5.68}$$

where $\mathrm{w}_{\mathrm{tot}}$ is the particle size distribution (weight fraction) of the solid particles initially charged in the reactor. The solution of the resulting set of equations requires the evaluation of all flow-rates and hold-ups availing of a form of fuid-dynamics description, as discussed in the following section.

5.3.2 Simplified Fluid-Dynamics

The description of the reactor fluid-dynamics is based upon the semi-empirical relationships reported by Kunii & Levenspiel [111] and described in the following.

Note that the polymer particles under examination can be classified as Group A to B according to Geldart [160, 161].
Given the basic properties of gas (viscosity, μ_g , and density, ρ_g) and solid phase (density, ρ_p, average particle size, d_p, and sphericity, ϕ_s) of the generic compartment, key quantities such as the minimum fluidization gas velocity, u_{mf}, the corresponding void fraction, ε_{mf}, and the terminal velocity, u_t, are evaluated through the following equations:

$$\varepsilon_{mf} = 0.586{\phi_s}^{-0.72}\left(\frac{\mu_g^2}{\rho_g \eta d_p^3}\right)^{0.029}\left(\frac{\rho_g}{\rho_p}\right)^{0.021} \tag{5.69}$$

where

$$\eta = g(\rho_p - \rho_g) \tag{5.70}$$

with g equal to the gravitational acceleration. The minimum fluidizaton velocity u_{mf} can be found by solving the following quadratic equation

$$u_{mf}^2 \frac{1.75\rho_g^2 d_p^2}{\varepsilon_{mf}^3 \phi_s \mu_g} + u_{mf}\frac{150(1-\varepsilon_{mf})\rho_g d_p}{\varepsilon_{mf}^3 \phi_s^2 \mu_g} - \frac{\eta g d_p^3}{\mu_g}. \tag{5.71}$$

The terminal velocity is given by:

$$u_t = u_t^* \left[\frac{\rho_g^2}{\mu_g(\rho_p - \rho_g)g}\right]^{-1/3} \tag{5.72}$$

where:

$$u_t^* = \left(\frac{18}{d_p^{*2}} + \frac{2.335 - 1.744\phi_s}{d_p^{*0.5}}\right)^{-1}; \quad \text{and} \quad d_p^* = d_p\left[\frac{\rho_p(\rho_p - \rho_g)g}{\mu_g^2}\right]^{1/3}. \tag{5.73}$$

The bubble size a function of the reactor height is estimated thorugh:

$$d_b(z) = d_{b,m} - (d_{b,m} - d_{b,0})\exp\left(-\frac{0.3z}{d_t}\right). \tag{5.74}$$

The average bubble diameter and the initial bubble diameter can be estimated as:

$$d_{b,,m} = 0.652\left[\frac{\pi}{4}d_t^2\,(u_0 - u_{mf})\right]^{0.4}; \quad \text{and} \quad d_{b,0} = \frac{2.78}{g}\,(u_0 - u_{mf})^2. \tag{5.75}$$

The bubble velocity, which depends on the axial position as well, is calculated as:

$$u_b(z) = u_0 - u_{mf} + u_{br} \tag{5.76}$$

where:

$$u_{br} = 0.711\,(g d_b)^{1/2}\,. \tag{5.77}$$

The void fractions specific of each phase, that is the bubble fraction in the bed δ and the wake fraction inside a bubble α are computed through Eq. 5.78 and 5.79:

$$\delta = \frac{u_0 - u_{mf}}{v_b - u_{mf}\,(\alpha + 1)}, \tag{5.78}$$

$$\alpha = 0.4 \quad \text{or see comment iv.} \tag{5.79}$$

Eventually, the emulsion hold-up can be calculated as:

$$W_e(z) = (1 - \alpha\delta - \delta)\,(1 - \varepsilon_{mf})\,\rho_p \frac{\pi}{4} d_t^2 \Delta z \tag{5.80}$$

while the wake one through:

$$W_w(z) = \alpha\delta\,(1 - \varepsilon_{mf})\,\rho_p \frac{\pi}{4} d_t^2 \Delta z. \tag{5.81}$$

The solid flow-rate that leaves a compartment can be computed as:

$$F_e(z) = u_b \alpha\delta\,(1 - \varepsilon_{mf})\,\rho_p \frac{\pi}{4} d_t^2. \tag{5.82}$$

It is worth to notice that, according to Eq. 5.65, the solid flow-rate entering a given compartment as wake is equal.

The chosen relationships can be used under some hypothesis.

i. Spherical particles have been considered, *i.e.*, $\phi_s = 1$.

ii. Given the average particle size, the superficial gas velocity u_0 will be set to values larger than u_{mf}, to ensure fluidization, and smaller than u_t to prevent elutriation.

iii. The average bubble size is growing while travelling to the reactor top according to the exponential law described by Eq. 5.74. Since bubble breakage is expected above given size, the maximum value $d_{b,m}$ cannot overcome the limiting value suggested by Grace [162, 163] ($= 2u_g^2/g$). Accordingly, the bubble size predicted by Eq. 5.74 is set equal to such threshold value as soon as becoming larger.

iv. The value of the wake fraction inside the bubble, α, is usually constant and equal to 0.4. For larger accuracy, data reported as a function of the average particle size in Figure 8 of Chapter 5 of Kunii & Levenspiel [111] have been used after interpolation.

v. Since most properties are function of the axial position, z, inside the reactor, their evaluations have been carried out for each compartment considering its mid-point axial position, assuming such value representative of the entire compartment, while the Δz in Eq. 5.80 and Eq. 5.81 is the compartment height.

5.3.3 Solution Algorithm

Given the reactor geometry (height and diameter), the size distribution of the solid particles charged to the reactor, $w_{tot}(r)$, and the inlet gas velocity, u_0, the numerical solution of the compartmentalized model is carried out iteratively as follows:

i. Given a first guess average particle size (usually estimated from the particle size distribution $w_{tot}(r)$), equations reported in the simplified fluid-dynamics section (Sub-section 5.3.2) are used to evaluate the axial profile of bubble size.

ii. The compartment size is then estimated in order to include at least one entire bubble, that is, the compartment dimension is growing from bottom to top along the reactor axis.

iii. Solid flow-rates and hold-ups are evaluated through the simplified fluid-dynamics relationships for each compartment.

iv. Once evaluated $\overline{k}_{we,j}$ for each compartment through the first Eq. 5.64, the corresponding overall rate coefficient of particle spillage is calculated as:

$$\overline{k}_{we,j} = \frac{\overline{k}_{ew,j} W_{e,j} - F_{e,j-1} + F_{e,j}}{W_{w,j}} \tag{5.83}$$

from which the value of $\mathcal{C}_j$ is readily obtained.

v. Then, the particle size distributions in emulsion and wake for each compartment are calculated from Eq. 5.65, Eq. 5.66, Eq. 5.67 and Eq. 5.68 at each desired value of the particle size, that is ranging from the minimum to the maximum size according to the injected size distribution.

vi. Given the distributions, the entire procedure is repeated from step ii. until convergence criteria are met. Such convergence has been conveniently quantified comparing the $\overline{k}_{we,j}$ values predicted by two following iterations.

5.4 Results and Discussion

5.4.1 Part 1: Fluidization Study - CFD/Two-Phase Compartmentalized Model Comparison

In order to compare the two modeling approaches, CFD and SCM, the steady-state conditions established inside a fluidized bed reactor at constant gas flowrate and holdup of a solid phase with given particle size distribution are examined. As anticipated, the focus is on bed expansion only, assuming no solid elutriation, no reaction and no solid injection or withdrawal in addition to the initially charged amount.
The same reactor geometry used in the previous section to validate the CFD numerical setup is selected for the sake of convenience.
Note that a simpler cylindrical geometry is considered in the SCM case: this means that only the bottom part of the reactor is simulated, with height (and therefore number of compartments) large enough to contain the amount of particles initially charged to the reactor in the CFD case. Since the solid entrainment is minimal at the selected conditions (*i.e.*, a minor amount of solid is filling the conical region and most remains in the lower-cylindrical portion where the most interesting fluidization phenomena occur; see contours of Fig. 5.6), the comparison remains meaningful despite such difference in geometry.

The parameter values and operating conditions of all examined cases are summarized in Table 5.9.

Table 5.9: Parameter values and operating conditions used in all examined cases.

ρ_g	ρ_s	W (t = 0 s)	d_p	u_g
[kg m^{-3}]	[kg m^{-3}]	[kg]	[μm]	[m s^{-1}]
20	900	790	100-700	10-60

According to Geldart classification [160, 161], the solid phase is composed of particles A-B type, that is representative of polyethylene produced in gas phase by catalytic polymerization. Note that both the cases of particles with homogeneous (monodisperse) and heterogeneous size distribution (polydisperse) are considered, to better elucidate the interplay between particle size distribution and solid segregation along the reactor axis.

About the selected range of gas flows, it has been restricted to realistic values large enough to establish fluidization conditions as well as small enough to prevent solid loss by elutriation. More specifically, with reference to the fluidization regimes according to Kunii & Levenspiel [111] (Chapter 3, Figure 16b), the range of examined operating conditions can be represented in terms of the two dimensionless variables $d_p^* = Ar^{1/3}$ and $u^* = Re_p/Ar^{1/3}$, where Ar and Re_p are Archimedes and particle Reynolds number, respectively. This is shown in Fig. 5.12, where the explored region is indicated by the orange square (dashed edges), restricted to the sub-region with continuous edges to remain inside the so-called "bubbling" regime, which is the region of applicability of the simplified fluid dynamic relationships.

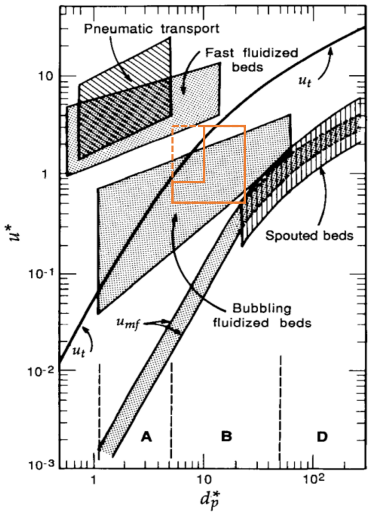

Figure 5.12: Particle fluidization regimes according to Kunii & Levenspiel [111]. The region marked in orange defines the regime explored with simulations.

The simulation results for all cases are presented below, first considering the monodisperse cases and then those involving solid phases with particle size distribution with different variance. The comparisons are carried out in terms of axial profiles of solid volume fraction (α_θ) and average particle size ($\overline{d}_p$). In the SCM case, compartment-average particle sizes are considered (number average of the weight size distribution of the compartment); in the CFD case, such average quantities have been evaluated according to Eq. 5.25 and Eq. 5.26 to obtain time and space average values inside the reactor.

Monodisperse Cases

Three different cases have been considered, with particle size equal to 223, 446 and 669 μm, respectively, and gas velocity ranging from 10 to 61 cm s^{-1} depending upon the specific particle size under examination (for example, gas velocity larger than 20 cm s^{-1} cannot be used with the smallest particle size because there would be too much solid entrainment). In all cases, the entire cylindrical region (2 m high) was initially filled with the solid particles at solid volume fraction typical of a fixed bed, $\alpha_s = 0.63$ (Appendix A.4). The results of the two models are compared in Fig. 5.13 in terms of radial average volume fraction of solid phase at different position along the reactor axis inside the cylindrical portion starting from 0.5 m distance from the gas distributor. Positions closer to the first part of the reactor were not considered because too close to the distributor: since completely different representations of the gas inlet region have been implemented in the two models, the resulting differences in the predicted fluid flow field prevent a fair comparison close to the reactor bottom.

Table 5.10 reports the average and phase-specific diameters as well as initial conditions for packed bed height and solid volume fraction considered for all monodisperse cases. Average (d) and phase-specific diameters (d_θ) are equal since only one solid phase is transported in monodisperse simulations.

Table 5.10: Parameter and solid initialization conditions for monodisperse cases. d and d_θ, indicating the particle diameter and the θ-th particle class diameter respectively, have the same value because the particle population is monodisperse and one solid phase only is enough to describe the whole distribution. h stands for indicating the initial bed height at initialization while α_θ is the associated solid volume fraction.

Case	d	d_θ	h (α_θ @ t = 0)	α_θ @ t = 0
	[μm]	[μm]	[m]	[−]
01-m	223	223	2	0.63
03-m	446	446	2	0.63
05-m	669	669	2	0.63

Results indicate very good agreement between SCM and CFD predictions, especially considering the huge difference in computational effort between the two cases. As expected, the bed expansion increases at increasing gas velocity while the solid volume fraction increases in all cases at increasing height inside the reactor. In quantitative terms, the values of average discrepancy between the two

predictions range from 7 to 19%, with an average value of approximately 10% and maximum error obtained for small particles at very low fluidization velocities in the upper part of the reactor (d = 223 μm, ug = 10 cm s^{-1}, h = 2 m). This is due to the fact that such small velocities are just sufficient to fluidize the bed but particles are not expanded and the solid remains packed.

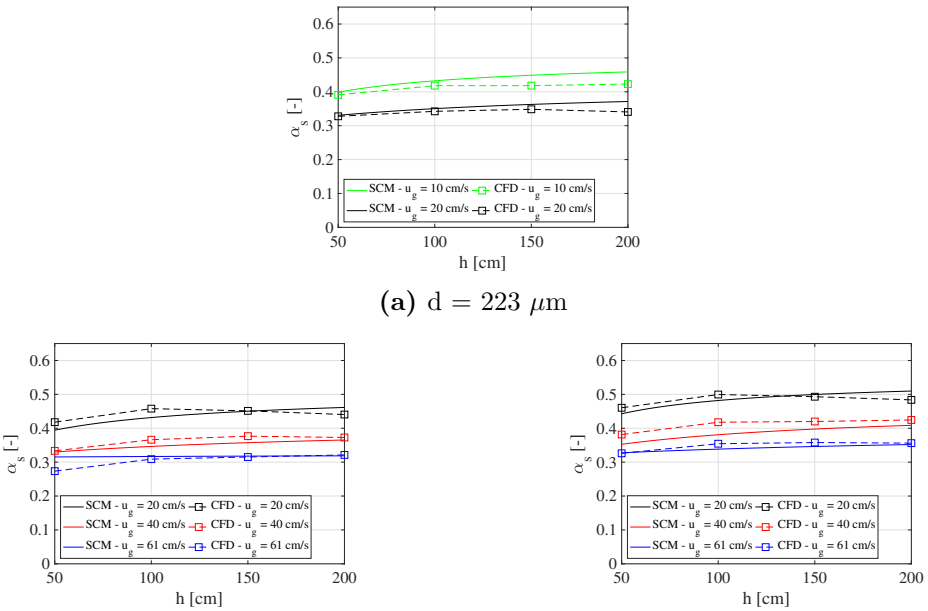

(a) d = 223 μm

(b) d = 446 μm

(c) d = 669 μm

Figure 5.13: Comparison between the time- and space-averaged cell-center data (CFD) and compartment data (SFD) of solid volume fraction at different reactor position for different particle diameters.

Polydisperse Cases

Another set of comparative simulations has been carried out considering solid particles with different size distributions. Specifically, Gamma distribution was assumed in three cases, considering two values of average particle size (d_{ave}) and distribution variance (σ):

$$f(d) = \frac{\beta^{\kappa}}{\Gamma(\kappa)} d^{\kappa-1} e^{-\beta d} \tag{5.84}$$

where $\Gamma(\kappa)$ is the Gamma function and the parameters characterizing the distribution are:

$$\kappa = \frac{{d_{ave}}^2}{\sigma}; \tag{5.85}$$

$$\beta = \frac{d_{ave}}{\sigma}. \tag{5.86}$$

As representative of solid phases with a very broad distribution, a fourth case was also examined corresponding to a mixture of three monodisperse particles each one with the same mass fraction.

While size distributions were readily accounted for in SCM (as w_{tot} in Eq. 5.68), in the CFD case the method presented by Marchisio & Fox [49, 156] was used to calculate a three node quadrature (with nodes indicated with indexes QP0, QP1 and QP2) with DQMOM approach.
The first six moments of the distributions are used to retrieve quadrature quantities, *i.e.*, weights (α_θ) and abscissas ($\alpha_\theta d_\theta$) through the Wheeler moment inversion algorithm [35] and such diameters are assigned to the different non-reactive solid phases (each one advected with its own velocity) to account for polydispersity.

The specific numerical values of all these parameters are summarized in Table 5.11. To better understand the different size distributions of the solid phase initially charged to the reactor in the first three cases, they are shown in Fig.5.14.

Table 5.11: Parameters and quadrature approximation values of Gamma distribution tested (01-p to 03-p) and heterogeneous three-modal distribution function (04-p). d_{ave} indicates the average diameter of the distribution, σ is the distribution variance, d_θ stands for the diameter associated to the θ-th solid phase and α_θ is the associated solid volume fraction.

Case	d_{ave} [μm]	σ [μm]	d_θ [μm]	α_θ @ t = 0 [–]
01-p	446	100	QP0: 559.40 QP1: 408.51 QP2: 262.81	QP0: 0.1654 QP1: 0.4100 QP2: 0.0546
02-p	669	100	QP0: 830.09 QP1: 644.05 QP2: 543.50	QP0: 0.1437 QP1: 0.4157 QP2: 0.0706
03-p	446	60	QP0: 543.50 QP1: 432.53 QP2: 337.75	QP0: 0.1396 QP1: 0.4165 QP2: 0.0739
04-p	500	-	QP0: 800.00 QP1: 500.00 QP2: 200.00	QP0: 0.2100 QP1: 0.2100 QP2: 0.2100

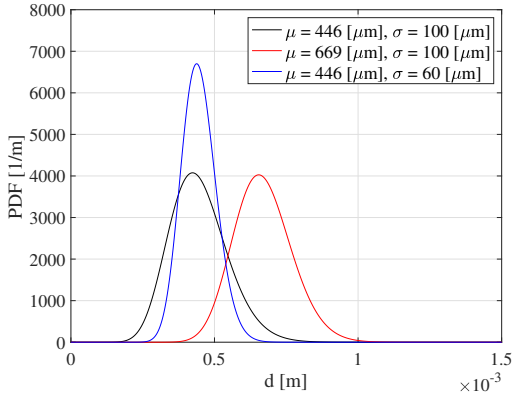

Figure 5.14: Graphic representation of the Gamma distributions tested. μ corresponds to the average diameter d_{ave}.

The comparisons between the predictions of the two approaches, SCM and CFD, for the first three cases, 01-p to 03-p, are shown in Fig. 5.15 and Fig. 5.16. In terms of solid volume fraction (Fig. 5.15), the SCM predicted values are typically larger than the CFD ones, with average error below 15% but maximum errors up to 29% at the largest gas velocity. The agreement is improving at increasing average particle size, where the error remain below 10% in all cases. Therefore, the discrepancy could be imputed to the tail of the smallest particles in the distributions: such particles are Geldart type A and the applicability of the simplified fluid dynamic equations could be questionable, especially at high gas velocity. The comparison is much better in terms of average particle sizes (Fig. 5.16): not only the discrepancy is below 1% in all cases but the (limited) solid segregation is invariably well predicted, with the expected accumulation of larger particles at the reactor bottom. Such segregation is small in all cases, *i.e.*, the gas velocity is large enough to ensure very good mixing in all cases, thus pushing the reactor towards well mixed conditions.

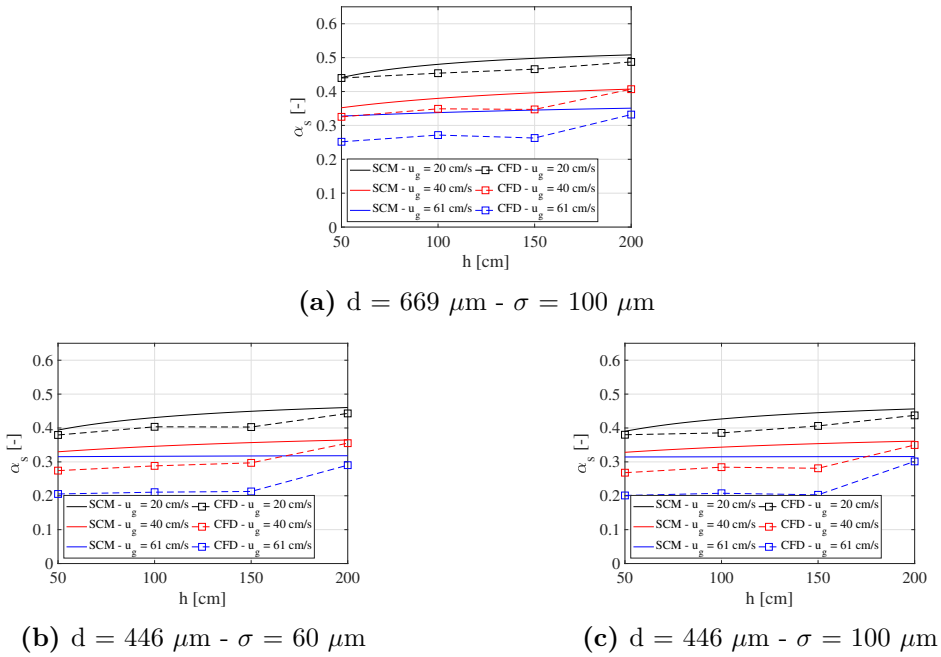

(a) d = 669 μm - σ = 100 μm

(b) d = 446 μm - σ = 60 μm

(c) d = 446 μm - σ = 100 μm

Figure 5.15: Comparison between the time- and space-averaged cell-center data (CFD) and compartment data (SFD) of solid volume fraction at different reactor position for different distributions.

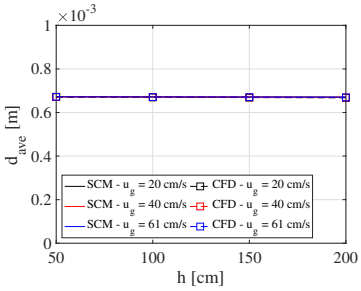

(a) d = 669 μm - σ = 100 μm

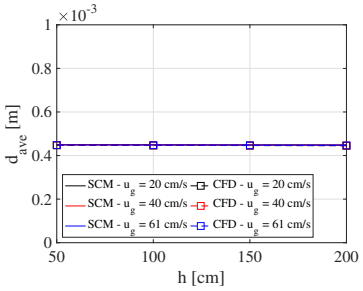

(b) d = 446 μm - σ = 60 μm

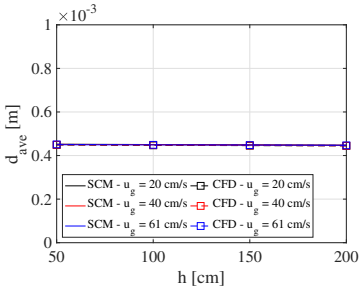

(c) d = 446 μm - σ = 100 μm

Figure 5.16: Comparison between the time- and space-averaged cell-center data (CFD) and compartment data (SFD) of particles average diameter at different reactor position for different distributions.

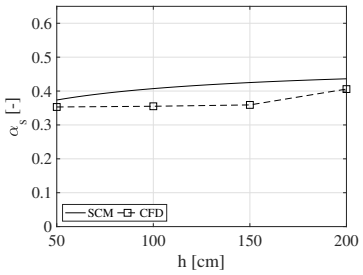

(a) solid volume fraction

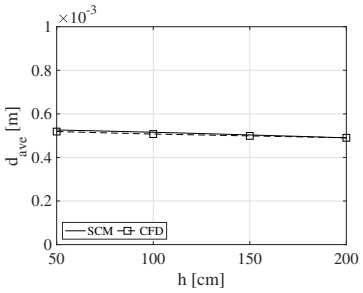

(b) average diameter

Figure 5.17: Comparison between the time- and space-averaged cell-center data (CFD) and compartment data (SFD) of solid volume fraction (a) and average particle diameter at different reactor position for a distribution built with d_0 = 800 μm/α_0 = 0.21 – d_1 = 500 μm/α_1 = 0.21 – d_2 = 200 μm/α_2 = 0.21.

In the most heterogeneous case of trimodal particle size distribution (04-p in Table 5.11), the same kind of behavior is found, as described by Fig. 5.17, with a limited overestimation of the solid volume fraction by the SCM (average error 13%) and of the variation of particle size with the reactor height (average error of approximately 1%).

Table 5.10 summarizes the average error between the predictions of average diameter by SCM and CFD, using the latter ones as reference. The differences are always less than 2 %, thus confirming a very good agreement.
The values of all the predictions of both models for case o4-p are specified in tabular form in Table 5.12. Overall, the agreement between the fully detailed CFD model and the oversimplified compartmentalized model for the average size is good, with an average error of about 1% and a maximum error measured on solid volume fraction of about 15-20%.
Even though the description of the complex gas-solid flow field established in this type of reactors based on the semi-empirical relationships available in the literature should be checked for the specific solid and operating conditions under examination, it appears appropriate to study reactive systems at a modest computational cost.
The combination between detailed CFD simulations and any model based on such simplified descriptions implemented here is a feasible approach in this direction.

Table 5.12: Time- and space-averaged CFD and SCM predictions of average particle diameter at different reactor height for case 04-p in Table 5.11 and u_g = 20 cm s^{-1}. Errors (Err) are evaluated using CFD values as reference.

h [cm]	CFD [μm]	SCM [μm]	|Err| [%]
50	519	526	1.35
100	507	516	1.78
150	499	503	0.78
200	490	490	0.00

5.4.2 Part 2: CFD Modelling of Continuous Polyolefin Production Process

The DQMOM and particle growth model CFD implementation are verified by solving a simplified case without the fluid dynamics field. Average particle size and solid hold-up predictions are then presented for different solid feed rates and outlet topologies.

Verification of the Particle-Growth Model Implementation

The implementation via user-defined function (UDF) of the DQMOM approach and the particle growth model described by Eq. 5.56 have been validated against the analytical solution described by Eq. 5.87 (see Appendix B for the detailed derivation):

$$\mathrm{d}_{\theta}^{\mathrm{an}} = 2\mathrm{r}_{\mathrm{c},\theta}\left(\frac{\rho_{\mathrm{c}}\cdot \mathrm{K_p}\cdot \mathrm{M}\cdot \mathrm{C}^{*}\cdot \mathrm{PM_{mon}}}{(1-\zeta)\cdot\rho_{\mathrm{s}}}\mathrm{t}+1\right). \tag{5.87}$$

The test simulation has been set-up by deactivating flow and turbulence equations (no flow field) and solving only continuity and transport equations for phases diameters in a computational domain with no solid feed and withdrawal.
The analysis is carried out by comparing the phases diameter averaged in the whole domain (Fig. 5.18a) and the cell-based averaged diameter contours (Fig. 5.18b).
The volume-average cell-based phase diameter is computed as:

$$\mathrm{d}_{\theta,\mathrm{ave}}^{\mathrm{num}} = \frac{\sum_{i=1}^{n}\mathrm{V}_{\mathrm{c}}^{i}\alpha_{\theta}^{i}\mathrm{d}_{\theta}^{i}}{\sum_{i=1}^{n}\mathrm{V}_{\mathrm{c}}^{i}\alpha_{\theta}^{i}} = \frac{\sum_{i=1}^{n}\mathrm{V}_{\mathrm{c}}^{i}\alpha_{\theta}^{i}\mathrm{d}_{\theta}^{i}}{\sum_{i=1}^{n}\mathrm{V}_{\mathrm{c}}^{i}\alpha_{\theta}^{i}} \tag{5.88}$$

where n is the number of cells in the computational domain, i is the cell index and $\mathrm{V_c^i}$ is the i-th cell volume. α_{θ}^{i} is the θ-th solid phase volume fraction of the i-th cell.
The average diameter plotted in the contours is defined accordingly to Eq. 5.27 and, therefore:

$$\mathrm{d}_{43} = \frac{\mathrm{m}_4}{\mathrm{m}_3} = \mathrm{d}_{\mathrm{ave}}. \tag{5.89}$$

with moments defined as specified by Eq. 5.28.
Note that, in this text, the average diameter is based upon the usage of moments of order 4 and 3 and, therefore, the equality $\mathrm{d}_{43} = \mathrm{d}_{\mathrm{ave}}$ holds.

The cell-based average diameter computed from moments of order 4 and 3 assumes the form:

$$\mathrm{d}_{43}^{i} = \frac{\sum_{\theta=1}^{N} w_\theta \mathrm{d}_\theta^4|^i}{\sum_{\theta=1}^{N} w_\theta \mathrm{d}_\theta^3|^i} \tag{5.90}$$

where N is the number of solid phases and w_θ is the number of particles per unit volume of phase θ contained in the i-th cell:

$$\omega_\theta^i = \frac{\alpha_\theta^i}{V_{\mathrm{p},\theta}^i}. \tag{5.91}$$

Fig. 5.18 shows the temporal evolution of the average phases diameter in the whole domain **(a)** and the contours of the d_{43} diameter at time t = 0 and t = 10 s **(b)**.

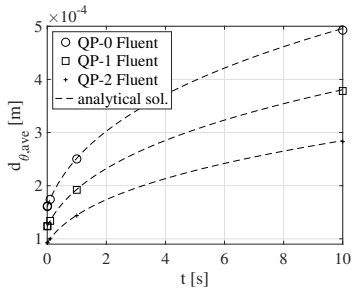

(a) volume-average phases diameter (according to Eq. 5.88) – numerical vs. analytical

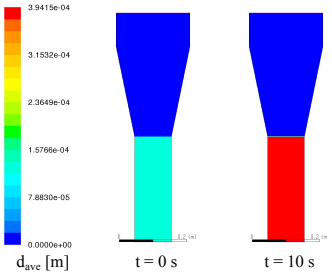

(b) average diameter (according to Eq. 5.91) contour as function of time

Figure 5.18: Validation of the Kim & Choi [155] model implementation in Fluent against analytical solution (Eq. 5.87).

A very good agreement between the analytical solution obtained through Eq. 5.87 and the numerical one computed with Fluent, meaning that the model has been implemented correctly.

Particle Size and Hold-up Predictions

Simple material balances are used to estimate the final particle size and set the initial diameter of the pre-polymerized solid arranged as packed bed inside the reactor. The simplified estimation is intended to provide particle information and speed-up the transient start-up phase of the process. Material balance predictions are summarizied in Table 5.5. Note that the total solid volume fraction sums to 0.4. The quantity of particles at the beginning of the simulation is chosen to be two third of the packing limit to replicate the average solid distribution calculated in the fluidization study (ensuring no elutriation), in which the initial bed expanded to occupy the first part of the conic region desiged for solid disengagment reasons. Simulations are carried out as reported in Table 5.14, using the solid phases diameters and volume fractions listed in Table 5.13. Two different solid feeds have been investigated to assess the influence of fresh catalyst mass-flow rate on the reactor hold-up and the related final particle size. The initial diameter of the solid phases is guessed through material balances, as described above. The FBR has been ran fluidizing the particles for the first 10 s of operation, with no solid feed/withdrawal, in order to initialize the multiphase flow-field. At time t = 10 s, the polymerization reaction is started and a constant solid feed is set (see Table 5.5). At the same time, the particles discharge has been allowed by opening one of the outlets located on the right wall of Fig. 5.9. The inlet gas velocity is adjusted to sustain the reaction without taking the solids out of the system from the gas outlet. The reaction rate is larger at beginning and therefore the gas conversion is high at the initial stages, decreasing gradually with time. The gas conversion is up to 50% between 10 and 20 s of physical time. When the reactor starts emptying itself, the gas feed is decreased to compensate the reduction in gas consumption and the ethylene conversion is kept between 10% and 20 %. Lastly, from 30 s on, the system is operated in quasi-steady state regime with constant hold-up and gas consumption of about 2-5%, always below 10%.
Simple material balance estimations predict a remarkably smaller particle size at the end of the process if the catalyst feed is increased. If the solid mass-flow rate is increased of 10 times, the predicted final particle diameter is reduced of approximately 30%. Fig. 5.19 and Fig. 5.20 show the outlet particle size, computed according to Eq. 5.89, and the outlet particle size compared to the solid hold-up inside the reactor for the two feed-rate conditions tested and the three different solid outlet topologies represented in Fig. 5.9. It is shown that a simulated physical time of about 3 times the estimated particle residence time is sufficient to describe the quasi-steady state operation of the reactor. This supports the decision of analyzing the first 100 s of simulation. Note that, in every analyzed simulation, the temporal representation of the process starts after 10 s of physical time, that is after the initial non-reactive fluidization carried out with no solid feed/withdrawal.

Table 5.13: Parameters and quadrature approximation values of Gamma distribution tested for the fresh catalyst (feed) and initial packed bed (05/06-p). d_{ave} indicates the average diameter of the distribution, σ is the distribution variance, d_θ stands for the diameter associated to the θ-th solid phase and α_θ is the associated solid volume fraction. Note that the total solid volume fraction sums to 0.4.

Case	d_{ave} [μm]	σ [μm]	d_θ [μm]	α_θ @ t = 0 [−]
catalyst			QP0: 32.80	QP0: 0.1004
(feed)	25.00	5	QP1: 23.33	QP1: 0.2617
			QP2: 15.87	QP2: 0.0379
			QP0: 97.34	QP0: 0.1010
05-p	73.98	15	QP1: 68.90	QP1: 0.2610
			QP2: 46.58	QP2: 0.0375
			QP0: 140.05	QP0: 0.0975
06-p	108.52	20	QP1: 102.36	QP1: 0.2625
			QP2: 72.09	QP2: 0.0400

Table 5.14: Simulation procedure adopted for reactive cases. Step 1 summarizes information at initalization whose particle data (volume fractions and diameter) can be gathered in Table 5.13. t is time, solid in/out is intendend to explain if the solid feed/withdrawal is allowed or not, u_g is the gas velocity at the gas feed and χ is the single-passage gas conversion. Lastly, operation mode describes how the simulation is ran in any phase.

Step	t [s]	solid in/out	u_g [cm s^{-1}]	χ [%]	operation mode
1	0	×	-	-	initialization
2	0 → 10	×	20	0	fluidization
3	10 → 20	✓	40	20-50	reaction
4	20 → 30	✓	30	10-20	reaction
5	30 → 100	✓	30	2-10	reaction

Fig. 5.19 highlights that the particle average diameter at the outlet is constant shortly after the reaction starting phase. Few seconds after the initial start-up, usually 1 rt, the average diameter of the discharged polymer stabilizes on a value really close to the prediction given by analytical solution of the simplified material balances. This is verified especially when the catalyst is fed with the largest mass-flow rate.

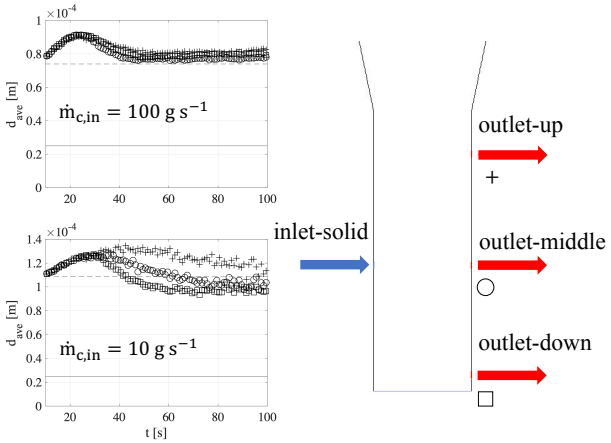

Figure 5.19: Particle average diameter at outlet as function of time when $\dot{m}_{c,in} = 100$ g s^{-1} (top plot) and $\dot{m}_{c,in} = 10$ g s^{-1} (bottom plot) for three different outlet positions. Solid lines indicate the catalyst particle feed diameter while dashed lines indicate the withdrawn particle average diameter.

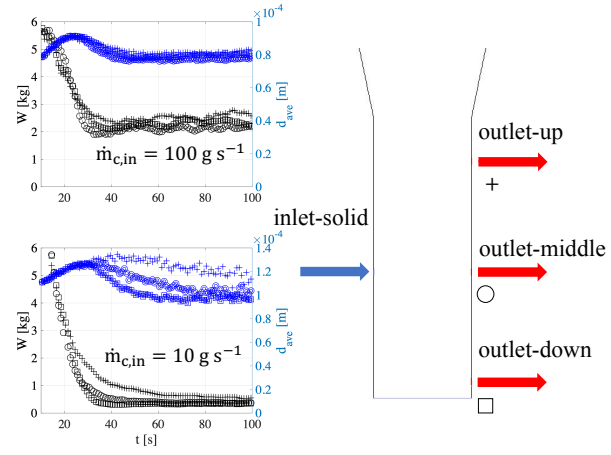

Figure 5.20: Particle average diameter at outlet and solid hold-up as function of time when $\dot{m}_{c,in} = 100$ g s^{-1} (top plot) and $\dot{m}_{c,in} = 10$ g s^{-1} (bottom plot) for three different outlet positions.

Fig. 5.19 also shows that an increase in the catalyst feed rate has the effect of homogeneizing the oulet particle size, regardless of the solid withdrawal position. A smaller feed-rate causes much larger variations and an effect on particle size is visible. When particles are withdrawn from outlet-up geometry, the particle size is larger because the particle drainage is less effective and bigger solid particles segregate in the cylindrical zone.
Fig. 5.20, by comparing average size with hold-up in the reactor, highlights that the particle diameter at the outlet is homogeinezed by the solid feed and hold-up: the higher is the solid feed-rate, the higher is the hold-up and the more uniform is the average particle size along the reactor. With $\dot{m}_{c,in} = 100\ g\,s^{-1}$, indeed, the solid mass in the reactor is more than 4 times larger than in the case with $\dot{m}_{c,in} = 10\ g\,s^{-1}$ and the curves representing the average particle size at the outlet are really close one to the other.
In all examined cases, the stationary hold-up is by far smaller than one expected for this kind of systems in which a steady-state operation mode is reached when the quantity of particles inside the reactor is comparable to the quantities set at initialization, *i.e.,* those observed in pure fludization cases.
This major discrepancy could be imputed to the 2D schematization, which does not allow for a realistic description of the reactor volume, especially in terms of feed/withdrawal area with respect to the whole system. Moreover, the 2D computational domain constrains the flow to a pure two-dimensional description, eliminating the tridimensional velocity components that move and mix the multiphase mixture far from the outlet. The adopted geometric representation forces the flow towards the outlet, withdrawing the solid and reducing the hold-up.
Despite such major issue, the agreement between the estimated and simulated average particle size is surprisingly good, regardless of the solid mass in the reactor because the average residence time computed through material balances is well replicated by CFD simulations.
Fig. 5.21 shows the averaged (dt = 1 s) residence time, rt, for the two catalyst feed conditions and the three outlet topologies tested.
Simplified material balances are based upon the constant and considable hold-up assumption. This condition is not verified in CFD predictions and, therefore, the numerical evaluation of the residence time, rt^{num}, is modified to include the reactor hold-up instead of the reactor volume:

$$rt^{num} = \frac{W}{\sum_{\theta=1}^{N} \dot{m}_{\theta,out}}\Big|_{\bar{t}} = \frac{W}{\dot{m}_{s,out}}\Big|_{\bar{t}}, \tag{5.92}$$

where W is the reactor hold-up given by CFD at any simulation instant and $\dot{m}_{s,out} = \sum_{\theta=1}^{N} \dot{m}_{\theta,out}$ is the calculated total solid discharged through the outlet. Note that the total solid is computed by summing the contributions of each solid phase and its definition is coherent with the rt estimation of Eq. 5.45.

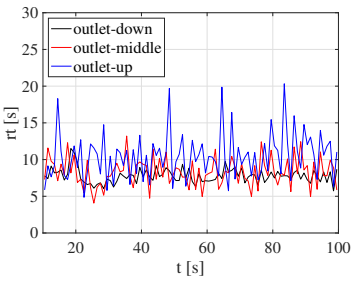

(a) $\dot{m}_{c,in} = 100\ g\,s^{-1}$, $rt^{est} = 10.3\,s$

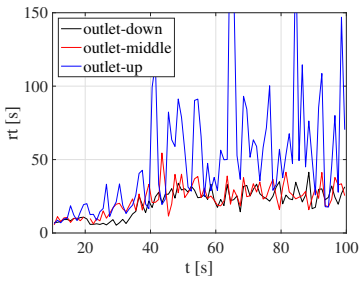

(b) $\dot{m}_{c,in} = 10\ g\,s^{-1}$, $rt^{est} = 32.6\,s$

Figure 5.21: Particle residence time calculated from CFD for the two solid feed conditions and three outlet considered topologies.

Plot 5.21a highlights that the particles have a comparable residence time, without any remarkable difference induced by the oulet location. On the other hand, plot 5.21a underlines how the 10 $g\,s^{-1}$ solid feed condition requires a longer time to stabilize the rt, causing larger fluctuations especially for the outlet-up geometry. These oscillations are also found in the less stable diameter shown in Fig. 5.19 and Fig. 5.20. The agreement is worse because particles cannot reach the outlet easily, due to larger inertia and lower hold-up.

Contours of Fig. 5.22 show the particle diameter and solid distribution inside the reactor for the three outlet locations. The figure refers to the $\dot{m}_{c,in} = 100\ g\,s^{-1}$ and images are taken at the end of the process, for t = 100 s. It is shown that the geometry with the top outlet condition generates larger particles, that tend to remain in the reactor, while the other two topologies provide comparable results. The solid is distributed uniformly in each reactor, except for a large gas bubble formed in the bottom part of the geometry.
The multiphase flow is always well mixed, confirming the predictions obtained for the pure fluidization cases.
Fig. 5.23 analyzes the particle average size and solid distribution for the $\dot{m}_{c,in} = 100\ g\,s^{-1}$ condition applied to the outlet-up reactor. Images are taken at different physical times to study the evolution of the studied properties.
The reactor operation can be divided into an initial, relative short start-up phase, called reaction transient, and a longer quasi-steady state phase that lasts for about 50-60 s.
The initial stage is characterized by high mixing and a temporary increase in particle size due to the rapid reaction rate experienced at the beginning. This behaviour is washed after few seconds and the solid distribution assumes a quasi-steady state distribution that is conserved in the whole remaining simulation time.

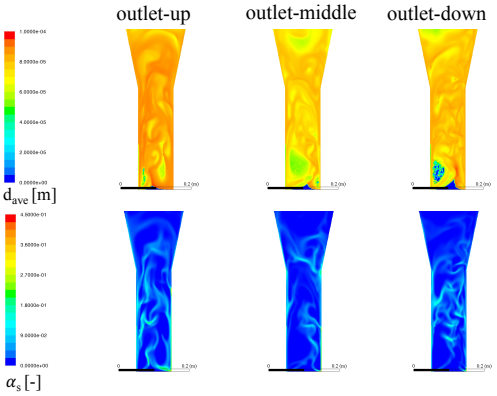

Figure 5.22: Particle average diameter and volume fraction contours for the three tested outlet conditions when $\dot{m}_{c,in} = 100\ g\,s^{-1}$ @ $t = 100$ s. Detail of the reactor cylindrical and disengagement zones.

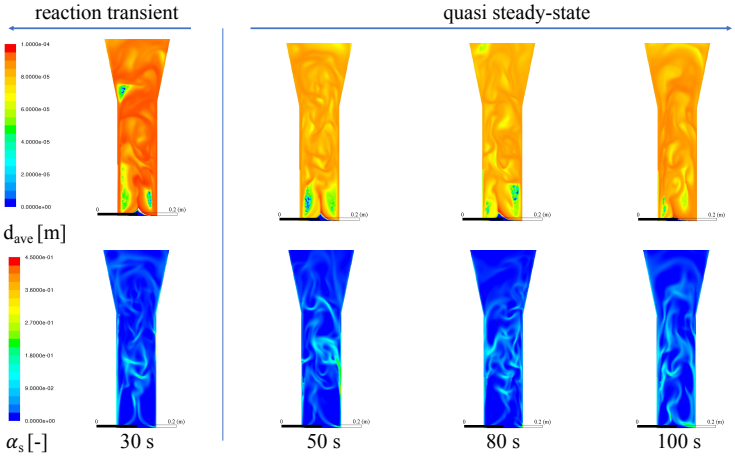

Figure 5.23: Particle average diameter and volume fraction contours for the outlet-up withdrawal topology when $\dot{m}_{c,in} = 100\ g\,s^{-1}$. Detail of the reactor cylindrical and disengagement zones.

The analysis highlights that it is possible to obtain a reasonable estimation of the particle size while the solid distribution and hold-up is completely underestimated, most probably because of the 2D geometry schematization.

5.4.3 Concluding Remarks

Focusing on the fluidization behavior of non-reactive Geldart-type A-B particles in steady-state FBRs, a model comparison has been carried out. Namely, the predictions of a 2D multifluid CFD model and of a 1D compartmentalized model with simplified fluid dynamics description are compared in terms of steady-state solid distribution inside the reactor operated in batch and without reaction (pure fluidization). The multiphase CFD model set-up has been firstly validated against relevant literature data. A proper analysis has been carried out to identify the best numerical setup and suitable initial conditions.
Monodisperse and polydisperse populations of solid particles have been studied at different gas velocity to assess the prediction capabilities of the simplified approach. The results show that the semiempirical fluid dynamics description typically used in SCM is adequate to properly describe the fluidization behavior of solid monodisperse particles in terms of solid volume fraction distribution, with errors smaller than 20% in all cases. When considering broad size distributions, particle segregation is very well predicted in terms of average volume fraction, with discrepancy between the two models between 15 and 30%.
The agreement is even better in terms of average diameters along the reactor axis (mean error below 1%), also in the case of very broad size distributions.
Overall, these results support the use of compartmentalized models to predict the fluidization behavior of non-reactive, polydisperse particles in FBRs at conditions typical of polyolefins production and with computational effort negligible with respect to CFD simulations.
In addition, a strategy for studying the continuous polymerization process in fluidized bed reactors with solid feed and withdrawal through Euler-Euler CFD simulations has been studied. The 2D reactor previously studied has been scaled-down to reduce the particle residence time and to build a computationally-affordable model. An over-simplified particle growth model has been implemented through the DQMOM approach and validated against its analytical solution. Simple material balances are used to guess the average particle size at the end of the polymerization and initialize a packed bed of pre-polymerized solid to speed-up the start-up transient phase. Different catalyst inlet mass-flow rates and polymer outlet topologies have been studied to understand how the reactor hold-up and the polymer discharge are affected. It is shown that CFD provides comparable predictions to the material balance estimations in terms of average size of the withdrawn particles while the hold-up is by far underestimated for any condition tested. It is found that solid outlet position does not affect the final predictions if a large quantity of catalyst is fed. A larger difference in average size predictions is found with the small feed-rate condition when different particles outlet positions are tested, due to the lower quantity of solid that remains inside the reactor. Results show

that the flow-field established within the 2D domain does not allow the correct prediction of the mass hold-up because particles are driven towards the outlet by the in-plane velocity components, due to the lack of third-dimension mixing given by the geometry schematization chosen.

Chapter 6

Conclusions

6.1 Summary and Major Outcomes

This dissertation aimed at investigating the fluid-dynamics of gas-solid flows for two particular applications: the spiral jet milling of active pharmaceutical ingredients and the olefins polymerization process in fluidized bed reactors.
In this regard, CFD has been exploited throughout the study and Euler-Euler models have been built to analyze the phases motion of the investigated systems.

The main reasearch line regarded the micronizaton process. The first part of the work has been devoted to the analysis of a strategy to mimic the caking mechanism, *i.e.,* the formation of large rigid aggregates that stick on the micronization chamber walls and reduce the process effectiveness. The spiral jet mill volume reduction due to caking is studied through single-phase CFD simulations on a real-scale spiral jet mill operated at two different operating conditions, at constant gas feed-rate or constant absolute pressure. The aggregates formation on the mill walls has been simulated by gradually reducing the chamber diameter, accordingly to relevant experimental observations about typical crusts thickness.
Simulations showed that the gas flow-field is influenced by the progressive chamber shrinkage and the different operating conditions causes relevant variations in radial and tangential velocity profiles.
The variation of the chamber diameter while operating has the effect of reducing the flow homogeneity, modifying the gas flow features in the two micronization chamber semi-halfs. More specifically, if the nozzle total pressure is reduced while caking is advancing, the fluid spin ratio is kept almost constant into the domain and the classification of particles is controlled by regulating the gas mass-flow rate at nozzles. On the other hand, if the nozzles total pressure is increased when the chamber diameter is reduced, gas velocity components increase in the central part

of the domain, while radial ones increase near plates. This means that, if the mass-flow rate at nozzles is kept constant, the system affected by caking is prone to classify larger particles, because of the inward radial velocity components that force the motion of large particles towards the outlet. Moreover, it is highlighted that much of the micronization chamber hosts positive radial velocity components and, therefore, a large portion of the spiral jet mill can only promote particles collisions. Particles classification, instead, takes place in two thin-zones near the upper and the lower plates. Due to this, the aggregates formation on the outer walls and plates is detrimental for classification purposes. Simulations underline that a control strategy based upon nozzles pressure and, therefore, gas mass-flow rate regulation is promising to continue the micronization process despite caking and pospone the apparatus stoppage.

Besides the analysis related to caking and the detailed investigations of the gas velocity profiles within the micronization chamber, a novel comprehensive model to study the spiral jet milling at process-scales has been built.

The 3D gas velocity profiles computed through single-phase CFD simulations have been used as input data for a 1D, radially evolving compartment-based model that computes the solid velocity by means of an algebraic formulation and breakage kinetic through a semi-empirical kernel. Model parameters are tuned over experiments designed on purpose.

The developed computational framework provides process-scale information of the outlet particle size distribution for both ductile (lactose) and fragile (paracetamol) substances in few minutes of computational time.

Coherently to the main model assumption of dilute flow conditions, best predictions are obtained for high-energy processes (high gas pressure and low solid feed-rates) with a maximum error of about 23% obtained for D90 at 7 bar(g).

The proposed model appears to be a promising computational tool for the descripton of the whole micronization process in terms of mean quantities rather than the detailed simulation of particles trajectories and interactions.

The second part of this thesis deals with the simulation of the solid distribution and particle growth modeling of polyethylene inside fluidized bed reactors.

Firstly, a standard compartment-based three-phase model with simplifed fluid dynamics description (SCM) has been built and its prediction performance has been compared to a detailed Euler-Euler multiphase CFD model with kinetic theory of granular flows.

Focusing on the fluidization behaviour of Geldart type A-B, non-reactive particles in steady-state processes taking place in a batch reactor, the compartmentalized model provides an adequate description of the FBR multiphase mixing and solid volume fraction is calculated with a maximum error of 20% when monodisperse

populations of particles are analyzed. If considering broad-size distributions, particles motion is also well predicted with a maximum discrepancy of 15-30% for volume fractions and a relative error always smaller than 1% for average particle size along the reactor axis. In addition, an approach to scale-down fluidized bed reactors for reducing the particle residence time and provide computationally-affordable models has been proposed and numerically tested. Simple material balances are exploited to guess the final particle size and initialize a packed ped of solid with diameters close to the final ones.
A CFD-PBE model based upon DQMOM has been implemented to solve a simple particle growth model able to simulate the polymerizaton process. Different solid feed-rates and solid outlet locations have been inestigated, highlighting that the multiphase mixture is always well mixed and no particle segregaton takes place along the reactor axis.
Numerical particle residence time and average particle diameters are in accordance to those estimated by simple material balances while the reactor holdup is massively underpredicted for each feed condition and withdrawal location tested, meaning the the 2D geometric shcematization does not allow for the simulation of FBR ran in continuous operation mode.
In conclusion, results support the usage of simplified multi-kinetic models for predicting the fluidization behaviour of solid particles in the bubbling fluidization regime while 2D FBR geometries appear not suitable to model the continuous polymerization process due to the impossibility of correctly predicting the reactor holdup in any condition.

6.2 Future Work

Besides the research work described in this thesis, other activities related to caking and particles electrification in spiral jet mills have been carried out.

In this scenario, the following next steps are planned.

- Further development of the uncoupled quasi-3D model to include the electrostatic force effects on solid particles, through charge transport and particle triboelectrification equations.
- Analysis and development of another breakage kernel formulation for describing the particle size reduction process in spiral jet mills.
- Evaluation of the proposed simulation strategy on 3D FBR geometries for studying the continuous polymerization with solid feed and withdrawal.

Appendix A

Validation Results of the FBR Multiphase Model

This appendix gives supplementary information about the Simonin model used to describe the turbulent interactions intercurring between between the fluid and solid granular phases and it presents the detailed analysis performed to assess a suitable computational grid for describing the fluidization of polyethylene particles, the correct geometric schematization and the solid packed bed initial conditions for having results independency on the quantity of particles filled in the reactor.

A.1 Simonin Model for Turbulent Interaction in Granular Flows

The equations describing the turbulent interactions for the granular phase when the Simonin model is employed are taken from the work of Simonin & Viollet [152], Elgobashi & Abou-Arab [164], the Theory Guide of Fluent code by Ansys [28] and Csanady [165].

For sake of completeness, a list of the aforementioned relationships is given.

$$\nu_\theta = \frac{1}{3}\mathrm{k}_{\theta\mathrm{g}}\tau^{\mathrm{t}}_{\theta\mathrm{g}} + \frac{2}{3}\mathrm{k}_\theta\tau^{\mathrm{F}}_{\theta\mathrm{g}} \tag{A.1}$$

$$\mathrm{k}_{\theta\mathrm{g}} = \mathrm{k}_{\mathrm{g}}\left(\frac{\eta_{\theta\mathrm{g}}}{1+\mu_{\theta\mathrm{g}}}\right) \tag{A.2}$$

$$\mathrm{k}_\theta = 2\mathrm{k}_{\mathrm{g}}\left(\frac{\eta_{\theta\mathrm{g}}}{1+\mu_{\theta\mathrm{g}}}\right) \tag{A.3}$$

$$\tau_{\theta\mathrm{g}}^{\mathrm{t}} = \frac{\tau_{\mathrm{g}}^{\mathrm{t}}}{\sigma_1\sqrt{1 + C_\beta \xi_\tau^2}} \tag{A.4}$$

$$\tau_{\theta\mathrm{g}}^{\mathrm{F}} = \frac{\rho_{\mathrm{g}} \mathrm{d}_\theta^2}{18\mu_{\mathrm{g}} \mathrm{K}_{\theta\mathrm{g}}} \left(1 + \mathrm{C}_{\mathrm{VM}} \frac{\rho_{\mathrm{g}}}{\rho_\theta}\right) \tag{A.5}$$

$$\tau_{\mathrm{g}}^{\mathrm{t}} = \frac{3}{2} \mathrm{C}_\mu \frac{\mathrm{k}_{\mathrm{g}}}{\varepsilon_{\mathrm{g}}} \tag{A.6}$$

$$\xi_\tau = \frac{|\mathbf{u}_\theta - \mathbf{u}_{\mathrm{g}}|}{\sqrt{\frac{2}{3}\mathrm{k}_{\mathrm{g}}}} \tag{A.7}$$

$$C_\beta = 1.8 - 1.35\cos^2\psi \tag{A.8}$$

$$\eta_{\theta\mathrm{g}} = \frac{\tau_{\mathrm{g}}^{\mathrm{t}}}{\tau_{\theta\mathrm{g}}^{\mathrm{F}}} \tag{A.9}$$

$$\mathrm{D}_{\mathrm{t},\theta\mathrm{g}} = \frac{1}{3} \mathrm{k}_{\theta\mathrm{g}} \tau_{\theta\mathrm{g}}^{\mathrm{t}} \tag{A.10}$$

$$\mathrm{D}_\theta = \mathrm{D}_{\mathrm{t},\theta\mathrm{g}} + \left(\frac{2}{3} \mathrm{k}_\theta \tau_{\theta\mathrm{g}}^{\mathrm{F}}\right) \tag{A.11}$$

A.2 Mesh Construction and Multiphase Set-Up Validation

The results dependency to spatial discretization was studied building three different grids, named "coarse", "medium" and "fine", as listed by Table A.1. In order to build a completely structured mesh, the computational domain was divided into segments as shown by Fig. 5.5 in Section 5.2.1.

Table A.1: Computational grid details, number of elements as function of the geometry feature.

Grid	# a	# b	# c	# d	# e	# tot
coarse	80	80	230	120	30	30400
medium	120	120	400	200	45	77400
fine	220	220	655	300	70	225500

The analysis is performed by comparing time-averaged solid volume fraction (see Equations 5.25 and 5.26 of the main manuscript) and solid velocity magnitude results obtained with different mesh and momentum discretization equation schemes against literature data (Che *et al.* [144]).
Time-averaged solid volume fraction data reported in Fig. A.1 show that a good fluidization behavior can be obtained even with the coarser grid and with the lowest order discretization schemes.
However, a slightly better agreement is obtained in the upper part of the cylindrical part of the reactor when the finest grid and the most accurate discretization scheme are used.
Data reported in Fig. A.2, instead, clearly show that the best fluidization predictions in terms of solid velocity are obtained using the "fine" grid and the most accurate interpolation scheme for momentum conservation.

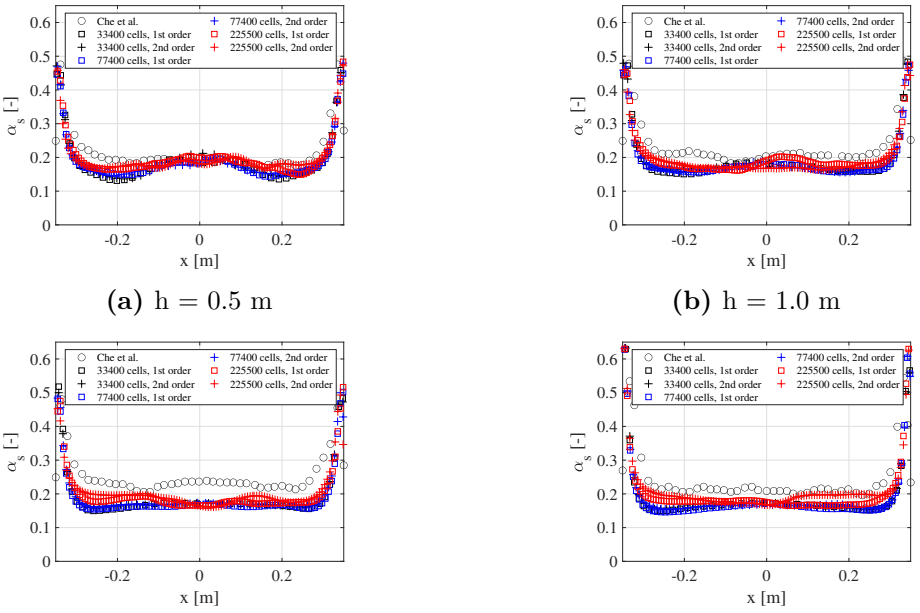

(a) h = 0.5 m **(b)** h = 1.0 m

(c) h = 1.5 m **(d)** h = 2.0 m

Figure A.1: Comparison between the time-averaged cell-centered data of solid volume fraction at 0.5 m (a), 1.0 m (b), 1.5 m (c), 2.0 m (d) for grids listed in Table A.1 and different discretization order of momentum equations. Monodisperse particles with size d = 446 μm.

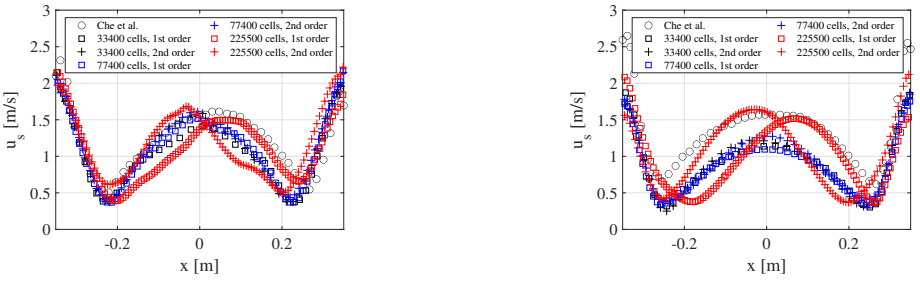

(a) h = 0.5 m **(b)** h = 2.0 m

Figure A.2: Comparison between the time-averaged cell-centered data of solid velocity magnitude at 0.5 m (a) 2.0 m (b) for grids listed in Table A.1 and different discretization order of momentum equations. Monodisperse particles with size d = 446 μm.

For these reasons, all the computations presented in this work are conducted using the 225500 cells of the grid named “fine” while the momentum equations were discretized with 2nd order total variation diminishing (TVD) scheme.

A.3 Assessment of Geometric Simplifications

The capacity of a 2D axial-symmetric geometry to reliably predict the fluidization behavior within fluidized bed reactors has been investigated comparing its results with those of a 2D planar one. Mesh constraints have been put to have the “fine” mesh in both cases, as depicted by Fig. A.3.

Simulations show that the 2D axial-symmetric geometry completely fail in predicting the correct fluidization behavior. The symmetry condition does not allow the correct prediction of the random chaotic motion of the solid phase within the reactor and, as shown qualitatively in Fig.A.4 and quantitatively in Fig.A.5, an over-segregation of particles near the centerline of the reactor is also generated. Therefore, the 2D planar geometry has been used for all the fluidization simulations.

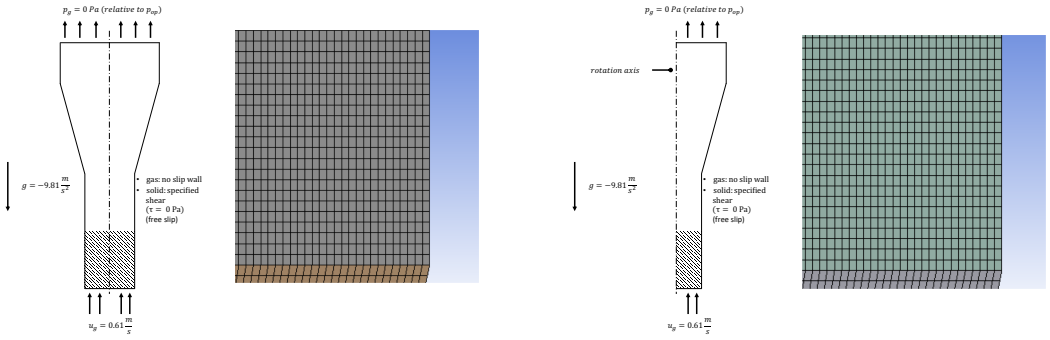

(a) 2D planar geometry

(b) 2D axial-symmetric geometry

Figure A.3: Geometry schematic, boundary conditions and computational grid detail for the 2D planar case (a) and the 2D axial-symmetric case (b).

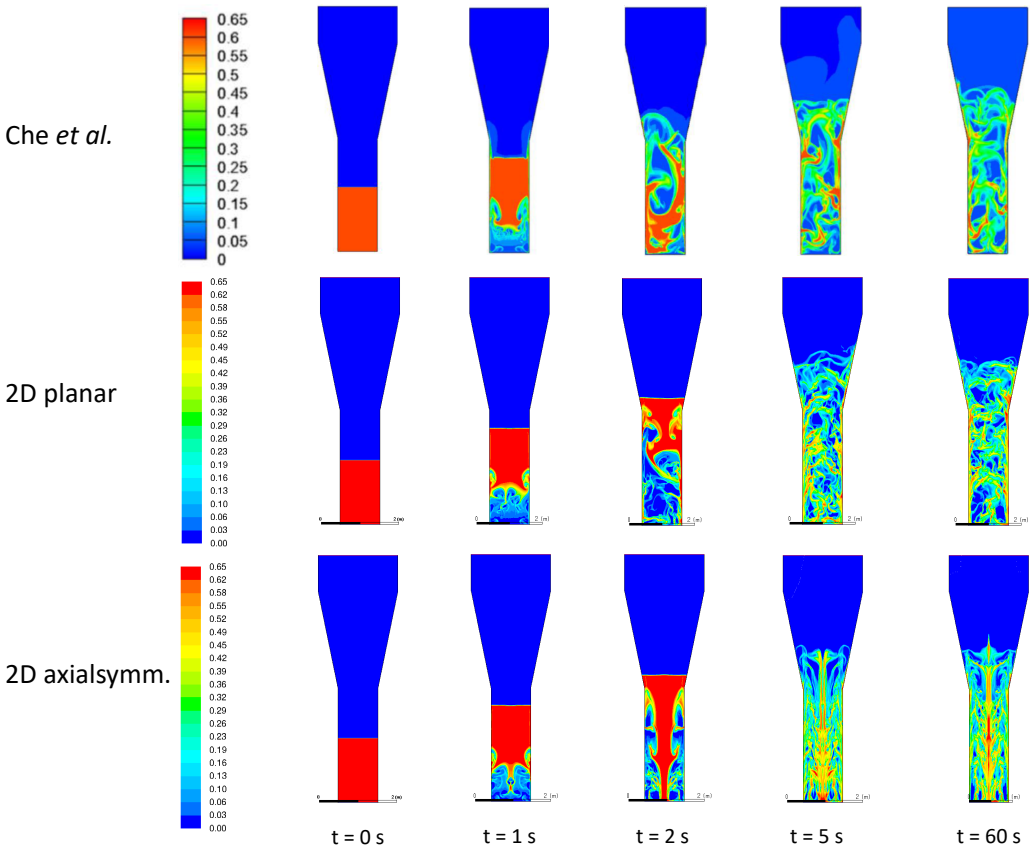

Figure A.4: Comparison between the solid volume fraction contours, at different physical times, for the reference case (Che *et al.* [144]), 2D planar geometry and 2D axialsymmetric geometry. Monodisperse particles with size d = 446 μm, fine computational grid.

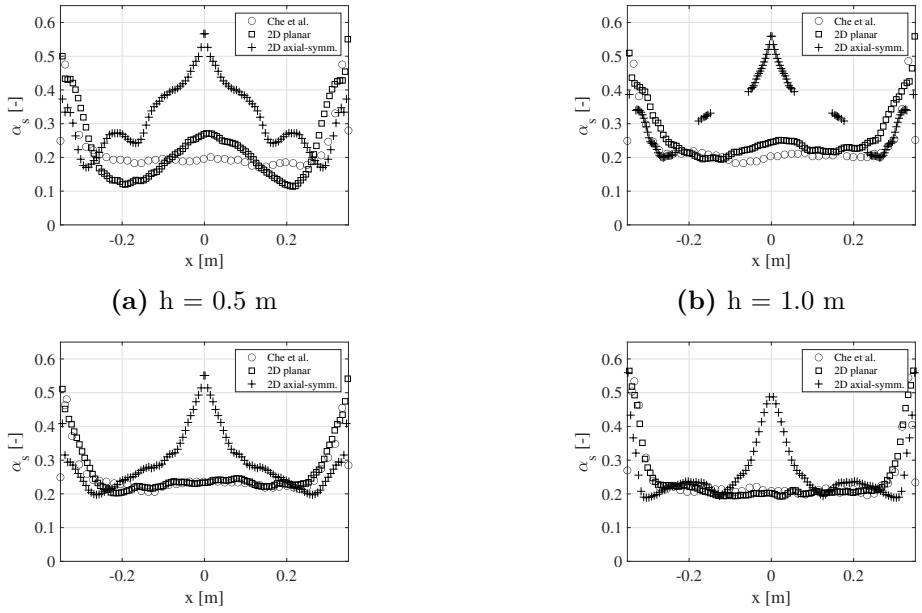

(a) h = 0.5 m **(b)** h = 1.0 m

(c) h = 1.5 m **(d)** h = 2.0 m

Figure A.5: Comparison between the time-averaged cell-centered data of volume fraction at different reactor height for the reference case (*et al.* [144]), 2D planar geometry and 2D axial-symmetric geometry. Monodisperse particles with size d = 446 μm.

A.4 Assessment of Initial Conditions

Three different initial heights of packed bed have been investigated to understand how the initial quantity of solid loaded into the reactor may affect the results. As shown in Fig. A.6, the solid phase distribution was studied when h = 1.137 m (half of the bottom part), h = 2 m (whole bottom part) and h = 4.347 m (whole reactor).
The predictions are not affected by the initial bed height when the solid phase is filling at least the entire cylindrical region. This statement becomes even more strong when looking at the time-averaged data in Fig. A.7 in terms of solid volume fraction as a function of radial position as well as at the time- and space-averaged results in Fig. A.8 for both gas and solid volume fractions. Accordingly, a packed bed height h = 2 m is therefore used as initial condition for all the simulations.

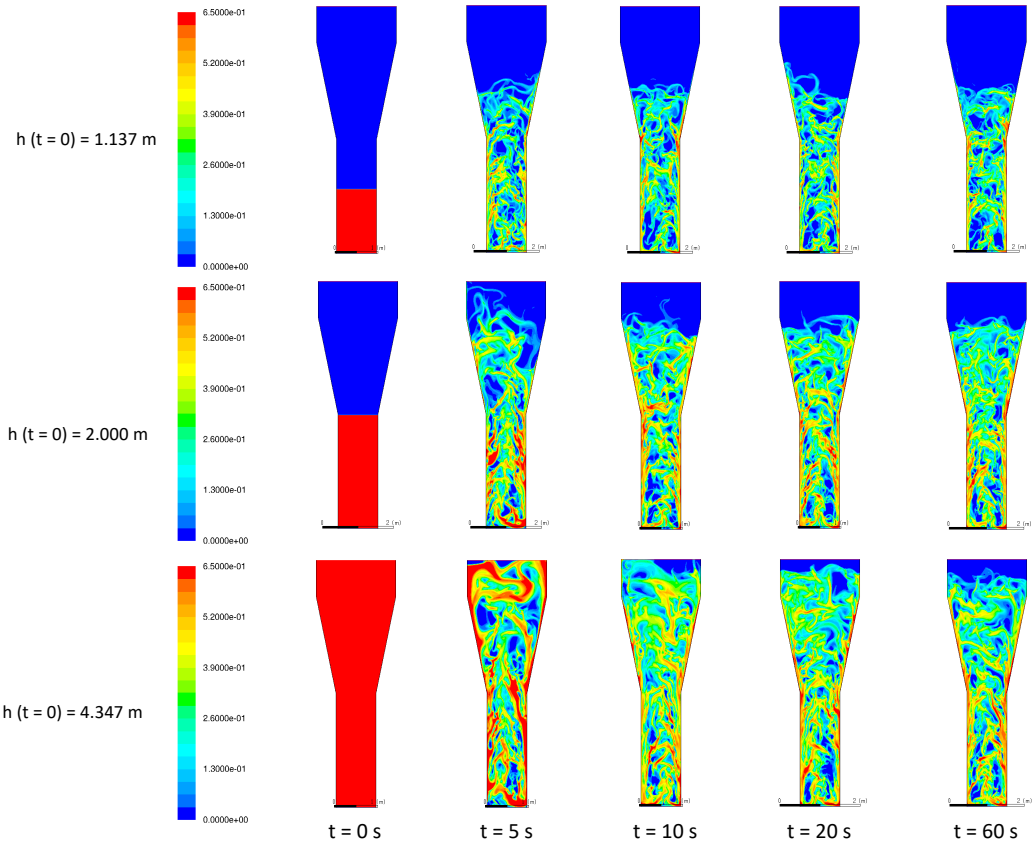

Figure A.6: Comparison between the volume fraction contours at different physical times for different packed bed initialization height. Monodisperse particles with size d = 446 μm.

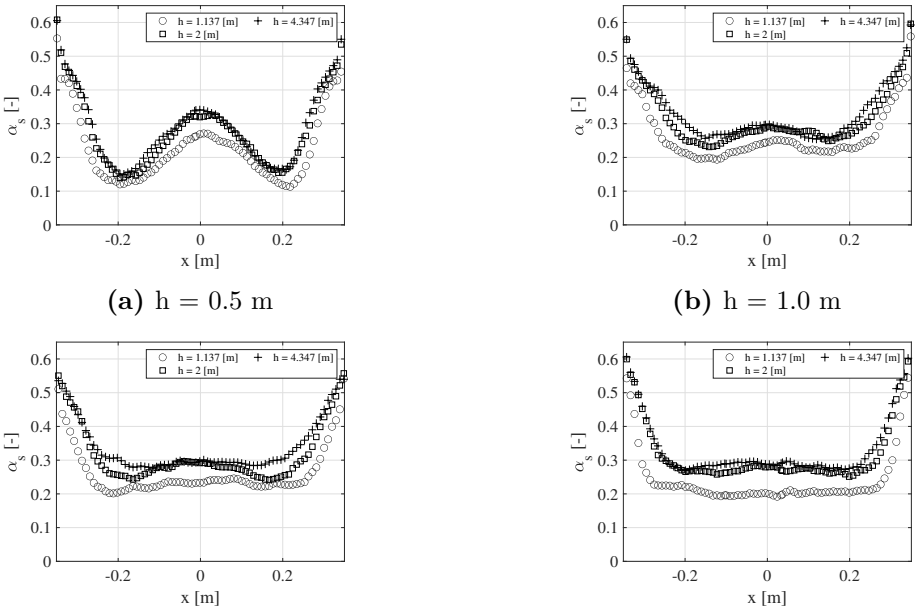

(a) h = 0.5 m **(b)** h = 1.0 m

(c) h = 1.5 m **(d)** h = 2.0 m

Figure A.7: Comparison between time-averaged cell-centered data of volume fraction at different reactor position for different packed bed initialization height. Monodisperse particles with size d = 446 μm.

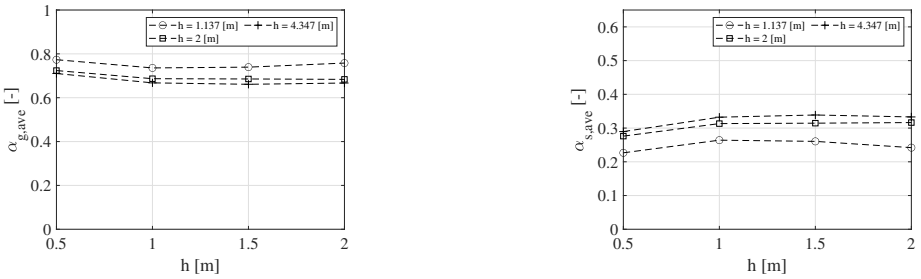

(a) average gas volume fraction **(b)** average solid volume fraction

Figure A.8: Comparison between the time- and space-averaged cell-centered data of gas volume fraction (a) and solid volume fraction (b) at different reactor position for different packed bed initialization height. Monodisperse particles with size d = 446 μm.

Appendix B

Reactor Scaling Procedure and Particle Growth Model Implementation

This appendix reports supplementary highlights the passages to obtain the analytical solution of the Kim & Choi model [155] particle growth model.

B.1 Particle Growth Analytical Solution Derivation

The differential form of the Kim & Choi model [155] is:

$$\frac{\mathrm{d}r}{\mathrm{d}t} = \frac{\mathrm{r_c^3} \cdot \rho_\mathrm{c} \cdot \mathrm{K_p} \cdot \mathrm{M} \cdot \mathrm{C^*} \cdot \mathrm{PM_{mon}}}{3\,(1-\zeta)\,\mathrm{r^2} \cdot \rho_\mathrm{s}} = G \tag{B.1}$$

with

$$\mathrm{C^*} = \mathrm{C^*_{ref}} \cdot 0.0337; \tag{B.2}$$

$$\mathrm{K_p} = \mathrm{K_{p,ref}} \cdot \exp\left\{\left[\frac{-\mathrm{E_{att,p}}}{\mathcal{R}}\left(\frac{1}{\mathrm{T}}\right)\right]\right\}. \tag{B.3}$$

Since there is no dependancy of $\mathrm{C^*}$, the differential equation is simply solvable as:

$$3\int_{\mathrm{r_0}}^{\mathrm{r}} \mathrm{r^2 dr} = \frac{\mathrm{r_c^3} \cdot \rho_\mathrm{c} \cdot \mathrm{K_p} \cdot \mathrm{M} \cdot \mathrm{C^*} \cdot \mathrm{PM_{mon}}}{(1-\zeta)\,\rho_\mathrm{s}} \int_0^t \mathrm{d}t; \tag{B.4}$$

$$\mathrm{r^3}|_{\mathrm{r_0}}^{\mathrm{r}} = \frac{\mathrm{r_c^3} \cdot \rho_\mathrm{c} \cdot \mathrm{K_p} \cdot \mathrm{M} \cdot \mathrm{C^*} \cdot \mathrm{PM_{mon}}}{(1-\zeta)\,\rho_\mathrm{s}} \mathrm{t}|_0^t; \tag{B.5}$$

$$r^3 = \frac{r_c^3 \cdot \rho_c \cdot K_p \cdot M \cdot C^* \cdot PM_{mon}}{(1-\zeta)\,\rho_s} t + r_0^3. \tag{B.6}$$

But $r_0 = r_c$ and $d = 2 \cdot r$, then:

$$d = 2r_c \left(\frac{\rho_c \cdot K_p \cdot M \cdot C^* \cdot PM_{mon}}{(1-\zeta)\,\rho_s} \cdot t + 1 \right)^{1/3}. \tag{B.7}$$

The Kim & Choi model of Equation B.1 can be also written in terms of a particle volumetric variation over time, using volume concentrations instead of mass ($C^* = C^* \cdot \rho_c$) ones:

$$v_c = 8k_v \cdot {r_c}^3 \rightarrow {r_c}^3 = \frac{v_c}{8k_v}; \tag{B.8}$$

$$\frac{dv}{dt} = \frac{d}{dt}\left(k_v \cdot d^3\right) = \frac{d}{dt}\left(8k_v \cdot r^3\right) = 8k_v \cdot 3r^2 \frac{dr}{dt}. \tag{B.9}$$

Substituting into Equation B.1 one obtaines

$$\frac{1}{8k_v 3r^2}\frac{dv}{dt} = \frac{V_c \cdot K_p \cdot M \cdot C^* \cdot PM_{mon}}{3 \cdot 8k_v\,(1-\zeta)\,r^2 \cdot \rho_s} = G_v. \tag{B.10}$$

The differential equation has the form:

$$\frac{dv}{dt} = \frac{V_c \cdot \rho_c \cdot K_p \cdot M \cdot C^* \cdot PM_{mon}}{(1-\zeta)\,\rho_s} \tag{B.11}$$

Again, there is no dependancy of C^*, then:

$$\int_{v_0}^{v} dv = \frac{v_c \cdot \rho_c \cdot K_p \cdot M \cdot C^* \cdot PM_{mon}}{(1-\zeta)\,\rho_s} \int_0^t dt; \tag{B.12}$$

$$v|_{v_0}^{v_p} = \frac{v_c \cdot \rho_c \cdot K_p \cdot M \cdot C^* \cdot PM_{mon}}{(1-\zeta)\,\rho_s} t|_0^t; \tag{B.13}$$

$$v = v_c \left(\frac{K_p \cdot \rho_c \cdot M \cdot C^* \cdot PM_{mon}}{(1-\zeta)\,\rho_s} t + 1 \right); \tag{B.14}$$

$$d = v_c^{1/3} \left(\frac{K_p \cdot \rho_c \cdot M \cdot C^* \cdot PM_{mon}}{(1-\zeta)\,\rho_s} t + 1 \right)^{1/3} {k_v}^{-1/3}. \tag{B.15}$$

Appendix C

Fluent Solver Setting for Transonic Flows

This appendix reports the detailed Pressure-Based Coupled Solver numerical settings of Fluent.

C.1 Pressure-Based Coupled Solver Settings

The flow-field inside the micronization chamber of spiral jet mills is mostly transonic (0.3<Ma<0.8), except for very localized domain regions located downstream nozzles final sections. These flows can be modeled availing of the Pressure-Based Coupled Solver (PBCS) of Fluent which provides superior computational time speed with respect to denssity-based solver [28].
The following tables list the major setting used for simulations.

Table C.1: Major solver settings. PT of time formulatons stands for pseudo-transient.

Pressure-velocity form.	Velocity form.	Time form.	Gravity
Coupled solution	Absolute	Steady-state (PT)	OFF

Table C.2: Detaild of the single-phase k-ε realizable turbulence model constants.

$C_{1,\varepsilon}$	C_2	C_3	σ_μ	σ_ε
1.44	1.9	0	1.0	1.2

Table C.3: Detail of transport equations residuals level and pseudo-transient under-relaxation (PTUR) factors. p indicates the pressure-correction equation, BF indicates body forces. Note that only variables transported by balance equations are relaxed.

	p	**u**	h	k	ε	ρ	μ	BF
residuals	10^{-7}	10^{-7}	10^{-8}	10^{-3}	10^{-3}	-	-	-
PTUR	0.5	0.4	0.75	0.5	0.5	1.0	1.0	1.0

Bibliography

[1] Higashitani, K. et al. *Powder technology handbook*. CRC Press, 2019.

[2] Boccardo, G. et al. "Microscale simulation of particle deposition in porous media". In: *Journal of colloid and interface science* 417 (2014), pp. 227–237.

[3] Boccardo, G. et al. "Validation of a novel open-source work-flow for the simulation of packed-bed reactors". In: *Chemical Engineering Journal* 279 (2015), pp. 809–820.

[4] Boccardo, G. et al. "A robust upscaling of the effective particle deposition rate in porous media". In: *Journal of contaminant hydrology* 212 (2018), pp. 3–13.

[5] Boccardo, G. et al. "Fine and ultrafine particle deposition in packed-bed catalytic reactors". In: *Chemical Engineering Science* 198 (2019), pp. 290–304.

[6] Crevacore, E. et al. "Recirculation zones induce non-Fickian transport in three-dimensional periodic porous media". In: *Physical Review E* 94.5 (2016), p. 053118.

[7] Crevacore, E. et al. "Pore-Scale Simulations of Particle Transport for Groundwater Remediation: the Effect of Gravitational Settling". In: *Chemical Engineering Transactions* 60 (2017), pp. 193–198.

[8] Icardi, M. et al. "Pore-scale simulation of fluid flow and solute dispersion in three-dimensional porous media". In: *Physical review E* 90.1 (2014), p. 013032.

[9] Bnà, S. et al. "Investigation of particle dynamics and classification mechanism in a spiral jet mill through computational fluid dynamics and discrete element methods". In: *Powder Technology* 364 (2020), pp. 746–773.

[10] Scott, L. et al. "Influence of holdup on gas and particle flow patterns in a spiral jet mill". In: *Powder Technology* 377 (2021), pp. 233–243.

[11] Scott, L. et al. "Effect of grinding nozzles pressure on particle and fluid flow patterns in a spiral jet mill". In: *Powder Technology* 394 (2021), pp. 439–447.

[12] Scott, L. et al. "Analysis of hold-up and grinding pressure in a spiral jet mill using CFD-DEM". In: *EPJ Web of Conferences*. Vol. 249. EDP Sciences. 2021, p. 12004.

[13] Bhonsale, S. et al. "Numerical simulation of particle dynamics in a spiral jet mill via coupled CFD-DEM". In: *Pharmaceutics* 13.7 (2021), p. 937.

[14] Gidaspow, D. and B. Ettehadieh. "Fluidization in two-dimensional beds with a jet. 2. Hydrodynamic modeling". In: *Industrial & Engineering Chemistry Fundamentals* 22.2 (1983), pp. 193–201.

[15] Hartge, E.-U. et al. "CFD-simulation of a circulating fluidized bed riser". In: *Particuology* 7 (2009), pp. 283–296.

[16] Wang, T. et al. "Coupled CFD-PBM simulation of bubble size distribution in a 2D gas-solid bubbling fluidized bed with a bubble coalescence and breakup model". In: *Chemical Engineering Science* 202 (2019), pp. 208–221.

[17] Fan, R. et al. "Application of the direct quadrature method of moments to polydisperse gas–solid fluidized beds". In: *Powder technology* 139.1 (2004), pp. 7–20.

[18] Akbari, V. et al. "2D CFD-PBM simulation of hydrodynamic and particle growth in an industrial gas phase fluidized bed polymerization reactor". In: *Chemical Engineering Research and Design* 104 (2015), pp. 53–67.

[19] Yao, Y. et al. "CFD-PBM modeling polydisperse polymerization FBRs with simultaneous particle growth and aggregation: the effect of the method of moments". In: *Powder technology* 272 (2015), pp. 142–152.

[20] Ray, M. et al. "An Euler-Euler model for mono-dispersed gas-particle flows incorporating electrostatic charging due to particle-wall and particle-particle collisions". In: *Chemical Engineering Science* 197 (2019), pp. 327–344.

[21] Du, S. and L. Liu. "Numerical simulation of particle growth process in a polysilicon fluidized bed reactor". In: *Particulate Science and Technology* (2019).

[22] Rokkam, R. G. et al. "Computational fluid dynamics and electrostatic modeling of polymerization fluidized-bed reactors". In: *Powder Technology* 203.2 (2010), pp. 109–124.

[23] Patil, D. et al. "Critical comparison of hydrodynamic models for gas–solid fluidized beds—Part I: bubbling gas–solid fluidized beds operated with a jet". In: *Chemical engineering science* 60.1 (2005), pp. 57–72.

[24] Passalacqua, A. and L. Marmo. "A critical comparison of frictional stress models applied to the simulation of bubbling fluidized beds". In: *Chemical Engineering Science* 64.12 (2009), pp. 2795–2806.

[25] Askari, E. et al. "Modelling of bubbly flow using CFD-PBM solver in OpenFOAM: study of local population balance models and extended quadrature method of moments applications". In: *ChemEngineering* 2.1 (2018), p. 8.

[26] Bi, H. and J. Grace. "Flow regime diagrams for gas-solid fluidization and upward transport". In: *International Journal of Multiphase Flow* 21.6 (1995), pp. 1229–1236. ISSN: 0301-9322. DOI: https://doi.org/10.1016/0301-9322(95)00037-X. URL: https://www.sciencedirect.com/science/article/pii/030193229500037X.

[27] Marchisio, D. L. "Introduction to Computational Models for Multiphase Flows". In: *Particulates Flow and Separation Technologies in Industrial Applications*. von Karman Insitute. 2021.

[28] ANSYS. *Fluent Theory Guide - v. 17.1, PDF file*. ANSYS, Inc. Support Service, First-time accessed: April 2017.

[29] ANSYS. *A Solution for Every Multiphase Challenge - v. 16.0, PDF file*. ANSYS, Inc. Online Presentation, First-time accessed and downloaded: February 2016.

[30] Tronci, G. et al. "Validation of the Diffusion Mixture Model for the simulation of bubbly flows and implementation in OpenFOAM". In: *Computers & Fluids* (2021), p. 105026.

[31] Arastoopour, H. et al. *Transport Phenomena in Multiphase Systems*. 2021.

[32] 13, C. *Granular Flows*. http://authors.library.caltech.edu/25021/1/chap13.pdf. Online, First-time accessed: August 2017.

[33] Vescovi, D. "Granular shear flows: constitutive modeling and numerical simulations". PhD thesis. Politecnico di Milano, 2014.

[34] Sabia, C. et al. "A detailed CFD analysis of flow patterns and single-phase velocity variations in spiral jet mills affected by caking phenomena". In: *Chemical Engineering Research and Design* 174 (2021), pp. 234–253.

[35] Marchisio, D. L. and R. O. Fox. *Computational models for polydisperse particulate and multiphase systems*. Cambridge University Press, 2013.

[36] Ramkrishna, D. *Population balances: Theory and applications to particulate systems in engineering*. Elsevier, 2000.

[37] Kumar, S. and D. Ramkrishna. "On the solution of population balance equations by discretization—I. A fixed pivot technique". In: *Chemical Engineering Science* 51.8 (1996), pp. 1311–1332.

[38] Kumar, S. and D. Ramkrishna. "On the solution of population balance equations by discretization—II. A moving pivot technique". In: *Chemical Engineering Science* 51.8 (1996), pp. 1333–1342.

[39] Kumar, S. and D. Ramkrishna. "On the solution of population balance equations by discretization—III. Nucleation, growth and aggregation of particles". In: *Chemical Engineering Science* 52.24 (1997), pp. 4659–4679.

[40] Shiea, M. "Simulation of polydisperse bubbly flows: An investigation on physical and numerical aspects". PhD thesis. Politecnico di Torino, 2020.

[41] Hidy, G. M. and J. R. Brock. *The dynamics of aerocolloidal systems: International reviews in aerosol physics and chemistry*. Vol. 1. Elsevier, 2016.

[42] Hounslow, M. et al. "A discretized population balance for nucleation, growth, and aggregation". In: *AIChE journal* 34.11 (1988), pp. 1821–1832.

[43] Hulburt, H. M. and S. Katz. "Some problems in particle technology: A statistical mechanical formulation". In: *Chemical engineering science* 19.8 (1964), pp. 555–574.

[44] Li, D. et al. "Quadrature-based moment methods for the population balance equation: An algorithm review". In: *Chinese Journal of Chemical Engineering* 27.3 (2019), pp. 483–500.

[45] McGraw, R. "Description of aerosol dynamics by the quadrature method of moments". In: *Aerosol Science and Technology* 27.2 (1997), pp. 255–265.

[46] Wright, D. L. et al. "Bivariate extension of the quadrature method of moments for modeling simultaneous coagulation and sintering of particle populations". In: *Journal of colloid and interface science* 236.2 (2001), pp. 242–251.

[47] Yuan, C. and R. O. Fox. "Conditional quadrature method of moments for kinetic equations". In: *Journal of Computational Physics* 230.22 (2011), pp. 8216–8246.

[48] Yuan, C. et al. "An extended quadrature method of moments for population balance equations". In: *Journal of Aerosol Science* 51 (2012), pp. 1–23.

[49] Marchisio, D. L. et al. "Quadrature method of moments for population-balance equations". In: *AIChE Journal* 49.5 (2003), pp. 1266–1276.

[50] Marchisio, D. L. and R. O. Fox. "Solution of population balance equations using the direct quadrature method of moments". In: *Journal of Aerosol Science* 36.1 (2005), pp. 43–73.

[51] Shiea, M. et al. “Numerical methods for the solution of population balance equations coupled with computational fluid dynamics”. In: *Annual review of chemical and biomolecular engineering* 11 (2020), pp. 339–366.

[52] Sack, R. and A. Donovan. “An algorithm for Gaussian quadrature given modified moments”. In: *Numerische Mathematik* 18.5 (1971), pp. 465–478.

[53] Wheeler, J. C. “Modified moments and Gaussian quadratures”. In: *The Rocky Mountain Journal of Mathematics* 4.2 (1974), pp. 287–296.

[54] Gordon, R. G. “Error bounds in equilibrium statistical mechanics”. In: *Journal of Mathematical Physics* 9.5 (1968), pp. 655–663.

[55] Midoux, N. et al. “Micronization of pharmaceutical substances in a spiral jet mill”. In: *Powder Technology* 104.2 (1999), pp. 113–120.

[56] Nakach, M. et al. “Jet milling industrialization of sticky active pharmaceutical ingredient using quality-by-design approach”. In: *Pharmaceutical development and technology* 24.7 (2019), pp. 849–863.

[57] Adali, M. B. et al. “Spray freeze-drying as a solution to continuous manufacturing of pharmaceutical products in bulk”. In: *Processes* 8.6 (2020), p. 709.

[58] Rodnianski, V. et al. “Aerodynamic classification in a spiral jet mill”. In: *Powder technology* 243 (2013), pp. 110–119.

[59] KQNNO, H. and S. SAITO. “Pneumatic conveying of solids through straight pipes”. In: *Journal of chemical engineering of Japan* 2.2 (1969), pp. 211–217.

[60] Müller, F. et al. “Spiral jet mills: hold up and scale up”. In: *International Journal of Mineral Processing* 44 (1996), pp. 315–326.

[61] Crowe, C. et al. *Multiphase Flows with Droplets and Particles*. CRCPress, Taylor & Francis Group, 1998.

[62] Sowa, M. et al. “Particle engineering of an active pharmaceutical ingredient for improved micromeritic properties”. In: *Chemical Engineering & Technology* 40.7 (2017), pp. 1282–1292.

[63] Zhang, L. et al. “Deposition fraction of aerosol particles in a human oral airway model on stable condition”. In: *Aerosol and Air Quality Research* 6.3 (2006), pp. 259–267.

[64] Ghadiri, M. and Z. Zhang. “Impact attrition of particulate solids. Part 1: A theoretical model of chipping”. In: *Chemical Engineering Science* 57.17 (2002), pp. 3659–3669.

[65] Zhang, Z. and M. Ghadiri. "Impact attrition of particulate solids. Part 2: Experimental work". In: *Chemical Engineering Science* 57.17 (2002), pp. 3671–3686.

[66] Moreno-Atanasio, R. and M. Ghadiri. "Mechanistic analysis and computer simulation of impact breakage of agglomerates: effect of surface energy". In: *Chemical engineering science* 61.8 (2006), pp. 2476–2481.

[67] Zafar, U. et al. "A review of bulk powder caking". In: *Powder Technology* 313 (2017), pp. 389–401.

[68] Chen, M. et al. "Caking of crystals: Characterization, mechanisms and prevention". In: *Powder Technology* 337 (2018), pp. 51–67.

[69] Carpin, M. et al. "Impurities enhance caking in lactose powder". In: *Journal of Food Engineering* 198 (2017), pp. 91–97.

[70] Carpin, M. et al. "How does particle size influence caking in lactose powder?" In: *Journal of Food Engineering* 209 (2017), pp. 61–67.

[71] Listiohadi, Y. et al. "Moisture sorption, compressibility and caking of lactose polymorphs". In: *International journal of pharmaceutics* 359.1-2 (2008), pp. 123–134.

[72] Hartmann, M. and S. Palzer. "Caking of amorphous powders—Material aspects, modelling and applications". In: *Powder Technology* 206.1-2 (2011), pp. 112–121.

[73] Chen, M. et al. "Amorphous and humidity caking: A review". In: *Chinese Journal of Chemical Engineering* 27.6 (2019), pp. 1429–1438.

[74] Brosh, T. et al. "DEM–CFD simulation of particle comminution in jet-mill". In: *Powder Technology* 257 (2014), pp. 104–112.

[75] Kalman, H. et al. "A new method to implement comminution functions into DEM simulation of a size reduction system due to particle-wall collisions". In: *Granular Matter* 11.4 (2009), pp. 253–266.

[76] Brunaugh, A. and H. Smyth. "Process optimization and particle engineering of micronized drug powders via milling". In: *Drug delivery and translational research* 8.6 (2018), pp. 1740–1750.

[77] Ma, Z. et al. "In-line Particle Size Measurement for Control of Jet Milling". In: *Particle & Particle Systems Characterization: Measurement and Description of Particle Properties and Behavior in Powders and Other Disperse Systems* 18.2 (2001), pp. 99–106.

[78] Macdonald, R. F. W. "Optimisation and modelling of the spiral jet mill". PhD thesis. Newcastle University, 2017.

[79] Han, T. et al. “DEM Simulation of Particle Comminutionin Jet Milling”. In: *Particulate science and technology* 20.4 (2002), pp. 325–340.

[80] Masterson, V. M. and X. Cao. “Evaluating particle hardness of pharmaceutical solids using AFM nanoindentation”. In: *International journal of pharmaceutics* 362.1-2 (2008), pp. 163–171.

[81] Meier, M. et al. “Influence of mechanical properties on impact fracture: Prediction of the milling behaviour of pharmaceutical powders by nanoindentation”. In: *Powder Technology* 188.3 (2009), pp. 301–313.

[82] Zügner, S. et al. “Influence of nanomechanical crystal properties on the comminution process of particulate solids in spiral jet mills”. In: *European journal of pharmaceutics and biopharmaceutics* 62.2 (2006), pp. 194–201.

[83] Vegt, O. M. de. *Jet milling from a particle perspective*. 2007.

[84] Wilson, D. et al. “POWDER COMPACTION: PROCESS DESIGN AND UNDERSTANDING”. In: *Chemical Engineering in the Pharmaceutical Industry: Drug Product Design, Development, and Modeling* (2019), pp. 203–225.

[85] Cao, X. et al. “Correlating particle hardness with powder compaction performance”. In: *Journal of pharmaceutical sciences* 99.10 (2010), pp. 4307–4316.

[86] Taylor, L. et al. “Mechanical characterisation of powders using nanoindentation”. In: *Powder Technology* 143 (2004), pp. 179–185.

[87] Design-Expert. *version 11*. Minneapolis, Minnesota: Stat-Ease Inc., 2019.

[88] Eriksson, L. et al. “Design of experiments”. In: *Principles and Applications, Learn ways AB, Stockholm* (2000).

[89] Batchelor, C. K. and G. Batchelor. *An introduction to fluid dynamics*. Cambridge university press, 2000.

[90] Shih, T.-H. et al. “A new $k - \varepsilon$ eddy viscosity model for high reynolds number turbulent flows”. In: *Computers & fluids* 24.3 (1995), pp. 227–238.

[91] Versteeg, H. K. and W. Malalasekera. *An introduction to computational fluid dynamics: the finite volume method*. Pearson education, 2007.

[92] Kader, B. “Temperature and concentration profiles in fully turbulent boundary layers”. In: *International journal of heat and mass transfer* 24.9 (1981), pp. 1541–1544.

[93] Meshing. *version 2020 R2*. Canonsburg, Pennsylvania: Ansys, Inc., 2020.

[94] Çengel, Y. and J. Cimbala. “Fluid Mechanics: fundamentals and applications, Mac Graw Hill, New York”. In: (2006).

[95] Luczak, B. and M. Eng. "Flow conditions inside spiral jet mills and impact on grinding performance". PhD thesis. Universitätsbibliothek Duisburg-Essen, 2018.

[96] FLUENT. *version 2020 R2*. Canonsburg, Pennsylvania: Ansys, Inc., 2020.

[97] Barth, T. and D. Jespersen. "The design and application of upwind schemes on unstructured meshes". In: *27th Aerospace sciences meeting*. 1989, p. 366.

[98] Rhie, C. and W. L. Chow. "Numerical study of the turbulent flow past an airfoil with trailing edge separation". In: *AIAA journal* 21.11 (1983), pp. 1525–1532.

[99] Kelley, C. T. and D. E. Keyes. "Convergence analysis of pseudo-transient continuation". In: *SIAM Journal on Numerical Analysis* 35.2 (1998), pp. 508–523.

[100] Schiller, L. "A drag coefficient correlation". In: *Zeit. Ver. Deutsch. Ing.* 77 (1933), pp. 318–320.

[101] MATLAB. *version 9.9.01538559 (R2020b)*. Natick, Massachusetts: The MathWorks Inc., 2020.

[102] Salman, A. et al. "Descriptive classification of the impact failure modes of spherical particles". In: *Powder Technology* 143 (2004), pp. 19–30.

[103] Rowe, R. and R. Roberts. "1 The mechanical properties of powders". In: *Advances in pharmaceutical sciences*. Vol. 7. Elsevier, 1995, pp. 1–IV.

[104] Shariare, M. H. et al. "Influence of solvent on the morphology and subsequent comminution of ibuprofen crystals by air jet milling". In: *Journal of pharmaceutical sciences* 101.3 (2012), pp. 1108–1119.

[105] Austin, L. G. "Introduction to the mathematical description of grinding as a rate process". In: *Powder Technology* 5.1 (1971), pp. 1–17.

[106] Gommeren, H. et al. "Dynamic modeling of a closed loop jet mill". In: *International Journal of Mineral Processing* 44 (1996), pp. 497–506.

[107] Gommeren, H. et al. "Modelling and control of a jet mill plant". In: *Powder Technology* 108.2-3 (2000), pp. 147–154.

[108] Kukkonen, S. and J. Lampinen. "GDE3: The third evolution step of generalized differential evolution". In: *2005 IEEE congress on evolutionary computation*. Vol. 1. IEEE. 2005, pp. 443–450.

[109] Baur, D. "Design, modeling and optimization of multi-column chromatographic processes". PhD thesis. ETH Zurich, 2017.

[110] Abbasi, M. R. et al. "A review on modeling and control of olefin polymerization in fluidized-bed reactors". In: *Reviews in Chemical Engineering* 35.3 (2019), pp. 311–333.

[111] Kunii, D. and O. Levenspiel. *Fluidization engineering*. Butterworth-Heinemann, 1991.

[112] Alves, R. F. et al. "Gas-Phase Polyethylene Reactors—A Critical Review of Modeling Approaches". In: *Macromolecular Reaction Engineering* (2021), p. 2000059.

[113] Soares, J. B. and T. F. McKenna. *Polyolefin reaction engineering*. Wiley Online Library, 2012.

[114] McAuley, K. et al. "A comparison of two-phase and well-mixed models for fluidized-bed polyethylene reactors". In: *Chemical Engineering Science* 49.13 (1994), pp. 2035–2045.

[115] Dompazis, G. et al. "Dynamic evolution of the particle size distribution in multistage olefin polymerization reactors". In: *Computer Aided Chemical Engineering*. Vol. 20. Elsevier, 2005, pp. 427–432.

[116] An, M. et al. "Modeling the effects of solid particles in CFD-PBM simulation of slurry bubble columns". In: *Chemical Engineering Science* 223 (2020), p. 115743.

[117] Sriniketh, A. and B. Ashraf Ali. "Computational investigation of hydrodynamics and solid circulation in fluidized bed column". In: *Chemical Engineering Communications* 208.6 (2021), pp. 843–850.

[118] Hatzantonis, H. et al. "A comprehensive model for the prediction of particle-size distribution in catalyzed olefin polymerization fluidized-bed reactors". In: *Chemical Engineering Science* 53.18 (1998), pp. 3251–3267.

[119] Alizadeh, M. et al. "Modeling of fluidized bed reactor of ethylene polymerization". In: *Chemical Engineering Journal* 97.1 (2004), pp. 27–35.

[120] Ashrafi, O. et al. "Particle size distribution in gas-phase polyethylene reactors". In: *Advanced powder technology* 19.4 (2008), pp. 321–334.

[121] Alves, R. F. and T. F. McKenna. "Modelling of Condensed Mode Cooling during the Polymerization of Ethylene in Fluidized Bed Reactors". In: *Industrial & Engineering Chemistry Research* 60.32 (2021), pp. 11977–11994.

[122] McKenna, T. F. and J. B. Soares. "Single particle modelling for olefin polymerization on supported catalysts: A review and proposals for future developments". In: *Chemical Engineering Science* 56.13 (2001), pp. 3931–3949.

[123] Elvers, B. et al. *Ullmann's encyclopedia of industrial chemistry*. Verlag Chemie, 1991.

[124] Van Wachem, B. et al. “Comparative analysis of CFD models of dense gas–solid systems”. In: *AIChE Journal* 47.5 (2001), pp. 1035–1051.

[125] Chu, K. et al. “CFD–DEM simulation of the gas–solid flow in a cyclone separator”. In: *Chemical Engineering Science* 66.5 (2011), pp. 834–847.

[126] Ahuja, G. and A. Patwardhan. “CFD and experimental studies of solids hold-up distribution and circulation patterns in gas–solid fluidized beds”. In: *Chemical Engineering Journal* 143.1-3 (2008), pp. 147–160.

[127] Chen, X.-Z. et al. “Three-dimensional CFD-PBM coupled model of the temperature fields in fluidized-bed polymerization reactors”. In: *AIChE Journal* 57.12 (2011), pp. 3351–3366.

[128] Yan, W.-C. et al. “A CFD-PBM coupled model with polymerization kinetics for multizone circulating polymerization reactors”. In: *Powder technology* 231 (2012), pp. 77–87.

[129] Hayashi, K. et al. “Numerical study on granule aggregation and breakage in fluidized bed granulation by a novel PBM with DEM-CFD coupling approach”. In: *Powder Technology* 360 (2020), pp. 1321–1336.

[130] Lu, Y. et al. “A CFD–DEM study of bubble dynamics in fluidized bed using flood fill method”. In: *Chemical Engineering Journal* 274 (2015), pp. 123–131.

[131] Wang, S. et al. “CFD-DEM simulation of heat transfer in fluidized beds: Model verification, validation, and application”. In: *Chemical Engineering Science* 197 (2019), pp. 280–295.

[132] Chowdhury, F. et al. “A review on modeling approaches for the electrostatic charging of particles”. In: *Powder Technology* (2021).

[133] Hu, S. and X. Liu. “A CFD-PBM-EMMS integrated model applicable for heterogeneous gas-solid flow”. In: *Chemical Engineering Journal* 383 (2020), p. 123122.

[134] Hu, S. and X. Liu. “CFD-PBM simulation of gas–solid bubbling flow with structure-dependent drag coefficients”. In: *Chemical Engineering Journal* 413 (2021), p. 127503.

[135] Gouesbet, G. and A. Berlemont. “Eulerian and Lagrangian approaches for predicting the behaviour of discrete particles in turbulent flows”. In: *Progress in Energy and Combustion Science* 25.2 (1999), pp. 133–159.

[136] Loha, C. et al. “Assessment of drag models in simulating bubbling fluidized bed hydrodynamics”. In: *Chemical Engineering Science* 75 (2012), pp. 400–407.

[137] Chapman, S. and T. G. Cowling. *The mathematical theory of non-uniform gases: an account of the kinetic theory of viscosity, thermal conduction and diffusion in gases*. Cambridge university press, 1990.

[138] Jenkins, J. T. and S. B. Savage. "A theory for the rapid flow of identical, smooth, nearly elastic, spherical particles". In: *Journal of fluid mechanics* 130 (1983), pp. 187–202.

[139] Johnson, P. C. and R. Jackson. "Frictional–collisional constitutive relations for granular materials, with application to plane shearing". In: *Journal of fluid Mechanics* 176 (1987), pp. 67–93.

[140] Lun, C. et al. "Kinetic theories for granular flow: inelastic particles in Couette flow and slightly inelastic particles in a general flowfield". In: *Journal of fluid mechanics* 140 (1984), pp. 223–256.

[141] Gidaspow, D. *Multiphase flow and fluidization: continuum and kinetic theory descriptions*. Academic press, 1994.

[142] Gidaspow, D. et al. *Hydrodynamics of circulating fluidized beds: kinetic theory approach*. Tech. rep. Illinois Inst. of Tech., Chicago, IL (United States). Dept. of Chemical . . ., 1991.

[143] Schaeffer, D. G. "Instability in the evolution equations describing incompressible granular flow". In: *Journal of differential equations* 66.1 (1987), pp. 19–50.

[144] Che, Y. et al. "CFD prediction of scale-up effect on the hydrodynamic behaviors of a pilot-plant fluidized bed reactor and preliminary exploration of its application for non-pelletizing polyethylene process". In: *Powder Technology* 278 (2015), pp. 94–110.

[145] Wen, C. Y. "Mechanics of fluidization". In: *Chem. Eng. Prog. Symp. Ser.* Vol. 62. 1966, pp. 100–111.

[146] Ergun, S. "Fluid flow through packed columns". In: *Chem. Eng. Prog.* 48 (1952), pp. 89–94.

[147] Al-Hashemi, H. M. B. and O. S. B. Al-Amoudi. "A review on the angle of repose of granular materials". In: *Powder technology* 330 (2018), pp. 397–417.

[148] Launder, B. and D. Spalding. "The numerical computation of turbulent flows". In: *Computer Methods in Applied Mechanics and Engineering* 3 (1974), pp. 269–289.

[149] Patankar, S. V. and D. B. Spalding. "A calculation procedure for heat, mass and momentum transfer in three-dimensional parabolic flows". In: *Numerical prediction of flow, heat transfer, turbulence and combustion*. Elsevier, 1983, pp. 54–73.

[150] Vasquez, S. "A phase coupled method for solving multiphase problems on unstructured mesh". In: *ASME 200 Fluids Engineering Division Summer Meeting*. 2000.

[151] Venkatakrishnan, V. and T. BARTH. "Application of direct solvers to unstructured meshes for the Euler and Navier-Stokes equations using upwind schemes". In: *27th Aerospace Sciences Meeting*. 1989, p. 364.

[152] Celik, I. et al. *Proceedings of numerical methods for multiphase flows*. Tech. rep. New York, NY (United States); American Society of Mechanical Engineers, 1990.

[153] Chatzidoukas, C. et al. "Optimal grade transition campaign scheduling in a gas-phase polyolefin FBR using mixed integer dynamic optimization". In: *Computer Aided Chemical Engineering*. Vol. 14. Elsevier, 2003, pp. 71–76.

[154] Zacca, J. J. et al. "Reactor residence time distribution effects on the multistage polymerization of olefins—I. Basic principles and illustrative examples, polypropylene". In: *Chemical Engineering Science* 51.21 (1996), pp. 4859–4886.

[155] Kim, J. Y. and K. Y. Choi. "Modeling of particle segregation phenomena in a gas phase fluidized bed olefin polymerization reactor". In: *Chemical Engineering Science* 56.13 (2001), pp. 4069–4083.

[156] Marchisio, D. L. et al. "Implementation of the quadrature method of moments in CFD codes for aggregation–breakage problems". In: *Chemical Engineering Science* 58.15 (2003), pp. 3337–3351.

[157] Choi, K.-Y. and W. H. Ray. "The dynamic behaviour of fluidized bed reactors for solid catalysed gas phase olefin polymerization". In: *Chemical Engineering Science* 40.12 (1985), pp. 2261–2279.

[158] Choi, K. Y. et al. "Population balance modeling for a continuous gas phase olefin polymerization reactor". In: *Journal of applied polymer science* 53.12 (1994), pp. 1589–1597.

[159] Kim, J. Y. and K. Y. Choi. "Polymer particle mixing and segregation in a gas phase olefin polymerization reactor". In: *AIChE Symposium Series*. Vol. 95. 321. New York, NY: American Institute of Chemical Engineers, 1971-c2002. 1999, pp. 77–82.

[160] Geldart, D. and A. Wong. "Fluidization of powders showing degrees of cohesiveness—I. Bed expansion". In: *Chemical Engineering Science* 39.10 (1984), pp. 1481–1488.

[161] Geldart, D. and A. Wong. "Fluidization of powders showing degrees of cohesiveness—II. Experiments on rates of de-aeration". In: *Chemical Engineering Science* 40.4 (1985), pp. 653–661.

[162] Lasa, H. de. "Chemical Reactor Design and Technology: Overview of the New Developments of Energy and Petrochemical Reactor Technologies. Projections for the 90's". In: (2012).

[163] Dompazis, G. et al. "Development of a multi-scale, multi-phase, multi-zone dynamic model for the prediction of particle segregation in catalytic olefin polymerization FBRs". In: *Chemical engineering science* 63.19 (2008), pp. 4735–4753.

[164] Elghobashi, S. and T. Abou-Arab. "A two-equation turbulence model for two-phase flows". In: *The Physics of Fluids* 26.4 (1983), pp. 931–938.

[165] Csanady, G. "Turbulent diffusion of heavy particles in the atmosphere". In: *Journal of Atmospheric Sciences* 20.3 (1963), pp. 201–208.

This Ph.D. thesis has been typeset by means of the TEX-system facilities. The typesetting engine was pdfLATEX. The document class was `toptesi`, by Claudio Beccari, with option `tipotesi=scudo`. This class is available in every up-to-date and complete TEX-system installation.